Università degli Studi di Pisa

Facoltà di Scienze Matematiche, Fisiche e Naturali

Scuola di dottorato Galilei in Fisica

Phd Thesis

Search for Direct CP violation in charged Kaons with NA48/2 experiment

Supervisors

Prof. **Italo Mannelli**

*Prof.***Giuseppe Pierazzini**

Candidate

Dott. **Gianluca Lamanna**

(XVIII ciclo)

Winter 2006

TIGER, tiger, burning bright
In the forests of the night,
What immortal hand or eye
Could frame thy fearful symmetry?
William Blake, 1757-1827

La simmetrie c'est l'ennui...
Victor Hugo, 1802-1885

Abstract

The main goal of the NA48/2 experiment, at CERN-SPS, is to investigate direct CP violation in charged Kaon decays. The most relevant effect is expected in the difference between K^+ and K^- Dalitz Plot distribution in the three pions kaon decay.
This thesis describes my analysis to measure the $K^{\pm} \to \pi^{\pm}\pi^0\pi^0$ asymmetry parameter A_g^0 using $\sim 47 \cdot 10^6$ events collected by the NA48/2 experiment during ~ 45 days in 2003.

Contents

Introduction

In spite of the fact that more than 40 years have passed since the discovery of the CP violation, the full understanding of this phenomenon is still far to be reached. After the discovery of direct CP violation in the neutral kaon decay into two pions in the early 90s, by the NA31 experiment, and the clear confirmation after few years by NA48 and KTEV experiments, CP violation in its various forms has been recently detected in the B system, in agreement with the expectation of the Standard Model. A complete as possible study of the tiny effects due to the violation of this symmetry in all the systems where it can be carried out, represents an important window on the contribution of new physics beyond the Standard Model. In fact new effects could appear in particular in the heavy quark loops which are at the core of the mechanism allowing CP violation in the decay. In the kaon sector the most promising places, besides ε'/ε, where this kind of contributions could play some role, are the rates of GIM suppressed rare decays and the charge asymmetry between charged kaons. In particular in $K^{\pm} \to 3\pi$ this asymmetry could give a strong qualitative indication of the validity of the CKM description of the direct CP violation or reveal the existence of possible sources outside of this paradigm.

Quantitative tests or predictions are, at the moment, very difficult from a theoretical point of view due to the complexity of the calculation involving non-perturbative hadronic effects. As soon as the intense theoretical efforts to improve the understanding of this sector of the particle interactions will produce tools to make reliable predictions, the experimental measurements could also be used as sensitive quantitative test.
From an experimental point of view, the easiest way to look for any possible differences between K^+ and K^- decay into three pions is to compare the *shape* of the *Dalitz plot* distribution instead of the decay rates. This dissertation is devoted to describe my analysis of the CP violation parameter A_g^0 obtained from the $K^{\pm} \to \pi^{\pm}\pi^0\pi^0$ decays, using the data taken by the NA48/2 collaboration[1] in 2003. Simultaneous high intensity K^+ and K^- beams, particular care to equalize as much as possible already at the data taking level the detector acceptance between the two charges, the use of a high resolution spectrometer and of a liquid Krypton electromagnetic calorimeter, are the key points of the experimental technique.

The thesis is organized as follows.
In **Chapter 1** the motivations for the search of CP violation in charged kaon

[1]The groups of the NA48/2 collaboration come from: Cambridge, CERN, Dubna (JINR), Chicago, Edinburgh, Ferrara, Firenze, Mainz, Evanston, Perugia, Pisa, Saclay, Siegen, Torino, Vienna

sector are discussed. After a first part introducing the importance of the symmetries in physics and in the kaon sector in particular, the phenomenology of the CP violation is briefly described. The direct CP violation in the neutral kaon decays is also briefly reviewed for completeness. In the last part of the chapter the direct CP violation in the charged kaons is presented and, finally, the experimental status before NA48/2 is presented.

Chapter 2 is devoted to describe the NA48/2 experiment. In particular the novel beam line design is sketched and commented. All the subdetectors and, in greater detail the LKr electromagnetic calorimeter are described. The data acquisition system is presented in the last part of the chapter. In the whole experiment description the strategies to reduce the charged asymmetric characteristics are outlined.

The signal selection and reconstruction procedure are presented in **Chapter 3**. Both the online and offline $K^{\pm} \to \pi^{\pm}\pi^0\pi^0$ identification are discussed. The reconstructed Dalitz plot characteristics are described in the last section.

Some corrections have to be applied on the data as described in **Chapter 4**. These corrections are obtained directly from the data exploiting the good resolution of the LKr calorimeter and of the Spectrometer. In particular the LKr corrections are shown in the first part of the chapter, while the effects due to the misalignment between the calorimeter and the spectrometer, the internal spectrometer misalignment and the contribution of the earth magnetic field, are described in the second part.

In **Chapter 5** the analysis strategy is outlined. In this chapter the experimental asymmetries of the detector that could introduce "fake" signal of CP violation are discussed. The frequent reversal of the magnetic fields polarity along the beam line and the spectrometer is the key factor for their control. The idea of the "quadruple ratio" and the method to extract Δg, defined as the difference between the linear slope parameters in K^+ and K^- Dalitz Plot density distribution as a function of the invariant mass of the pair of neutral pions, are discussed.

The results of this procedure are shown in **Chapter 6**. The data quality selection and the final statistics are presented in the first part of the chapter. In the second part some cross checks are presented following the discussion of the result for the asymmetry parameter.

In **Chapter 7** the systematic uncertainties study is discussed. Several sources of systematics are considered using different approaches. Most of the effects studied have no significant influence on the final result. The largest systematic uncertainty comes from the charged pion interaction in the LKr calorimeter.

The trigger efficiency, correction and systematics are studied in the **Chapter 8**. The measurement of the trigger system efficiency is discussed in the first part of the chapter; in the second part the systematic errors coming from the trigger chain and the techniques to reduce them are presented. The main trigger systematics comes from the neutral part of the level 1 trigger.

Finally the final result based on 2003 data sample is summarized in **Chapter 9** in which several checks on the result stability are discussed.

Three appendixes complete the dissertation: the preliminary result on the A_g^0 parameter obtained analyzing the 2004 data sample, the CP violating A_g parameter

measurement in $K^{\pm} \to \pi^{\pm}\pi^{+}\pi^{-}$ and the presence of subtle cusp effect in $K^{\pm} \to \pi^{\pm}\pi^{0}\pi^{0}$ from which it is possible to extract informations about the pion scattering lengths.

Chapter 1

Physical Motivation

Since its discovery, CP violation has been of paramount importance in the understanding of weak interactions and, in general, in the deep understanding of the nature itself. Before 1964, when the first kind of CP violation was discovered in the neutral Kaon system by Christenson, Cronin, Fitch and Turlay, the description of the weak interaction had been already modified to take into account the observation of the parity violation, by the famous Wu's experiment, using the so called "V-A" structure of the interaction. However the simultaneous application of the Charge conjugation (C) and the Parity inversion (P) was believed to be a valid symmetry (CP) of the nature. The observation of a small violation of this symmetry in the neutral kaon system was essential to redefine the structure of the Standard Model (SM).

1.1 The discrete symmetries C,P and T

Symmetries play an important role in physics. The invariance of a system with respect to a given transformation is very useful to determine the interaction structure; at the same time violation of some symmetry of the system can give important informations about the underlying process. In general a symmetry is an operation on a state that leaves the state unchanged: "... a thing is symmetrical if there is something we can do to it so that after we have done it, it looks the same as before.." (Feynman).

The continuous symmetries (the symmetries which are continuously connected with the identity) can be related to a conservation law, as stated by Noether's theorem [1]. For example the space homogeneity (spatial translation) is related to the conservation of momentum as well the homogeneity of the time leading to energy conservation.

The discrete symmetries are different with respect to the continuous symmetries because they are not continuously connected with the identity transformation. The important point in the discrete symmetries is that they can be *violated*.

The main three discrete symmetries are:

- **Parity (P)**: The Parity symmetry corresponds to the macroscopic invariance of the systems with respect to the change of the arbitrary definition of left and

right. Mathematically speaking this consists of invariance under the operation:

$$\vec{x} \rightarrow \vec{x}' = -\vec{x}$$

The different behaviour of the physical quantities under parity reflection allows for a classification. For instance $\vec{r}$ (position) or $\vec{p} = d\vec{r}/dt$ (momentum) will be called *vector* because they change sign due to the parity, while the angular momentum $\vec{L} = \vec{r} \wedge \vec{p}$ will be called *pseudo-vector* because it does not change sign. The scalar quantities will be called *scalar* or *pseudo-scalar* if they do not change or change sign respectively, under the transformation. In quantum mechanics a parity operator P is defined, for which the particles are eigenstates. According to their eigenvalue, the particles are classified as vector, pseudo vector, scalar or pseudo scalar. The parity is a good quantum number in all the processes driven by the electromagnetic and strong interaction. The best limit on parity violation in electromagnetic interactions comes from searches of the electric dipole moment of the electron $(0.07 \pm 0.07) \cdot 10^{-26}$ e cm [2]. Test of the P invariance in processes due to the strong interactions is given by upper limits in the research for the decay of the η particle in an even number of pions (for instance[5] $BR(\eta \rightarrow \pi^+\pi^-) < 1.3 \cdot 10^{-5}$, CL=90% and $BR(\eta \rightarrow 4\pi^0) < 6.9 \cdot 10^{-7}$, CL=90%). Concerning the weak interactions, Parity is not a good quantum number as will be discussed below.

- **Charge Conjugation (C)**: For historical reasons the interchanging of particle and antiparticle is called *charge conjugation*. In spite of this name, the C operation can be also applied to the neutral particles, like the neutron. This operation reverses the internal quantum numbers: electric charge, colour, hypercharge, baryon or lepton number, but leaves the space-time coordinates and the momentum unchanged. Only particles that coincide with their antiparticles are eigenstates of the charge conjugation. These particles (for instance the π^0 and the η) are useful to test the invariance of the interactions with respect to the charge conjugation. The eigenvalue -1 is assigned to the photon for classical reasons. In this way, thanks to the dominant $\pi^0 \rightarrow \gamma\gamma$ decay, the C=1 can be assigned to the π^0. The final state of electromagnetic decay $\pi^0 \rightarrow 3\gamma$ has the wrong C parity and the search for it sets the limit on the C violation in the electromagnetic interaction $BR(\pi^0 \rightarrow 3\gamma) < 3.1 \cdot 10^{-8}$ CL=90% . In the same way the non observation of the $\omega \rightarrow 3\pi^0$ decay is compatible with C conservation in strong interactions. Weak interactions do not preserve the charge conjugation quantum number.

- **Time reversal (T)**: The *time reversal* is the transformation

$$t \rightarrow t' = -t \ .$$

The application of the anti-unitary operator T acts changing the sign of the momenta and the angular momenta (like spin) and swapping, in a reaction, the initial and final state. Limits on the invariance of the electromagnetic interactions under time reversal come from electric dipole moment experiment. The weak interaction is not invariant under time reversal as shown directly by the CPLEAR experiment [3].

Up to 1957 the C,P,T discrete symmetries were assumed exact in every interaction, but the observation of symmetry breaking effect in the weak interactions led the physicist to formulate a new theory.

The first problem concerning the parity violation in the weak interactions was pointed out by Lee and Yang in 1956 [7] looking for the solution to the so called $\theta - \tau$ *puzzle*. θ and τ were the names given to two weak decaying particles with the same mass, lifetime, charge, spin and production cross section, but distinguishable by the opposite parity of the final state:

$$\begin{array}{l} \theta^+ \rightarrow \pi^+\pi^0 \text{ (P=+1)} \\ \tau^+ \rightarrow \left\{ \begin{array}{c} \pi^+\pi^+\pi^- \\ \pi^+\pi^0\pi^0 \end{array} \right\} \text{ (P=-1)} \end{array} \tag{1.1}$$

The alternative suggested by Lee and Yang was that the θ and τ particles were actually the same particle[1] and that parity was not conserved in the weak interaction. In fact they found in the literature experimental evidence for parity conservation in strong and electromagnetic interactions but not for the weak interactions. Then they proposed a series of experimental tests to check the invariance of the parity in processes driven by the weak interaction. The first experiment to be carried out was performed by madame Wu and others [6] in the 1956 by measuring the spatial distribution of the electron, produced from a weak process (the β decay), in the reaction:

$$^{60}Co \rightarrow ^{60} Ni^* + e + \nu$$

where the spin of the $^{60}Co \rightarrow$ atoms was carefully aligned. The fact that most of the electrons of the beta decay came out in a fixed direction with respect to the cobalt's spin (the photons isotropy in the secondary reaction $^{60}Ni^* \rightarrow ^{60} Ni + \gamma$ was used as reference) was an indication of parity violation. It was immediately clear that this violation is maximal, in the sense that only the left handed component of the particle wave function (the right one for the antiparticles) takes part in the weak Hamiltonian. This fact has been confirmed by the observation that the helicity of the neutrino, that interacts only by weak interaction, is fixed and equal to -1 [8]. In the Hamiltonian of the weak interaction the leptonic current enters with both vectorial and axial terms in the form $\bar{\psi_e}\gamma^\mu(1-\gamma^5)\psi_\nu$, in the so called *V-A* coupling. The non-existence of the right-handed neutrino is also an evidence of C violation. Anyway the simultaneous operation of charge conjugation and parity, the so called **CP**, recovers the symmetry as is schematically show in fig. 1.1 for the decay of the charged pions in a muon and a neutrino. The symmetry CP was then assumed to be conserved in all kinds of interactions.

To test experimentally this assumption, in 1964 Christenson, Cronin, Fitch and Turlay [9] undertook an experiment to look for the CP forbidden process $K_L \rightarrow \pi^-\pi^+$. Unexpectedly they observed the signal showing that also CP is not a good symmetry for the weak interaction.

G.Luders, in 1954, published [10] the first demonstration that under very general assumption, in a local quantum field theory, the combined operation CPT must be

[1] Today this particle is called K^+.

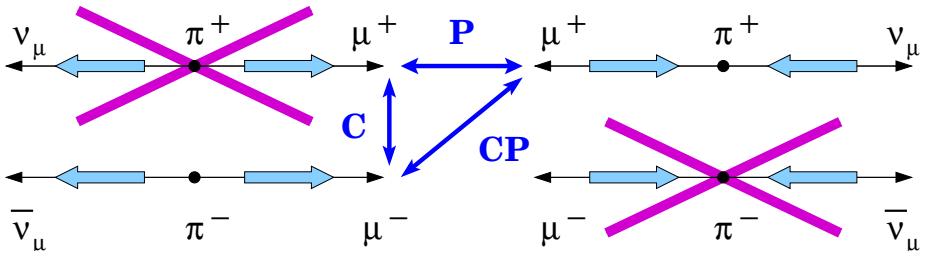

Figure 1.1: Pion decay in muon and neutrino. Only left-handed neutrino and right-handed anti-neutrino has been observed.

a good symmetry. Other authors [11] played a role in the formulation of the so called *CPT theorem*. The specific requirements for this theorem to hold are that if a quantum field theory:

- is "local"
- has a state of minimum energy
- has total probabilities which do not change in time
- has a finite number of point-like particles

as a consequence:

- particles and their respective antiparticles must have equal mass, lifetime and coupling constant;
- particles and antiparticles must also have opposite charges and magnetic moments;
- the observation of CP violation is also an indirect observation of T violation.

The validity of the CPT theorem is tested by looking for a difference between particles and antiparticles in terms of mass or lifetime. At the moment the best measurement of the validity of the CPT theorem comes from the measurement in the neutral kaon system of $|m_{K^0} - m_{\bar{K}_0}|/m_{K^0}$ which is smaller than one part in 10^{18} [12] . The CPT invariance can be also tested by different methods such as anti-hydrogen spectroscopy (this method is used by the ATHENA experiment at CERN [13]), in trapped ions experiment (WASHINGTON-ATOMIC experiment [14]) or by studying the electron-positron system [15].

Several parameters connected with the CPT conservation test have been measured by the CPLEAR experiment [16] [17]. The same experiment has published the most direct observation of the T violation in the kaon system [18]. The CPT violation experiments are an useful test for the SM and a mean to look for Physics beyond the SM since several models including gravity (like the String Theory for example) are not locally gauge invariant and hence they are not subjected to the CPT theorem.

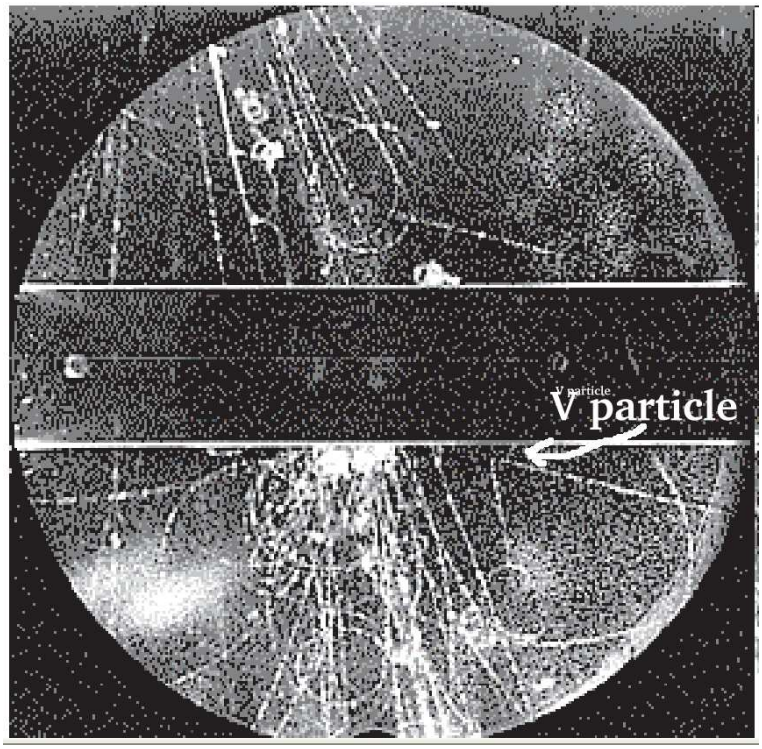

Figure 1.2: First observation of a V particle in a cloud chamber in 1944

1.2 The Kaon System

Around the 1940 some unusual events were found while studying the interaction of cosmic ray particles in a thin layer of Pb in a cloud chamber [19] [20] (fig. 1.2) . The events observed were compatible with the production (through strong interaction) of some new particle (called V because of the topology of the decay) which decayed in few cm, and had thus a lifetime of $10^{-10 \text{ to } -8}$ s, compatible with what could be expected for decays induced by weak interaction. The phenomenology of this particle (which occurred in the negative, positive and neutral version) suggested the introduction of a new quantum number, the *strangeness* (S), conserved in strong (and electromagnetic) interactions but not in weak interactions. Nowadays we know that the V particles are, mainly, *K mesons*, the most common strange meson system, and Λ hyperons. The kaons are produced by strong interaction in "associated production" with strange baryons (hyperons) or other kaon, in order to conserve strangeness. Examples of kaon production reactions are:

$$\begin{aligned}
\pi^- p &\rightarrow \Lambda^0 K^0 \\
\bar{p}p &\rightarrow K^+ \pi^- \bar{K^0} \\
\bar{p}p &\rightarrow K^0 \bar{K^0} \\
\bar{p}p &\rightarrow K^+ K^- \\
pp &\rightarrow K^+ \bar{K^0} \pi^+
\end{aligned}$$

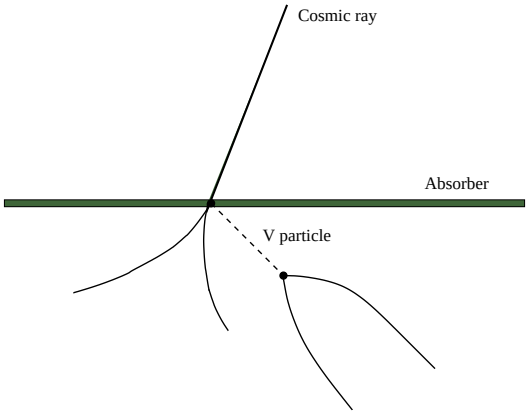

Figure 1.3: Production in a thin absorber by a cosmic ray and decay of a neutral kaon in a pion pair $K^0 \to \pi^+\pi^-$. The neutral kaon is undetectable seen in the cloud chamber, but the decay product can be identified as pions by measuring the deflection in a magnetic field.

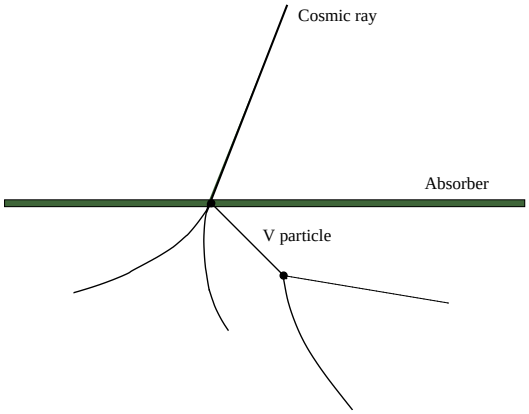

Figure 1.4: The charged Kaon is identified by a charged track in the cloud chamber. The neutrino in the $K^+ \to \mu^+\nu$ is invisible.

In the present phenomenological description the kaons as flavour eigenstates are expressed in terms of quark content as:

$$|K^0 >= \bar{s}d \quad |\bar{K^0} = s\bar{d} \quad |K^+ >= \bar{s}u \quad |K^- >= s\bar{u}$$

At the quark level the strangeness assignment is S=+1 for the $\bar{s}$ quark and S=-1 for the s quark, in such way K^0 and K^+ have S=+1 and the $\bar{K^0}$ and K^- have S=-1. According to the Gell-Mann-Nishijima formula[2]:

$$Q = I_3 + \frac{B+S}{2}$$

the kaons and the antikaons are grouped in two isodoublets:

$$K = \begin{pmatrix} K^+ \\ K^0 \end{pmatrix} \qquad \bar{K} = \begin{pmatrix} K^- \\ \bar{K^0} \end{pmatrix} \tag{1.2}$$

It is important to notice that in this definition the kaons are not eigenstates of the C charge conjugation. However the possibility exists, and was introduced by Pais and Piccioni in 1955 [21], of considering coherent mixtures of neutral kaons and antikaons which are CP eigenstate.

The kaons are the lightest strange mesons and therefore they decay only via weak interaction (which does not conserve S); this makes the kaon system (both the neutral and charged one) an excellent laboratory to study the properties of this interaction, also because, in spite of the fact that the kaons are not present in the ordinary matter, it is quite easy to produce them at GeV energies in accelerators.

[2]The quantity Y=B+S is called *Hypercharge*, B is the so called baryon number (0 for mesons), I_3 is the third component of the isotopic spin, Q is the electric charge

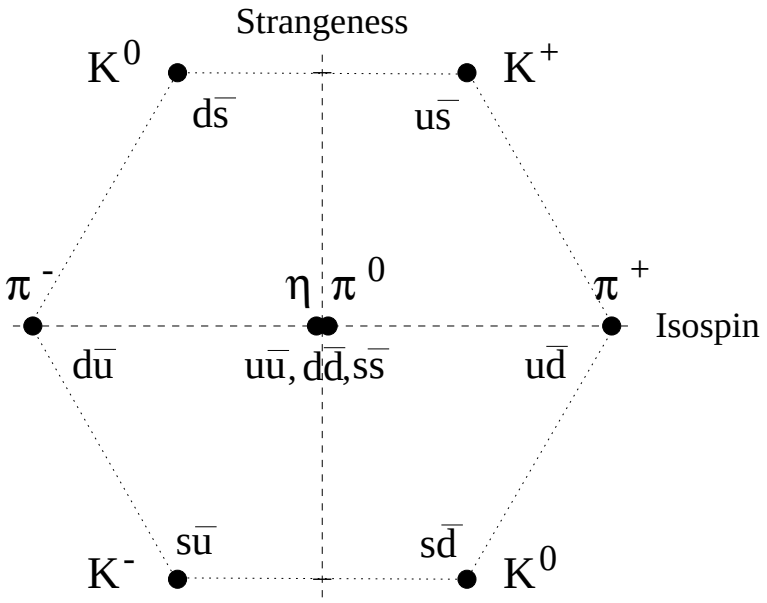

Figure 1.5: The pseudo-scalar ($J^P = 0^-$ meson octet in the SU(3) representation.

Another way to produce kaon, is the weak decay of the Φ meson. Indeed this meson, that is a $s\bar{s}$ system with $J^{PC} = 1^{--}$, decays in a pair of kaons with a BR of[3]:

$$\begin{array}{ll} \Phi \to K^+K^- & BR : (49.1 \pm 0.6)\% \\ \Phi \to K^0_S K^0_L & BR : (34.0 \pm 0.5)\% \end{array}$$

The idea to use this particle to massively produce charged and neutral kaons is exploited in the Φ *factory*, where the Φ's are produced using the reaction $e^+e^- \to \gamma \to s\bar{s}$ at the the resonance energy (1020 MeV). Practically a symmetric e^+e^- collider with a single beam energy of 510 MeV is used to produce Φ almost at rest and a 4π detector around the interaction point is used to observe the kaon decay (see the KLOE experiment [22]).

1.2.1 The neutral kaons

The strong eigenstates of the neutral kaons are K^0 and $\bar{K^0}$ as defined above, but the observed physical states are the so called K_L and K_S. The subscript L and S comes from the observation that these two state, that are quasi-CP eigenstates, have a very different lifetime (Long and Short). Indeed for the K_L and K_S we have that $\tau_L = (5.114 \pm 0.021) \cdot 10^{-8}$ and $\tau_S = (8.953 \pm 0.006) \cdot 10^{-11}$ respectively [5]. In spite of this relevant difference the mass of the two states is quite similar $m_{K^0} = m_L \simeq m_S = (497.648 \pm 0.022) MeV/c^2$ with $\Delta m_K = m_L - m_S = (3.483 \pm 0.006) \cdot 10^{-12} MeV/c^2$.

Due to the fact that K^0 and $\bar{K^0}$ are the antiparticles of each other, they are

[3]The subscript S and L for the neutral kaons will be explain in the following.

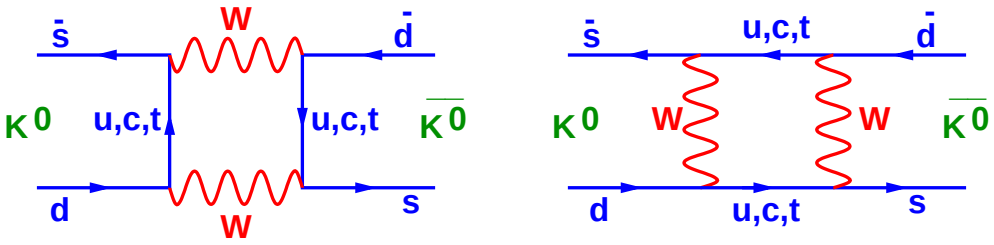

Figure 1.6: The box diagrams describing the $\Delta S = 2$ transition, responsible of the $K^0 - \bar{K}^0$ missing.

related through CP transformations:[4]:

$$\begin{aligned} CP|K^0> &= -|\bar{K}^0> \\ CP|\bar{K}^0> &= -|K^0> \end{aligned} \tag{1.3}$$

By using these relations, it is possible to define CP eigenstates in this way:

$$\begin{aligned} |K_1> &= \sqrt{\tfrac{1}{2}}(|K^0> - |\bar{K}^0>) \\ |K_2> &= \sqrt{\tfrac{1}{2}}(|K^0> + |\bar{K}^0>) \end{aligned} \tag{1.4}$$

Indeed, from the (1.3), it is clear that:

$$\begin{aligned} CP|K_1> &= +1|K_1> \\ CP|K_2> &= -1|K_2> \end{aligned} \tag{1.5}$$

usually $|K_1>$ and $|K_2>$ are referred as *CP even* and *CP odd* eigenstates of the neutral kaons.

The K^0 and $\bar{K}^0$ cannot decay by strong interaction because are the lightest strange mesons, so the only way to decay is through the weak interaction. Thanks to the weak interaction they can mix with the $\Delta S = 2$ process illustrated in the "box diagrams" (fig. 1.6). The evolution of any state is described by the Schrodinger equation:

$$i\frac{\partial}{\partial t}|\psi(t)> = \mathcal{H}_{eff}|\psi(t)>$$

The Hamiltonian $\mathcal{H}_{eff}$ is not Hermitian, but it can be written as the sum of a hermitian matrix (M) and an anti-hermitian matrix (-iΓ/2):

$$\mathcal{H}_{eff} = M - i\frac{\Gamma}{2}$$

where the mass matrix M represents the interactions of K^0 and $\bar{K}^0$ due to strong interaction and the weak $\Delta S = 2$ transition and the decay matrix Γ represents the component of the weak amplitude in which $\Delta S = 1$. The elements of this matrix

[4]The relative phase of $|K^0>$ and $|\bar{K}^0>$ is arbitrary and any physical quantities is independent of its choice.

could be written in terms of the transition amplitude between the $|K^0>$ and $|\bar{K^0}>$ as:

$$\begin{array}{lll} (\mathcal{H}_{eff})_{11} = & M_{11} - \frac{i}{2}\Gamma_{11} = & < K^0|\mathcal{H}_{eff}|K^0 > \\ (\mathcal{H}_{eff})_{12} = & M_{12} - \frac{i}{2}\Gamma_{12} = & < \bar{K^0}|\mathcal{H}_{eff}|K^0 > \\ (\mathcal{H}_{eff})_{21} = & M_{21} - \frac{i}{2}\Gamma_{21} = & < K^0|\mathcal{H}_{eff}|\bar{K^0} > \\ (\mathcal{H}_{eff})_{22} = & M_{22} - \frac{i}{2}\Gamma_{22} = & < \bar{K^0}|\mathcal{H}_{eff}|\bar{K^0} > \end{array} \tag{1.6}$$

Thanks to the hermiticity of the matrix M and Γ and by applying the invariance under CPT transformation, the $\mathcal{H}_{eff}$ could be written as:

$$\mathcal{H}_{eff} = \begin{pmatrix} M_0 - \frac{i}{2}\Gamma_0 & M_{12} - \frac{i}{2}\Gamma_{12} \\ M_{12}^* - \frac{i}{2}\Gamma_{12}^* & M_0 - \frac{i}{2}\Gamma_0 \end{pmatrix} \tag{1.7}$$

The eigenstates of this Hamiltonian are the physical observed states $|K_S>$ and $|K_L>$:

$$\begin{aligned} |K_S> &= \frac{1}{\sqrt{|p|^2+|q|^2}}(p|K^0> + q|\bar{K^0}>) \\ |K_L> &= \frac{1}{\sqrt{|p|^2+|q|^2}}(p|K^0> - q|\bar{K^0}>) \end{aligned} \tag{1.8}$$

and p and q related by:

$$\frac{p}{q} = \sqrt{\frac{M_{12} - \frac{i}{2}\Gamma_{12}}{M_{12}^* - \frac{i}{2}\Gamma_{12}^*}}$$

Using eq. (1.4) in eq. (1.8) it is also possible to write the states $|K_S>$ and $|K_L>$ in terms of the CP eigenstates $|K_1>$ and $|K_2>$:

$$\begin{aligned} |K_S> &= \frac{1}{\sqrt{2(|p|^2+|q|^2)}}((p+q)|K_1> + (p-q)|K_2>) \\ |K_L> &= \frac{1}{\sqrt{2(|p|^2+|q|^2)}}((p-q)|K_1> + (p+q)|K_2>) \end{aligned} \tag{1.9}$$

By defining $\bar{\varepsilon} = (p-q)/(p+q)$, the previous equations can be written as:

$$\begin{aligned} |K_S> &= \frac{1}{\sqrt{1+|\bar{\varepsilon}|}}(|K_1> + \bar{\varepsilon}|K_2>) \\ |K_L> &= \frac{1}{\sqrt{1+|\bar{\varepsilon}|}}(|K_2> + \bar{\varepsilon}|K_1>) \end{aligned} \tag{1.10}$$

If $Re(bar\varepsilon) = 0$ (i.e. $|p/q| = 1$) the physical states $|K_S>$ and $|K_L>$ coincide with the CP eigenstates $|K_1>$ and $|K_2>$. In case $Re(\bar{\varepsilon} \neq 0)$ the eigenstates of the time propagation $|K_S>$ and $|K_L>$ are not eigenstates of CP and this means that CP violation occurs in the mixing of $|K_S>$ and $|K_L>$.

1.2.2 The charged Kaons

In the charged kaons system a mixing mechanism is not possible because of the different electric charge of K^+ and K^-. Hence only CP violation in the decay (*direct violation*) can occur.

The charged kaons, with a mass of $(493.677 \pm 0.016) MeV/c^2$, are easily produced by strong interaction and decay by weak interaction with a mean life time of [5] $(1.2385 \pm 0.0024) \cdot 10^{-8}$, mainly in the leptonic mode with a muon ($K \to \mu\nu$, also know as $K_{\mu 2}$ mode) and in a pair of pions ($K \to \pi\pi^0$, also know as $K_{\pi 2}$ mode or θ^+ mode). In the $\sim 7\%$ of the total the charged kaons decay in three pions ($K \to 3\pi$, also know as $K_{3\pi}$). The two 3π modes, the "charged" mode ($K^\pm \to \pi^\pm\pi^+\pi^-$ or the τ mode) and the "neutral" mode ($K^\pm \to \pi^\pm\pi^0\pi^0$ or the τ' mode) are the most promising places in which CP violation could be detected, as explained in par. 1.5 .

Channel	BR
$e^+\nu_e$	$(1.55 \pm 0.07) \cdot 10^{-5}$
$mu^+\nu_\mu$	$(63.44 \pm 0.14)\%$
$\pi^0 e^+\nu_e$	$(4.98 \pm 0.07)\%$
$\pi^0\mu^+\nu_\mu$	$(3.32 \pm 0.06)\%$
$\pi^0\pi^0 e^+\nu_e$	$(2.2 \pm 0.4) \cdot 10^{-5}$
$\pi^+\pi^- e^+\nu_e$	$(4.09 \pm 0.09) \cdot 10^{-5}$
$\pi^+\pi^-\mu^+\nu_\mu$	$(1.4 \pm 0.9) \cdot 10^{-5}$
$\pi^+\pi^0$	$(20.92 \pm 0.12)\%$
$\pi^+\pi^0\pi^0$	$(1.757 \pm 0.0024)\%$
$\pi^+\pi^+\pi^-$	$(5.590 \pm 0.0031)\%$
$\pi^0 e^+\nu_e\gamma$	$(2.69 \pm 0.20) \cdot 10^{-4}$
$\pi^+\pi^0\gamma$	$(2.75 \pm 0.15) \cdot 10^{-4}$

Table 1.1: Branching ratio of the main charged kaon decay modes [5].

1.3 CP violation in the Standard Model

In the Standard Model CP violation arises from the fact that the eigenstates of the weak interaction differ from the eigenstates of the strong interaction[5]. This is formalized in the quark mixing matrix, the Cabibbo-Kobayashi-Maskawa (CKM) matrix [23][24] , with a single complex phase.

The CKM matrix can be write as:

$$V_{CKM} = \begin{pmatrix} V_{ud} & V_{us} & V_{ub} \\ V_{cd} & V_{cs} & V_{cb} \\ V_{td} & V_{ts} & V_{tb} \end{pmatrix} \tag{1.11}$$

[5]This condition is necessary but not sufficient

In the SM the interaction of quarks with gauge bosons of the electroweak sector is described by:

$$\mathcal{L} = -i\frac{g_W}{2\sqrt{2}}\sum_{i,j}\bar{u_i}'\gamma^\mu(1-\gamma^5)d_j' W_\mu^+ + h.c. \tag{1.12}$$

where the u_i^i and the d_i' are the weak eigenstates of the *up-type* (u,c,t) and *down-type* (d,s,b) quarks respectively and $i,j = 1,2,3$ run over the quark generations. The eigenstates of strong interaction (as mass eigenstates) can be written as a linear combination of the weak eigenstates as:

$$u_i = \sum_{i'=1}^{3} V_{ii'}u_{i'}' \qquad d_j = \sum_{j'=1}^{3} V_{jj'}d_{j'}' \tag{1.13}$$

Where the matrix V is a generic 3x3 matrix. By using eq. (1.13), the Lagrangian eq. (1.12) becomes:

$$\mathcal{L} = -i\frac{g_W}{2\sqrt{2}}\sum_{i,j}(V_{jk}V_{ki})\bar{u_i}\gamma^\mu(1-\gamma^5)d_j W_\mu^+ + h.c. \tag{1.14}$$

this gives the definition for the CKM matrix as presented in eq. (1.11).

The Field Theory requires (for the total probability conservation) this matrix to be unitary ($V_{CKM}\cdot V_{CKM}^\dagger = 1$). In general a 3×3 unitary matrix has 3 real parameters and 6 phases, but in the case of the quark fields only the relative phase among the eigenstates could be observed; only a phase is free, the other 5 phases can be absorbed in the re-phasing of the CKM elements[6]. Therefore the CKM matrix could be parameterized by using three rotation angles $(\theta_{12},\theta_{13},\theta_{23})$ and one single phase (δ):

$$V_{CKM} = \begin{pmatrix} c_{12}c_{13} & s_{12}c_{13} & s_{13}e^{-i\delta} \\ -s_{12}c_{23} - c_{12}s_{23}s_{13}e^{i\delta} & c_{12}c_{23} - s_{12}s_{23}s_{13}e^{i\delta} & s_{13}c_{13} \\ s_{12}s_{23} - c_{12}s_{23}s_{13}e^{i\delta} & -c_{12}s_{23} - s_{12}c_{23}s_{13}e^{i\delta} & c_{23}c_{13} \end{pmatrix} \tag{1.15}$$

where $c_{ij} = cos\theta_{ij}$ and $s_{ij} = sin\theta_{ij}$. From experimental results it can be deduced that the mixing angles have a hierarchical structure and the matrix can be expressed with the so called *Wolfenstein expansion* [25], in which the parameters are A,λ,ρ and η. In particular the parameter $\lambda = sin\theta_{12} = |V_{us}|$ (where the quantity θ_{12} is called "Cabibbo angle"). With these parameters at order λ^3, the Wolfenstein parametrization is:

$$V_{CKM} = \begin{pmatrix} 1-\frac{\lambda^2}{2} & \lambda & A\lambda^3(\rho - i\eta(1-\frac{\lambda^2}{2})) \\ -\lambda & 1-\frac{\lambda^2}{2} - i\eta A^2\lambda^4 & A\lambda^2(1+i\eta\lambda^2) \\ A\lambda^3(1-\rho-i\eta) & -A\lambda^2 & 1 \end{pmatrix} \tag{1.16}$$

It is quite easy to see that the imaginary parameter η (connected with the complex phase δ) is the responsible for the CP violation in the CKM matrix. In fact, starting from the eq. (1.14), we can explicitly write down the terms of the sum as:

$$V_{ij}\bar{u_i}\gamma^\mu(1-\gamma^5)d_j W_\mu^+ + V_{ij}^*\bar{d_j}\gamma^\mu(1-\gamma^5)u_i W_\mu^- \tag{1.17}$$

[6]It is important to remark that a complex phase is allowed because there are at least three quark families, while in case of only 2 quark families no non trivial phase can be present.

where now V_{ij} is the CKM matrix. Under CP transformation the terms in equation (1.17) transform as:

$$\begin{array}{rcl} W_\mu^\pm & \rightarrow & -(-1)^\mu W_\mu^\mp \\ \bar{u_i}\gamma^\mu d_j & \rightarrow & -(-1)^\mu \bar{d_j}\gamma^\mu u_i \\ \bar{u_i}\gamma^\mu\gamma^5 d_j & \rightarrow & -(-1)^\mu \bar{d_j}\gamma^\mu\gamma^5 u_i \end{array} \tag{1.18}$$

with similar transformation for the d term. By using the relations above the eq. (1.17) becomes, under CP conjugation:

$$V_{ij}\bar{d_j}\gamma^\mu(1-\gamma^5)u_i W_\mu^- + V_{ij}^*\bar{u_i}\gamma^\mu(1-\gamma^5)d_j W_\mu^+ \tag{1.19}$$

The two equations (1.17) and (1.19) are the same (CP invariance) only if the matrix $V_{ij} = V_{ij}^*$, that is if the matrix elements are real. This happens if

- The masses of the quarks with the same charge are equal;
- One of the three real parameters is 0 or $\pi/2$;
- The single complex phase is 0 or π.

The first condition is due to the fact that if two quark masses are equal, the relative phase between the two quarks can be removed. Thanks to the experimental observation that quarks equally charged have very different masses, we concentrate on the last two conditions. They are both obvious considering the eq. (1.16), but to summarize these conditions it is useful to define the parameter:

$$\begin{array}{l} \mathcal{I}m[V_{ij}V_{kl}V_{il}^*V_{kj}^*] = J\sum_{m,n=1}^{3}\varepsilon_{ikm}\varepsilon_{jln} \qquad \text{for any choice of } i,j,k,l = 1,2,3 \\ J = c_{12}c_{23}c_{13}^2 s_{12}s_{23}s_{13}sin\delta \end{array} \tag{1.20}$$

This parameter, introduced by Jarlskog [26], is different from zero if there is CP violation in the standard model. The Jarlskog CP parameter has a interesting geometrical interpretation. From the unitarity condition of the CKM matrix $V_{CKM}^\dagger V_{CKM} = 1$ follows that have to be valid the following relations obtained considering the orthogonality between the columns:

$$\begin{array}{l} V_{ud}V_{us}^* + V_{cd}V_{cs}^* + V_{td}V_{ts}^* = 0 \\ V_{us}V_{ub}^* + V_{cs}V_{cb}^* + V_{ts}V_{tb}^* = 0 \\ V_{ud}V_{ub}^* + V_{cd}V_{cb}^* + V_{td}V_{tb}^* = 0 \end{array} \tag{1.21}$$

and between the rows:

$$\begin{array}{l} V_{ud}V_{cd}^* + V_{us}V_{cs}^* + V_{ub}V_{cb}^* = 0 \\ V_{cd}V_{td}^* + V_{cs}V_{ts}^* + V_{cb}V_{tb}^* = 0 \\ V_{ud}V_{td}^* + V_{us}V_{ts}^* + V_{ub}V_{tb}^* = 0 \end{array} \tag{1.22}$$

Each of these relations define a *triangle* on the complex plane. In the fig. 1.7 the triangle derived from the third relation in eq. (1.21) is shown[7]. Using the Wolfenstein

[7]Someone of this triangles is not easily representable because one of the terms is much larger than the others.

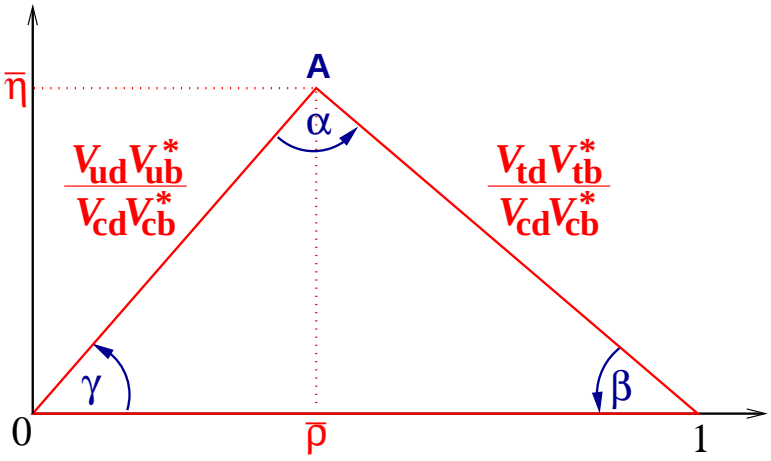

Figure 1.7: The unitary triangle. The sides of the triangle have been rescaled according to $V_{cd}V_{cb}^*$.

representation (1.16) the three terms for this triangle could be written as:

$$\begin{aligned} V_{ud}V_{ub}^* &= A\lambda^3(\bar{(}\rho + i\eta)) \\ V_{cd}V_{cb}^* &= -A\lambda^3 \\ V_{td}V_{tb}^* &= A\lambda^3(1-\bar{\rho}-i\bar{\eta}) \end{aligned} \tag{1.23}$$

where

$$\bar{\rho} = \rho(1-\frac{\lambda^2}{2}) \qquad \bar{\eta} = \eta(1-\frac{\lambda^2}{2})$$

Then the sides of the triangle can be written as (normalizing the base to 1):

$$0\bar{A} = -\frac{V_{ud}V_{ub}^*}{V_{cd}V_{cb}^*} = \bar{\rho}+i\bar{\eta} \qquad \bar{AB} = -\frac{V_{td}V_{tb}^*}{V_{cd}V_{cb}^*} = 1-\bar{\rho}-i\bar{\eta}$$

and also the angles could be defined as:

$$\alpha = arg\left[-\frac{V_{td}V_{tb}^*}{V_{ud}V_{ub}^*}\right] \qquad \beta = arg\left[-\frac{V_{cd}V_{cb}^*}{V_{td}V_{tb}^*}\right] \qquad \gamma = arg\left[-\frac{V_{ud}V_{ub}^*}{V_{cd}V_{cb}^*}\right] \tag{1.24}$$

It can be shown that the Jarlskog parameter [28], that in the Wolfenstein representation can be expressed as:

$$J \sim \lambda(1-\frac{\lambda^2}{2})A^2\lambda^5\eta$$

is related to the area of the unitary triangles, $Area = |J|/2$, different from 0 only if there is CP violation in the CKM matrix.

The CKM matrix is very important to understand the dynamics of quarks and the CP violation is a fundamental ingredient in this investigation. The matrix elements are evaluated mainly by using B and K decays that are sensitive to quark coupling. For the magnitude of the elements of the CKM matrix the experimental

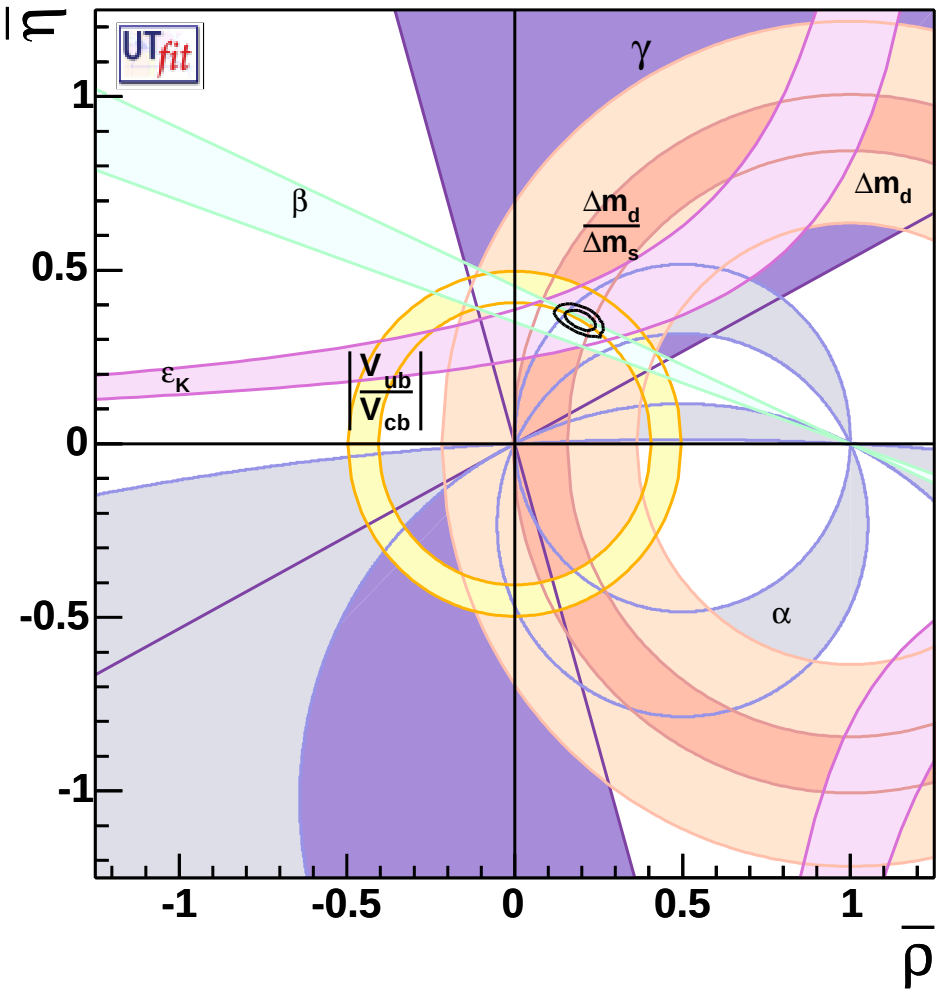

Figure 1.8: The unitarity triangle as obtained with a global fit to the experimental data from the UTFIT collaboration [27]. The position of the vertex is represented with an elliptical contour.

situation at the moment is the following [5]:

$$V_{CKM} = \begin{pmatrix} 0.9736 \text{ to } 0.97407 & 0.2262 \text{ to } 0.2282 & 0.00387 \text{ to } 0.00405 \\ 0.2261 \text{ to } 0.2281 & 0.97272 \text{ to } 0.9732 & 0.04141 \text{ to } 0.04231 \\ 0.0075 \text{ to } 0.00846 & 0.04083 \text{ to } 0.04173 & 0.999096 \text{ to } 0.999134 \end{pmatrix} \tag{1.25}$$

The pictorial representation of the present situation is shown in fig. 1.8, in which the unitary triangle defined above is presented.

1.3.1 Types of CP violation

In the previous section the possibility to explain CP violation in the framework of the standard model has been presented, but nothing was said about the mechanism from

which the CP violation arises. In a specific channel CP violation could be generated at different levels in the weak decay process and could influence the amplitude with $\Delta S = 1$ or $\Delta S = 2$ contributions.

In a given reaction of the decay of a pseudo-scalar meson P^0 into a hadronic final state f, the weak Lagrangian can be written as:

$$A_f = \sum_j A_j e^{i\phi_j} e^{i\delta_j} \tag{1.26}$$

i.e. a sum of the weak terms, in which, besides the weak phase Φ, a strong phase δ (Fermi-Thomas theorem) has been included to take into account the strong re-scattering in the final state. The relation above transforms under the application of the CP operator as:

$$\bar{A}_f = \sum_j A_j e^{-i\phi_j} e^{i\delta_j} \tag{1.27}$$

The sign of the weak phases changes due to the CP conjugation, while the strong phases are left unchanged. By using the previous equation it is possible to define the different kinds of CP violation as in the following:

- **CP violation in Mixing.** This occurs when the weak eigenstates are not identical to the CP eigenstates. In the par. 1.2.1 we have already presented a system in which the Mixing could happens: the neutral kaons. In the case in which $|p/q| \neq 1$ in the eq. (1.9) the physical eigenstate are not the same that the CP eigenstate . This kind of CP violation could be observed by looking at the decay rates of two weak eigenstates P_1 ans P_2 in a common final state f and computing, for instance, an asymmetry parameter:

  $$a = \frac{\Gamma(P_1 \to f) - \Gamma(P_2 \to f)}{\Gamma(P_1 \to f) + \Gamma(P_2 \to f)} = \frac{1 - |p/q|^4}{1 + |p/q|^4}$$

  Due to the fact that this kind of CP violation is an effect not directly present in the decay amplitude is also know as *indirect CP violation*. For instance the semileptonic decays of neutral B and K mesons exhibit exclusively this kind of asymmetry.

- **CP violation in Decay.** This kind of CP violation occurs if the decay amplitude of the decay $P \to f$ is not equal to that of its CP conjugate decay $\bar{P} \to \bar{f}$, that is $|A_f/\bar{A}_{\bar{f}} \neq 1|$. Also in this case an asymmetry parameter could be defined as in the previous case:

  $$a = \frac{\Gamma(P \to f) - \Gamma(\bar{P} \to \bar{f})}{\Gamma(P \to f) + \Gamma(\bar{P} \to \bar{f})} = \frac{1 - |\bar{A}_{\bar{f}}/A_f|^2}{1 + |\bar{A}_{\bar{f}}/A_f|^2} \tag{1.28}$$

  We can expand the amplitude ratio by using the relations (1.26) and (1.27):

  $$|\frac{\bar{A}_{\bar{f}}}{A_f}| = |\frac{\sum_j A_j e^{-i(\phi_j - \delta_j)}}{\sum_j A_j e^{i(\phi_j + \delta_j)}}| \tag{1.29}$$

  It is evident from eq. (1.29) that CP violation requires the presence of at least two weak processes contributing to the amplitude (if there is only a process

the last equation gives $A_f/\bar{A}_{\bar{f}} = 1$. For example in the case of two weak and strong phases in the amplitude:

$$\begin{array}{l} A(P \to f) = |A_1|e^{i\phi_1}e^{i\delta_1} + |A_2|e^{i\phi_2}e^{i\delta_2} \\ A(\bar{P} \to \bar{f}) = |A_1|e^{-i\phi_1}e^{i\delta_1} + |A_2|e^{-i\phi_2}e^{i\delta_2} \end{array} \tag{1.30}$$

the asymmetry parameter defined in eq. (1.28) gives:

$$\begin{aligned} a &= \frac{2|A_1||A_2|sin(\delta_1-\delta_2)sin(\phi_1-\phi_2)}{|A_1|^2+|A_2|^2+2|A_1||A_2|cos(\delta_1-\delta_2)cos(\phi_1-\phi_2)} \\ &\sim 2\frac{A_2}{A_1}sin(\delta_1-\delta_2)sin(\phi_1-\phi_2) \end{aligned}$$

where the last is valid if $|A_2| << |A_1|$. Therefore to have a CP violation effect in the decay both the weak and the strong phases of the two processes involved in the total decay amplitude has to be different. As pointed out above, this kind of CP violation can occur also in the charged mesons decay where the CP in the mixing is forbidden by the electric charge conservation. The CP violation in the decay is frequently called *Direct CP violation*.

- **CP violation due to the interference of decays with and without mixing.** This kind of CP violation (also known as *mixing-induced* CP violation) can occur if P^0 and $\bar{P}^0$ can decay in a common CP eigenstate f_{CP}. In order to classify this kind of CP violation, the parameter λ_f is defined as:

$$\lambda_f = \frac{q}{p}\frac{\bar{A}_{\bar{f}}}{A_f} \tag{1.31}$$

It is possible to show that this parameter is independent of any phase convention [28]. The mixing-induced asymmetry occurs even if $|\lambda_f| = 1$ but $\mathcal{I}m\lambda_f \neq 0$. In this case the time variation of the asymmetry parameter a for the decays defined above is:

$$a = \frac{\Gamma(P_1(t) \to f_{CP}) - \Gamma(P_2(t) \to f_{CP})}{\Gamma(P_1(t) \to f_{CP}) + \Gamma(P_2(t) \to f_{CP})} = -\mathcal{I}m\lambda_f sin(\Delta m t) \tag{1.32}$$

The classical example of this kind of process is the decay of the B^0 and $\bar{B}^0$ into the CP=-1 state $J/\Psi K_S$ that can be related to the angle β of the unitary triangle defined in eq. (1.24):

$$\frac{\Gamma(B^0(t) \to J\Psi K_S) - \Gamma(\bar{B}^0(t) \to J\Psi K_S)}{\Gamma(B^0(t) \to J\Psi K_S) + \Gamma(\bar{B}^0(t) \to J\Psi K_S)} \simeq sin(2\beta)sin(\Delta m_B t) \tag{1.33}$$

The observation $sin(2\beta) \neq 0$ allows for an unitary triangle area different from zero and has been the first evidence of CP violation in the B sector [29].

1.4 Direct CP violation in Neutral Kaon system

In the neutral kaon system both direct and mixing CP violation are present. Both has been observed in the neutral kaon decay in a pair of pions. The pions form

an isotriplet of I=1 with $I_3 = +1$ for the π^+, $I_3 = 0$ for the π^0 and $I_3 = -1$ for the π^-. Due to the Bose symmetry the pion pair with angular momentum J=0 (that is the spin of the Kaon) can have total isospin $I = 0$ or $I = 2$. By using the Glebsch-Gordan coefficients the $\pi^+\pi^-$ and $\pi^0\pi^0$ states can be written as:

$$\begin{aligned} &< \pi^+\pi^-| = \sqrt{\tfrac{2}{3}} < (\pi\pi)_{I=0}| + \sqrt{\tfrac{1}{3}} < (\pi\pi)_{I=2}| \\ &< \pi^0\pi^0| = -\sqrt{\tfrac{1}{3}} < (\pi\pi)_{I=0}| + \sqrt{\tfrac{2}{3}} < (\pi\pi)_{I=2}| \end{aligned} \tag{1.34}$$

The amplitudes can be written as:

$$\begin{aligned} A(K^0 \to \pi^+\pi^-) &= \sqrt{\tfrac{2}{3}} A_0 e^{i\delta_0} + \sqrt{\tfrac{1}{3}} A_2 e^{i\delta_2} \\ A(K^0 \to \pi^0\pi^0) &= -\sqrt{\tfrac{1}{3}} A_0 e^{i\delta_0} + \sqrt{\tfrac{2}{3}} A_2 e^{i\delta_2} \end{aligned} \tag{1.35}$$

where the $\delta_{0,2}$ are the strong re-scattering phases and $A_{0,2}$ the amplitudes, respectively, for I=0,2 isospin states. Here the weak phases are included in the amplitude definition in such a way that the application of CP conjugation gives the following

$$A(K^0 \to (\pi\pi)_I) = A_I e^{i\delta_I} \qquad A(\bar{K^0} \to (\pi\pi)_I) = A_I^* e^{i\delta_I} \tag{1.36}$$

It is useful to define some quantities in order to write CP violating parameters in an easiest way:[8]:

$$\varepsilon = \frac{A(K_L \to (\pi\pi)_{I=0})}{A(K_S \to (\pi\pi)_{I=0})} \tag{1.37}$$

$$\omega = \frac{A(K_S \to (\pi\pi)_{I=2})}{A(K_S \to (\pi\pi)_{I=0})} \tag{1.38}$$

$$\varepsilon_2 = \frac{1}{\sqrt{2}} \frac{A(K_L \to (\pi\pi)_{I=2})}{A(K_S \to (\pi\pi)_{I=0})} \tag{1.39}$$

$$\tag{1.40}$$

Instead of using ε_2 it is more convenient to use ε', defined by:

$$\varepsilon' = \varepsilon_2 - \frac{\varepsilon\omega}{\sqrt{2}}$$

The ε' parameter can be related to the ratio of the amplitude between K_L and K_S with the same isospin, defined by

$$\eta_0 = \frac{A(K_L \to (\pi\pi)_{I=0})}{A(K_S \to (\pi\pi)_{I=0})} \qquad \eta_2 = \frac{A(K_L \to (\pi\pi)_{I=2})}{A(K_S \to (\pi\pi)_{I=2})}$$

by the following relation

$$\varepsilon' = \frac{\omega}{\sqrt{2}}(\eta_2 - \eta_0) = \frac{\eta_0}{\sqrt{2}} \left[\frac{A(K_L \to (\pi\pi)_{I=2})}{A(K_L \to (\pi\pi)_{I=0})} - \frac{A(K_S \to (\pi\pi)_{I=2})}{A(K_S \to (\pi\pi)_{I=0})} \right] \tag{1.41}$$

[8]All the amplitudes are normalized to the dominant $A(K_S \to (\pi\pi)_{I=0}$.

The parameter ω can be written by using the relations (1.36) as:

$$\omega = e^{i(\delta_2-\delta_0)}\frac{\mathcal{R}eA_2 + i\bar{\varepsilon}\mathcal{I}mA_2}{\mathcal{R}eA_0 + i\bar{\varepsilon}\mathcal{I}mA_0} \simeq e^{i}(\delta_2 - \delta_0)\frac{\mathcal{R}eA_2}{\mathcal{R}eA_0} \tag{1.42}$$

where the approximation $\bar{\varepsilon}\mathcal{I}mA_I << \mathcal{R}eA_I$ has been used. Due to the empirical validity of the $\Delta I = 1/2$ rule , ω is smaller than 1 and is measured to be 1/22. The ratios of the amplitudes in the K_S and K_L decay in charged and neutral pions, can be defined as:

$$\eta_{+-} = \frac{A(K_L \to \pi^+\pi^-)}{A(K_S \to \pi^+\pi^-)} \tag{1.43}$$

$$\eta_{00} = \frac{A(K_L \to \pi^0\pi^0)}{A(K_S \to \pi^0\pi^0)} \tag{1.44}$$

$$\tag{1.45}$$

By using the parameters defined in eq. (1.37) the η parameters become:

$$\begin{array}{l} \eta_{+-} \simeq \varepsilon + \frac{\varepsilon'}{1+\omega/\sqrt{2}} \simeq \varepsilon + \varepsilon' \\ \eta_{00} \simeq \varepsilon - \frac{\varepsilon'}{1-\sqrt{2}\omega} \simeq \varepsilon - 2\varepsilon' \end{array} \tag{1.46}$$

The last approximation is obtained due the small value of ω. To understand the meaning of ε and ε', we have to analyze the CP properties of the 2 and 3 pions system. The CP eigenvalues for pairs of pions are:

$$\begin{array}{l} CP|\pi^+\pi^- >= +1|\pi^+\pi^- > \\ CP|\pi^0\pi^0 >= +1|\pi^0\pi^0 > \end{array} \tag{1.47}$$

while for three pions system:

$$\begin{array}{l} CP|\pi^+\pi^-\pi^0 >= (-1)^L|\pi^+\pi^-\pi^0 > \\ CP|\pi^0\pi^0\pi^0 >= -1|\pi^0\pi^0\pi^0 > \end{array} \tag{1.48}$$

The CP eigenvalues for the K_1 and K_2 CP eigenstates are defined in the eq. (1.5). The CP conserving decays are therefore $K_1 \to \pi\pi$ and $K_2 \to \pi\pi\pi$ and, according to the eq. (1.10), the biggest part of the $K_S \to \pi\pi$ and $K_L \to \pi\pi\pi$. The ε parameter defined in eq. (1.37) corresponds to the $\bar{\varepsilon}$ defined in the eq. (1.10); therefore this parameter shows the quantities of "wrong" CP contents in the K_S or K_L, that is the CP violation due to the mixing[9]. By using the eq. (1.46) and the fact that $\omega << 1$ we can express ε and ε' as a function of the η parameters as:

$$\varepsilon \simeq \frac{1}{3}(\eta_{00} + 2\eta_{+-}) \qquad \varepsilon' \simeq \frac{1}{3}(\eta_{00} - \eta_{+-})$$

The experimental similarity in modulus and in phase of the η_{00} and η_{+-} parameters indicates, according to the equations above, that $|\varepsilon'| << |\varepsilon|$. The ε' parameter is related to direct CP violation because, according to the eq. (1.41), it depends

[9]Actually $\varepsilon = \bar{\varepsilon}$ is valid only in the particular phase convention $\mathcal{I}m(A_0) = 0$ (Wu-Yang phase convention); the $\mathcal{R}e(\varepsilon) = \mathcal{R}e(\bar{\varepsilon})$ instead is valid with any phase convention

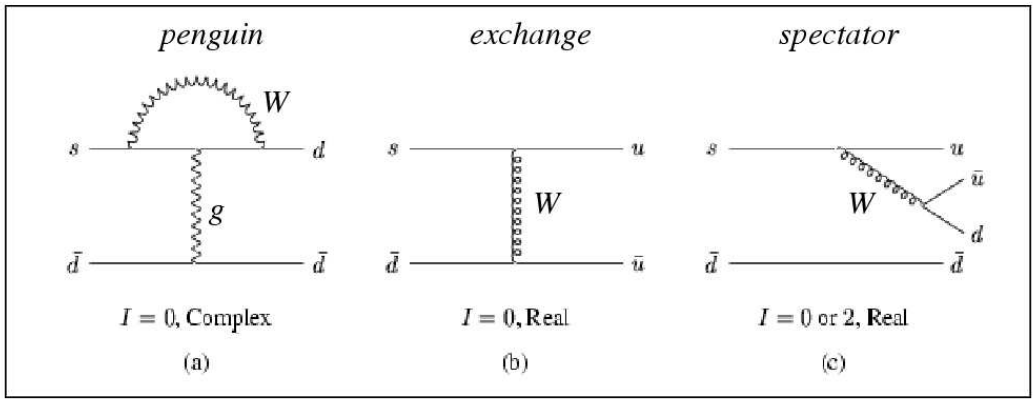

Figure 1.9: Three diagrams contributing to the $\Delta S = 1$ transition responsible of direct CP violation

directly on the ratio of the amplitude in the two possible isospin channels. This could be also shown noticing that, under some approximations [30] and by using eq. (1.42) and (1.41), we have:

$$\begin{aligned} \varepsilon' &\simeq \frac{i}{\sqrt{2}} e^{i(\delta_2-\delta_0)} \frac{\mathcal{R}e(A_2)}{\mathcal{R}e(A_0)} \left[\frac{\mathcal{I}m(A_2)}{\mathcal{R}e(A_2)} - \frac{\mathcal{I}m(A_0)}{\mathcal{R}e(A_0)} \right] \\ &\simeq \frac{i}{\sqrt{2}} e^{i(\delta_2-\delta_0)} \mathcal{I}m(\frac{A_2}{A_0}) \\ &\simeq \frac{i}{\sqrt{2}} e^{i(\delta_2-\delta_0)} sin(\phi_2 - \phi_0) \end{aligned}$$

The real part of the last equation is similar (apart from a trivial variable exchange) to the last expression in eq. (1.31) that was used to define the CP violation in the decay. Therefore $\mathcal{R}e(\varepsilon')$ is a measurement of direct CP violation. Experimentally it is convenient to define the quantity ε'/ε. This is useful because the experimental observation that the phase of ε is very close to the phase of ε' allows to say that $\mathcal{R}e(\varepsilon'/\varepsilon) \sim \varepsilon'/\varepsilon$.

From the definition of η_{+-} and η_{00}, the *double ratio* R could be defined as:

$$R = |\frac{\eta_{00}}{\eta_{+-}}|^2 = \frac{\Gamma(K_L \to \pi^0\pi^0)/\Gamma(K_S \to \pi^0\pi^0)}{\Gamma(K_L \to \pi^+\pi^-)/\Gamma(K_S \to \pi^+\pi^-)} \tag{1.49}$$

This quantity is directly accessible experimentally and is related to ε'/ε by:

$$R \simeq 1 - 6\mathcal{R}e(\frac{\varepsilon'}{\varepsilon})$$

obtained by using the eq. (1.46).

The computations of the ε and ε'/ε parameters are very complicated due to the presence of hadronic matrix elements. In particular as mentioned before, the dominant indirect CP violation (through the mixing) is generated by the $\Delta S = 2$ second order box diagram in the fig. 1.6. The calculation of this parameter yields the order of magnitude of 10^{-3} (see [31] for a full description of the computation procedure and result). The direct CP violation is due to $\Delta S = 1$ transitions. At the second order three kinds of processes contribute, as depicted in fig. 1.9. In these

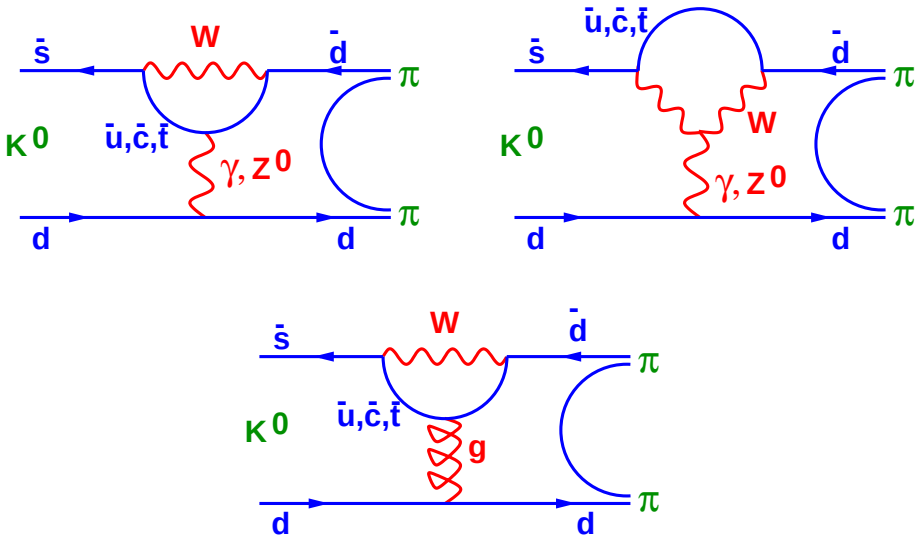

Figure 1.10: Three penguin diagrams describing the direct CP violation in the $\Delta S = 1$ transition of $K \to \pi\pi$

three subprocesses only the *penguin diagram* introduces a relative complex phase between the I=0 and I=2 amplitude, while the *exchange diagram* cannot have the I=2 component because the $q\bar{q}$ and only the real elements V_{us} and V_{ud} of the CKM matrix are involved; in the *spectator diagram* the contribution is real both in A_0 and A_2, thanks to the free quark transition $s \to u\bar{u}d$. Formally, in the framework of the SM calculations, the physical observable can be written as [32]:

$$\frac{\varepsilon'}{\varepsilon} = \mathcal{I}m\lambda_t \frac{G_F}{2|e|\mathcal{R}eA_0\omega}\left[\Pi_0 - \frac{\Pi_2}{\omega}\right] \tag{1.50}$$

where $\lambda_t = -V_{ts}^* V_{td}$. The operators Π_0 and Π_2 describe the amplitude of the penguin diagram. Actually the penguin diagram shown in fig. 1.9 is one of three possible contribution of diagram of this type (fig 1.10). If a gluon line couples to the loop with the $d\bar{d}$ line, diagram is called "QCD penguin" and is responsible of the I=0 (and of the relative hadronic phase) transition, while if the loop is coupled by a photon or a Z^0 we have a "electroweak penguin" responsible for the weak phase and with I=2.

The operators $\Pi_{0,2}$ can be expanded within the Operator Product Expansion as follows:

$$\begin{array}{l} \Pi_0 = \sum_{i=3}^{10} y_i < Q_i >_0 (1-\Omega) \simeq y_6 < Q_6 >_0 (1-\Omega) \\ \Pi_2 = \sum_{i=7}^{10} y_i < Q_i >_2 \simeq y_8 < Q_8 >_2 \end{array} \tag{1.51}$$

Where the y_i are the Wilson coefficients, calculated with perturbative-QCD techniques [33], the Ω parameterises the isospin breaking effects [34] and the Q_i are the quarks operator [32]; the latter is the most complicated part to calculate with high accuracy. The last approximation, in eq. (1.51), comes from the fact that phenomenological analysis [35] indicates the Q_6 and Q_8 contributions to be dominant, as shown in fig. 1.11. Several approaches have been adopted in order to calculate the

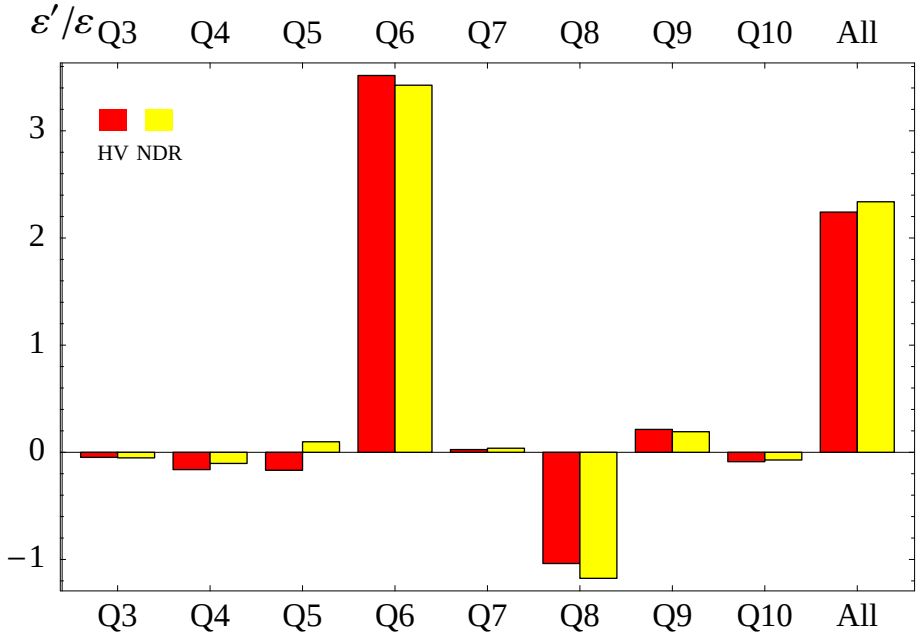

Figure 1.11: Contributions of the different operators in the ε'/ε calculation. The different colors come from different approaches in the renormalization (the plot is in unit of 10^{-3}). More details can be found in [35].

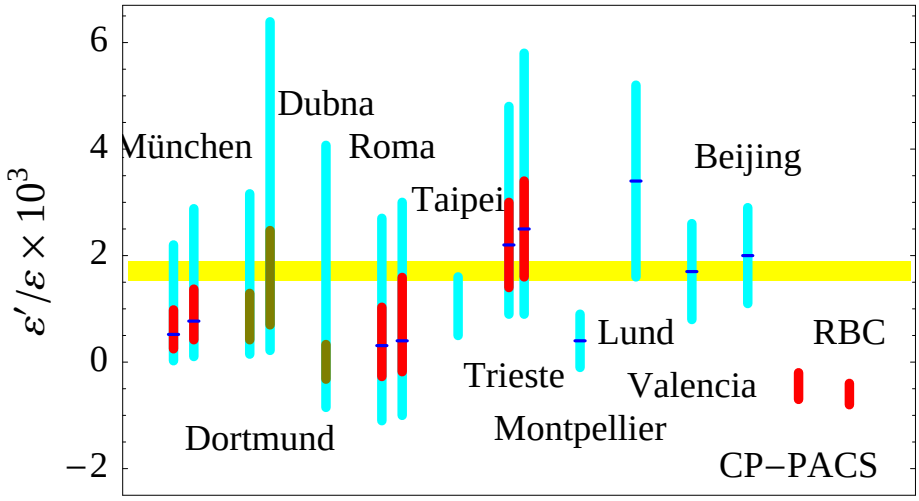

Figure 1.12: Theoretical results obtained from several groups. The central band corresponds to the experimental result

value of ε'/ε as shown in the (incomplete) fig. 1.12. In [36] several references can be found on the theoretical results and approaches on ε'/ε calculation.

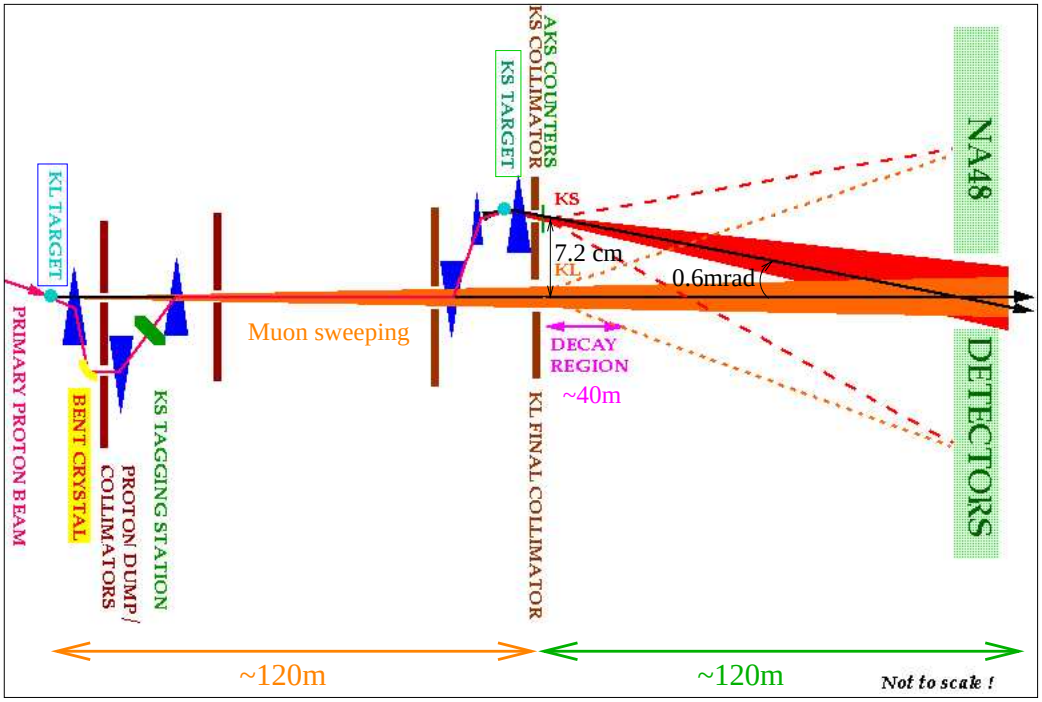

Figure 1.13: Layout of the beam line of the NA48 experiment. The K_S and K_L beams are produced on different target but they converge on the same detector. Part of the protons, that does not interact on the K_L target, are bring by using magnets and a bent crystal on a second target near to the fiducial region t produce the K_S.

1.4.1 Experimental evidence for direct CP violation in $K \to \pi\pi$ decay

Several generations of experiments tried to measure experimentally the value of ε'/ε. Here we just want to describe only the last two that at the end of the nineties have given a definitive positive answer on the observation of the direct CP violation: NA48 at CERN (SPS) and KTEV at FNAL (Tevatron). However It should be mentioned the merit of the first observation goes to NA31 at CERN [37], that in 1993 measured a value of

$$\mathcal{R}e(\frac{\varepsilon'}{\varepsilon}) = (2.3 \pm 0.65) \times 10^{-3}$$

while the E731 experiment at FNAL found a value compatible with 0 (at 10^{-3} precision level). A comprehensive review of all direct CP violation experiments can be found in [30].

NA48 at CERN

In order to measure the quadruple ratio as defined in the eq. (1.49) the method chosen by NA48 is measuring the four decay modes simultaneously in the same fiducial region, using two high intensity and quasi collinear K_S and K_L beams.

The beams are produced in two different beryllium targets using 450 GeV/c protons coming from the SPS accelerator, by using an innovative beam line transportation technique which includes a bent crystal (fig. 1.13). The two beams illuminate in a very similar way the same detector, composed by a magnetic spectrometer and a Liquid krypton calorimeter, together with other counters used for trigger, veto and monitoring purposes (all these detectors will be described in detail in chap. 2). In order to distinguish the K_S from K_L decays, a coincidence was required between the decay event time and the passage of a proton in a tagging station located along the K_S beam line.

Thanks to the simultaneous collection of the four decay modes with the same detector acceptance, the measurement effectively does not require Monte Carlo corrections (only small corrections are required due to the not perfect collinearity of the two beams and other small effects). The analysis has been performed in energy bins with a weighting technique to take into account the different longitudinal distribution of K_S and K_L decays due to the very different lifetimes of the two particles. The result obtained, based on 3 years of data taking, is [38]:

$$\mathcal{R}e(\frac{\varepsilon'}{\varepsilon}) = (1.47 \pm 0.22) \times 10^{-3}$$

KTEV at FNAL

Also the KTEV procedure is based on the possibility to collect the decay of K_S and K_L at the same time from the same decay region, in order to measure the direct CP violation through the double ratio. The main difference is about the beams production technique. The K_S beam is obtained by using the regeneration of K_S from a pure K_L beam. In fig. 1.14 the layout of the KTEV beam line is shown. The two K_L beams are generated by the 800 GeV Tevatron proton beam. The position of the active regenerator, on which one of the two K_L beams impinges in order to produce the K_S beam, is frequently swapped in order to cancel acceptance systematics. The tagging of the neutral kaon type is based on the vertex reconstruction, thanks to the fact that the two kaon beams, also after the K_S regeneration, remain 20 cm separated. The central detector is composed by a Magnetic spectrometer and a CsI Cristal calorimeter with a very good energy resolution to reconstruct the neutral modes. The analysis is heavily based on a sophisticated Monte Carlo simulation to understand the differences between the K_L and the K_S acceptances. The result, based on 1996 and 1997 data, is [39]:

$$\mathcal{R}e(\frac{\varepsilon'}{\varepsilon}) = (2.07 \pm 0.28) \times 10^{-3}$$

1.5 CP violation in Charged Kaon decays

As explained above, in the neutral kaon system there is a relatively large amount of CP violation due to the $\Delta S = 2$ transition, responsible for the mixing. In addition, there is a direct CP violation, coming from the decay through a $\Delta S = 1$ transition

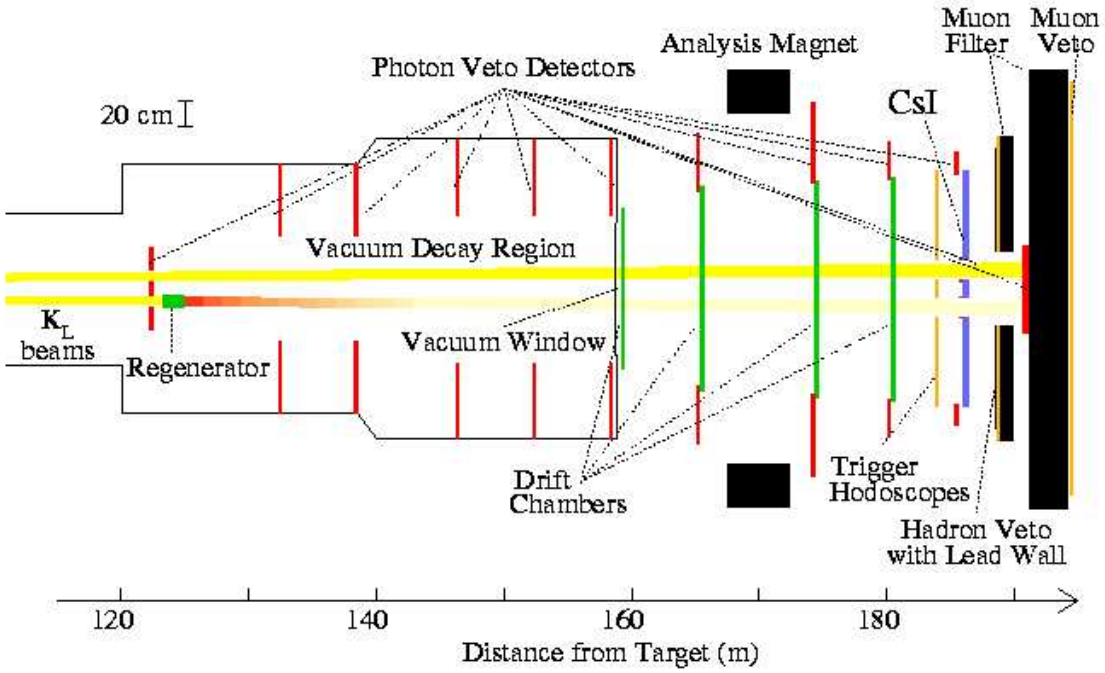

Figure 1.14: The KTEV detector's layout. The general scheme is quite similar with respect to the NA48 experiment, but the way to product the beams is very different.

directly in the decay amplitude. In the charged kaon system the mixing, $K^+ \leftrightarrow K^-$ is forbidden by charge conservation. Thus any asymmetry in charged kaon decays is due to the direct $\Delta S = 1$ CP violation. On the other hand observation of direct CP violation outside of the neutral Kaon sector will give complementary information in the understanding of the CKM paradigm and, at the same time, could open new perspective on the presence of new physics. To better understand the physical observables more sensitive to CP violation effect we introduce the Dalitz plot for the $K \to 3\pi$ decay and then we describe the contribution to the total amplitude of the decay.

1.5.1 The $K \to 3\pi$ Dalitz plot

The *Dalitz Plot* was invented by Dalitz in 1953 [40] to investigate whether there was any correlation among the produced particles in a 3-body decays. The energy distribution of the produced particles is a product of the matrix element for the decay and the phase space factor. If the matrix element is a constant this distribution is a function of the pure phase space factor, otherwise any departure from the constant phase space is directly connected to a non-constant matrix element. The study of the regions where this difference is large or small can be used to get informations about the behaviour of the interactions involved in the decay process.

In general the phase space factor represents the number of quantum states available for a particle with momentum in the range between p_i and $p_i + dp_i$. This is given by $\frac{Vd^3\vec{p_i}}{(2\pi)^3}$, where V is the normalization volume. In the case of three particles in the final state, neglecting the spin, the total phase factor is just the product of the single factors. In the center of mass the momentum conservation yields $\vec{p_3} = -(\vec{p_1} + \vec{p_2})$.

Thanks to this relation, and using a Lorentz contraction factor m/E to transform the volumes in Lorentz invariant quantities, it is possible to perform an integration over $\vec{p_3}$. The phase space factor becomes:

$$dN = const. \frac{p_1^2 dp_1 p_2^2 dp_2 d(cos\theta_{12})}{E_1 E_2 E_3}$$

Where θ_{12} is the angle between the particles 1 and 2. By using the relativistic energy-momentum relation $E^2 = p^2 + m^2$ it can be shown that $p_1 p_2 d(cos\theta_{12}) = E_3 dE_3$ and the previous relation can be simplified as:

$$dN = const. \frac{E_1 dE_1 E_2 dE_2 E_3 dE_3}{E_1 E_2 E_3}$$

Considering the relation $E_f = E_1 + E_2 + E_3$ for fixed values of E_1 and E_2 we have that $dE_f = dE_3$, so:

$$\frac{dN}{dE_f} = const. dE_1 dE_2$$

This expression means that, if only phase space is taken into account, the number of states is uniformly distributed in the $E_1 E_2$ plane.

Let us move to the case of the $K^\pm \to \pi^\pm \pi^0 \pi^0$ decay: we want to construct the Dalitz plot in order to define useful quantities in the study of the CP violation in charged kaon decay. The Lorentz-invariant quantities

$$s_i = (P_K - P_i)^2 = (m_K - m_i)^2 - 2 m_K T_i \ , \ \text{i=1,2,3} \tag{1.52}$$

where P stands for the 4-momentum and T for the kinetic energy, and

$$s_0 = \frac{1}{3} \sum_{i=1} 3 s_i = \frac{1}{3} (m_K^2 + m_1^2 + m_2^2 + m_3^2)$$

can be introduced in order to define the independent and adimensional *Dalitz variables*:

$$U = \frac{s_3 - s_0}{m_{\pi^\pm}^2} \tag{1.53}$$

$$V = \frac{s_2 - s_1}{m_{\pi^\pm}^2} \tag{1.54}$$

$$\tag{1.55}$$

The Q value for this decay is quite small, indeed

$$Q = T_1 + T_2 + T_3 = m_k - \sum_{i=1}^{3} m_i \sim 84 MeV$$

In order to evaluate the phase space integral the T_i can be expressed in polar coordinates [41] considering the center of the fig. 1.15 as origin of the Dalitz Plot. In this way the kinetic energy can be written as:

$$T_{1,2} = \frac{Q}{3} [1 + r cos(\frac{2}{3}\pi \pm \phi)] \tag{1.56}$$

$$T_3 = \frac{Q}{3} (1 + r cos\phi) \tag{1.57}$$

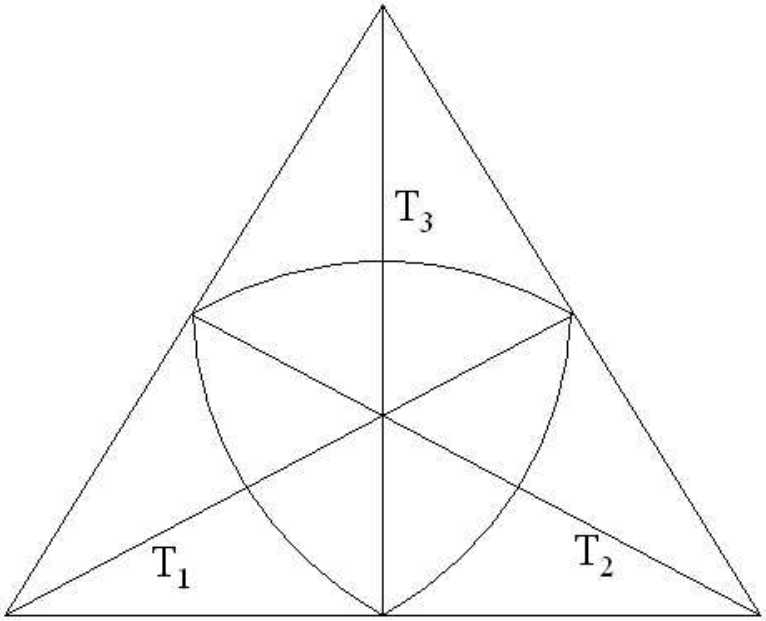

Figure 1.15: Dalitz plot for $K \to 3\pi$. The three axes at 120° represent the kinetic energies of the three pions in the kaon rest frame. In the centre of the Dalitz plot $T_1 = T_2 = T_3 = Q/3$.

where ϕ and r are in the range $-\pi < \phi < \pi$ and $0 \leq r \leq r_0$, and r_0 is a function of ϕ defining the contour of the Dalitz Plot. This contour can be expressed through the equation:

$$1 - (1+\alpha)r_0^2 - \alpha r_0^3 cos(3\phi) = 0 \tag{1.58}$$

with $\alpha = 2Qm_K/(2m_k - Q)^2$. In the non-relativistic limit $Q \to 0$ and eq. (1.58) is reduced to $r_0 = 1$, *i.e.* a circle. The Dalitz variable, as defined in the eq. (1.53) , can be expressed in polar coordinates as:

$$U = -\frac{2}{3}\frac{m_K}{m_{\pi^\pm}^2} Qrcos\phi \tag{1.59}$$

$$V = \frac{2}{\sqrt{3}}\frac{m_K}{m_{\pi^\pm}^2} Qrsin\phi \tag{1.60}$$

The decay rates can be obtained integrating over the Dalitz Plot in polar variables:

$$\Gamma(K \to 3\pi) = \frac{1}{(4\pi)^3 m_K}\frac{\sqrt{3}}{18} Q^2 \iint r|A(r,\phi)|^2 dr d\phi$$

where $A(r,\phi)$ is the transition amplitude containing the dynamics of the interaction responsible of the decay and causing the departure from the flat phase space. Thanks to the fact that the kinetic energy in the kaon rest frame is quite small, it is possible to perform a Taylor expansion [42] of the decay amplitude as:

$$|A(K \to 3\pi)|^2 \propto 1 + gU + jV + hU^2 + kV^2 + ... \tag{1.61}$$

Due to the Dalitz Plot symmetry, given by Bose symmetry, the coefficient j is 0. The other coefficients can be experimentally measured. In the table 1.2 the value are presented both for charged and neutral kaon[10] [4].

Channel	$K^{\pm} \to \pi^{\pm}\pi^0\pi^0$	$K^{\pm} \to \pi^{\pm}\pi^+\pi^-$	$K_L \to \pi^+\pi^-\pi^0$	$K_L \to \pi^0\pi^0\pi^0$
$\Gamma(10^6 s^{-1})$	1.39 ± 0.032	4.50 ± 0.025	2.43 ± 0.04	4.06 ± 0.04
$g(10^{-1})$	6.38 ± 0.20	-2.15 ± 0.035	6.78 ± 0.08	-
$h(10^{-2})$	5.1 ± 1.3	1.2 ± 0.8	7.6 ± 0.6	-5.0 ± 1.4
$k(10^{-2})$	0.4 ± 0.7	-1.01 ± 0.34	0.99 ± 0.15	-

Table 1.2: Experimental values of Dalitz plot parameters for K^+ and K_L in 3π decays [4]

1.5.2 Decay amplitudes of $K \to 3\pi$

The transition amplitude can be calculated starting from the weak Hamiltonian, according to the two possible transition rules $\Delta I = 1/2$ and $\Delta I = 3/2$ (the final isospin is I=1,2). In terms of isospin decomposition the transition amplitude is given by[11] [43] :

$$\begin{aligned} A_{++-} = A(K^{\pm} \to \pi^{\pm}\pi^+\pi^-) &= 2A_1(s1, s2, s3) + B_1(s1, s2, s3) + B_2(s1, s2, s3) \\ A_{+00} = A(K^{\pm} \to \pi^{\pm}\pi^0\pi^0) &= A_1(s1, s2, s3) - B_1(s1, s2, s3) + B_2(s1, s2, s3) \end{aligned} \tag{1.62}$$

where the amplitude A_1 (belonging to the I=1 isospin state) is completely symmetric under s_i permutation[12] and the B_i (for both the allowed isospin states I=1,2) are symmetric for the exchange $s_1 \to s_2$ and obey to the relation:

$$B_i(s1, s2, s3) + B_i(s3, s2, s1) + B_i(s1, s3, s2) = 0$$

A difference with respect to the $K \to 2\pi$ case is that here two $\Delta I = 1/2$ states are present: the symmetric (A_1) and the antisymmetric one (B_1).

By using the Dalitz variables U and V and the mentioned symmetry properties of the s_i, the amplitude components can be expanded as:

$$\begin{aligned} A_i(s1, s2, s3) &= a_i + c_i(U^2 + V^2/3) + ... \\ B_i(s1, s2, s3) &= b_i U + D_i(U^2 + V^2/3) + e_i U(U^2 + V^2/3) + ... \end{aligned} \tag{1.63}$$

The various coefficients, $a_i, b_i, ...$ are real if the strong rescattering in the final state is neglected and CP is conserved. In this case the amplitudes (1.62), considering

[10] Before the NA48/2 experiment. We use the PDG04 values to be coherent with the our results already published [108] [130]

[11] at this point we assume no CP violation, so we confuse the K^+ and the K^- amplitudes

[12] The subscript 3 indicates the odd pion.

only the linear terms in the expansion, become:

$$\begin{aligned} A_{++-} = A(K^{\pm} \to \pi^{\pm}\pi^{+}\pi^{-}) = 2a_1 + (b_1 + b_2)U + ... \\ A_{+00} = A(K^{\pm} \to \pi^{\pm}\pi^{0}\pi^{0}) = a_1 - (b_1 - b_2)U + ... \end{aligned} \tag{1.64}$$

If the strong rescattering is taken into account, the expressions become more complicated and relative phases appear among the various isospin components of the amplitude. Unlike in $K \to \pi\pi$, these phases are not constants as a function of the position in the Dalitz Plot. The result is given by [44][45][46] in the approximation of small values of U and V (*i.e.* the central part of the Dalitz plot):

$$\begin{aligned} A(K^{\pm} \to \pi^{\pm}\pi^{+}\pi^{-}) = (2\alpha_1 - \alpha_3)e^{i\delta_{1S}} + [(\beta_1 - \frac{1}{2}\beta_3)e^{i\delta_{1M}} + \sqrt{3}\gamma_3 e^{i\delta_2}]U + \\ 2(\zeta_1 + \zeta_3)(U^2 + \frac{1}{3}V^2) - (\xi_1 + \xi_2 - \xi_3)(U^2 - \frac{1}{3}V^2) \\ A(K^{\pm} \to \pi^{\pm}\pi^{0}\pi^{0}) = -\frac{1}{2}(2\alpha_1 - \alpha_3)e^{i\delta_{1S}} + [(\beta_1 - \frac{1}{2}\beta_3)e^{i\delta_{1M}} - \sqrt{3}\gamma_3 e^{i\delta_2}]U - \\ (\zeta_1 + \zeta_3)(U^2 + \frac{1}{3}V^2) - (\xi_1 + \xi_2 + \xi_3)(U^2 - \frac{1}{3}V^2) \end{aligned} \tag{1.65}$$

where the various coefficients $\alpha, \beta, \gamma, \zeta, \xi$ are related to the $\Delta I = 1/2$ (index 1) or $\Delta I = 3/2$ transition while the phases δ are related to the three possible final isospin states: $|(3\pi)_{I=1}, symm. >$ (index 1S), $|(3\pi)_{I=1}, mixsymm. >$ (index 1M) and $|(3\pi)_{I=2} >$ (index 2). The difference between the relative phases is quite small due to the small phase space available for the decay

$$\delta_{1S} - \delta_{1M} \simeq 0.08$$

The eq. (1.65) does not include effects due to the isospin breaking. If the isospin breaking is included the I=1 and I=2 amplitude can get mixed and this leads to other phases [47].

1.5.3 Strong rescattering

The study of the interaction in the final state is important because the strong rescattering in the final state introduces the complex phases as in eq. (1.65), that are responsible for CP violation. On the other hand a more accurate treatment of these topics is out of the purpose of this job and we refer the reader back to literature for more details on this topic. Nevertheless we want to show the formalism needed to address the following discussions.

In the previous section we have already shown that the amplitudes for both $K^{\pm} \to \pi^{\pm}\pi^{+}\pi^{-}$ and $K^{\pm} \to \pi^{\pm}\pi^{+}\pi^{-}$ are made up by two elementary components, the A and B_i defined in the eq. (1.63) in the simplest case, coming from the presence of two isospin transitions $\Delta I = 1/2$ and $\Delta I = 3/2$. In particular the $\Delta I = 1/2$, that is the main component due to the experimental observation of the relative suppression of all the transitions with $\Delta I \neq 1/2$, has two contributions from the

symmetric A matrix and the B_1 component of mixed symmetry. In the case of no strong interaction in the final state this can be formalized with:

$$\begin{pmatrix} A^{I=1}_{++-} \\ A^{I=1}_{+00} \end{pmatrix} = T \begin{pmatrix} A(s_i) \\ B_1(s_i) \end{pmatrix} \tag{1.66}$$

where, according to the eq. (1.63), the matrix T can be written as:

$$T = \begin{pmatrix} 2 & 1 \\ 1 & -1 \end{pmatrix} \tag{1.67}$$

The introduction of the final state interaction could be done considering in eq. (1.66) the presence of a *Rescattering Matrix* for the I=1 final state:

$$\begin{pmatrix} A^{I=1}_{++-} \\ A^{I=1}_{+00} \end{pmatrix}_R = T_R \begin{pmatrix} A(s_i) \\ B_1(s_i) \end{pmatrix} = T \cdot R \cdot T^{-1} \begin{pmatrix} A(s_i) \\ B_1(s_i) \end{pmatrix} \tag{1.68}$$

In general we expect small re-scattering phases due to the limited phase space and then it is possible to expand the rescattering matrix as:

$$R = 1 + i \begin{pmatrix} \alpha(s_i) & \beta'(s_i) \\ \alpha'(s_i) & \beta(s_i) \end{pmatrix} \tag{1.69}$$

with $\alpha, \beta, \alpha', \beta' << 1$. In order to take into account the I=2 component, not included in the T matrix, another rescattering phase can be defined as:

$$B_2(s_i)_R = B_2(s_i)[1 + \delta(s_i)] \tag{1.70}$$

The computations of the scattering phases defined above have to be done taking into account the strong interaction at low energy (for instance the LO of ChPT). They can be expanded [48] around the center of the Dalitz plot (subscript 0) as:

$$\alpha(U,V) \simeq \alpha_0 + \alpha_1(U^2 + \frac{V^2}{3})$$

$$\alpha'(U,V) \simeq \alpha'_0 + \alpha'_1(U^2 - \frac{V^2}{3})$$

$$\beta(U,V) \simeq \beta_0 + \beta_1(U^2 - \frac{V^2}{3})/U$$

$$\beta'(U,V) \simeq \beta'_0(U^2 + \frac{V^2}{3})/U$$

$$\delta(U,V) \simeq \delta_0 + \delta_1(U^2 - \frac{V^2}{3})/U$$

In this way each one can be written as a sum of a Real part, in which are not present CP violation effects and strong rescattering in the final state, described by the eq. (1.64), and an imaginary part that includes the CP violation and in which the complex phases are obtained from the phases calculated (with some procedure) at the center of the Dalitz plot. In particular we can get:

$$(A_{++-})_R = 2a_1[1 + i\alpha_0] + b_1 U \left[1 + i(\beta_0 + \frac{a_1}{b_1}\alpha'_0)\right] + b_2 U[1 + i\delta_0] \tag{1.71}$$

$$(A_{+00})_R = a_1[1 + i\alpha_0] - b_1 U\left[1 + i(\beta_0 + \frac{a_1}{b_1}\alpha_0')\right] + b_2 U[1 + i\delta_0] \tag{1.72}$$

in which we stopped the expansion to linear terms (for this reason there are not V terms). From the last equations it is quite clear that the imaginary parts receive contribution both from $\Delta I = 1/2$ and $\Delta I = 3/2$, as well as from the symmetric (a_1) and the non-symmetric (b_1) of the I=1 final state ($\Delta I = 1/2$). This is an important difference with respect to the $K \to 2\pi$ system, in which only the phases between $\Delta I = 1/2$ and $\Delta I = 3/2$ are present and contribute to the direct CP violation. This fact in principle can give an enhancement to CP violation effects with respect to ε'/ε, but, as we will see, this is not true in practice due to the fact that U dependent terms with a_1, have the same weak phase with respect to the constant term, and this gives, according to [49] and [47], the dependence of direct CP effect with $(\alpha_0 - \beta_0) < 0.1$.

1.5.4 CP violating asymmetry in charged kaons

There are two ways to look for direct CP violation in charged kaon decays:

- Through the asymmetry between the partial decay rates defined as:

$$\Delta\Gamma = \frac{\Gamma(K^+ \to 3\pi) - \Gamma(K^- \to 3\pi)}{\Gamma(K^+ \to 3\pi) + \Gamma(K^- \to 3\pi)} \tag{1.73}$$

- Looking to the asymmetry between the *shape* of the Dalitz plot in the charged conjugate modes. In particular the asymmetry of the linear slope parameter g (defined in eq. (1.61)):

$$A_g = \frac{g^+ - g^-}{g^+ + g^-} \tag{1.74}$$

It must be noted that, since the integral of the dominant linear term U on the whole Dalitz plot is zero, the asymmetries in the width are very suppressed with respect to the slope asymmetries (the asymmetry predictions are at least 2 order of magnitude smaller). In this job we will consider the slope asymmetries only. Considering as usually, that under CP operator the amplitude, in which at least two components have to be included, transform as:

$$A(K^+ \to 3\pi) = ae^{i\delta_a} + be^{i\delta_b} \overset{CP}{\longmapsto} A(K^- \to 3\pi) = a^* e^{i\delta_a} + b^* e^{i\delta_b} \tag{1.75}$$

once we choose $\eta = 0$ for the phase originated by CP conjugation. Using the linear coefficient of U obtained from the square of eq. (1.71) and (1.72), the parameters A_g^c and A_g^0 can be defined for $K^\pm \to \pi^\pm\pi^+\pi^-$ and $K^\pm \to \pi^\pm\pi^0\pi^0$, respectively, as:

$$A_g^c = \frac{\mathcal{I}m(a_1^* b_1)(\alpha_0 - \beta_0) + \mathcal{I}m(a_1^* b_2)(\alpha_0 - \delta_0)}{\mathcal{R}e(a_1^* b_1) + \mathcal{R}e(a_1^* b_2)} \tag{1.76}$$

$$A_g^0 = \frac{\mathcal{I}m(a_1^* b_1)(\alpha_0 - \beta_0) - \mathcal{I}m(a_1^* b_2)(\alpha_0 - \delta_0)}{\mathcal{R}e(a_1^* b_1) - \mathcal{R}e(a_1^* b_2)} \tag{1.77}$$

From the last equations it is quite clear the mentioned difference with respect to the $K \to 2\pi$ case: while in the equation (1.49) the differences of the strong phase

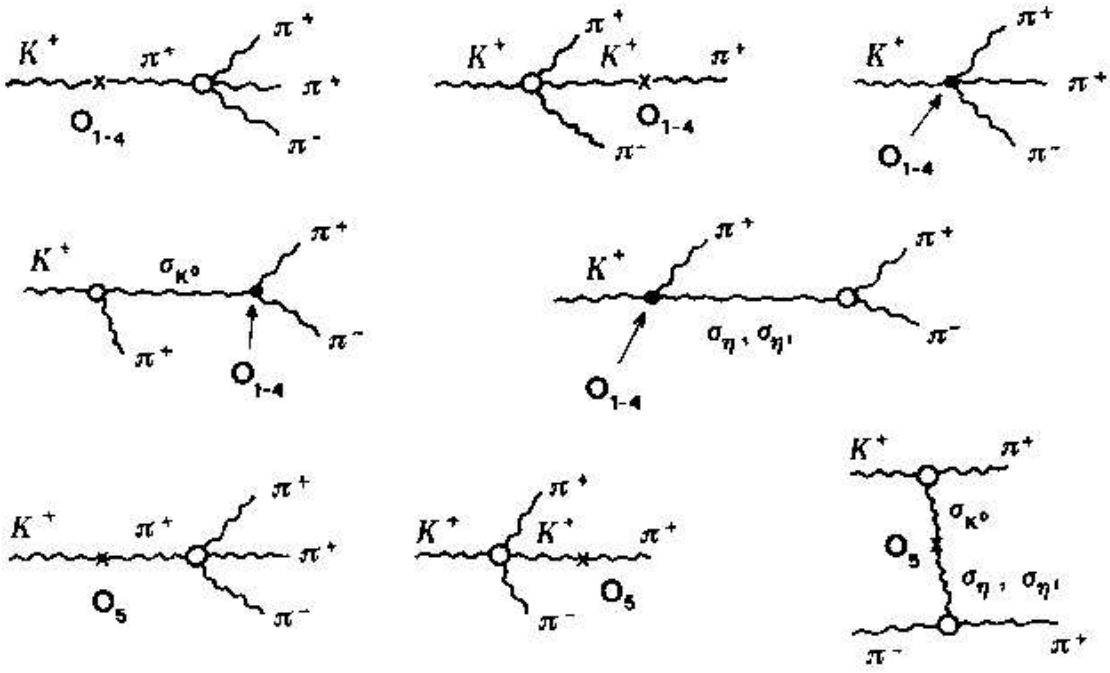

Figure 1.16: Example of diagrams induced by Q operators.

between I=1 and I=2 states, is the only term that contributes to CP violation, in the case of $K \to 3\pi$ two terms contribute independently.

Sometime in the literature the asymmetry coefficient for the linear term A_g as defined in eq. (1.74) is called Δg. In this work we will call A_g the asymmetry parameter and Δg the difference between the linear slope, related to A_g by the following relation:

$$A_g = \frac{\Delta g}{2g} \tag{1.78}$$

Where $\Delta g = g^+ - g^-$.

1.5.5 A_g calculation in the SM framework

The theoretical predictions of A_g require the calculation of the transition amplitudes and complex phases present in the eq. (1.71) and (1.72). In the framework of the full Lagrangian SM, this kind of calculation is not an easy task to do, because of the presence of strong interactions. However, in the low energy limit it is possible to define an *effective* Lagrangian, where the interacting fields are not directly the quarks but the meson ones (the so called Chiral Perturbation theory (ChPT) [50]), and can be parametrized by the effective four-quark operators Q_i and the complex Wilson coefficient C_i [51][52]:

$$\mathcal{L}(\Delta S = 1) = \sqrt{2} G_F V_{ud} V_{us}^* \sum_i \tilde{C}_i Q_i \tag{1.79}$$

The operators present in eq. (1.79) describe the possible diagrams that could contribute to the final amplitude at the LO (leading order) p^2 in the Chiral expansion; in particular for $i = 1, 2, 3, 4$ we have *non-penguin diagrams* (the $i = 4$ is the only $\Delta I = 3/2$ operator while the others are $\Delta I = 1/2$), the $i = 5, 6$ represent the *gluonic penguin* (QCDP) and the $i = 7, 8$ the *electroweak penguin operator* (EWP). The QCDP contains the required imaginary parts to generate CP violation in the decay. An expression for this operator can be found in[13] [53]. While the calculation at order p^2 is relatively easy, some problems arise when NLO (Next to Leading Order) or NNLO (Next NLO) contributions are added. Since that the computation of the hadronic matrix elements $< 3\pi|\mathcal{H}_{eff}|K >$ involves, in some cases, long distance contributions, different approaches can be used ($1/N_c$, QCD Lattice, σ model, pure ChPT, etc.). Some authors claim that in the higher order some effects can enhance the A_g value. By using a model-independent approach at order p^4, it is possible [49] to put an upper limit to $\sim 10^{-5}$, on which most part of the authors agrees. In the table 1.3 the principal predictions for the A_g value are shown.

Authors	$\|A_g^c\|$	$\|A_g^0\|$	Ref.
H.Y. Cheng (1990)	$< 10^{-5}$	-	[55]
D'Ambrosio et al.(1991)	$< 0.7 \cdot 10^{-5}$	-	[49]
Isidori et al. (1992)	$\sim 10^{-6}$	-	[47]
E.P. Shabalin (1993)	$2.5 \cdot 10^{-3}$	-	[56]
A.A. Bel'kov et al. (1993)	$\sim 0.23\|\varepsilon'/\varepsilon\|$	$\sim 0.13\|\varepsilon'/\varepsilon\|$	[57]
D'Ambrosio et al. (1998)	$< 10^{-5}$	-	[43]
E.P. Shabalin (1998)	$\sim 2 \cdot 10^{-4}$	-	[58]
Maiani et al. (1995)	$2.3 \cdot 10^{-6}$	$1.3 \cdot 10^{-6}$	[59]
Gamiz et al. (2003)	$2.4 \cdot 10^{-5}$	$1.1 \cdot 10^{-5}$	[125]
E.P. Shabalin (2005)	$0.8 \cdot 10^{-5}$	-	Privat. comm.
A.A. Belkov (1989)	$\sim 7 \cdot 10^{-3}$	$1.5 \cdot 10^{-}3$	[61]
G. Faldt et. al. (2005)	$\sim 2.9 \cdot 10^{-5}$	$0.18 \cdot 10^{-5}$	[63]

Table 1.3: Theoretical results on A_g^c and A_g^0. Only the central value is shown.

1.5.6 Physics beyond the standard model effects

The supersymmetry [65] is one of the most promising models beyond the SM. The direct search for supersymmetric particles is one of the main topics for the new big hadronic machines at 1 TeV scale. However the possible contribution of SUSY particles can influence the value of the CP violation observables. Indeed new physics can contribute to the CP violation phenomena, either introducing new phases in addition to the δ_{CKM} phase or with a new flavour structure. In any MSSM (Minimal SuperSymmetric Model) at least two new genuine phases, ϕ_α and ϕ_β, can be introduced by using the minimal amount of free independent SUSY parameters

[13] In the literature there are two conventions for these operators ($\mathcal{O}$ and Q), a "conversion table" can be found in [52]

[66][67] . It can be shown that these phases lead to a contribution to the electric dipole moment of light quarks, described by the following equation [68][69][70]:

$$d_N^e \sim 2\left(\frac{100GeV}{\tilde{m}}\right)^2 sin(\phi_{\alpha,\beta}) \times 10^{-23} \text{ e cm}$$

where $\tilde{m}$ is the mass of the light squarks. Considering that the present experimental upper bound on the EDM is $< 0.63 \cdot 10^{-25}$ (90% C.L.), if the SUSY masses are at the 100 GeV scale, the $\phi_{\alpha,\beta}$ are quite small and some author puts these phases to vanish. However several authors [71][72][73], with different arguments, argue that in the EDM case cancellations exist among SUSY contributions and the presence of sizable SUSY phases is still possible. These new phases are not going to produce sizable effect on the CP violating observable until the SUSY model is not provided with a new flavor structure in addition to the CKM structure of the SM. The most promising contribution is from a misalignment between the quark and the squark matrices coming from the chromomagnetic penguins (CMO) [74]; in this framework an enhancement of A_g at level of 10^{-4} is possible for particular values of relevant SUSY parameters. This effect could be, in principle, cross-checked by studying the CP violation in $K \to \pi\pi\gamma$ and hyperon decay, for which a similar enhancement is predicted[14] [75] [76].

Other calculations, based on different approaches (see [77] and [78] for a complete review about the CP violation beyond the SM), predict higher value of the asymmetry: for instance a model based on the existence of an extended Higgs doublet [58] predicts a value of $\sim 4 \cdot 10^{-4}$ for the A_g^c parameter. All the authors agree that a A_g value greater than $0.5 \cdot 10^{-4}$ would be a signal of contribution of new physics in the CP violation.

1.5.7 ε'/ε vs A_g

The measurement of A_g^c and A_g^0 could give very important informations about the size of the contributions from different operators in the calculation of the ε' parameter. In particular the contribution from ImG_8 (the most relevant contribution to the effective Lagrangian) could be constrained with respect to $Im(e^2G_E)$ to understand if the former is large as predicted by some authors [79] [80] [81]. As described by [82] using higher order in the ChPT approach, the measurement of the asymmetry in the slope in the charged kaon decays is a crucial test of the ε' calculation technique and an important test of new physics contribution to CP violation as well. Fig. 1.17 shows the present understanding of the contribution of the ImG_8 operator: in the plane ImG_8 vs $Im(e^2G_E)$ the rectangles represent the result obtained with higher dimensional operators and $1/N_c$ approaches, the vertical band the lattice calculations for $Im(e^2G_E)$ and the small circle the leading order calculation in the large N_c expansion. The red band comes from the experimental value of ε', while the dotted blue band is obtained for two different values of A_g^c ($\sim -1 \cdot 10^{-5}$ and

[14]However in all these cases the presence of hadronic parameters introduces some uncertainties in the calculation, while in other decays like $K \to \pi\nu\bar{\nu}$ the situation is cleaner; however this channel is much more challenging from an experimental point of view.

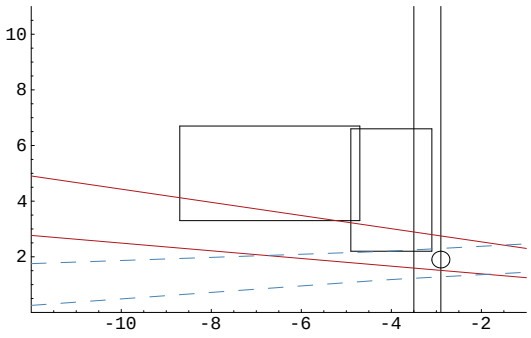

Figure 1.17: In the vertical coordinate the contribution of $\mathrm{Im}G_8$ is represented while in the horizontal coordinate the $e^2 ImG_E$ is shown. The quasi-horizontal blue band represents the $|A_g^c| \sim 1 \cdot 10^{-5}$ (see the text for further explanation)

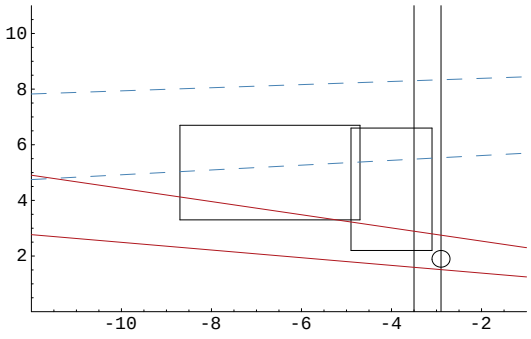

Figure 1.18: The only change with respect to the previous picture is the blue band obtained for an higher value of A_g^c ($|A_g^c| \sim 3.5 \cdot 10^{-5}$)

$\sim -3.5 \cdot 10^{-5}$). A discrepancy as in the fig 1.18 could give an indication of a different flavour dynamics out of the SM.

Concerning the other asymmetries, in particular the A_g^0 parameter, complementary informations could be provided to understand the different contribution to the ε' calculation or to look for signals of new physics.

1.5.8 Experimental limit on A_g

In spite of the small value predicted by the SM several experiments in the past tried to search for signal of CP violation in the charged kaon sector. The first generation of the experiments in the 70's reached a sensitivity of few 10^{-3} for the $K^{\pm} \to \pi^{\pm}\pi^{+}\pi^{-}$ asymmetry (A_g^c) and 10^{-2} for the $K^{\pm} \to \pi^{\pm}\pi^{0}\pi^{0}$ asymmetry (A_g^0). The most recent generations of experiments have improved the experimental precision, but did not manage to go below 10^{-3} both for A_g^c and A_g^0. We briefly discuss these experiments whose results are summarized in table 1.4

Asymmetry	*# of events*	*Experiment*
$A_g^0 = (19 \pm 125) \cdot 10^{-4}$	115K	CERN PS(1975) [83]
$A_g^0 = (2 \pm 19) \cdot 10^{-4}$	620K	Protvino IHEP (2005) [84]
$A_g^c = (-70 \pm 53) \cdot 10^{-4}$	3.2M	BNL AGS (1970) [85]
$A_g^c = (22 \pm 15 \pm 37) \cdot 10^{-4}$	54M	HyperCP (2000) prelim.[86]

Table 1.4: Summary of the experimental situation both in "neutral" (A_g^0) and "charged" (A_g^c) mode, before NA48/2 results

Ford 1970. Experiment to measure A_g^c at AGS

The first experiment to search for CP violation in the charged kaon system, outside of the neutral kaon sector for which the CP violation was already established since six

years, was performed by Ford et al. at the Alternate Gradient Synchrotron (AGS) at Brookhaven [85] in 1970. In fig. 1.19 the schematic of the experiment is shown. The 3 GeV/c K^+ and K^- beams (not simultaneous) are analyzed by a differential Cerenkov detector and defined by three scintillator counters (only the last is shown in the picture). In the 58% of the total $K^\pm \to \pi^\pm\pi^+\pi^-$ decay the topology of the event is similar to the picture. In this case the 16-counter hodoscope placed on the odd pion (the pion with different charge with respect to the kaon charge) trajectory triggered the spark chamber ahead and behind the wide magnet D_4. The first chambers measured the direction of the three pions while the chambers behind the magnet were missed by the even pions and measured the odd pion momentum. The background (mainly $K^\pm \to \pi^\pm e^+ e^- \gamma$) was below 1%. The most critical point was the stability of the magnetic field in the spectrometer magnet D_4: this parameter was monitored using Hall and NMR probes and a systematic error was evaluated at level of $5 \cdot 10^{-4}$. The total statistics collected was ~ 3.2 million of events (one half for each charge sign). The final result, including both statistical and systematic error, was

$$A_g^c = (-7.0 \pm 5.3) \cdot 10^{-3}$$

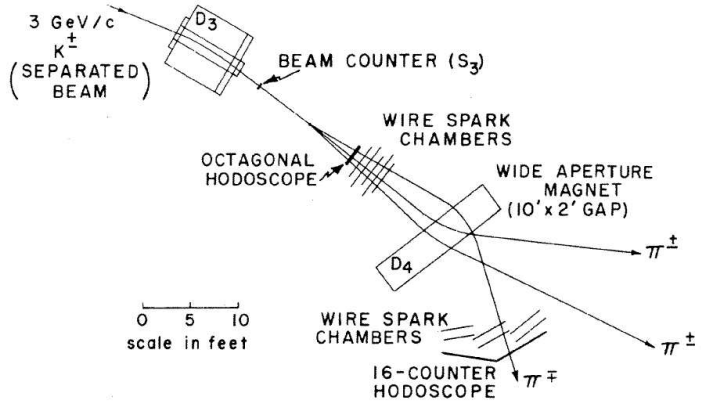

Figure 1.19: Experimental arrangement of the Brookhaven experiment. The first Cerenkov counter to distinguish between pions and kaons is out of the figure.

Smith 1975. First attempt to measure A_g^0 at CERN

The original purpose of this experiment [83], performed in the early 70s at CERN was to measure the asymmetry in the total decay rate of the $K^\pm \to \pi^\pm\pi^0\pi^0$ decays. The detector layout is shown in fig. 1.20: the 5 GeV/c unseparated kaon beam, positive or negative, was produced by the primary protons beam from the PS accelerator, then a differential Cerenkov counter tagged positively the kaons. A pair of scintillator hodoscopes traced the kaon direction. The decay vertex was obtained with the intersection of the kaon direction with the trajectory of the charged pion produced in the kaon decay in the $K^\pm \to \pi^\pm\pi^0\pi^0$ mode. The four vector of the charged pion was measured by means of a spectrometer composed by a large aperture magnet

and a system of spark chambers (S1 and S2 in the picture). The gammas from the π^0 decay were detected with an $\gamma-$hodoscope composed by lead and scintillator with two planes of scintillator in front in order to detect charged particles. The $\gamma-$hodoscope was used with trigger purpose and to identify, with conditions on the multiplicity of the hits, the main background $K^{\pm} \to \pi^{\pm}\pi^0$. Nevertheless in the 3γ category (three hits on the γ-hodoscope), that represents $\sim 13\%$ of the data, a background of $\sim 11\%$ was estimated while in the 4γ category ($\sim 1\%$ of the whole data sample) the background was $\sim 2\%$. The model used in the MonteCarlo simulation for the answer of the $\gamma-$hodoscope and of the detector acceptance for K^+ and K^- decays gives the main contribution to the systematic error. The final result for the asymmetry was:

$$A_g^0 = (0.19 \pm 1.25) \cdot 10^{-2}$$

based on ~ 59000 K^+ and ~ 56000 K^- decays.

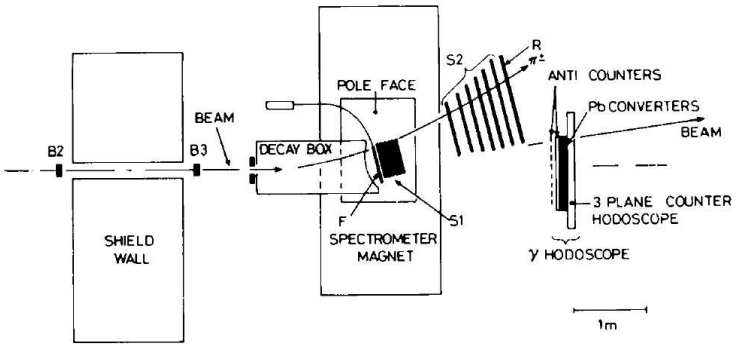

Figure 1.20: The CERN experiment to measure the properties of the $K^{\pm} \to \pi^{\pm}\pi^0\pi^0$ decay.

E871 (HyperCP) at Fermilab

In the fig. 1.21 the principal detectors of the E871 experiment [86] are shown. The main goal of this experiment was to study the CP violation in the hyperons decays (for this reason this experiment is also known as HyperCP experiment), but during 2 months in 1997 a special setup was used to efficiently collect kaon decays to measure, in particular, the A_g^c value. The kaons were produced by the 800 GeV/c protons impinging, at different time, on two targets of different length (2.2 and 6.0 cm) in order to produce particles of opposite sign with approximately the same flux in the central detector. The main part of the detector is the spectrometer, composed by 8 MWPC, four ahead and four behind of the analysing magnet. The trigger was performed by using two scintillator hodoscopes (one the "same sign" and "opposite sign" pions) and a hadronic calorimeter. The analysis strategy, based on Monte Carlo simulation, aimed at measuring independently the linear slope value in the positive and negative kaons. The result was:

$$g^+ = -0.18091 \pm 0.00030$$

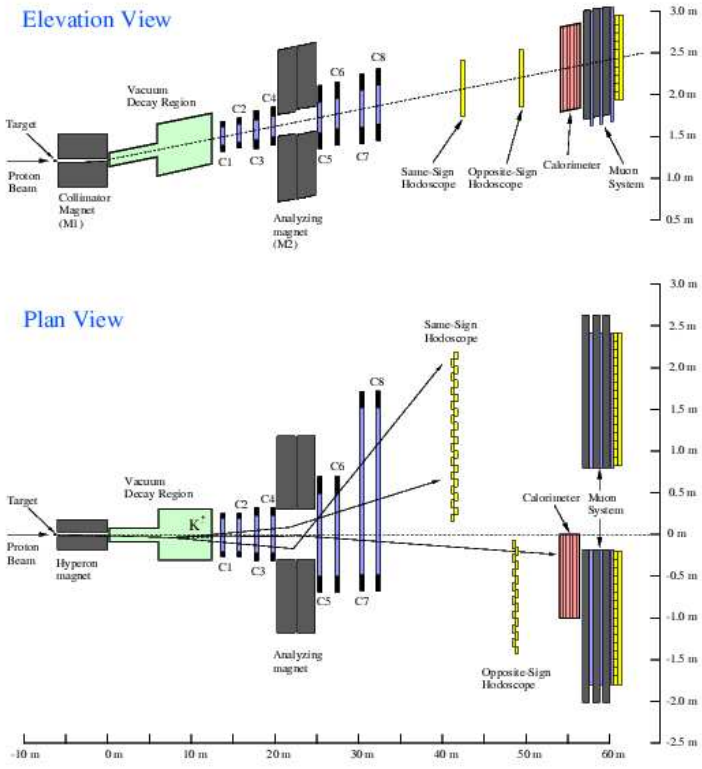

Figure 1.21: Two views of the E871 (HyperCP) experiment.

$$g^- = -0.18187 \pm 0.00055$$

based on 41.8 million of K^+ and 12.4 million of K^- decays. This leads to the preliminary asymmetry measurement[15]:

$$A_g^c = (2.2 \pm 1.5_{stat} \pm 3.7_{syst}) \cdot 10^{-3}$$

where the main contributions to the systematic error comes from the different beams properties between K^+ and K^- and from the uncertainty on magnetic field value.

Recent A_g^0 measurement at IHEP accelerator

In the TNF-IHEP facility recently an experiment [84] has been performed to measure the Dalitz Plot properties of the $K^\pm \to \pi^\pm\pi^0\pi^0$ and in particular the charged asymmetry parameter A_g^0. The 35 GeV/c hadron beam was produced by the 70 GeV/c protons from the IHEP accelerator. A magnetic system allowed to select positive and negative beams. The pions was distinguished from the kaons with a system of different Cerenkov detectors (fig. 1.22), with an efficiency in the selection at level of 1%. The decay products from $\pi^\pm\pi^0\pi^0$ were selected using a lead-scintillator electromagnetic calorimeter (GEPARD) and three scintillating hodoscopes (without

[15]The result is not published yet

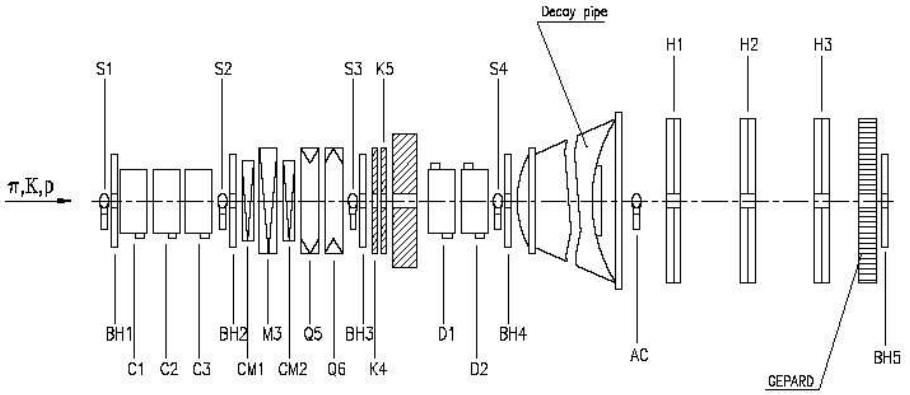

Figure 1.22: The TNF-IHEP experiment set up. The H1,H2 and H3 are the scintillating hodoscopes placed before of the GEPARD calorimeter. The Cerenkov PID system is composed by the C1-C3 and D1-D2 detector.

any magnetic spectrometer). The main sources of background were the $K^{\pm} \to \pi^{\pm}\pi^0$ (0.21%) and $K^{\pm} \to \pi^{\pm}\pi^+\pi^-$ (0.03%). The main systematic error was given by the uncertainty in the beam geometry, in particular the difference in the beam energy of $\sim 50MeV$ and the angular difference of $\sim 5\mu rad$ (with respect to the nominal axis, both in X and Y plane) between the K^+ and the K^- beam. The final result was:

$$A_g^0 = (0.2 \pm 1.8_{stat} \pm 0.5_{syst}) \cdot 10^{-3}$$

based on $2.8 \cdot 10^5$ K^+ and $3.4 \cdot 10^5$ K^- decays.

A pictorial view of the experimental situation together with the theoretical predictions is shown in fig. 1.23 . It is evident that there is a gap between the SM expected value and the present experimental sensitivity; that it is why observation of a CP violation could give hints of new physics. The purpose of the NA48/2 is to cover this gap.

1.5.9 Other CP violation effects in the charged kaon sector

There is some other place in which direct CP violation could be observed in the charged kaon decays.

The amplitude of the decay $K^{\pm} \to \pi^{\pm}\pi^0\gamma$ is composed of two parts: the inner-bremsstrahlung term (IB) and the direct emission term (DE). The contribution to the CP violation from the first part is suppressed by $\Delta I = 1/2$ while the second one allows to define an interference term, that is the source of asymmetry both in rate or in the Dalitz plot. The SM prediction for the CP violation in this channel, it is one order of magnitude greater with respect to the $K \to 3\pi$, but the BR is smaller ($BR(K^{\pm} \to \pi^{\pm}\pi^0\gamma) \simeq 2.8 \cdot 10^{-4}$) [43]. For the decays $K^{\pm} \to \pi^+\gamma\gamma$, $K^{\pm} \to \pi^+e^+e^-$ and $K^{\pm} \to \pi^+\mu^+\mu^-$ there are theoretical predictions in the SM at level $\sim 10^{-4}$, but the tiny BR for these channels is a serious limit to the study of CP violation through these asymmetries [64].

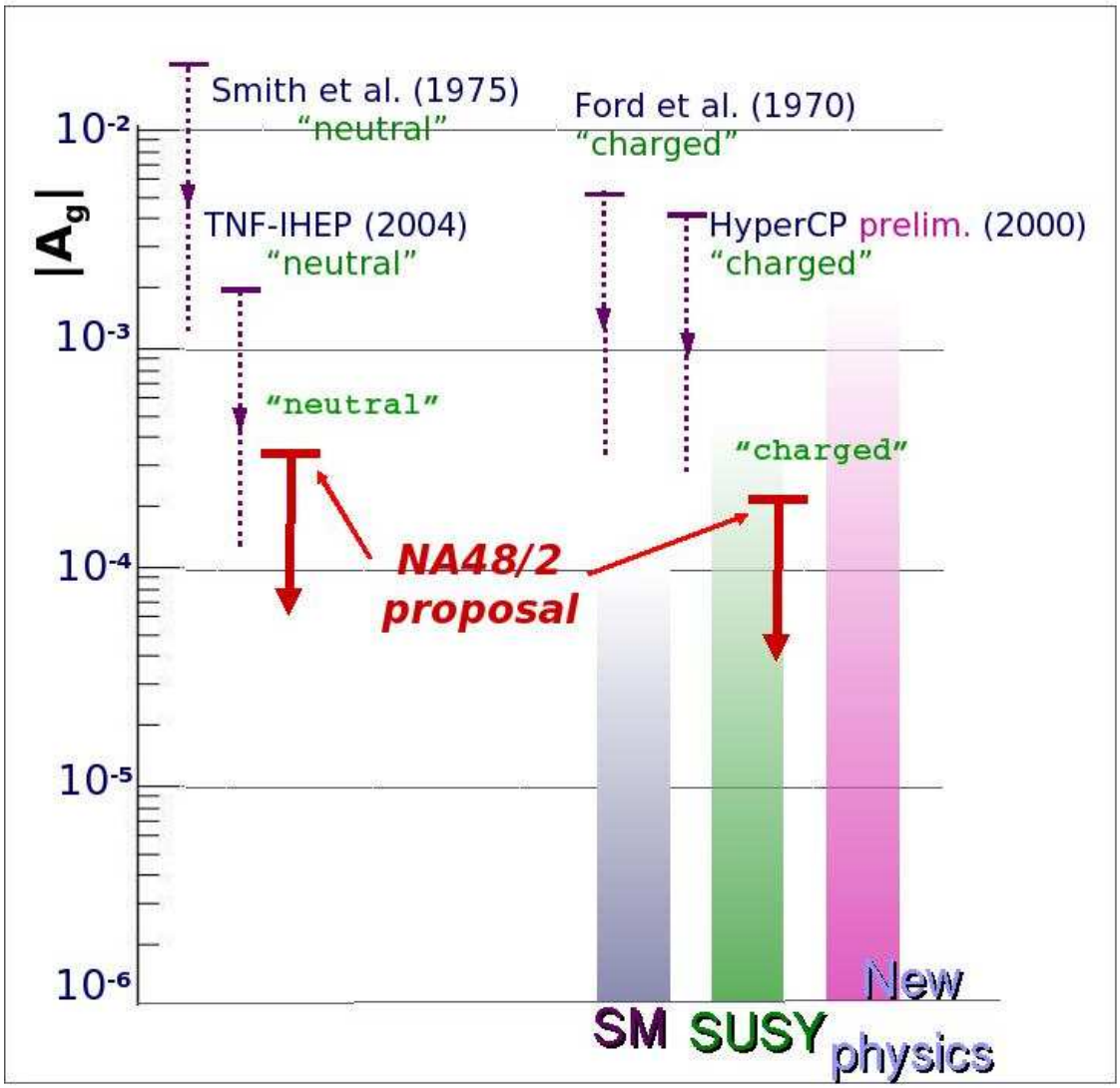

Figure 1.23: Comparison between the theoretical predictions and the experimental precision reached so far. As reference the goal of the NA48/2 is shown both in the "charged" (A_g^c) and in the "neutral" (A_g^0) decay

Chapter 2

Experimental Setup

A complete new beam line design and an upgrade version of the NA48's detector has been employed to take data for the NA48/2 experiment. The NA48/2 beam line allows the presence of simultaneous K^+ and K^- beams in the decay region instead of the neutral K_S and K_L as in the classical NA48 set-up. A new Kaon Spectrometer on the kaon beams, in order to measure the kaon momentum, and a beam position monitor in the end of the experiment (just in front of the beam dump), to check online the beam geometry, are the main changes in the central detector. Some other upgrade in the spectrometer readout (instrumentation of the third chamber and remapping of the drift chambers electronics) and some improvements in the level 2 charged trigger system, have been included for the NA48/2 data taking.

2.1 The Beams

The most important change with respect to the NA48 setup is the beam. Instead of the two simultaneous K_S and K_L beams, employed for the ε'/ε measurement, the NA48/2 use 2 charged kaon beams produced in the same target and selected in a narrow momentum band.

2.1.1 The SPS accelerator

The primary protons to produce both K^+ and K^- are slow extracted from the SPS (Super Proton Synchrotron) accelerator. To reach the nominal SPS protons energy of 400 GeV a multi stage acceleration system is used. The protons are produced from a duo-plasmatron source and then accelerated up to 50 MeV/c from the Linac-2, with a pulse length from 10 to 150 ms every 1.2 s and an intensity up to 180 mA. A system of 4 vertically stacked small synchrotrons, called PS booster (PSB), provides to increase the proton energy up to 1.69 GeV/c giving a bunched structure to the beam. The $3 \cdot 10^{13}$ protons per pulse (ppp) given from the PSB arrive to the PS (Proton Synchrotron) accelerator [87] that further increases the proton energy up to 14 GeV/c. Thanks to the 200 MHz radio frequency systems, the PS provides also to control the longitudinal emittance and the bunch properties,in order to adapt the beam to the SPS characteristics. The PS fills the SPS with two *trains* composed of $\sim$ 2000, 5 ns spaced, proton bunches, each 2 ns wide. The SPS accelerates the

protons up to 400 GeV/c. Every 16.8 seconds the protons are extracted from the accelerator by a controlled non linear betatron resonance of the ring. The amplitude of the betatron oscillation depends on the particle momentum. By adjusting the betatron oscillation frequency it is possible to move the desired amount of particles in the resonance region. A magnetised septum allows to extract the particles in the resonance orbit that cross its field [88]. It is important to mention that in the past the SPS worked also as injector for the LEP (Large Electron Positron) accelerator (accelerating positrons and electrons) and also as proton anti-proton collider (for example to perform the U1 and U2 experiment), and in the future will be a fundamental part of the acceleration chain for the LHC (Large Hadron Collider) accelerator. In the fig. 2.1 an old sketch of the CERN accelerator complex [89] is shown.

2.1.2 Beams production

After extraction the protons are transported along a $\sim 800m$ long beam line, and focused on a cylindrical (2mm in diameter) beryllium target in the T10 station, placed in the ECN3 hall in the North Area (NA) of CERN Prevessin site. The primary $7 \cdot 10^{11}$ ppp typically delivered from the SPS with a period of 16.8 s, a flat top of 4.8s and energy of 400 GeV, hit the 400 mm long target (corresponding to one interaction length for protons) with a $\theta = 0$ angle, to produce several types of particles (mainly protons, neutrons, photons, muons, pions, hyperons, kaons and electrons). A collimator placed 24 meter after the target defines the acceptance angle to be $\pm 0.36 mrad$. All neutral particles are dumped along the 0 degrees direction in a suitable absorber, thanks to the magnet system described in the next section.

2.1.3 Simultaneous K^+ K^- beams: the Achromats

The charged particles produced in the target are split according to the sign of their charge by using a dipole magnet and deflected back by a second dipole with the same strength and opposite polarity of the first. A set of collimators defines a narrow momentum band around the nominal value of 60 GeV/c (fig. 2.2). After this both the split charged particle beams are brought back along the 0 degree line. This first set of dipoles and collimators is called *Front End Achromat*. Following it a defining collimator is placed before a quadrupole (FDFD) system that has the purpose of focusing the beams with an angle of convergence of $\sim 0.04 mrad$. Instead of two parallel beams, as originally proposed [90] the collaboration realized that, in order to match better the purpose of the experiment, two "focused" beams, superimposed (in $\sim 2mm$) on a spot of $\sim 5mm$ (r.m.s) at the end of the decay region (fig. 2.3), were preferable and this solution was adopted despite the more complex beam transport line required.

After that a *second achromat* is placed to reduce the muons contribution and to house the first detector (the KABES) to measure directly the kaon momentum (see 2.2.1). At the end of the achromats the beams are composed of charged particles of 60 GeV ($\sim \pm 3.8\%$ r.m.s) according to the table 2.1

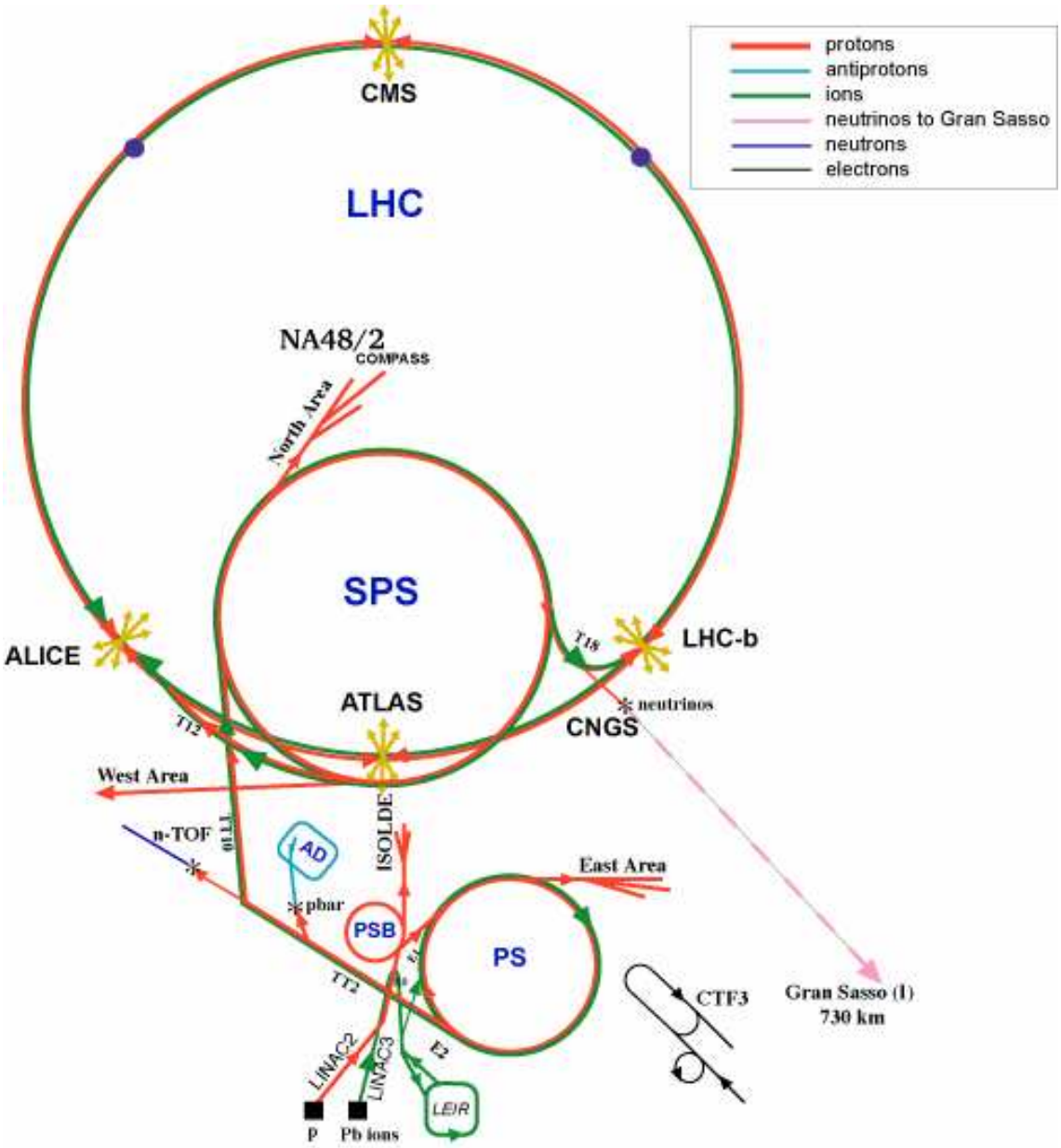

Figure 2.1: Schematics of the CERN accelerator complex. The NA48/2 experiment is located in the North Area on the beam lines extracted from the SPS accelerator. At the moment the LHC accelerator is under construction.

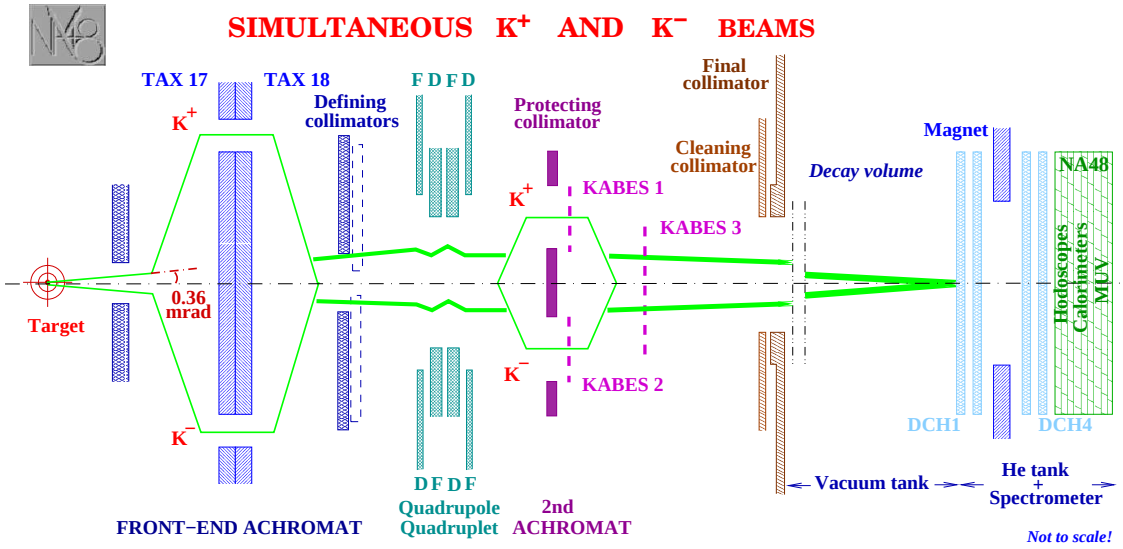

Figure 2.2: Vertical view of the achromats system and beam line. The magnets disposition before the focusing system defines the first achromat. The second one houses the Kabes detector

Particle	Particles per pulse (in 10^6)	
	+	-
K	2.2	1.3
π	23	17
p	6.1	0.6
e	6.0	6.0
Other	~ 1	~ 1
total	38	26

Table 2.1: Fluxes of positive and negative particles at the begin of the decay region

2.2 The Detector

The central detector for the NA48/2 setup is essentially the same with respect to the standard NA48 setup (as described for instance in [38]). In fig. 2.4 it is possible to see a sketch of the central detector. The decay region has been extended upstream by 24 meters, to compensate the smaller $K^{\pm}$ lifetime with respect to the K_L and in order to increase the detector acceptance for the $K^{\pm} \to \pi^{\pm}\pi^{+}\pi^{-}$ decays. The momentum and the direction of charged kaon are measured with a spectrometer based on MICROMEGAS (par 2.2.1). The charged particles produced in the kaon decays are detected by using a magnetic spectrometer with 4 drift chambers (described in the par. 2.2.4) and a plastic scintillator hodoscope for trigger and accurate timing (par. 2.2.5). A Liquid Krypton Calorimeter (par. 2.2.6) is devoted to measure the properties of the photons. Other veto counters and detectors with trigger purpose are included in the setup.

2.2.1 KABES

The first detector on the beam path is KABES (KAon BEam Spectrometer) [91], a TPC detector based on MICROMEGAS [92] as illustrated in fig. 2.5. The gas mixture employed is $Ne(79\%) + C_2H_6(11\%) + CF_4(10\%)$. The maximum rate at which this device works is $\sim 2MHz$, in the center of the beam spot. The read-out electronics employs the HPTDC (High Performance TDC) chip, developed at CERN (ref.). All the system is designed to stand a single rate strip of 8 Mhits/s with a total rate of 40 Mhits/s (for each KABES station). The purpose of this device in NA48/2 arises from the necessity to enhance the resolution on kinematics quantities especially in rare decay studies, where a good resolution for signal to background separation is very important. KABES informations could be useful also in the asymmetry studies, for events in which only 2 of the pions are detected, both in $K^{\pm} \to \pi^{\pm}\pi^{+}\pi^{-}$ and in $K^{\pm} \to \pi^{\pm}\pi^{0}\pi^{0}$ decay. This detector is subdivided in three stations, each of them to record the time and the spatial coordinates of the particle. The first two stations are placed on the two displaced paths of the second achromat, where the two beams are split according to the charge. The last station is located downstream the achromat where the two beams become collinear. Starting from the vertical impact point in each station, it is possible to deduce the Kaon momentum and by reconstructing the kaon track through the various stations, it is possible to define the kaon trajectory. The good time resolution, at level of $\sim 0.7ns$, is exploited by the reconstruction program to identify the nearest kaon track to the event in the

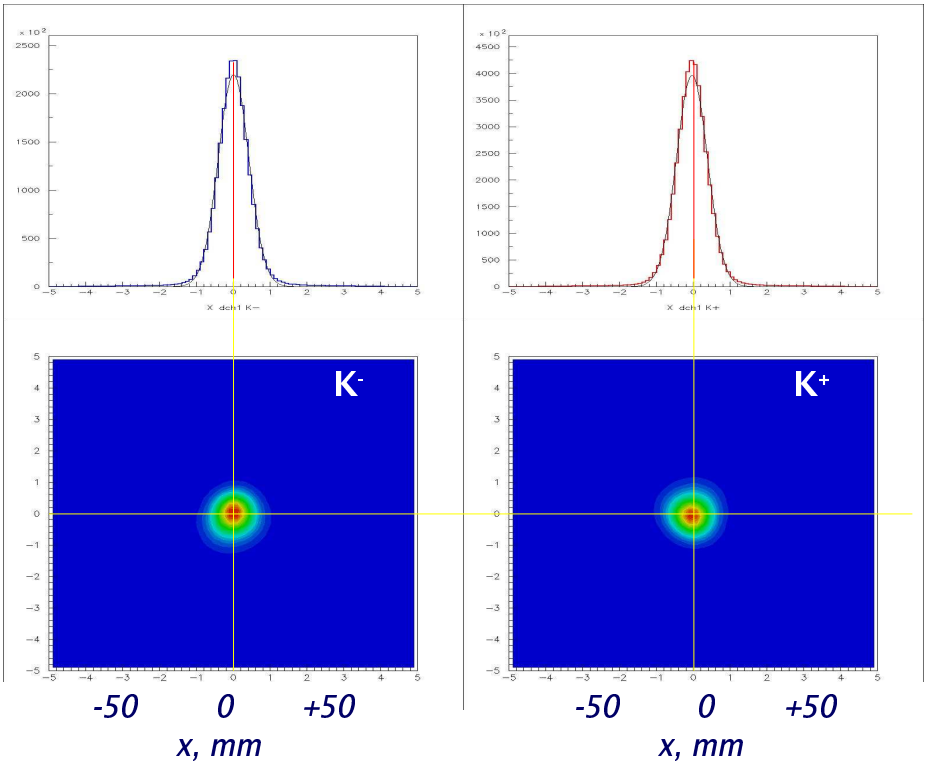

Figure 2.3: Beam spot at the spectrometer position for K^+ and K^-

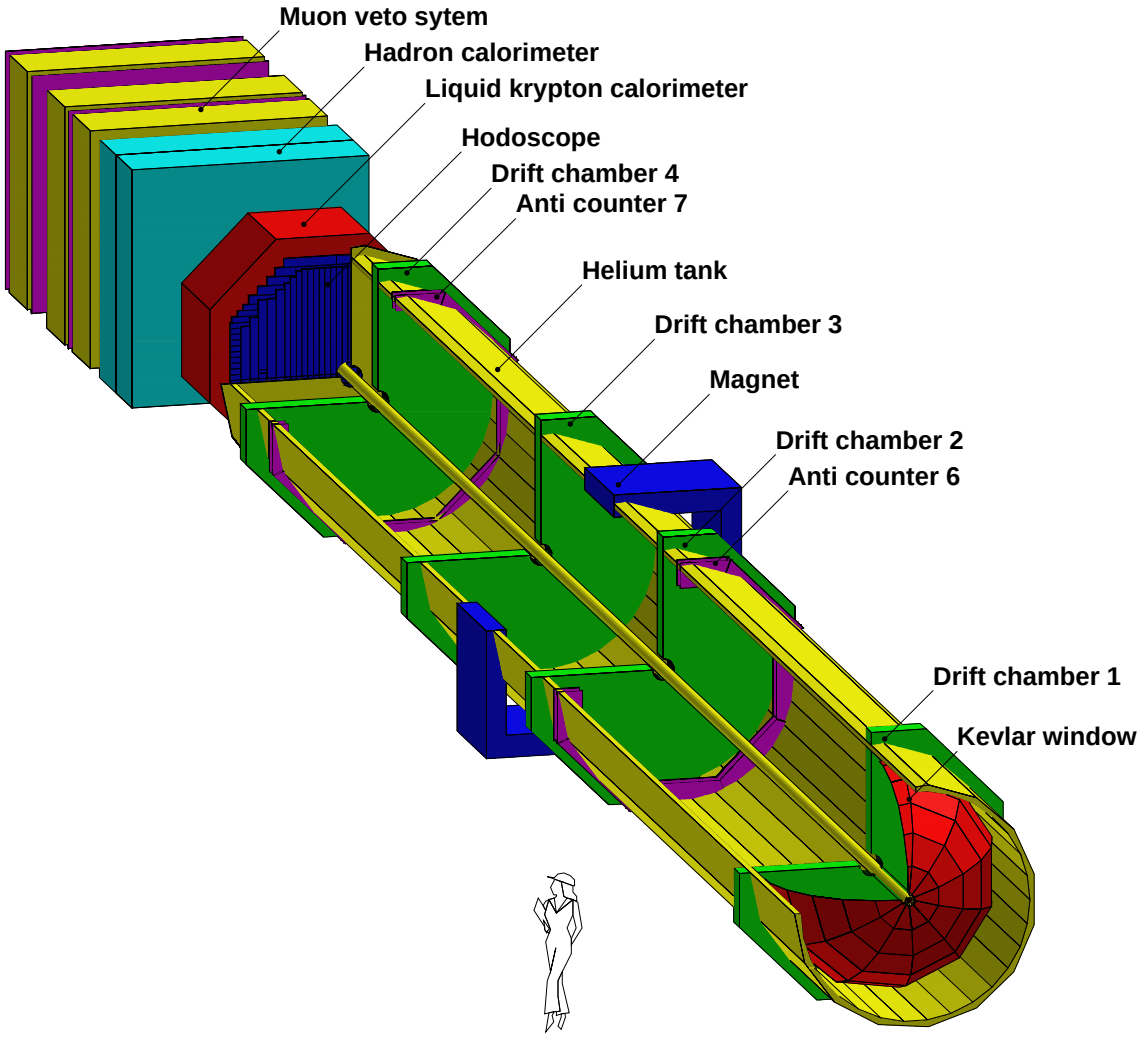

Figure 2.4: Schematics of the central detectors. It is possible to distinguish the magnet spectrometer, the charged hodoscope counters, the electromagnetic and hadronic calorimeters and the muon veto system. The beam pipe passes through all detectors reaching the beam dump at the end of the experimental hall.

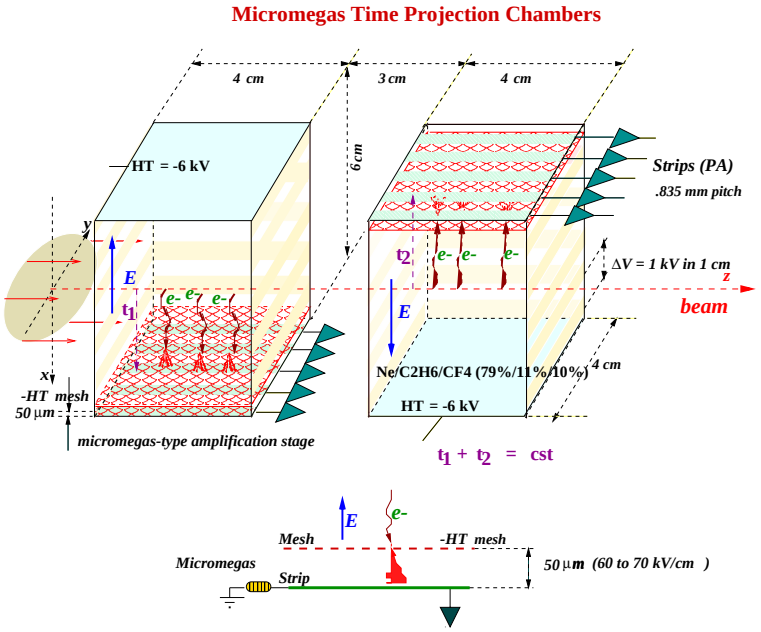

Figure 2.5: Working principle of the MICROMEGAS detector.

central detector (fig. 2.6) (this time is defined by the CHOD (par. 2.2.5)). The momentum resolution of KABES has been evaluated studying the convolution with the spectrometer resolution in $K^{\pm} \to \pi^{\pm}\pi^{+}\pi^{-}$. In this way a value of 1.1 % has been measured, as can be seen in fig. 2.7 . The KABES system (fig. 2.5) performances are summarized in table 2.2 at the nominal proton intensity of $7 \cdot 10^{11}$ ppp .

Horizontal position	$100\mu m$
Vertical position	$130\mu m$
Time	~ 0.65

Table 2.2: Kabes performances

2.2.2 Decay region

To avoid interactions of kaon decay product before the detection the decay region is contained in an evacuated (at $< 10^{-4}$ mbar) cylindrical tank (called *blue tube*) of diameter 1.92 m, increasing to 2.4 m in its last 48 m. The total length is ~ 113 m (see fig. 2.8). The downstream part of the blue tube is closed with a thin (0.8 mm thick), convex hemispherical shaped, 1.3 m radius Kevlar window. The purpose is to separate the vacuum in the decay region from the Helium at atmospheric pressure in the spectrometer. The thickness of the window is 0.9 mm, corresponding to $3 \cdot 10^{-3} X_0$.

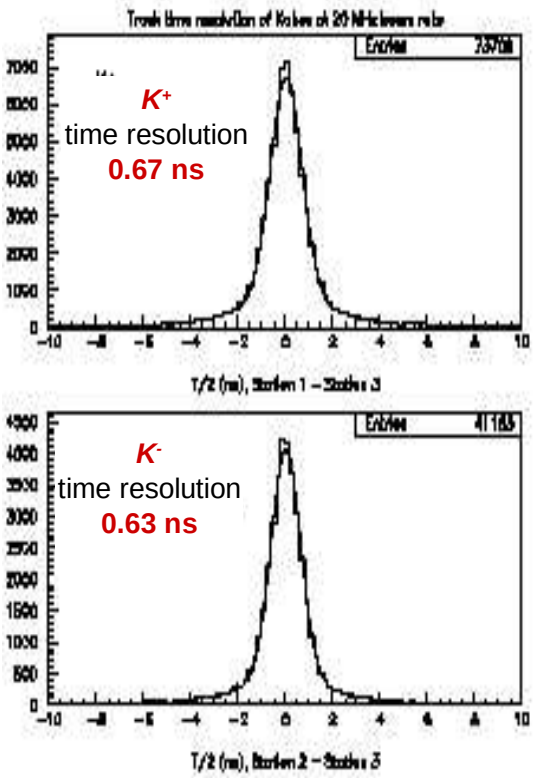

Figure 2.6: Kabes time resolution

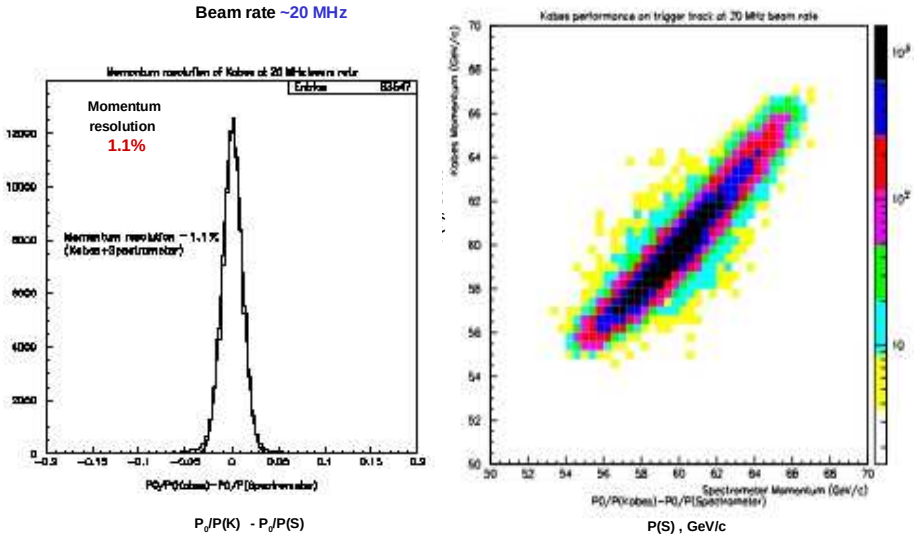

Figure 2.7: Kabes momentum resolution

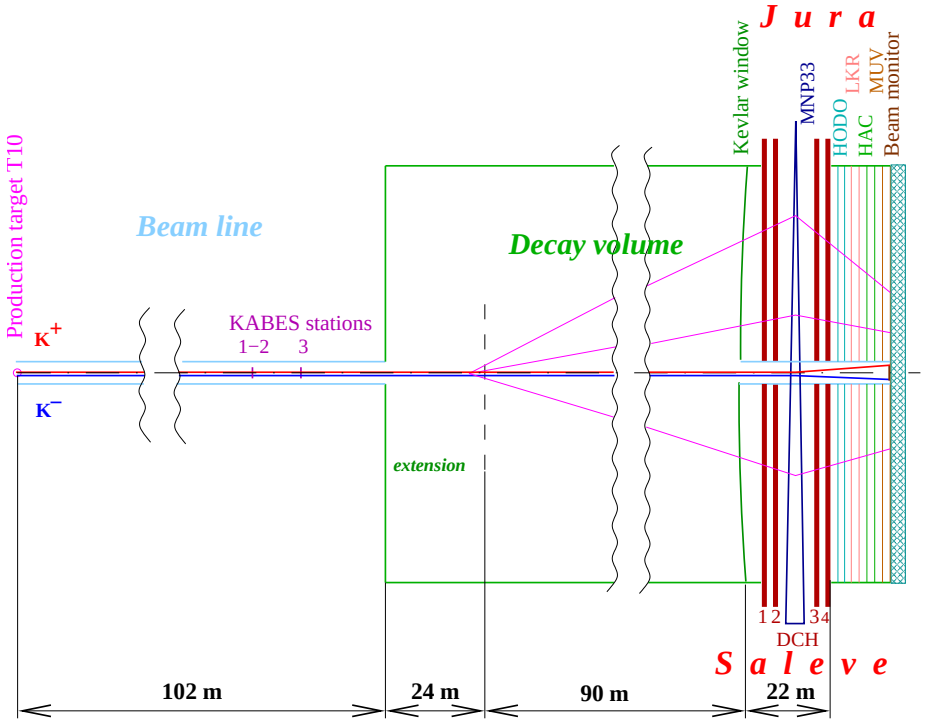

Figure 2.8: An aerial view of the NA48/2 decay region. In evidence the extension of 24 m to increase the detector acceptance. The "Jura" and "Saleve" are the conventional name for the right and left side according to the mountains position with respect to the experimental hall

Downstream the Kevlar windows the beam, containing mainly undecayed kaons and pions, continues in vacuum contained in a carbon fiber pipe of 152 mm diameter and 1.2 mm thick. In the decay region a small residual magnetic field, mostly due to the Earth field, is present. Just before the 2003 run, this *blue field* (the magnetic field in the blue tube) has been carefully measured directly (by using Hall probes) in order to allow a posteriori correction on reconstructed tracks and in order to include the effect in Monte Carlo simulations; in fig. 2.9 it is possible to see the maps for the horizontal and vertical component of this residual magnetic field.

2.2.3 The AKL

The AKL anticounters system consists of 7 rings of irons and scintillator placed along the decay region (5 of them) and in the spectrometer (the last 2). In the fig. 2.10 the position of the AKL rings is shown. The purpose of these detectors is to detect photons outside the detector acceptance. It was designed for NA48 to identify the missing photons in the $K_L \to 3\pi$ decay [1], but it is used also in NA48/2 to reduce the trigger rate. Each pocket is composed of two layers of scintillator preceded by a 3.5 mm thick plate of steel acting as photons converter (with 95% of

[1]Due to the fact that the geometrical disposition has been optimized for this kind of decay, the acceptance for the K^+ products could be totally different

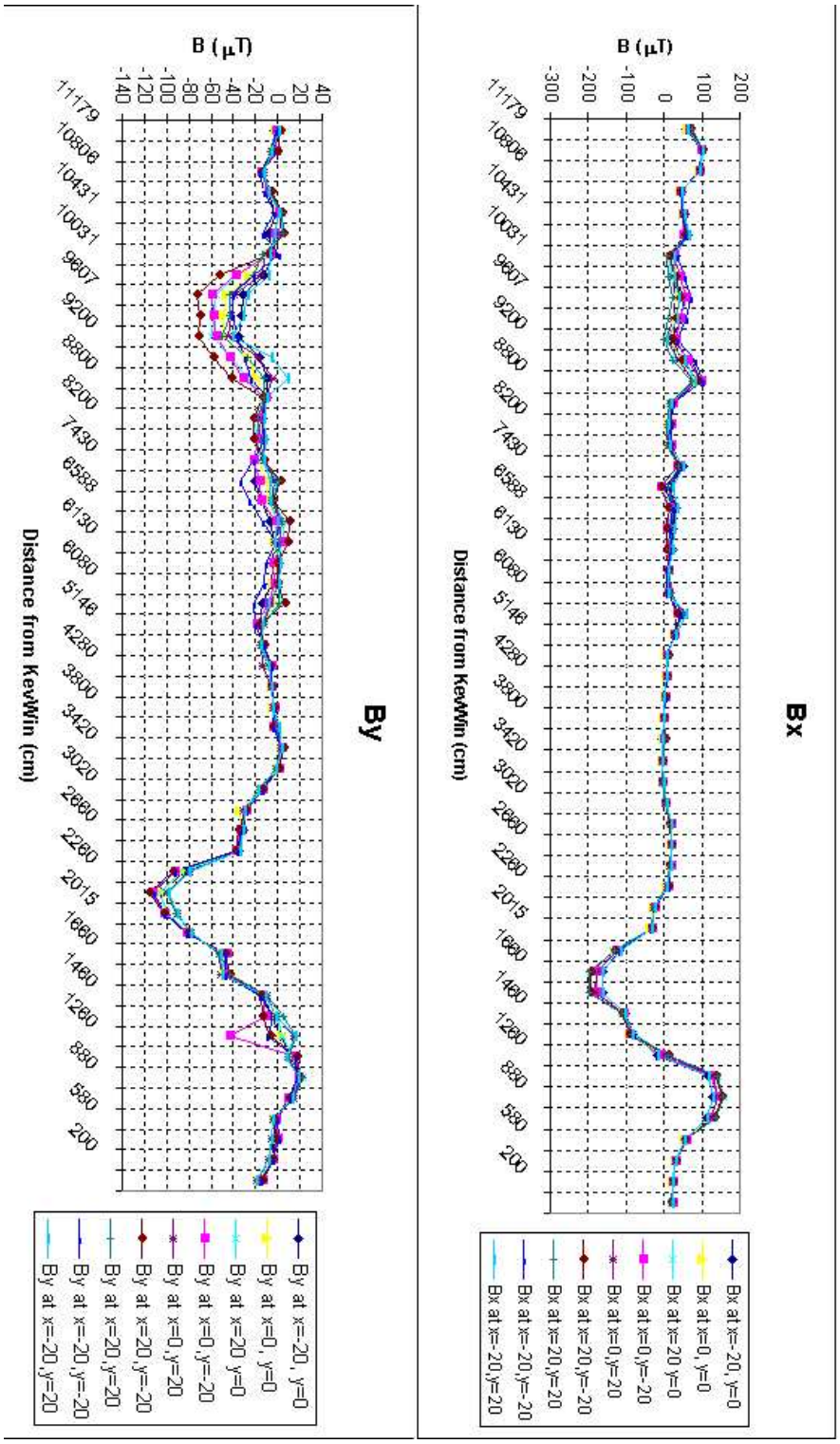

Figure 2.9: X and Y component of the "Blue field". The different colors correspond to different position at which the map has been measured

conversion efficency). Each layer is composed by 12 plastic scintillators 10 mm thick for pockets 1 to 4 and 8 plastic scintillators for pockets 5 to 7. All the scintillators are readout on both sides.

2.2.4 Magnetic Spectrometer (DCH)

The magnetic spectrometer is equipped with 4 drift chambers (DCH) and a dipole magnet (fig. 2.11) placed in the center, between the DCH2 and the DCH3, providing a pt_{kick} of 120 MeV/c. The magnet polarity is frequently swapped in order to reduce the systematics due to the different detector acceptance for K^+ and K^- as explained in chap. 5. The field inversion is directly monitored by using Hall probes and by checking the reconstructed kaon masses in the $K^{\pm} \to \pi^{\pm}\pi^{+}\pi^{-}$ decay mode. The whole spectrometer volume is kept at atmospheric pressure and filled with pure helium to reduce multiple Coulomb scattering. Each drift chamber is composed by 8 planes of sense wires (fig. 2.12), aligned along the orthogonal wire directions (the so called *views* fig. 2.12) X and Y, and the rotated directions at 45° U and V, in order to solve reconstruction ambiguities (fig. 2.14). Each view is equipped with 2 planes staggered by half wire pitch, in order to avoid left-right ambiguities and to increase the spatial resolution of the reconstructed point (fig. 2.13). The total number of wires is 256 for plane and the maximum drift time is 100 ns (corresponding to the half wire pitch of $5mm$), obtained with a gas mixture of Argon (50%) + Ethane (50%). The shape of the chambers is octagonal with a width of 120 cm. The resolution on the spatial position of the reconstructed hit is $< 100\mu m$. The fast rise time of the pulses and the performance of the HPTDC allow to obtain a time resolution of 700 ps. The momentum resolution of the spectrometer is (at 120 MeV

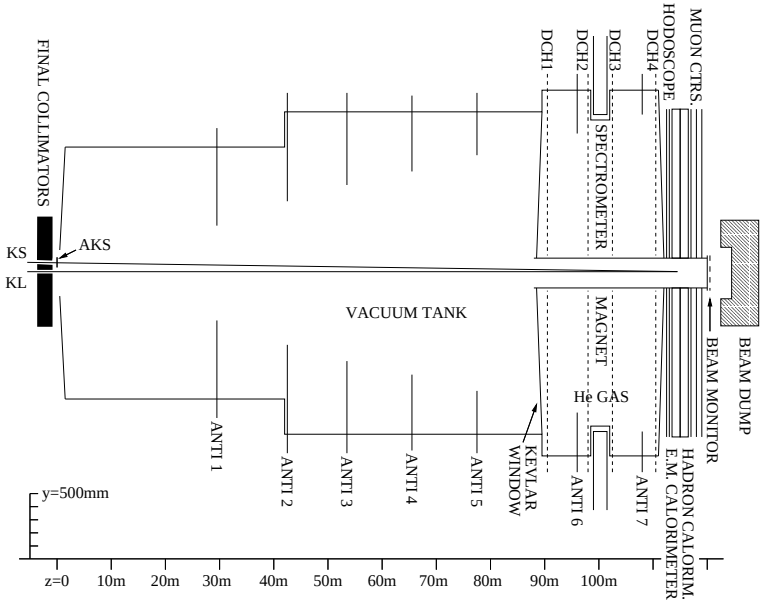

Figure 2.10: AKL rings position in the decay region and spectrometer layout.

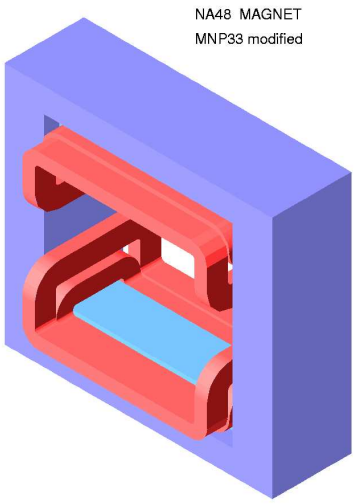

Figure 2.11: The spectrometer magnet MNP33. The central aperture measures 2.45 x 2.20 m^2.

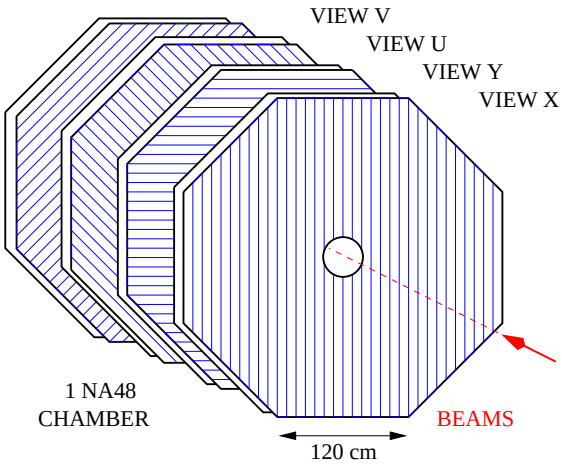

Figure 2.12: Drift chambers disposition

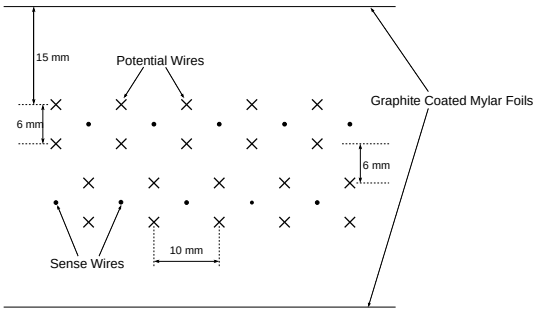

Figure 2.13: Internal structure of the drift chamber. Two staggered planes of sense wires compose a view. In each plane there are 256 sense wires, each sense wire is surrounded by 4 potential wires.

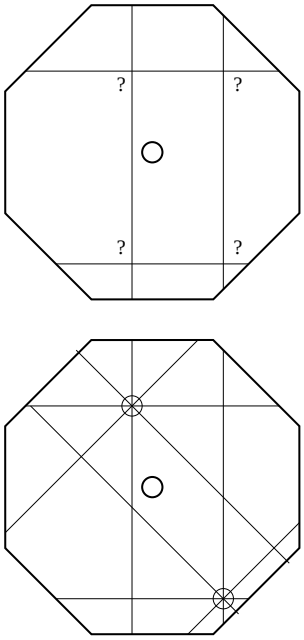

Figure 2.14: The use of the U and V views can solve the ambiguities in the reconstruction.

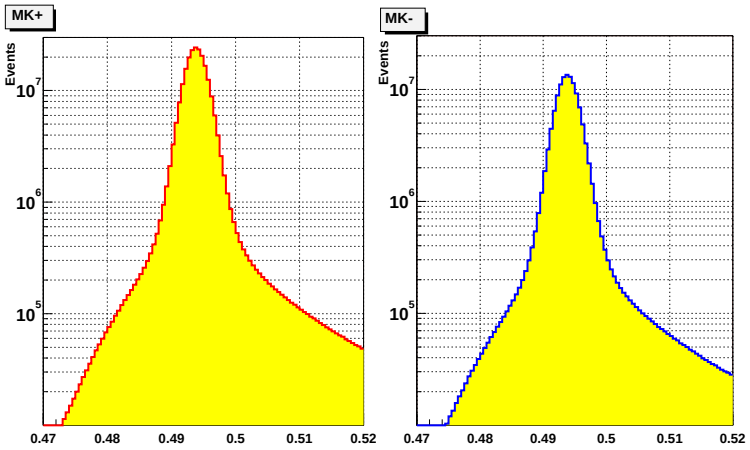

Figure 2.15: The invariant mass reconstructed for 3 charged particle assumed to be the product of $K^{\pm} \to \pi^{\pm}\pi^{+}\pi^{-}$ decay.

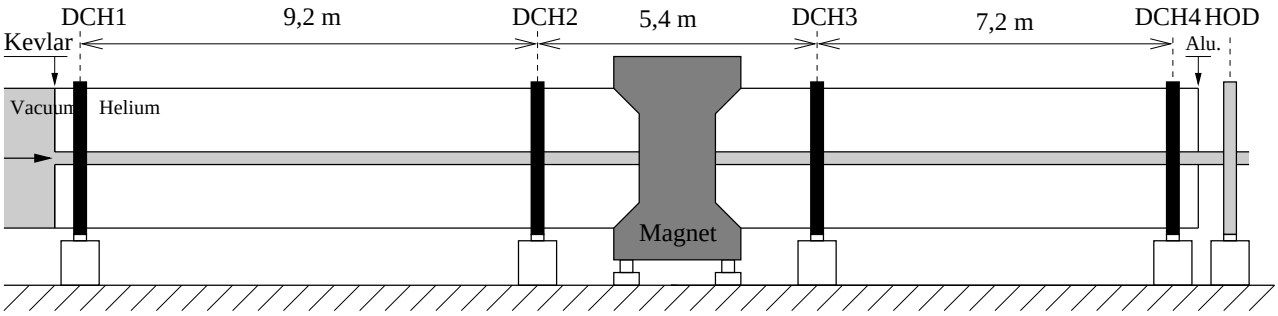

Figure 2.16: Lateral view of the spectrometer in which it is possible to see the relative chambers position

of pt_{kick} corresponding to $\sim 0.5Tm$ of integrated field)

$$\frac{\sigma(P)}{P} = 1.0\% \oplus 0.044 \cdot P(GeV)\%$$

where the first term is related to the multiple scattering and the second one to the spatial point resolution. Thanks to this performance the resolution on the reconstructed kaon mass in the $K^{\pm} \to \pi^{\pm}\pi^{+}\pi^{-}$ (obtained using only the spectrometer) is 1.7 MeV/c^2, as shown in fig. 2.15. The magnetic spectrometer is essential in the "charged" asymmetry measurement (the asymmetry in $K^{\pm} \to \pi^{\pm}\pi^{+}\pi^{-}$) in which all the kinematically relevant quantities are constructed from charged pion tracks. In order to symmetrize the DCH readout the wires have been remapped with respect to the ε'/ε era; in such a way a readout chip is responsible for 16 channels subdivided in left and right opposite positions. During the data taking, special runs with parallel muons, instead of the kaon beam, were taken to allow the inter-alignment between the chambers. During the 2003 data taking three of this runs were recorded. Due to the observation of a critical sensitivity on A_g measurement to the spectrometer

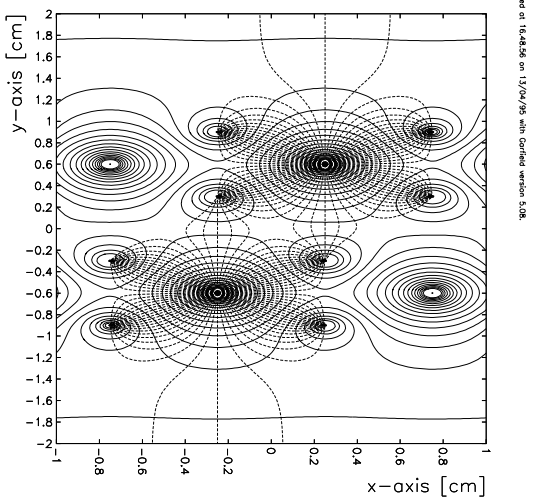

Figure 2.17: Electric field simulation between wires in a DCH plane.

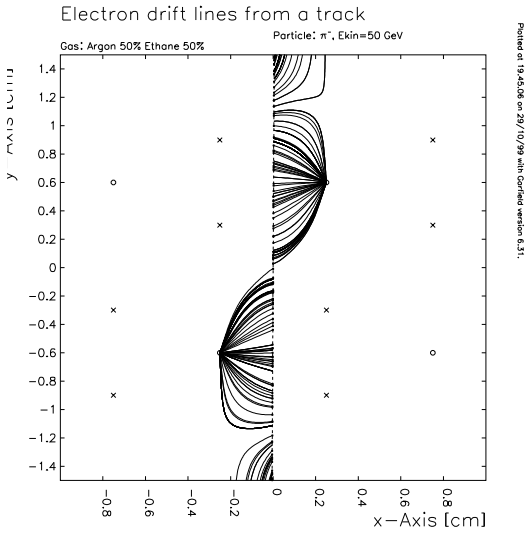

Figure 2.18: Signal induced from a 50 GeV/c pion through the chamber. It Is evident as the staggered structure can solve the left right ambiguity

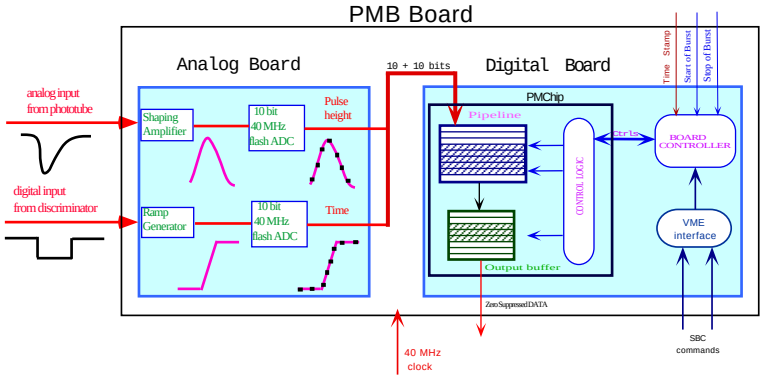

Figure 2.19: Conceptual design of the PMB board

internal alignment, in to the 2004 data taking more muon runs (10) have been collected. Special runs with a low intensity hadron beam (a low intensity version of the standard beam) that hits directly the chambers in different points were taken for the same purpose.

2.2.5 The charged hodoscope

The purpose of the charged hodoscope is to provide an accurate timing independently of the response of the wire chambers[2], to give a time reference both for offline and online reconstruction and also to provide a fast trigger condition at the L1 (par. 2.3.1). The hodoscope is composed by two plastic scintillator planes, one vertical and one horizontal. Each of them is subdivided in 64 slab of different length

[2]this is not so important for NA48/2 but was crucial for NA48 to allow the coincidence between the charged pions in the decay region and the proton on the KS target in a tagger detector.

and width, according to the geometry of the detector: the length is in the range 60 cm to 121 cm and the width is 6.5 cm or 9.9 cm, as can be seen in fig. 2.20. The central hole, in which the beam pipe passes through, has a 10.8 cm in radius. The thickness (equal for each slab) is 2 cm, corresponding to 0.05 L_0. The horizontal plane is at 80 cm from the LKr, while the vertical plane is 75 cm in front of the horizontal one; this distance is useful to distinguish the false coincidences due to the *back splash* coming from the LKr. The readout is performed by special VME modules called PMB (Pipeline Memory Board) that are schematically presented in fig. 2.19. The analog signal coming from the photomultipliers placed at the outer edge of each slab is first discriminated and then sent to a 10 bit 40 MHz FADC/FTDC together with the digital discriminator output. The analog signal is shaped and digitized to get the signal pulse height while the digital input is used to trigger a TDC ramp between two levels. In this way a better time resolution is achieved. The PMB modules have been specifically designed for the CHOD system, but are also used for the readout of the AKL, NHOD and for the NUT system. By using the impact point information from the spectrometer, the CHOD time resolution is $\sim 150ps$. Using logic conditions on the CHOD it is possible to define several trigger signals, useful to define easy and fast conditions at the first level of the trigger. For instance if a quadrant in each view (the two quadrants have to be geometrically compatibles) fires the Q1 signal is defined: this signal is essential for many *one track* triggers.

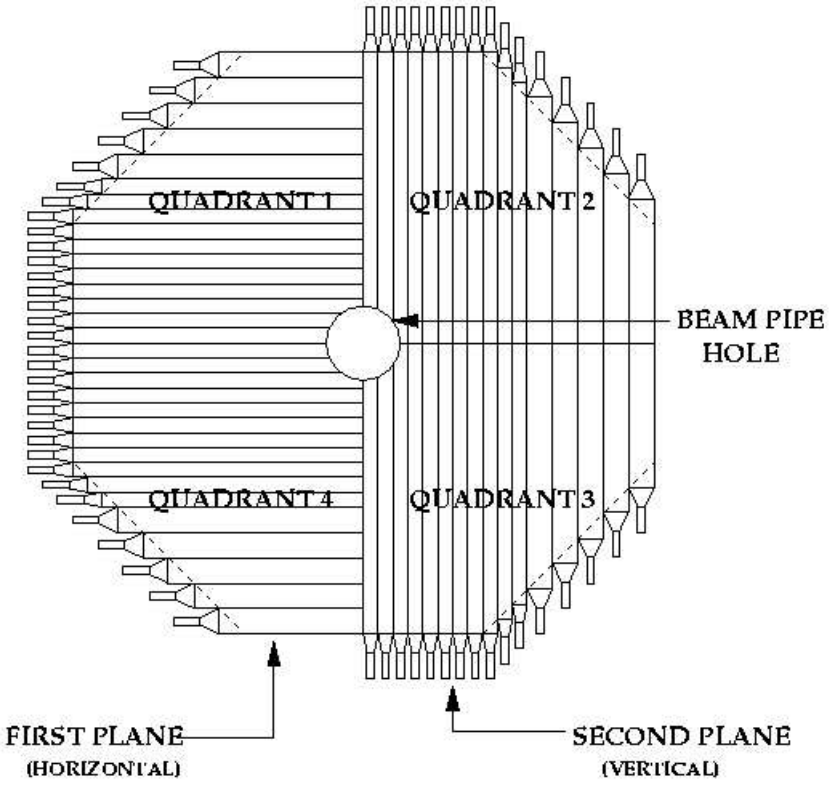

Figure 2.20: Sketch of the horizontal and vertical charged hodoscope planes.

2.2.6 The Liquid Krypton calorimeter

The fundamental detector for the neutral reconstruction is the Electromagnetic Calorimeter. The NA48/2 electromagnetic calorimeter is a quasi homogeneous liquid Krypton ionization chamber. This liquefied noble gas is chosen because of the linear response in energy of the detector, the absence of aging problems and the relative short radiation length which allows a compact detector along the longitudinal direction, without the use of passive and massive radiator medium, as in the standard sampling calorimeters.

Calorimeter characteristic

The calorimeter's shape is approximately octagonal in the transverse plane (transverse with respect to the beam line) and the length along the longitudinal direction is around 127 cm (the active part), corresponding to 27 radiation length [3]. The active part is subdivided in 13248 cells defined through Cu-Be-Co ribbons of $18mm \cdot 127cm$ and thickness of $40\mu m$. In this way the cells are defined with a dimension of $2cm \cdot 2cm$. The ribbons are not perfectly parallel. A projective geometry is chosen to assure a higher accuracy in the measurement of the angles between photon showers coming from a particular point ($\sim 90m$ in front of the LKr) in the decay region[4]. To assure the stability of the ribbons position at level of 0.3 mm , 5 special spacing plates are disposed longitudinally, in 5 different positions,$\sim 21cm$ spaced, in between the front and the back of the calorimeter(fig. 2.22). The plates also assure a constant tension of $\sim 2N$ for each ribbons and a peculiar 'zig zag' shape that minimizes inefficient ionization from showers developing along the cathode (the so called *accordeon geometry* fig. 2.21). In the middle of the cells a collecting anode is kept at a voltage of +3 kV and is connected via a low self inductance capacitor to the preamplifier (which is immersed in the Kripton). Only the initial part of the induced current by the electromagnetic shower is read-out, in order to improve the time resolution. A quite complex cryogenics system assures that the LKr temperature is kept constant at 121 K within $\pm 0.1\%$. The boiling temperature of the Kr at atmosperic pressure is 119.8 K. All the calorimeter is enclosed in a cryostat composed by an external aluminium vessel (4 mm thick) and an internal vacuum insulated steel container (29 mm thick) that contains $\sim 9m^3$ of liquid Krypton.. The temperature stability of the LKr is quite important, since that the dependence of the electron drift-velocity on the temperature (mostly due to the change in the liquid krypton density), $\Delta v_d/v_d \sim -0.87\% \cdot \Delta T$, is not negligible. The whole cryostat introduces some passive material ($\sim 0.65X_0$) in front of the LKr that corresponds, on average, to a 50 MeV loss in recostructed photon energy . The Krypton characteristics are summarized in table 2.3.

Calorimeter Read-out

The calorimeter readout [93] works in a current sensitive mode using the initial induced current which is proportional to the deposited ionization and therefore to the

[3] A shower of 50 GeV is fully contained (99%) in 27 X_0

[4] the point was chosen according to the acceptance for the $K_{L,S} \to \pi^0\pi^0$ in the ε'/ε era

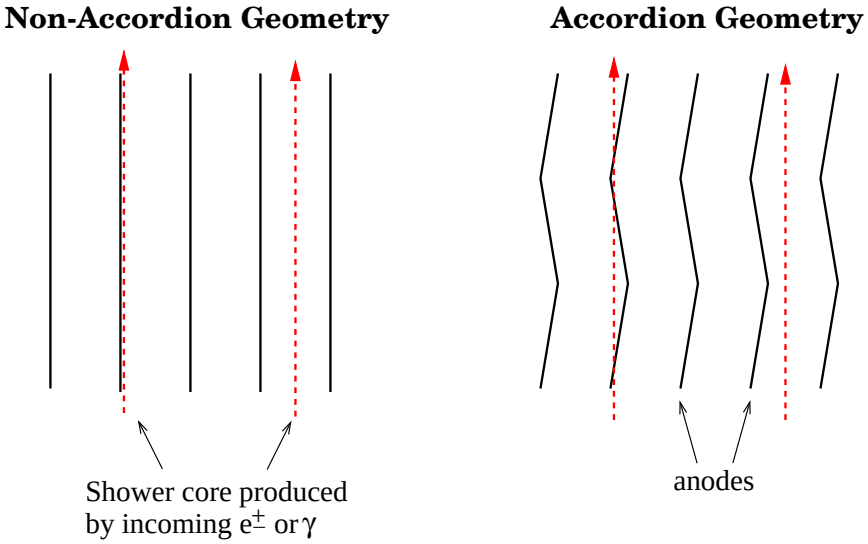

Figure 2.21: The accordion geometry assures that the showers developed along the ribbons direction are correctly measured

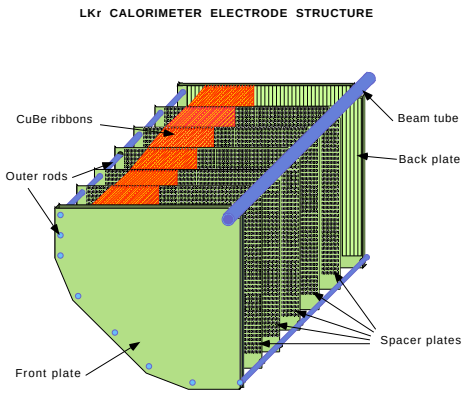

Figure 2.22: The LKr electrode structure.

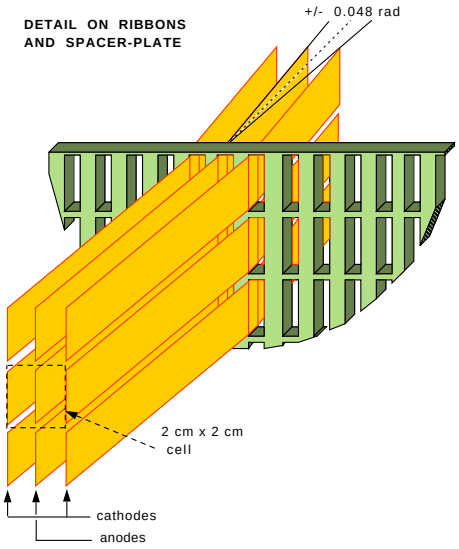

Figure 2.23: Details of the LKr cell structure. It is possible to see the "accordion" structure of the ribbons.

electromagnetic shower energy. The induced initial current to a good approximation does not depend on the spatial charge distribution in the cell. Moreover the fast shaping of the initial current allows a good time resolution. The calorimeter readout is designed to avoid any dead time. The front-end electronics is directly mounted on the detector back-plate in the cryostat in order to reduce the noise and to minimize the signal time extraction. The front-end electronics (fig. 2.24) includes essentially the preamplifiers and the electronic calibration system for the single channels. Individual coaxial cables connect the output of the preamplifiers to room temperature

Liquid krypton properties		
Atomic number	Z	36
Mass number	A	84
Density @ -150Â°C	$\rho(g/cm^3)$	2.41
Radiation length	X_0 (cm)	4.7
Molieré's radius	$R_M(cm)$	4.7
Energy to produce the pair e^-+ion	W(ev/pair)	20.5
Hadronic interaction length	$\lambda_l(cm)$	60
Boiling temperature (at 10^5 pascal)	$T_b(K)$	119.8
Fusion temperature (at 10^5 pascal)	T_m	116.0
Drift velocity @ 1 KV/cm	$v_d^e(mm/\mu s)$	2.7
Drift velocity @ 5 KV/cm	$v_d^e(mm/\mu s)$	3.7
Critical energy	$E_c(MeV)$	21.51

Table 2.3: Mains physics properties of the Krypton

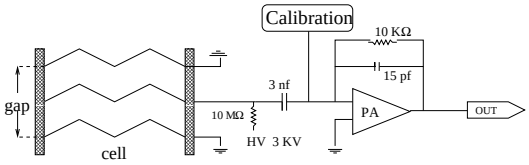

Figure 2.24: LKr electronic "cold" Front end

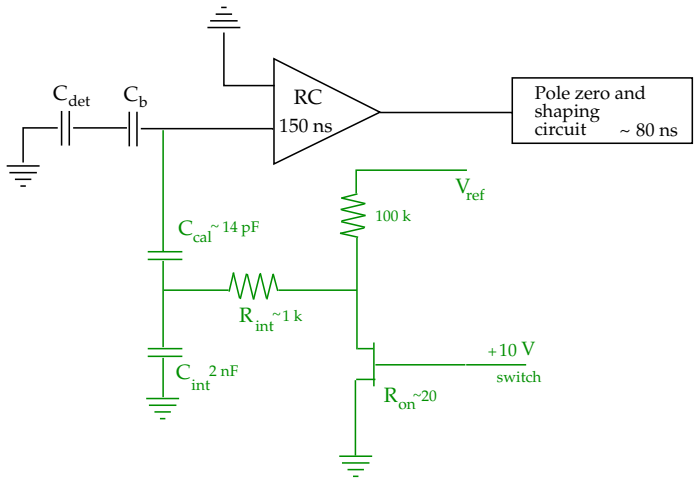

Figure 2.25: Simplified scheme of a calibration circuit. Every cell is equipped with a calibration circuit that can inject a programmable signal.

feedthroughs on which suitable transceivers are directly located. Outside the cryostat the transceiver drives the signals to the readout modules, the CPD (Calorimeter Pipeline Digitizer). An asynchronous digital sampling of the output signals is done every 25 ns by a 10 bits FADC with an automatic gain switching to cover the full dynamic range (3.5 MeV to 100 GeV), the gain value is recorded in two additional bits. The digitalized signals are stored in a $3.2\mu s$ deep pipelined memory for each channel (each cell) and then are sent to the Data Concentrator system, that operates a *zero suppression* for the cells with energy below a certain threshold, and applies a cluster finder algorithm to the cells above threshold. In this way it is possible to reduce at ~ 100 the number of the cells read for each electromagnetic shower

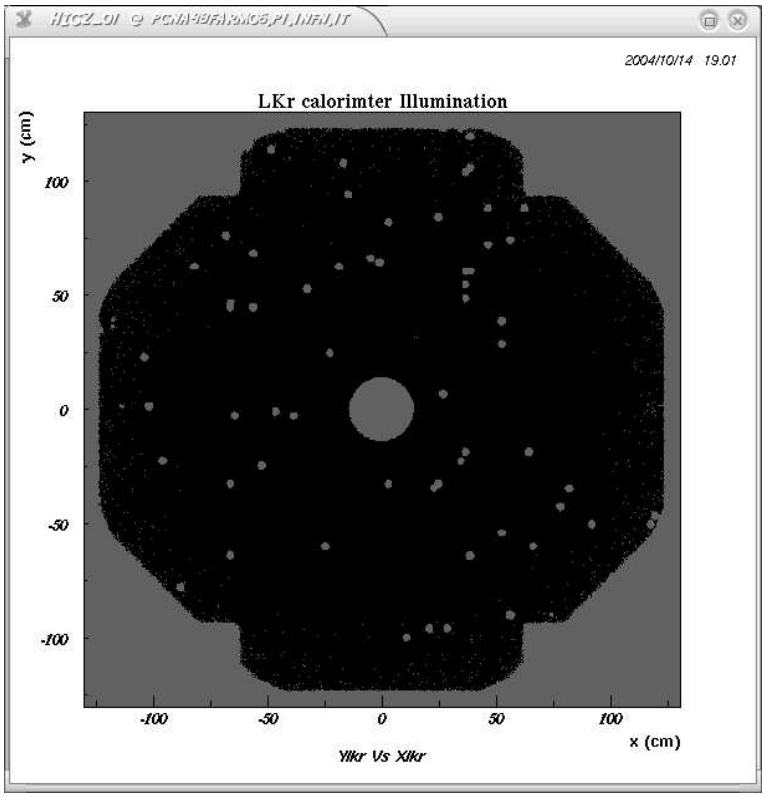

Figure 2.26: Position of the dead cells in the LKr.

Dead Cells

Due to their inadeguate response, small fraction of the 13248 cells (~ 60 cells) of the LKr calorimeter are defined as *dead cells*. The reason for that depends on different faults in the electronic chain; the most common problems are faulty preamplifiers, no calibration, bad pedestal, excessive noise, very unstable response to calibration pulses. In fig. 2.26 it is possible to see the dead cell position in 2003 run (the map is the same in 2004 run).

Calorimeter Performances

The calorimeter can manage an instantaneous rate of $\sim 1MHz$, with no dead time and full efficiency. The energy linearity response is frequently measured by comparing the electron energy in the decay $K_L \to \pi^{\pm} e^{\mp} \nu_e$ (the so called K_{Le3}) with the momentum measured by the spectrometer (fig. 2.28). The same decay is exploited to measure the uniformity of the detector. The overall energy scale has been measured by using the $K_S \to \pi^0\pi^0$ decay to fit the position of a special detector, that was useful to define the beginning of the decay region in the NA48 ε'/ε experiment (the so called AKS); this measurement was cross checked with special η *run*, in which η particles was produced by the π^- from a dedicated beam in a special polyethylene target placed in well defined position in the decay region. Decays $\eta \to 2\gamma$ and $\eta \to 3\pi^0$ were used to calculate the calibration factors. The energy resolution has

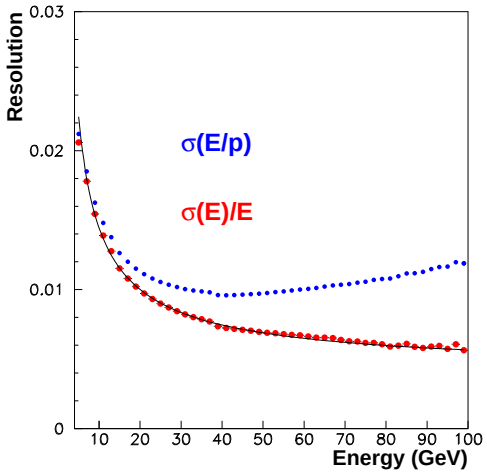

Figure 2.27: Resolution of the LKr as a function of the energy.

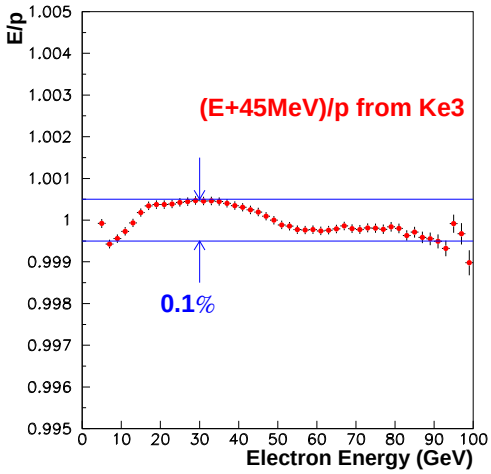

Figure 2.28: Linearity of the LKr measured by using electrons in the Ke3 decay. The linearity is better than 0.1% in the whole energy range.

been measured using dedicated electron run (with momentum spread of 0.1% and adjustable average momentum) and checked with the K_{Le3}. The measured energy resolution is parametrized by:

$$\frac{\sigma_E}{E} = \frac{0.032}{\sqrt{E(GeV)}} \oplus \frac{0.09}{E(GeV)} \oplus 0.0042$$

where the first is the typical term due to the Poisson stochastic fluctuations in the shower development, the second one is mainly due to the electronic noise and the natural LKr radioactivity[5] and the last one depends on the non perfect cells intercalibration (fig. 2.27). The space resolution of the LKr has been measured comparing the electron position in special electron runs, yielding the following result:

$$\sigma_{x,y} = (\frac{4.2}{\sqrt{E(GeV)}} \oplus 0.6)mm. \qquad (2.1)$$

At 20 GeV the resolution is at level of $\sim 1mm$. This good resolution is important, together with the good energy resolution, in the neutral reconstruction of the π^0 decay vertex. The LKr can't measure directly the gammas angle, but it is easy to demonstrate that the $\pi^0 \to \gamma_1\gamma_2$ vertex is at the distance Z from the LKr:

$$Z = \frac{1}{m_{\pi^0}}\sqrt{[(x_1 - x_2)^2 + (y_1 - y_2)^2]E_1E_2}$$

[5]The natural Krypton was made of 5 stable isotopes (Kr^{80},Kr^{82},Kr^{83},Kr^{84} and Kr^{86}) and one slightly radioactive, the Kr^{81} (half life $2.29 \cdot 10^5$ y). However at present the main component of the Krypton radioactivity ($\sim$ 300 Becquerel for $1cm^3$ of Liquid Kr) comes from the Kr^{85} (half life 10.756 y): this isotope was produced by the nuclear bomb tests in the past and nowadays in nuclear reactors.

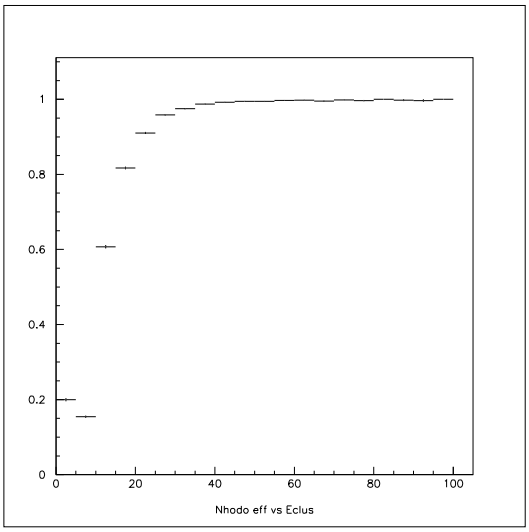

Figure 2.29: The neutral hodoscope is very low efficient at low energy.

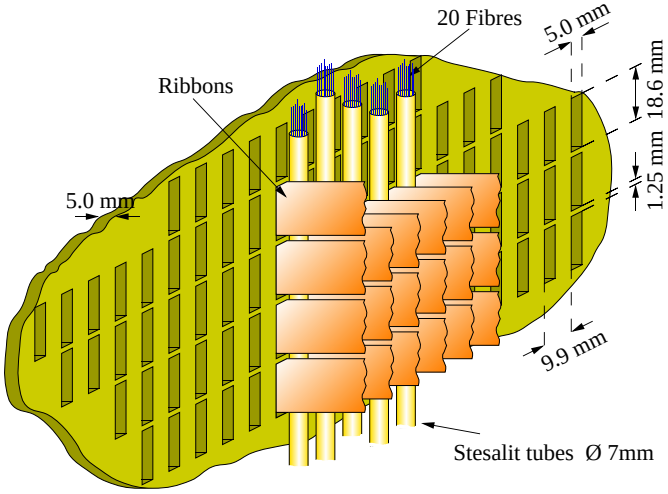

Figure 2.30: The bundles of the neutral hodoscope fibers

where the m_π^0 is the PDG mass of the π^0. In this way the resolution on the vertex position is better than $\sim 1m$ at more than 70 m from the LKr. In particular the resolution on the neutral vertex depends, in first approximation, on the energy and position resolution of the LKr according to the formula:

$$\sigma^2(Z) = \sum_i [(\frac{\partial Z}{\partial E_i}\sigma(E_i)^2 + (\frac{\partial Z}{\partial x_i})\sigma(x_i)^2 + (\frac{\partial Z}{\partial y_i})\sigma(y_i)^2]$$

where from the eq.(2.1):

$$\begin{cases} |\frac{\partial Z}{\partial E_i}| \sim \frac{\Delta Z}{2E_i} \\ |\frac{\partial Z}{\partial x_i}| \sim \frac{Z|\Delta x|}{d^2} \\ |\frac{\partial Z}{\partial y_i}| \sim \frac{Z|\Delta y|}{d^2} \end{cases} \tag{2.2}$$

The corresponding resolution on the angle,$\sigma\Theta/\Theta$, between 2 photons from a π^0 is at level of $1.5 \cdot 10^{-2}$ similar with respect to the spectrometer resolution on the charged pions. Due to the high transverse granularity if the LKr, pair of photons are individually resolved when the distance is larger than $\sim 2cm$. A good time resolution is important in order to reject background coming from accidental activity or pile-up: thanks to the initial current readout technique, the time resolution on the single shower is at level of 500 ps.

2.2.7 The Neutral hodoscope

In the inner part of the electromagnetic calorimeter a neutral hodoscope is placed at the depth[6] of 9.5 X_0. The NHOD is made of 256 vertical bundles of scintillating fibers immersed directly in the liquid krypton (fig. 2.30). The signal is read by 32 photo-multipliers, 8 for each quadrant. The neutral hodoscope provides an independent

[6]in this position a photon of 25 GeV reaches its maximum shower

measurement of the time of the shower and, especially, act as an independent source of minimum bias trigger (the so called TON) to check the efficiency of the neutral trigger systems. The typical time resolution is at level of 250 ps.

2.2.8 The Hadron Calorimeter

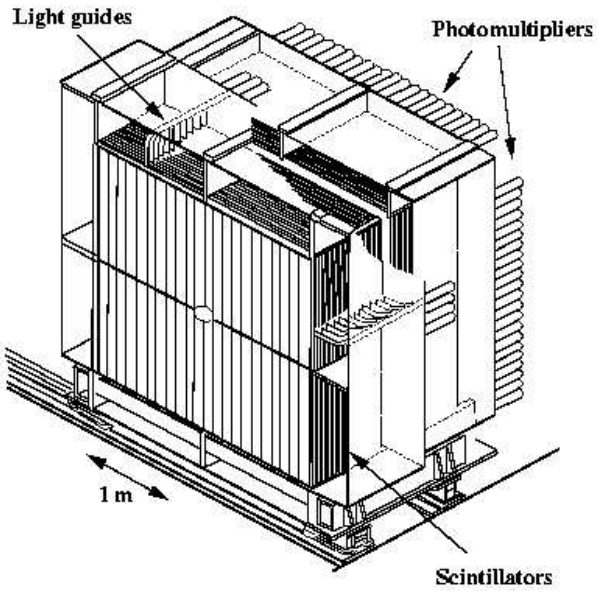

Figure 2.31: Picture of the HAC detector

After the LKr a conventional iron-scintillator sandwich calorimeter (HAC) is employed to measure hadron energies. The HAC is composed by two modules ("front" and "back"), the total thickness is 6.7 λ_{int}. Each module is made of 24 scintillator planes alternated with 2.5 cm thick iron planes, which are divided into 44 half-strips per plane and arranged in vertical and horizontal direction, for an active area of 2.7 x 2.7 m^2 as schematically shown in fig. 2.31. The readout is made using 176 photomultipliers. The light guides are arranged in such way that, in each module, all strips aligned in the same direction at the same transverse coordinate are seen from the same PM . Four shapers followed by CPDs (of the same type used in the LKr) are used to digitize the HAC's output. The energy resolution is

$$\frac{\sigma(E)}{E} = \frac{65\%}{\sqrt{E_{(GeV)}}}$$

The main purpose of the HAC is to contribute, for some neutral trigger (NUT), to determine the total energy of the event. In the NA48/2 run the role of the the HAC both in online and in offline reconstruction is mostly limited to control purpose.

2.2.9 The muon veto

The muon veto (MUV) (fig. 2.32) consists of three 80 cm thick iron walls, $\sim 5\lambda_{int}$, each followed by a plastic scintillator plane. The scintillator is subdivided in strips placed alternatively in vertical and horizontal direction. The first two planes of scintillators are composed of 11 plates each of 1 cm thick, while the last one is composed of 6 plates 6 mm thick. All the scintillator slabs are read from both side by photomultipliers. The time resolution of this system is at level of $\sim 700ps$, after impact point correction (extrapolating the muon position from the DCH). The punch-through probability from the HAC is $\sim 4\%$. The inefficiency was measured using the $K_{L\mu_3}$ decay below $\sim 1\%$. The readout is performed by using a custom built 1 GHz deadtimeless TDC system (riferimento da tesi di timothy) 85) The main purpose of the MUV is to reduce (in veto) the rate of some trigger, but is not employed in the $K \to 3\pi$ decay analysis.

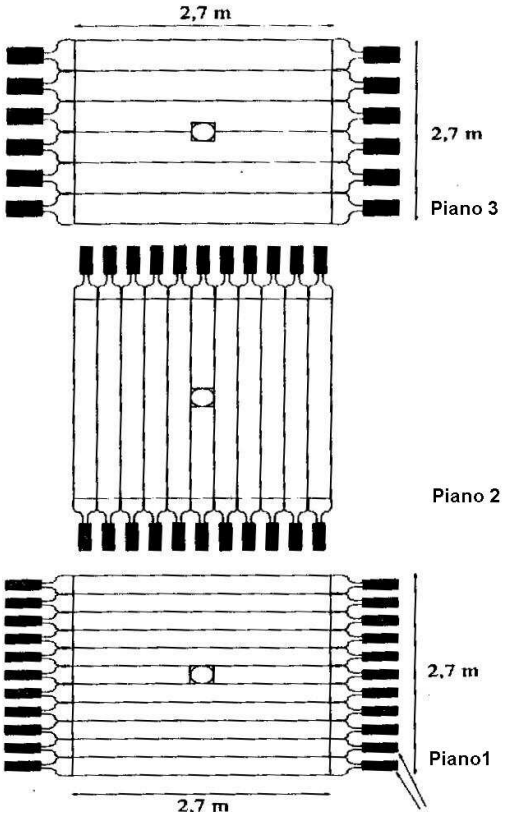

Figure 2.32: Muon veto planes geometry.

2.2.10 The beam position monitor

The beam stability, in terms of momentum and transverse position distribution, is an important issue for the asymmetry measurement in NA48/2. A dedicated detector was designed in order to give a fast online feedback on the beam geometry and position. This beam position monitor is placed at the end of the detector, just

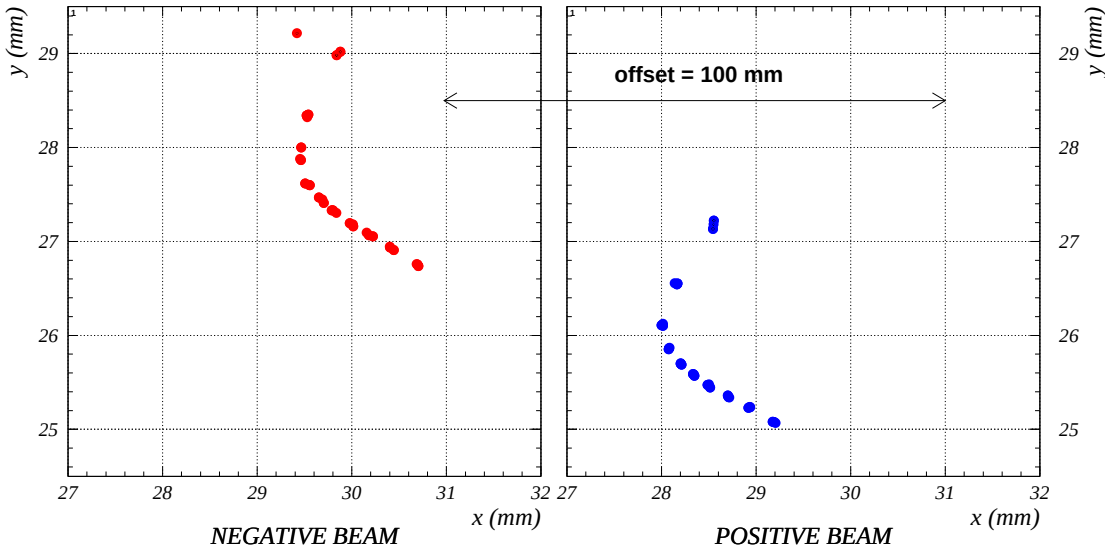

Figure 2.33: Coherent beam movement during the SPS spill

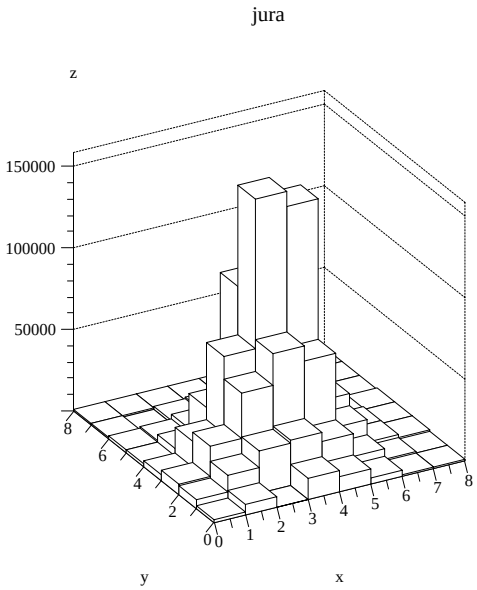

Figure 2.34: The beam in the "jura" side as seen by the Beam Monitor

in front of the beam dump, where the positive and the negative component of the beam are spatially separated by about 6 cm, due to the action of the spectrometer magnet. The monitor is composed of two 8 x 8 matrices of plastic scintillator blocks. Each block is 6 mm X 6 mm in transverse dimension and 9 mm thick. The blocks are separated by thin aluminium foils in order to reduce the optical cross talk. Each

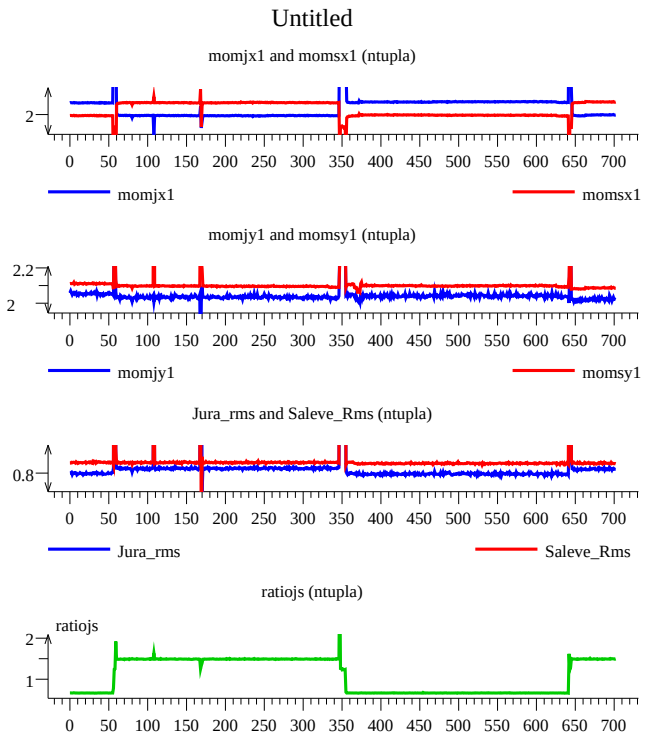

Figure 2.35: a) X first momentum; b) Y first momentum; c) RMS of the beam ; d) Jura-Saleve ratio.

matrix is placed in front of a multi-anode photomultiplier (Hamamatsu H8500) and the whole system is mounted on 4 independent motors, to permit horizontal (singular and common) and vertical movement. The two detectors are placed at a distance of $\sim 10cm$ to intercept the two beams (displaced after the spectrometer magnet). Since the gain of each photomultiplier pixel was not the same, after direct measurement with a source of light, a mask was applied on the scintillators in order to compensate for the gain variation. The residual non-uniformity is at level of 10%. In 2003 the beam monitor read-out electronics was placed directly on the back of the photomultiplier while in the 2004 run all the electronics have been displaced by 70 cm away from the beam, in order to avoid radiation damage[7]. The read-out is composed by amplifiers and discriminators. All the discriminators are read by a custom VME scaler board. The resolution on the center of gravity of the beam is at level of 0.1 mm. Several informations, like position or width of the beam, are checked online thanks to this detector. In fig. 2.35 it is possible to see an example of an online screen shot from the Beam monitor. The scalers read the detector several time during the spill (10 times in 2003 and 92 in 2004). This allows to follow the beams movements during the spill, due to the movement of the primary proton beam on the target (fig. 2.2.10).

[7]in 2003 $\sim$ 10 channels were lost during the run due to the radiation damage

2.3 Trigger

The NA48 trigger is a multilevel system (fig. 2.36), designed to avoid dead time with a rate in the main detectors at level of 1 MhZ. The acquisition system is pipelined and synchronized by a 40 MHz clock. Circular memories 204.8μs deep store the informations from any detector every 25 ns. The trigger system is subdivided in two parts: the charged and the neutral trigger. The first one is responsible for decision on the decay with charged particles and use the HOD and the DCH. The second one, by using LKr and HAC, takes decision on the neutral decays. Actually this scheme was rigorously valid in the NA48 experiment while in NA48/2, due to the fact that there aren't totally neutral decays, both triggers are involved in the events with neutral pions in the final state (for instance $K^{\pm} \to \pi^{\pm}\pi^0\pi^0$). It exists a third subsystem, the Trigger Supervisor, that collects the information from the two subsystems and takes the final trigger decision.

2.3.1 The Charged trigger

In order to reduce the rates from $2 \cdot 10^6$ events/burst registered by the detector to the $\sim 5 \cdot 10^4$ written on disk, the charged trigger is segmented in two stages. Each level of trigger has a reduction factor in the rate from input to output at level of ~ 10. The first level is a hardware system combining fast signals from HOD and DCH, while the second one is based on processors to perform a fast but rough reconstruction of the event using the DCH information.

L1 trigger: hodoscope signals

The purpose of the first level of the charged trigger chain is to reduce the rate at level of 150 kHz. At this level various logical signals are defined. The signal from the charged hodoscope, the chambers and the AKL are combined to define easily topological conditions on interesting decays. For instance using the CHOD the Q1 is defined asking for a signal in corresponding quadrants on both planes. The Q2 signal requires 2 or more time coincidences between signals in corresponding *subquadrant*[8] of both charged hodoscope planes. The AKL is usually in veto (signal !AKL) to limit the rate due to accidental or not fully contained events. All this signals are combined with the information coming from the LKr (the energy) at the L1TS inter level. Before the signal is sent to the second level of the charged trigger a time alignment of the signals from the detectors is performed and a 30 bit time-stamp is attached to the event. A 3 bit code (*strobe*) is defined from topological consideration to address the second level algorithm . In table 2.4 the typical rates (in Hz) for the principal L1 signals are shown.

L2 trigger: Mass Box (MBX)

The second level of the charged trigger, called Massbox (MBX), is a software trigger based on a processor farm. On the basis of the strobe coming from the level one, the decision is taken asynchronously with a maximum latency time of 100μs. By

[8] A subquadrant is defined as a quarter of one single charged hodoscope quadrant

using the DCH data the MBX performs a fast online reconstruction of space points and associates them to tracks segments. The subsequent possibility of applying several quite complicated algorithms (like vertex reconstruction or invariant mass calculation) is essential to obtain the rate reduction in NA48/2. The resolution on the kinematical quantities is worst than in the offline reconstruction, but it is sufficient to assure a high efficiency for all the triggers defined at this level (the inefficiency is at level of few %, and depends on the algorithm). The high rates in the NA48/2 experiment, with respect to the NA48 requirements, have required in 2003 an improvement of the MBX calculation power. In this way the so called *Massbox dead time* (the MBX sent a L1off to the L1TS to disable the request from the L1, if the event rate is too high) could be maintained very low (less than 0.5%). The L1TS requires coincidence between the L1 signals to strobe the particular algorithm

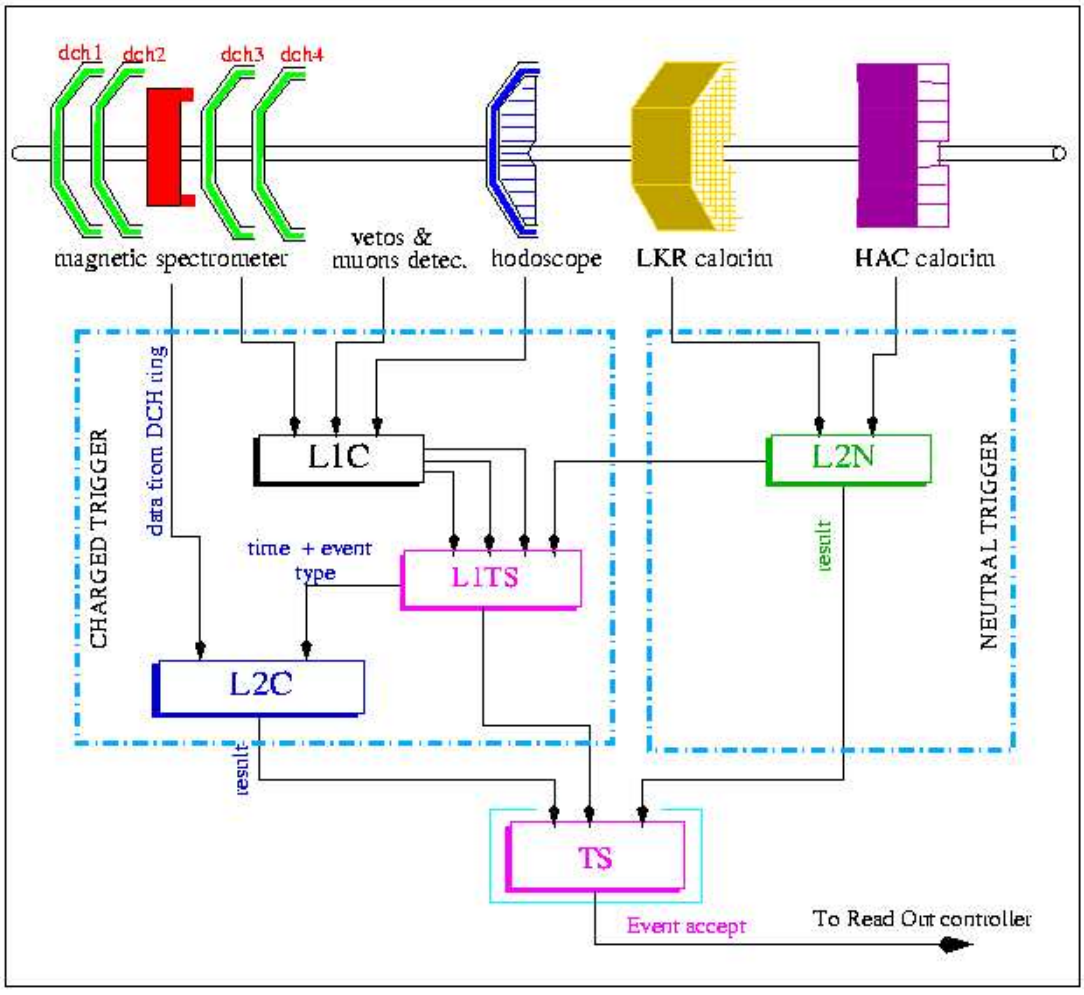

Figure 2.36: Diagram of the whole multilevel trigger system.

Trigger signal	Rate
Q1	$1.8 \cdot 10^6$
Q2	$2,9 \cdot 10^5$
Q2*!AKL	$2,5 \cdot 10^5$
TON	$7.0 \cdot 10^4$
E(LKr) $10GeV$	$2,4 \cdot 10^5$
1μ	$1.6 \cdot 10^6$

Table 2.4: L1 signal rates. The Q1 and Q2 signals are produced by the CHOD, the !AKL signal by the AKL veto counters, the TON by the Neutral Hodoscope, the E(LKr) by the Electromagnetic calorimeter and the 1μ by the Muon veto system

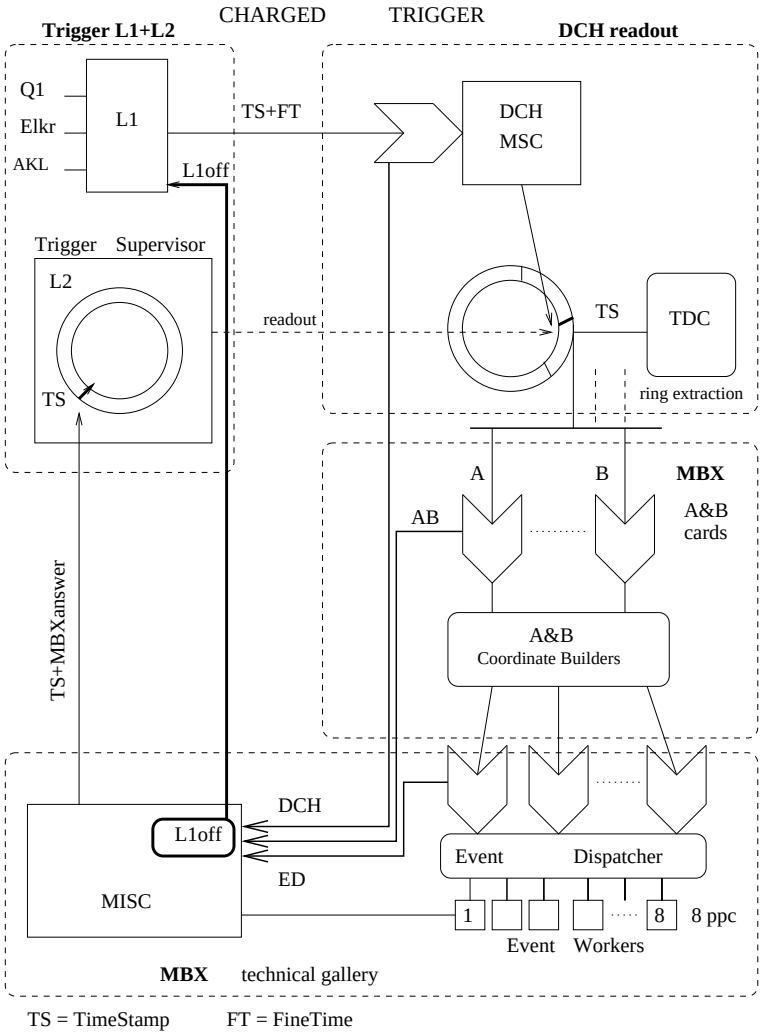

Figure 2.37: The charged trigger system. The L1 and the L2 are schematically shown with the connection with the DCH readout system through the Master Service Card.

used in the MBX (a schematic view of the whole charged trigger system is shown in fig. 2.37). The MBX system is subdivided into 4 subsystems as shown in the fig

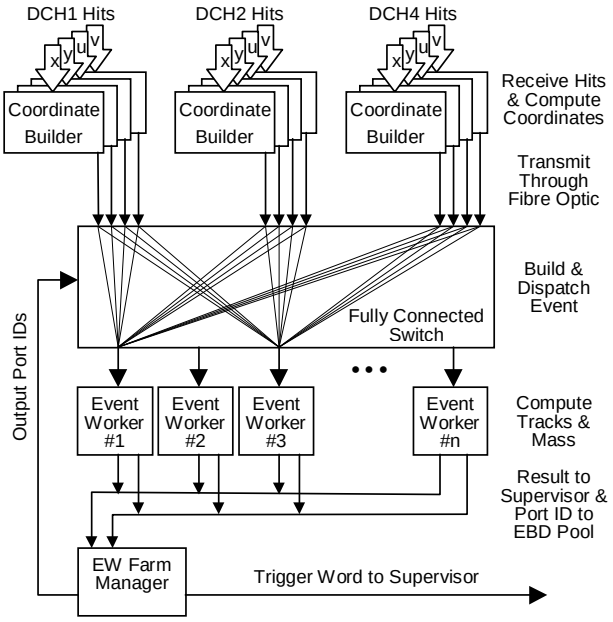

Figure 2.38: The level 2 of the charged trigger system.

2.38. These subsystems are described below:

- **Coordinate Builder (CB)**: Each chamber view has a *AB card* to calculate the hit coordinates by analyzing the time informations coming from the two planes in each view (namely the a and B planes) read from a DCH ring cards. The reference time for the hit association, used by a 40 MHz pipelined algorithm, is given by the Q1 fine-time signal. The geometrical coordinates are calculated by using a 2D Look-up table.

- **Event Builder and Dispatcher (EDB or ED)**: The ED receives the coordinates from the CB via optical link, puts together the information from the 16 views and sends them to one available Event Worker for processing.

- **The Event Worker (EW)**: The event worker uses the 12 coordinates coming from the ED to compute the particle *space points* and other interesting physical quantities used to decide if the event is compatible with a good topology.

- **The Event Worker Farm Manager (EWFM)**: Receives the Timestamps of a candidate event from the EW's and sends them to the TS for the final decision. It also informs the ED about which EWs are free to make a new computation and manages the X_{OFF} system. This is a mechanism which prevents the L1TS from sending any other new L1 strobe, if the ED system is busy. An X_{OFF} could be generated by an overloading of the DCH readouts, CB's or EDB systems. In particular the critical points are managed from FIFO's, that assure a certain level of queuing:

  – from the DCH Ring Card to the DCH Master Service Card (MS)

  – from the MS to the FIFO in front of the CB cards.

– from the AB cards (in the CB system) to the FIFO of the EDB system

The X_{OFF} rate is kept below $\sim 1\%$ by reducing, when necessary, the beam intensity. In the table 2.3.1 the rate of the principal L2 trigger signals, in 2003 run, is shown.

L2 Trigger	Rate
2 Vertex	22 KHz
1 Vertex and mass cut	13 KHz
Anti $\pi^+\pi^0$ cut	14.5 KHz
Anti K_{l2} cut	0.8 KHz

2.3.2 The neutral trigger

The neutral trigger, schematically presented in fig. 2.39 is completely independent from the charged one. It is implemented in a 40 MHz dead-time free pipeline, using the information of the electromagnetic calorimeter. The total latency of the trigger pipeline is 128 clock cycles corresponding to 3.2 μs. Several important kinetical quantities are directly calculated by dedicated hardware. In order to calculate these quantities, the calorimeter single-cell information is reduced to two orthogonal views of projective calorimeter information. The first step is to add the calorimeter cell signals from 16 (2x8) single cells with analogue sum circuits. These *super cells* are defined both in X and Y view. This operation is performed directly in the CPD readout system. The signal of the super-cell is digitized by a 10 bit 40 MHz FADC, and then filtered in order to remove all the super cells below a certain energy threshold. The digital signals are summed up into 64 horizontal and 64 vertical strips in the Vienna Filter Module (VFM) system. Each strip is 2 single cell wide (4

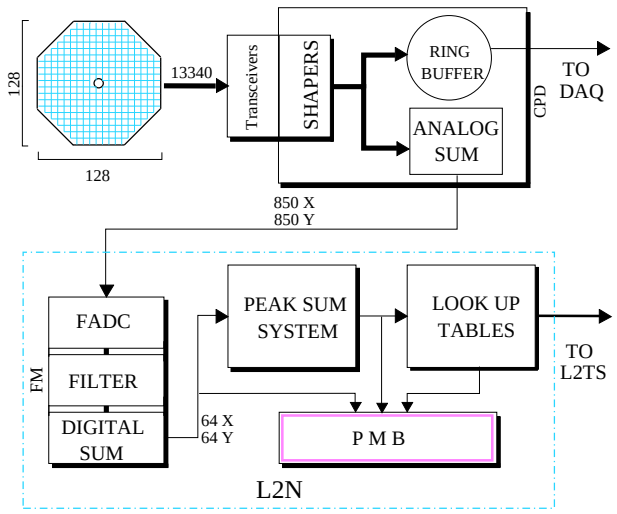

Figure 2.39: Neutral trigger logical scheme. The VFM, the PSS and the LUT system are shown with the monitoring PMB system

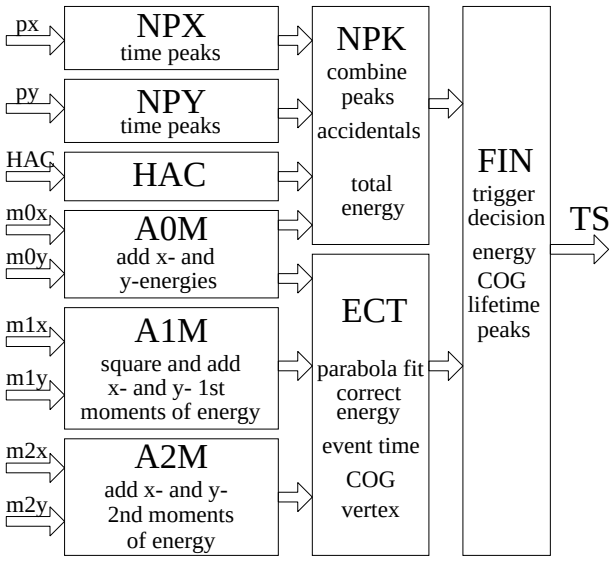

Figure 2.40: Block diagram of the LUT algorithm and connections

cm). The SPY system fans out the signal coming from the VFM into the Pipeline Memory Board (PMB) system and in the Peak Sum System (PSS). The purpose of the PMB is to store neutral trigger information for online monitoring and for offline comparison with the calorimeter readout . In the PSS the total energy deposited in the LKr, the first and the second energy moments and the number of peaks seen in the two views are calculated. The moments are calculated according to the formulae:

$$\begin{cases} m_{0,x} = \sum_{j=1}^{64} E_i^x \quad m_{0,y} = \sum_{j=1}^{64} E_i^y \\ m_{1,x} = \sum_{j=1}^{64} E_i^x (i-32) \quad m_{1,y} = \sum_{j=1}^{64} E_i^y (i-32) \\ m_{2,x} = \sum_{j=1}^{64} E_i^x (i-32)^2 \quad m_{2,y} = \sum_{j=1}^{64} E_i^y (i-32)^2 \end{cases} \tag{2.3}$$

In the Look-Up Table (LUT) the quantities coming from the PSS are merged from both views (fig. 2.40), and the trigger cuts are applied on the physical quantities calculated starting from the momenta:

$$\begin{cases} E = \frac{1}{2}(m_{0,x} + m_{0,y}) \\ r_{cog} = \frac{\sqrt{(m_{1,x})^2 + (m_{1,y})^2}}{E_{LKr}} \\ (d_{vertex})^2 = \frac{E_{LKr}(m_{2,x}+m_{2,y}) - (m_{1,x})^2 - (m_{1,y})^2}{m_{K_0}^2} \end{cases} \tag{2.4}$$

The trigger also uses the number of 'peaks' to generate the *NTPEAK signal* to trigger the L2 for one track events (and for minimum bias trigger too). A peak is defined as a local energy maximum in projective strips according to the conditions:

$$E_{i-1} < E_i \ , \ E_i > E_{i+1}$$

In the fig 2.41 a typical event of $K^{\pm} \to \pi^{\pm}\pi^0\pi^0$ (without the charged pion cluster) is shown with the neutral trigger answer. The peaks are counted in time windows of 3.125 ns to identify accidental hits in the calorimeter. The neutral trigger functionality is summarized in the fig. 2.42. The energy resolution of the neutral trigger system has been measured to be 2.7% over the full energy range.

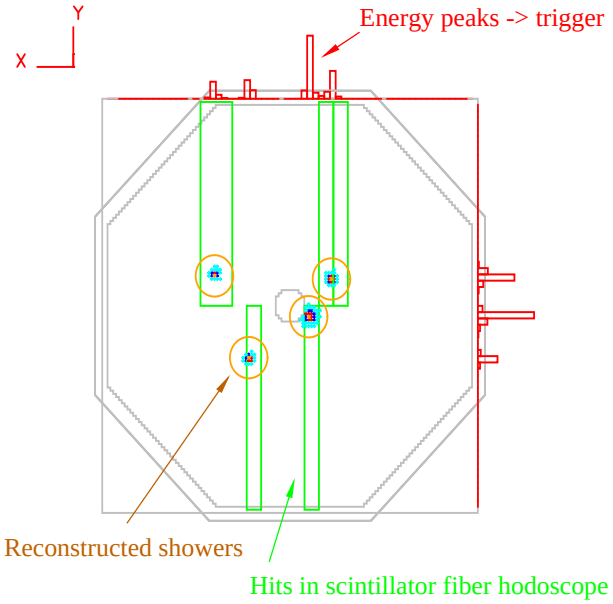

Figure 2.41: Neutral trigger answer for 4 photons event. In the red histograms represent the energy in the neutral trigger views, the green bars the NHOD hits while the circles are the reconstruction clustering

2.3.3 The Trigger Supervisor

The goal of the Trigger Supervisor (TS) [94] is to combine the information from the various trigger sources and take the final trigger decision. The architecture of the TS can be split in 4 parts (fig 2.43): Input, LUT, derandomizer and transmission . The TS provides the final trigger word, including a time-stamp indicating the event real time, whenever a required condition is fulfilled, and it broadcasts it to all the Read Out controllers (ROCs). In the TS the *downscalings* are defined. Several types of control triggers are considers in order to measure the trigger efficiency with differents downscalings according to the total bandwidth of the trigger. The already mentioned Q1, that is one signal to strobe the MBX, is also collected as minimum bias trigger for the charged mode. The neutral hodoscope provides the T0N trigger as minimum bias for the neutral mode (tab. 2.3.3).

Control trigger	Rate	Downscaling
CPRE	3.3 KHz	100
NPRE (TON)	0.6 KHz	200
NT PEAK	1.3 KHz	50
NT NOPEAK	1. KHz	80

2.3.4 The Data Acquisition

The NA48/2 data acquisition system is composed of 11 sub-detector PCs, 8 event builders and a control PC, as pictorially shown in fig. 2.44. A fast 200 Mbit/s switch

provides splitting of data in all the PCs, equipped with Linux operating system. The use of commercial hardware and open source software reduces the maintenance costs and allows an easy upgrade possibility of the system. The data sent by the sub-detectors are stored into the 11 sub-detector PCs and subdivided in 8 blocks. Each block is sent to an event builder from all the sub-detector PCs in such a way that all data from any single event are in the same block. The event builder builds the whole events, that are sent to the CERN computing server via a Giga-switch connection. The PC farm checks the integrity of the information from all the sub detectors: in case of mismatching of the event number from the various sources, the whole data sample of the burst is discarded.

2.3.5 L3 trigger

The final stage of the online processing is the reconstruction of the events performed by the last trigger level. The Level 3 trigger is entirely software based. This stage is not in "cut" mode in the sense that all the events are taken by this trigger. Anyway thanks to this level the data are rapidly available for monitoring purposes during the data taking. The typical time for the processing is $\sim 10min$.

2.3.6 Data processing

The raw data (coming from the PC farm) are stored on 10 disks servers of 1 TB average capacity in the CERN computer center. In normal conditions the amount of data transferred from the experiment to the disks is around $\sim 3TB/day$. The raw data are directly analyzed by the level 3 trigger (L3), that is a software working in the normal batch system at CERN, filtering the data and creating 5 different output

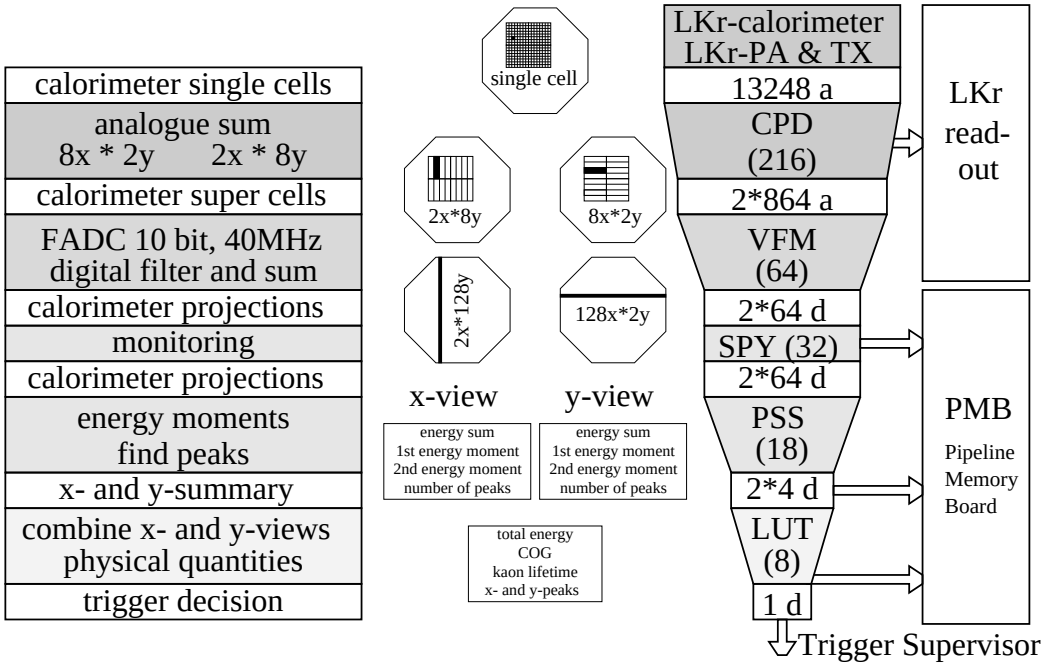

Figure 2.42: Flow of the Neutral trigger decision

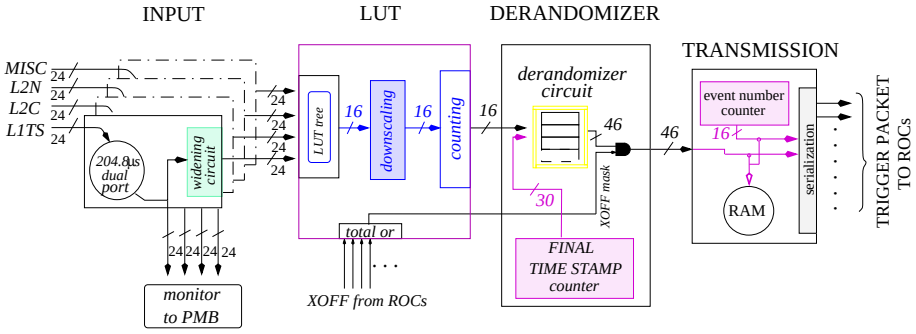

Figure 2.43: Logical scheme of the trigger supervisor system

streams. The L3 program produces the *Compact* format, that contains reconstructed information and physics quantities. Both Compact and raw data are recorded on tapes. The average time from data collection till the end of this process is about 30 minutes: this allows a quite fast feedback to check the data quality. The overall efficiency of the offline processing is slightly greater than 99%. The typical size of one burst is $\sim 500MB$ while a typical Compact file is $\sim 120MB$. In the following table the statistics on the collected data are shown:

Central Data Recording Statistics		
	2003	2004
Total number of triggers	$7 \cdot 10^9$	$11 \cdot 10^9$
Number of Bursts	$2.2 \cdot 10^5$	$3 \cdot 10^5$
Raw Data Total Size	80 TB	120 TB
Compact Data Total Size	20 TB	25 TB
Calibration Data Total Size	3.5 TB	4 TB

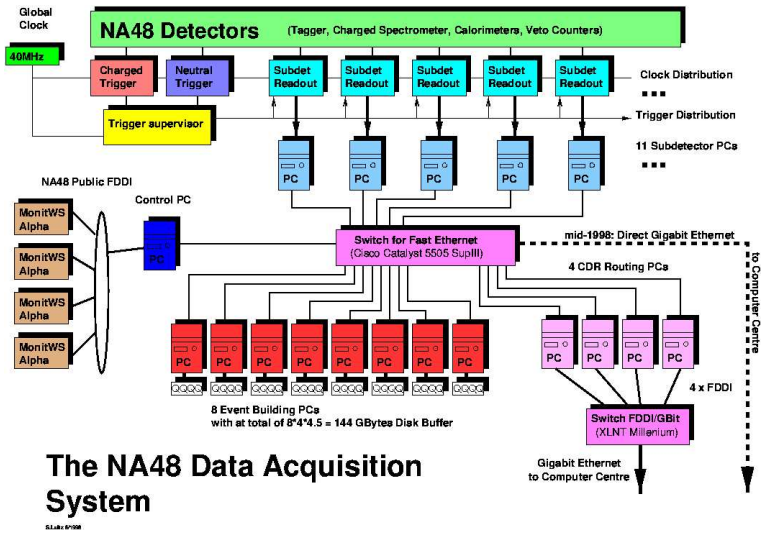

Figure 2.44: Schematic of the DAQ complex

To apply the best recomputed calibration constants the raw data are sometime reprocessed. During the reprocessing the *Super Compact* (SC) are produced to reduce the total amount of data for the analyzers. The SC format is smaller with respect to the Compact format because each event contains less information, but no selection is applied. The total SC production is further subdivided in two *Splits*: the so called *charged* and *neutral*. The events with at least 3 well reconstructed tracks are in the charged split (for the $K^{\pm} \to \pi^{\pm}\pi^{+}\pi^{-}$ asymmetry) while the events with one track and one isolated cluster are in the neutral.

2.3.7 2003 Data Taking

The NA48/2 2003 data taking period was 80 days long. The first week of proton time in nominal conditions was employed to set up the new beam line, the detectors and the triggers. Another week, during the data taking, with the "LHC structure" of the bunches (25 ns of the r.f. structure), not useful for the normal data taking, was exploited for calibration purpose and η runs. Five specials runs with muons were taken to allow the DCH alignment. For the same reason two special runs were taken with a low intensity hadron beam deflected directly on different spots of the chambers. The efficiency of the data taking was quite low (around $\sim$ 50%) for problems mostly indipendent from the NA48/2 apparatus and mainly due to SPS problems with cooling, vacuum, power cuts and so on. To implement the asymmetry measurement strategy the polarity of the magnetic fields (both in the spectrometer and in the beam line) have been frequently swapped (daily for the spectrometer magnetic field and on weekly basis the achromat fields).

2.3.8 2004 Data Taking

The NA48/2 experiment took data for about 90 days in 2004. During the second part of the 2004 data taking in order to increase the bandwidth available for other decays, the calorimeter readout was modified to discard information during the $K^{\pm} \to \pi^{\pm}\pi^{+}\pi^{-}$ events. On the basis of the experience from the 2003 data taking, the magnetic fields were swapped with a shorter period with respect to the previous year, for reason that will be discussed later. Due to the observed shifts in the drift chamber alignment during the 2003 run, in the 2004 data taking the muon runs have been more frequently collected, allowing a stability in the DCH relative positions at level of $20\mu m$. The last week of data taking was devoted to special runs and test runs for a possible NA48 future development. In particular a special run with a different trigger configuration, was collected data for semileptonic and leptonic kaon decays studies. Several tests have been performed to study the detector capabilities (in particular the LKr performances) for a possible experiment[9] aimed at collecting $\sim$ 100 events of the rare decay $K^{+} \to \pi^{+}\nu\nu$.

[9]In this moment the proposal P326 has been submitted to the CERN SPSC [95] (and is under discussion for approval) with a setup that would use only some parts (essentially the LKr and the beam line) of the old NA48/2 setup.

Chapter 3

Reconstruction and Selection of $K^{\pm} \to \pi^{\pm}\pi^0\pi^0$

An essential part of the analysis is the events selection. The events are collected according to the online multilevel trigger decision. Raw data, from which the interesting kinematic quantities are reconstructed, are reduced to a DST format called *Compact*. Further steps are implemented to simplify the analysis procedure reducing the amount of data available. In particular a micro-DST format, called *Super Compact*, is used to apply selection and cuts in order to identify the signal and to reduce the background contribution.

3.1 The data formats: Compact, Super Compact, Hyper Compact

The raw data format is not suitable for analysis purpose due to the large quantity of informations stored. The *Compact* format is obtained from the raw data directly in the L3 trigger level, to allow a fast feedback (with the so called "Compact Monitor", a program that during the normal data taking gives information about the interesting reconstructed physics quantities) and a first analysis to evaluate the detector performance. After this the detectors calibration constants (reference times, pedestals, etc.) are computed and a second version of Compact data is produced starting from raw data. Even the Compact data are too bulky to handle for analysis purpose. The *Super Compact* (SC) format is obtained starting from the Compact one without any selection, but reducing the informations available. For instance informations about the Charged Hodoscope (CHOD) are eliminated, because the correction on charged particle tracks is applied at Compact Level. In producing the SC format several routines are called, mainly regarding the LKr calorimeter, in order to correct at best for all known effects. To allow the analyzers to handle several billions of events, another format has been introduced: the *Hyper Compact* (HC), in which a tuned preselection of events is applied, with loose cuts. In the HC only the potentially interesting events are presented and the informations available are limited to the fundamental ones for the asymmetry analysis. Two different

versions of HC has been produced: the *Charged HC* and the *Neutral HC*, for the $K^{\pm} \to \pi^{\pm}\pi^+\pi^-$ and for the $K^{\pm} \to \pi^{\pm}\pi^0\pi^0$, respectively. While the use of the HC charged version is unavoidable due to the very high statistics in the three charged pions mode, for the neutral version this is not completely true and the SC format has been preferred[1]. The SC is the reference format for all the other analyses.

3.1.1 One track and neutral Split

To reduce the quantities of the data for the neutral mode analysis two splits have been produced from SC data[96]. The first one is the *one track split*, that is also useful for almost all the "one track" analysis. The conditions defining this split are:

- at least one track
- at least two gammas

where gammas are defined as LKr clusters without any charged track associated in a radius of 15 cm. Data for any interesting decay channel with one charged track in the final state can be found in this split. Only the K_{e2} ($K \to e\nu$) and the $K_{\mu 2}$ ($K \to \mu\nu$) channels (and the correspondent radiative decay processes with an additional gamma in the final state), for which a special dedicated split has been produced, are not included in this split. Since the "charged" split is defined for all the decays with three tracks (disregarding which kind of charged particle) there is a certain overlapping between the two splits[2]. Anyway it is important to remark that, for the neutral asymmetry analysis purpose, the split definition cannot introduce any loss in statistics. In order to reduce the amount of interesting events for the neutral asymmetry analysis another level of split has been defined. This split, derived starting from the one track split, is called *neutral split* and is defined to select $K^{\pm} \to \pi^{\pm}\pi^0\pi^0$ candidates with the following loose cuts:

- at least 4 good clusters. A good cluster is defined by
  - Cluster Energy > 5 GeV
  - Distance to closest dead cell > 2 cm
  - Distance to closest track impinging on the LKr > 10 cm
  - Distance to closest cluster > 10cm
- at least 1 good (well reconstructed) track

These requests are so loose that also in this split there is not significant loss of good events. The total amount of data for the one track split is ~ 2.8 TB and ~ 120 GB for the neutral split, starting from a total ~ 7.4 TB of SC data.

[1]The advantage in using SC rather then HC data is to avoid possible biases in the analysis due to the order of the cuts in the event selection.

[2]Both for decays matching the two split definitions (for instance the $K \to \pi\pi^0\pi^0_{Dalitz}$) and for the accidental activity.

3.2 Online selection

As discussed in the par. 2.3 the trigger is essentially subdivided in two levels. In the case of $K^{\pm} \to \pi^{\pm}\pi^0\pi^0$ both the neutral and the charged L1 part are involved. The L2 is based on the possibility to reconstruct the missing mass of the decay with the informations coming from the DCH, assuming the direction and the energy of the kaon to coincide with the nominal beam and the average energy

3.2.1 L1: pretrigger

The pretrigger for $K^{\pm} \to \pi^{\pm}\pi^0\pi^0$ is obtained asking for the Q1 condition in the hodoscope logic and for a condition on the number of peaks in the Neutral trigger. To define the Q1 condition both the horizontal and vertical hodoscope planes are divided in 8 parts. The AND of this subdivision defines 16 "logical" subquadrants: the Q1 is set if at least one subquadrant fires (fig. 3.1). As discussed in the following, the Q1 condition is very efficient for the signal events. The possibility to include also the $\overline{AKL}$ (in veto) condition has been investigated, but the rate reduction was quite small to justify this requirement. The NT-PEAK condition, in logical AND with the Q1, is fulfilled if there are at least 3 peaks in at least one projection of the neutral trigger. The NT-PEAK is not fully efficient (the efficiency is at level of $\sim 97 - 98\%$) both for electronics problems and for topological effects. The rate of this pretrigger is at level of $\sim 67 Kevents/burst$ with a purity around 15%. The rest of the events come mainly from $\pi^+\pi^0$ and K_{e3}.

3.2.2 MBX 1-track trigger

The L1 rate being too high for the data acquisition, a L2 trigger is important to decrease the rate and to increase the relative purity of the collected sample. A dedicated algorithm (also know as "1TRK-P") has been developed at the MBX level to reduce the total amount of the 2 body decays (the $\pi^+\pi^0$) which represents the main trigger background. By assuming the flight direction of $K^{\pm}$ along the beam axis, its nominal energy (60 GeV) and the measured four momentum for the charged track, the charged particle missing mass, if the track is compatible with a decay coming from the kaon beam, is related to the so called M_{FAKE}, defined as:

$$M^2_{FAKE} = M^2_K + M^2_\pi - S = P_K P_\pi \Theta^2 + M^2_K \frac{P_\pi}{P_K} + M^2_\pi \frac{P_K}{P_\pi} \qquad \text{where} \qquad S = (P_K - P_\pi)^2$$

The expression above can be written as:

$$M^2_{FAKE} = \frac{1}{\Delta x_F \cdot \Delta x_T}[P^2_{kick}(z_{DCH4} - z_{MAG})^2\Theta^2 + m^2_\pi|\Delta x_T|^2 + m^2_K|\Delta x_F|^2] \quad (3.1)$$

where Θ is the opening angle, $z_{DCH4} - z_{MAG}$ the longitudinal distance between the magnet and the DCH4, Δx_T the displacement of the track on DCH4 due to the magnet and

$$\Delta x_F = \frac{P_{kick}}{60 GeV/c}(z_{DCH4} - z_{MAG})$$

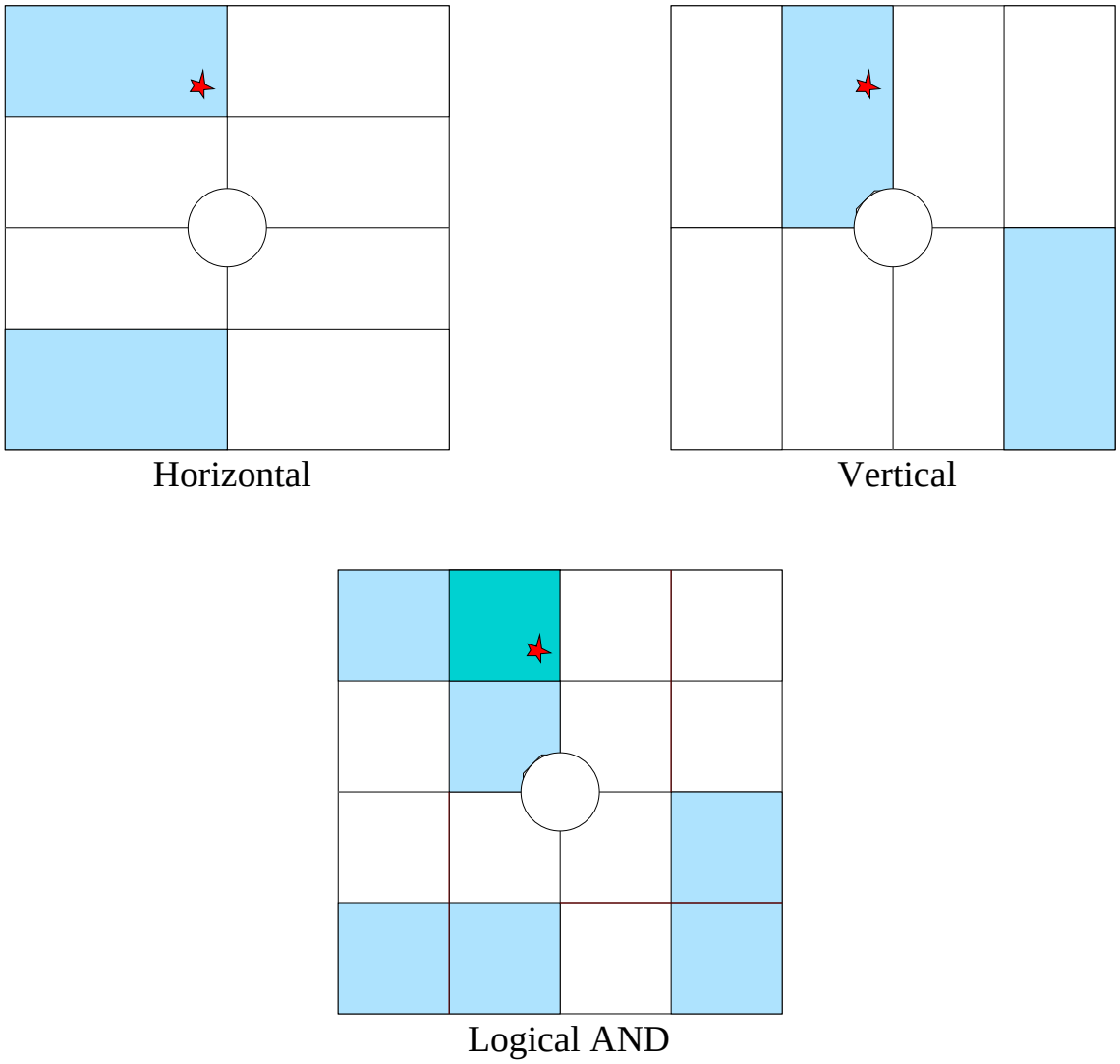

Figure 3.1: Each hodoscope plane is subdivided in eight parts. The logical AND defines 16 subquadrants. The Q1 is define if at least one of the subquadrant fires. In this example only a Q1 can be defined (given by the hit in the red point position) because for the other subquadrants with a signal (light blue) there is not correspondence in the other plane.

that is a constant. If M_{FAKE} is less than $475 MeV/c^2$ the 1TRK-P trigger is set. The rate after the MBX is at level of 14.5Kevent/burst . The efficiency of the 1TRK-P is at level of $\sim 96\%$ and will be discussed in more details in chap. 8 .

The trigger chain discussed here is the main component (99.9%) of the signal online collection. A very small fraction of events arrives to the L2 strobed by a Q2 signal (a signal generated by a coincidence in at least two of the CHOD subquadrants). The two signals that trigger the 1TRK-P algorithm are:

- L1code0: $(Q1 + Q2) * [NTPEAK + (Q1/10 * LKr(minbias)) + (Q1 * !Q2 * 1mu * !AKL/D4) * (KMU3\_PRE)]$
- L1code2: $(Q1 + Q2) * [Q2 * !AKL + Q1/100 + KLrandom]$

. Usually the $K^{\pm} \to \pi^{\pm}\pi^0\pi^0$ are triggered at L1 by Q1*NTPEAK, in the par. 6.2.1 we will see one condition in which the Q2 component of the L1code2 becomes relevant.

3.2.3 Control trigger for neutral events

To monitor the efficiency of the trigger chain for the signal events *minimum bias* triggers are collected. This kind of triggers require unbiased conditions with respect to the trigger whose efficiency they should measure. For this reason the rejection power for the minimum bias trigger is quite small (the purity with respect to the signal is quite low) and the rate is quite high. To avoid to saturate the trigger band these triggers are *downscaled*. In the table 3.1 the control triggers are summarized, together with the downscaling factor. The T0n is based on the neutral hodoscope signal (see par. 2.2.7). The NT-PEAK mentioned here is directly from the Neutral Trigger L1 without any condition on the MBX. The Q1/10 means that the Q1 signal is prescaled by a factor ten (to reduce the rate) and then there is a coincidence with the NT-MB, that is the condition $E_{LKr} > 10 GeV$ in the neutral trigger.

Control trigger	Purpose	Downscaling	Rate (Kevt/burst)
T0N	Q1 efficiency	100	1
NT-PEAK	Q1 and MBX efficiency	50	1
Q1/10*NT-MB	NT-PEAK efficiency	100	0.3

Table 3.1: Control triggers used to measure the trigger chain components.

3.3 Event reconstruction

The detectors involved in the reconstruction of the $K^{\pm} \to \pi^{\pm}\pi^0\pi^0$ decay are mainly the DCH and the LKr. Thanks to the fact that there is not any physical important background from other channels, the selection is quite easy and the only relevant sources of ambiguities are the combinatorial background and the presence of accidental activity.

For each detector a reconstruction program has been developed in order to obtain useful informations from the raw data at Compact level. The algorithm of this procedure will be briefly presented.

3.3.1 DCH reconstruction program

The charged tracks are fully reconstructed by using the DCHs. The raw informations from the DCH are the **Hits**, defined as a wire hit in any plane. Here will be described only an outline of the charged reconstruction:

- The **Hits** are grouped into **clusters**. A cluster in a DCH is defined if there is one hit in both planes of all the views (X,Y,U and V). Only space coincidence is required (by using the wire's number) while, at this stage, the time is not taken in to account. If a particle passes very close to a wire in one plane, then both the adjacent wires in the staggered plane are used (this case is defined as triplet, most of the clusters are doublets).

- The **Front segments** are built using clusters from the same view in DCH1 e DCH2. A front segment is, essentially, a projection of the track in one of the 4 possible views. Some of the front segments can be discarded if they do not correspond to a physical particle coming from the decay region.

- **Front tracks** are built by using the defined front segments. If there are less than four front segments the front track could be eventually defined by 3 or 2 segments adding, possibly, an additional cluster in DCH1 or 2. Moreover the extrapolated defined front track has to cross a virtual cylinder of 10 cm in diameter around the nominal beam axis, to exclude consideration of particles with trajectories external to the volume in which kaon decays can occur (fig. 3.2).

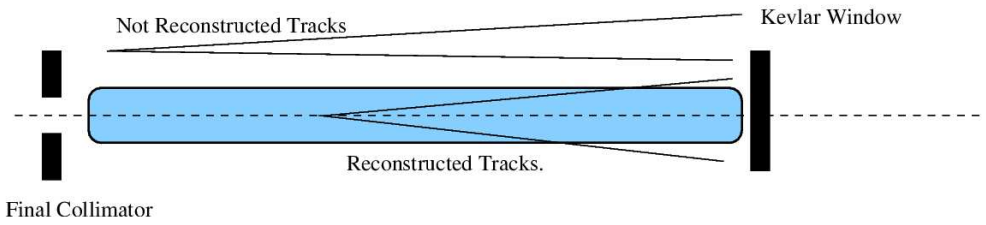

Figure 3.2: Example of tracks crossing and not crossing the virtual cylinder to identify, at the reconstruction level, if the decay comes from the fiducial region

- **Space points** are defined in DCH1 and DCH2 by using the front track direction and in the DCH4 using the clusters.

- **Full tracks** can now be built (still without using the timing information). The front tracks are matched with the space points in DCH4. Due to the small contribution along the Y direction of the spectrometer magnetic field (and the

small contribution of the earth magnetic field at this stage), the space point in the DCH4 is required to be along the front track extrapolation in the Y coordinate.

- To define **minitracks**, the timing information are included. The drift times are calculated using the known offset and applying a correction due to the signal propagation along the wire. All the hit drift times are used to define a track time and to define a quality variable. This variable measures which fraction of the hits is near in time to the average time of the total sample. A good value for this variable is close to unity.

- At this stage the **minispacepoints** are defined including the timing information. If the time of these points is inconsistent the track is rejected.

- For each minitrack a point can be defined in the DCH3 both in the x,y and in the u,v views. The clusters in the DCH3 can be added to the minitrack if they are geometrically and timely consistent with the interpolated point. This could also solve some ambiguities due to the sharing of space points between two minitracks in the DCH4 (also know as "ghost track" problem).

- The physical parameters of the track are calculated at this stage. Small corrections are applied to the position and time of the clusters, due to known effects and internal alignment of the spectrometer, then the momentum, charge, time, positions and slopes before and after the magnet can be calculated with their errors. At this stage the fully measured magnetic field map is employed, including also the so-called "blue tube" (see par. 2.2.2) field.

- With all the track parameters, the vertex and some physical quantities can be directly computed for some class of events (for instance the vertex and the invariant mass for the three tracks events).

The reconstruction of charged tracks is also important for other detector reconstructions. The CHOD needs the impact point position obtained from the extrapolation from the DCH4, to perform a slewing and impact point correction (due to the time of propagation of the light in the scintillator) to improve the resolution of the hit time. Due to the good time resolution achieved in the CHOD hit, the time measurement is taken as the time of the track. Also the MUV needs this information for similar purpose: if an extrapolated track is near to one cluster in both planes 1 and 2 a muon is flagged with a good time resolution.

3.3.2 LKr reconstruction program

The aim of the LKr reconstruction is to find energy, time, position and size of the clusters generated by any particle hitting on the Calorimeter. The procedure to define these quantities will be briefly discussed in the following steps:

- The first step is to look for *cluster* candidates. The pedestal of each cell is calculated averaging the first three samples and then is subtracted to obtain the cell energy. A *seed* is defined if the cell energy is greater than 0.20 GeV

in the sample with maximum energy and greater than 0.25 GeV in the whole pulse. If in a cell there is more than one (usually two) sample with energy over the threshold (two local maxima), the cell defines more seeds candidates.

- The seeds are ordered according to the energy and a loop is made to find the clusters. A cluster is defined when a cell has more energy than the 8 surrounding cells and its energy satisfies:

$$E_{seed}/GeV > 0.18 + 1.8E_{av}/GeV$$

where E_{av} is the average energy of the 8 surrounding cells. If this condition is fulfilled, the cluster position is estimated by calculating the energy barycentre of this 3x3 box.

- For each cell in the LKr a list of cluster within 11 cm from the cell is made. If there is only one cluster for which the cell time is within 20 ns, the energy of the cell is added to that cluster. If there is more than one, the energy of the cell is shared among the cluster according to the formula

$$E_i = E_{cell}\frac{W_i}{\sum W_i}$$

where the weight W_i, representing the expected fraction of energy in the cell due to the i-th cluster, is estimated using the cluster energy, the time and the distance with a shower profile simulation.

- By adding these contributions from other cells, the energy of the cluster is re-estimated. The barycentre is also recomputed, after few corrections, from known effects:
  - Residual spatial modulation due to the charge collection effect[3].
  - Energy loss for clusters too near to the inner (beam pipe) or outer calorimeter's edge.
  - Overall energy scale.

- Specific algorithms are applied if there are two clusters within 11 cm of each other. If there is a cluster with very low energy ($< 1.5GeV$) near ($< 10cm$) to an high energy cluster, the low energy cluster is assumed to come from the same photon and the two clusters are joined. If there is a dead cell (see 2.2.6) in a 5x5 box around a seed, a special procedure is applied to compute the energy and cluster position.

3.3.3 Standard selection of $K^{\pm} \to \pi^{\pm}\pi^0\pi^0$ events

In order to identify the good events for the "neutral" analysis, different approaches can be used. The requirement of a minimal experimental signature in the decay is mandatory in every approach used: at least 1 track in the spectrometer and at least

[3]This effect is very small thanks to the use of a high voltage.

4 clusters in the LKr. From all the tracks and all the possible clusters collected by the detector, a list of "good" clusters and "good" tracks are built applying some quality cuts as define in par. 3.3.6. The minimal numbers of "good" candidates in the lists are, obviously, again 1 track and 4 clusters. For each photons pair [ij] the distance d_{ij} of the decay vertex from the LKr reference plane, is reconstructed by imposing the nominal π^0 mass [4]:

$$d_{ij} = \frac{1}{m_{\pi^0}} \sqrt{E_i E_j [(x_i - x_j)^2 + (y_i - y_j)^2]}$$

This formula only derives from kinematical consideration and shows that it is possible to compute the decay position by using only the transverse position and the energy of the clusters in the LKr. The error on the Z position of the vertex is due essentially to the uncertainty on the energy values[4]. The error on the measurement is:

$$\frac{\delta d_{ij}}{d_{ij}} = \frac{1}{2} \sqrt{\left(\frac{\delta E_i}{E_i}\right)^2 + \left(\frac{\delta E_i}{E_i}\right)^2}$$

Numerically this means e.g. that for π^0 decay 100 m far from the LKr the error on the recostructed longitudinal vertex position is ~ 1 m (for γ energies in the range allowed in 3 π decay).

The pairing of a 4-uplet of photons to two pairs, each corresponding to a π^0 decay candidate, is chosen by minimizing the difference between the two "neutral" vertexes defined from the two pairs. The kaon decay vertex position is defined simply from the arithmetical average between the two vertexes; it can be shown that in this way the best resolution on the invariant $\pi^0\pi^0$ mass[5] is achieved, at least for $\pi^0\pi^0$ invariant mass close to $2m_{\pi^0}$. Looping on all the possible charged tracks, assuming the 4 photons already selected, the Kaon mass can be computed for each charged pion candidate. The charged track is chosen by minimizing the absolute value of the difference between the reconstructed kaon mass and the nominal kaon mass [4]. This selection, as mentioned, is called *Selection A* and it is the standard selection used in the following analysis. Several cuts are applied to the selected events in order to reduce the background contribution (see later).

3.3.4 Other selections

Other algorithms can be applied to the data in order to select the signal. For example the definition of the variable to be minimized searching for gamma pairs or to improve the charged track selection could be changed by using some "χ^2-like" variable to take into account the error in the energy or position measurement. Another possible approach is the direct selection of the best 5-uplet of photons and track minimizing the absolute difference between the reconstructed kaon mass and the nominal value (this is the so called *Selection B*) without any preselection on the photon pairs (as in selection A). By considering all the 5-uplets it is possible to find the vertex position by imposing the Kaon mass and then base the selection on the

[4]the error on the X and Y position is less important in first approximation.

[5]or equally the U variable, as will be shown later

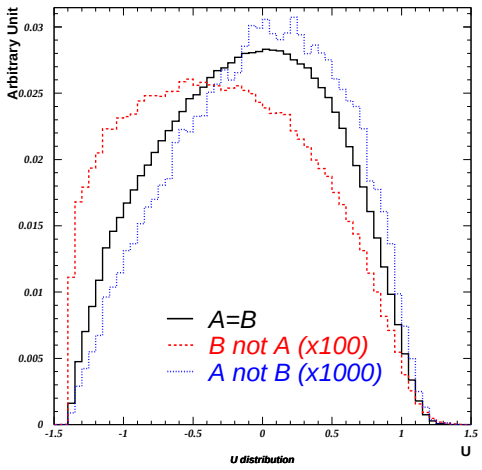

Figure 3.3: The U distribution is not the same for events selected only by one of the selection A and B. In this plot a qualitative comparison between the U distributions is shown (notice the different normalization for the three plots). The exclusive B category is at level of $\sim 1\%$ with respect to the A=B, while the exclusive A is at level of $\sim 0.1\%$.

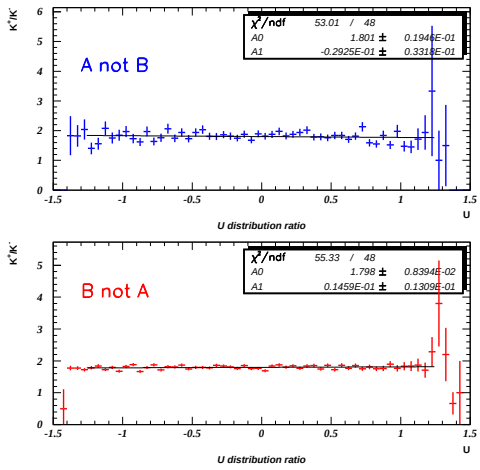

Figure 3.4: Due to the fact that no relevant slope is present in the K^+/K^- ratio, no big effect is expected in the asymmetry measurement.

minimization of the absolute difference of the reconstructed π^0 masses with respect to the nominal mass, instead of the Kaon mass (*selection C*). Anyway differences among all the possible selections are only due to accidental activity or resolution effects. This means that the same regions of the phase space can be differently populated according to the selection chosen. For instance in plot 3.3 it is possible to see the effect of the different selection choice in the U distribution, for events selected by one selection and not by the other one, with respect to the events selected by both selections. The U distribution for this kind of events is quite different; in spite of that, this difference is not important for the asymmetry measurement because, as we will see better later, the fact that the ratio between the U distributions for Kaons of opposite charge is flat (the selection does not depend on the charge of the Kaon, see fig. 3.4) for both categories it is enough to say that this cannot introduce an important bias in the asymmetry measurement. In the table 3.2 it is possible to see the effect of the different selections on the statistics and the percentage of wrong gamma pairings, obtained from the MC. Due to the fact that the percentage of gamma pairing is statistically compatible (and small) in every selection, the selection A is preferred as standard to be conservative with respect to the accidental contribution and because the selection A guarantees the best resolution in the interesting kinematical variables.

Selection	Statistics	Wrong Pairing
A	-	$(0.17 \pm 0.01)\%$
B	+1.4%	$(0.15 \pm 0.01)\%$
C	+7.2%	$(0.18 \pm 0.01)\%$

Table 3.2: The statistics variation is referred to the selection A. In the wrong pairing the 0.07% is common in all the selections.

3.3.5 Selection using KABES

By using the informations from the KABES detector (par. 2.2.1) it is possible to define an alternative selection by using the reconstructed Kaon momentum (*Selection D*). The main advantage being that the resolution in the kinematical quantities is improved. In this case (similar to the selection B) the decay vertex is obtained from the intersection of the pion track with the real kaon direction. The 5-uplet of gammas and charged pion is selected looking for the reconstructed kaon mass. The interesting point of this selection is the possibility to define the U variable in an alternative and independent way (**U2**) with respect to the standard way (**U1**)[6]. This gives us the unique chance to measure the asymmetry parameter in two ways that check each other. The main problem in the KABES use is that the efficiency reconstruction it is not very high, mainly due to the high beam rate. The typical loss in statistics due to the KABES is $\sim 15\%$ with respect to the standard selection, and in addition in the first part of the 2003 data taking the KABES detector was not fully working. The KABES detector could be also useful to gain statistics from the decays in which the charged pion track is lost due to acceptance. The knowledge of the Kaon momentum and direction allows to reconstruct the kinematics of the decay. This could turn into gain of $\sim 10\%$ in statistics[7]. Due to the difference in acceptance the Dalitz plot distribution for this kind of events is completely different with respect to the standard Dalitz Plot distribution; this can be seen by comparing the plot in fig. 3.6, in which U is plotted for this kind of events, with respect to the standard Dalitz Plot in the fig. 3.15. The loss of the charged track is mainly due to the presence of the central hole in the spectrometer (fig. 3.5); the events in which the charged pion runs close to the beam line (at rest in the center of mass frame) are located in the right part of the Dalitz Plot as will be commented later. It must be remarked that, in the 2003 data taking, the trigger was not fully efficient to collect events without charged tracks.

3.3.6 Standard Cuts

As mentioned above, several cuts are applied in order to reduce the background contribution and to check the quality of the measured quantities. The cuts are tuned by using the Monte Carlo. Those described here are referred to the Standard Selection, but similar cuts (in different order) are also applied in other selections. The track candidates are selected according to the cuts in the table 3.3. The track

[6]The difference between the two definition will be discussed in par. 5.1.

[7]This number depends on selection and cuts, because the acceptance is not well defined.

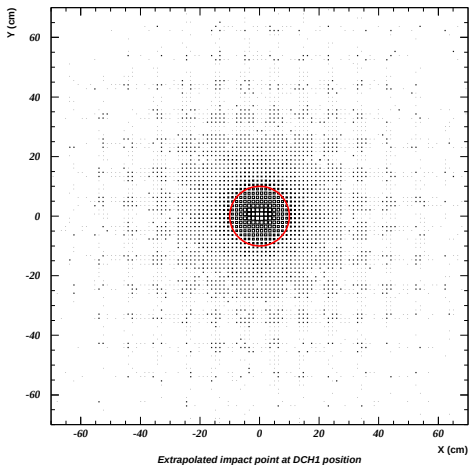

Figure 3.5: Reconstructed impact position of the lost charged pion track in the DCH1 position. In the great majority of these events ($> 82\%$) the charged pion is not seen by the spectrometer because it remains inside the beam pipe (Radius $< 10cm$).

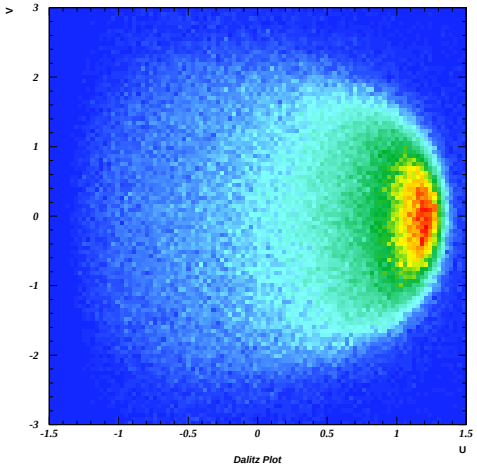

Figure 3.6: U distribution for events with lost charged pion.

quality is a quantity directly computed by the DCH reconstruction program using the number of hits used for the track reconstruction in each chamber. The ghost track rejection is a procedure to exclude the fake tracks generated by ambiguities coming from hits with similar Y coordinate in the DCH4, as already mentioned in par. 3.3.1. The procedure is applied to the track pairs with a distance smaller than 0.5 cm at the DCH1 level; if the track quality of the two tracks is the same (else the track with smaller quality is defined as "ghost") then the undeflected Y position on DCH4, obtained by linear extrapolation from the chambers 1 and 2, is compared to the real Y position; this distance is then used to decide which one of the two tracks must be defined as "ghost".

At least one track has to pass these cuts. The gamma candidates are selected according to the cuts in the table 3.4. In particular the Cluster Status is defined as follows:

- 0 if all the cells of the cluster have 3 well measured samples to fully reconstruct the pulse;
- 1 if at least one cell has a gain switching problem, but there is no saturation;
- 2 if at least one cell has a sample saturated, but there is not switching pathology;
- 3 Gain switching pathology + saturation, but all the cells of the cluster can still be correctly reconstructed;

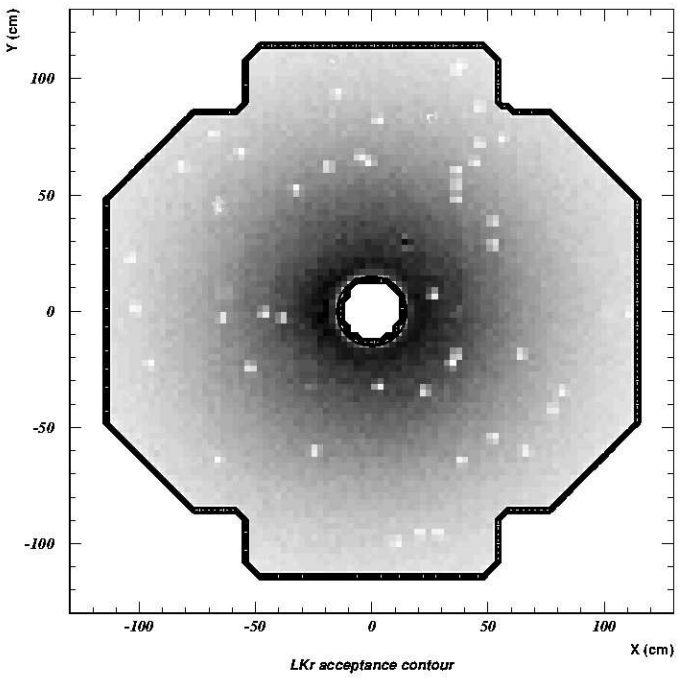

Figure 3.7: LKr geometrical acceptance. The particular shape of the contours is due to the readout and to avoid edge effect in the outer. A cut of 15 cm is applied around the center for the same reason.

Cut name	Condition
Track Quality	> 0.6
Track momentum	$[3, 66] GeV/c$
DCH1 radius	$[12., 120.] cm$
DCH4 radius	$[12., 120.] cm$
Ghost track rejection	

Table 3.3: Track preliminary cuts

- ≥ 4 At least one cell of the cluster can not be reconstructed (does not have two well measured samples). This kind of cluster is not useful to reconstruct good events.

The acceptance of the LKr is limited in the event selection, in order to avoid the edge of the detector where the quality of the reconstruction is degraded. A particular octagonal shape (with an inner radial cut of 15 cm) is used to follow the physical border defined by the CPD readout system (fig. 3.7). Then the total number of surviving clusters is checked: if this number is less than 4 the events is rejected.

Only the photons in a time window of 5 ns centered in the averaged time are considered. The selected quadruplet of gammas defines an *event time*. Only the tracks within 20 ns from the event time are considered in order to compute the

Cut name	Condition
Cluster energy	$[3, 60]GeV$
LKr acceptance	in the acceptance
Cluster status	< 4
Dead cell distance	$> 2cm$
Distance from other clusters	$> 10cm$
Distance from pion cluster	$> 15cm$

Table 3.4: Cluster preliminary cuts

kaon mass and to select the event. After the pairing (see par. 3.3.3), other cuts are applied to the selected event, as mentioned in the table 3.5.

Cut name	Condition
Neutral vertexes distance (fig. 3.10)	5 m
Longitudinal vertex position (fig. 3.9)	[-1600,8000] m
Cog	$< 4cm$
CDA (fig. 3.8)	$< 5cm$
Reconstructed kaon mass	$[487.7, 499.7]MeV/c^2$

Table 3.5: Selection cuts

The value of the cut on the neutral vertexes distance depends on the resolution of the reconstructed neutral vertex and is tuned with the Monte Carlo. For "historical" reason the origin (0) of the longitudinal reference system corresponds to the center of the K_S target position, dating back to the ε'/ε era. For the $K^{\pm}$ asymmetry measurement the decay region has been increased upstream by 24 m. The point at -2000 cm is, in this reference, the position of the end of the last collimator; the decay region begin at the position -1800 cm and 200 cm further downstream from this edge (in the position -1600 cm) is a safety cut to avoid that a decay with a vertex coming from an interaction in the final collimator, could be reconstructed in the decay region due to the resolution in the reconstruction.

The following three cuts assure that the reconstructed energy in the cluster is not biased due to other showers or missed cells. The COG cut (Center of Gravity), defined as the resultant of the photons and charged pion transverse momentum, before the deflection in the spectrometer magnet is motivated by the fact that the COG follows the original Kaon flight direction[8]. This cut it is useful to reduce the contribution from accidental activity.

The CDA (Closest Distance of Approach) for events with one track is defined as the smallest transverse distance between the charged track and the kaon nominal direction (0,0,1). The cut on this variable is useful to avoid contributions from charged particles originating from the decay region (scattering on the collimator, muons from the target, etc.). After all these cuts the reconstructed kaon mass has a quasi-Gaussian shape with tails, showing in fig. 3.12 . The good resolution on

[8]This direction is supposed along the z axis due to the fact that KABES is not used.

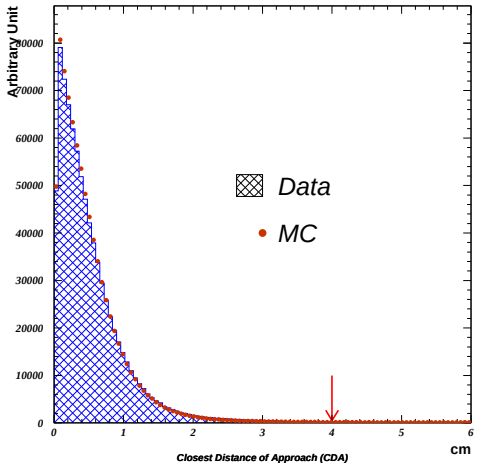

Figure 3.8: CDA distribution.

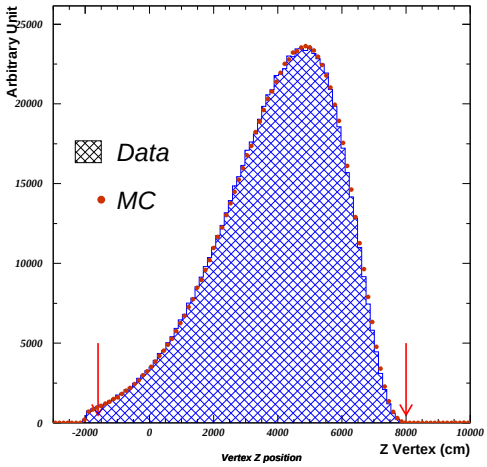

Figure 3.9: The LKr acceptance is the main reason for the shape of longitudinal distribution of the decay vertex.

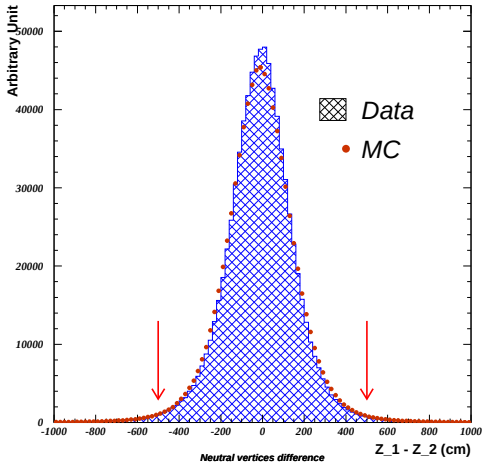

Figure 3.10: The π^0 vertexes are reconstructed by imposing the π^0 mass. The final decay vertex is obtained as an arithmetic average of these two vertexes.

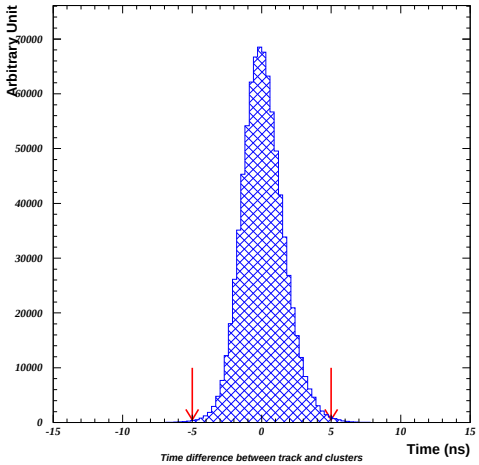

Figure 3.11: Time difference between track time and LKr time (obtained as arithmetical average of the gamma time). The time of flight between the two detectors (few meters apart) is compensated in this plot.

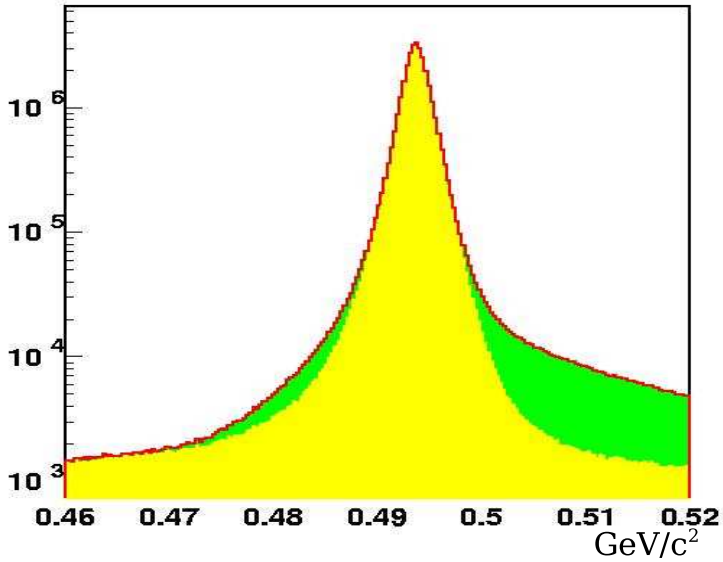

Figure 3.12: Recostructed kaon mass. The background, in green, is due to the $\pi \to \mu\nu$ decay in flight as obtained with a MC simulation. The contribution below the mass peek is negligible in first approximation.

this quantity (0.9 MeV/c^2) allows to cut around the nominal PDG Kaon mass, to reduce the background contribution.

3.3.7 Backgrounds

In the table 3.6 the main Kaon decay modes are summarized. The $K^{\pm} \to \pi^{\pm}\pi^0\pi^0$ is almost background free: since no other channels of sizable BR can mimic the signal signature within the resolution of the apparatus, the small accepted background comes from:

- pion decay;
- accidental activity;
- mismeasurement.

In plot 3.12 it is possible to see, from a Monte Carlo simulation, the pion decay contribution to the mass spectrum. However the small contamination of pion decay in flight cannot influence the asymmetry measurement. For this analysis it is better to avoid the use of the Muon veto counter to identify muons coming from the pion decay. In addition the background could be due to the accidental activity coming from the beam. The problem could be, in principle, dangerous at two levels: the reconstruction and the trigger. In the plot 3.13 and 3.14 the number of tracks and clusters in good events is shown; the contribution to the systematics error will be discussed later in chap. 7 while in chap. 8 the influence on the trigger performances of particles arriving early with respect to the time of the good event will be evaluated.

Decay mode	B.R.
$K^{\pm} \to \pi^{\pm}\pi^0\pi^0$	$(1.72 \pm 0.04) \cdot 10^{-2}$
$K^{\pm} \to \pi^{\pm}\pi^0$	$(21.13 \pm 0.14) \cdot 10^{-2}$
$K^{\pm} \to \pi^{\pm}\pi^+\pi^-$	$(5.576 \pm 0.031) \cdot 10^{-2}$
$K^{\pm} \to \pi^{\pm}\pi^0\gamma$	$(2.75 \pm 0.15) \cdot 10^{-4}$
$K^{\pm} \to \mu^{\pm}\nu$	$(63.43 \pm 0.17) \cdot 10^{-2}$
$K^{\pm} \to e\nu$	$(1.55 \pm 0.07) \cdot 10^{-5}$
$K^{\pm} \to \pi^0 e^{\pm}\nu$	$(4.87 \pm 0.06) \cdot 10^{-2}$
$K^{\pm} \to \pi^0 \mu^{\pm}\nu$	$(3.27 \pm 0.06) \cdot 10^{-2}$

Table 3.6: Main Kaon decay modes

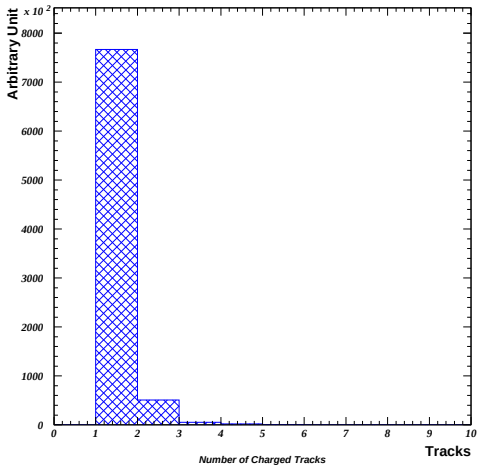

Figure 3.13: Most of the selected events have just one track. The additional track ($\sim 0.5\%$) is, usually, due to the accidental activity.

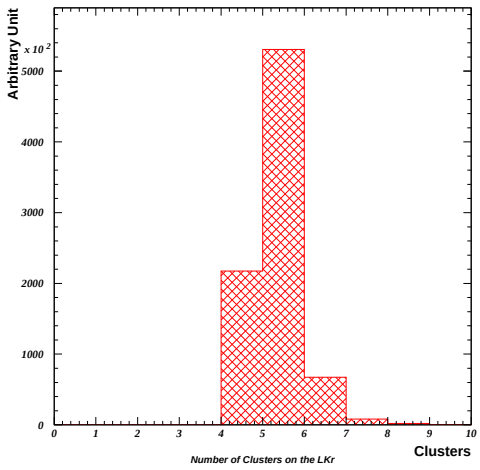

Figure 3.14: Most of the time the charged pion gives a cluster on the LKr, for this reason usually we have 5 clusters (the pion cluster in the selection is excluded from the loop to find the π^0 pair).

3.4 The experimental Dalitz plot distribution

In fig. 3.15 the Dalitz plot for the $K^{\pm} \to \pi^{\pm}\pi^0\pi^0$ decay is shown. This picture is obtained from real data reconstructed events. In fig. 3.16 the Dalitz for MonteCarlo generated events is shown. The difference between the two plots is mainly due to the acceptance of the detector and the efficiency of the reconstruction. In particular the lack of events in the right-hand side (for high U values) is due to loss of charged pions in the beam pipe (fig. 3.6): in fact from eq. (1.52) in par. 1.5.1 is clear that the maximum of the U variable is at $T_3 = 0$; this corresponds to charged pions (the odd pion) at rest in the center of mass system. In the Lab system these charged pions remain on the kaon axis direction and are not detected. The analog effect for the π^0 is not visible due to the fact that the $\pi^0 \to \gamma\gamma$ decay smears the acceptance. In the plots in fig. 3.19 the dependence of the averaged U variable on the DCH1 position of the charged pion impact pion is quite evident. Starting from eqn. (1.53)

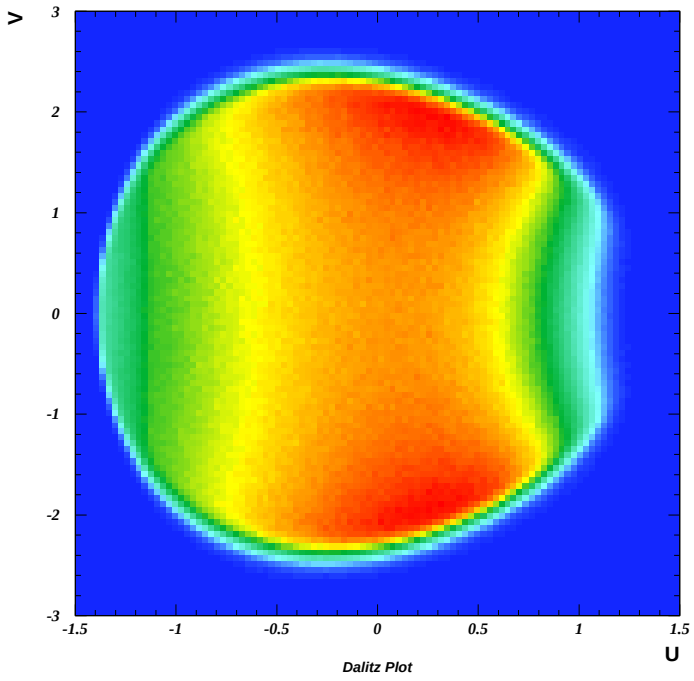

Figure 3.15: Dalitz plot distribution on real data. The presence of the beam pipe in the spectrometer limits the phase space giving the cut in the right part of the plot.

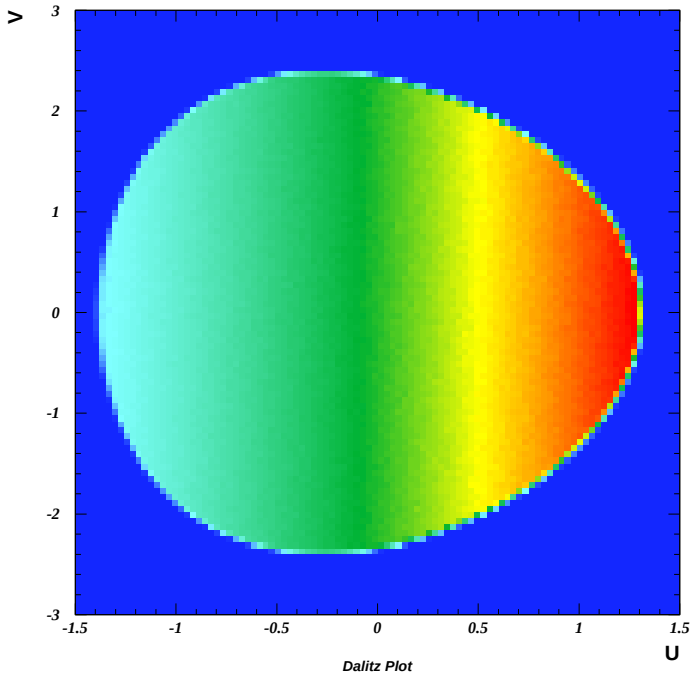

Figure 3.16: Dalitz plot obtained with a MonteCarlo generator (without detector simulation). The difference with respect to the plot on real data is given by the acceptance.

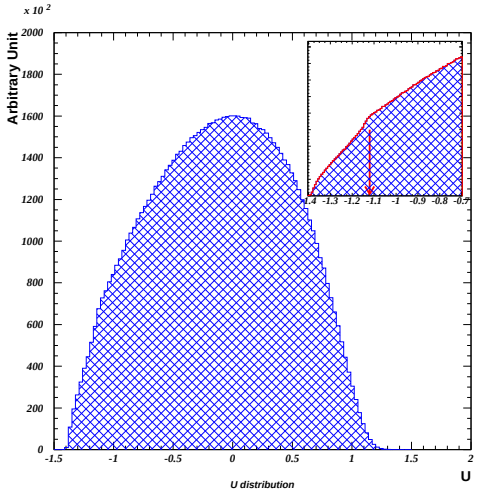

Figure 3.17: Projection of the Dalitz plot along the U direction. The insert shows the region in which a cusp structure is visible.

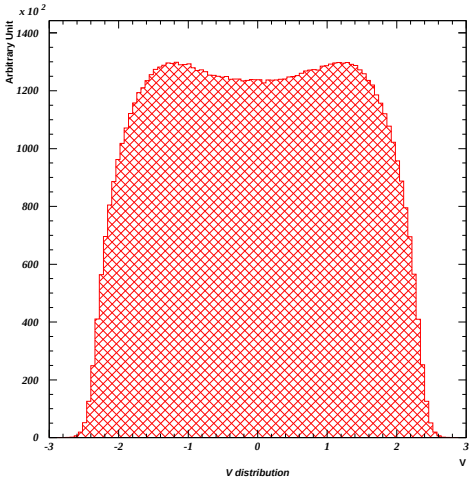

Figure 3.18: Projection of the Dalitz plot along the V direction

in par. 1.5.1 the following relation can be written:

$$U = \frac{1}{m^2_{\pi^\pm}}(M^2_{00} - \frac{m^2_K}{3}) - \frac{1}{3} - \frac{2}{3}(\frac{m_{\pi^0}}{m_{\pi^\pm}})^2 \tag{3.2}$$

in which M^2_{00} is the $\pi^0\pi^0$ invariant mass and m_{π^0}, $m_{\pi^\pm}$ and m^2_K are the PDG particles masses. The kinematical limits on U are determined by the lower and upper limits of the M_{00}:

$$m_{\pi^0} + m_{\pi^0} < M_{00} < m_K - m_{\pi^\pm}$$

This means that the limits in the U distribution are:

$$-1.386 < U < 1.310$$

In the plot 3.17 and 3.18 the Dalitz plot projections along the U and V directions are presented. In particular in the U distribution the limits are slightly differents with respect to the limits defined above due to resolution effect. The V distribution is symmetric due to the Bose symmetry of the π^0's, while the U distribution is given by the odd charged pion and then can show differences between conjugates modes in case of CP violation in the $K^\pm \to \pi^\pm\pi^0\pi^0$ decay. The *cusp structure* (see the insert in fig. 3.17) present in the U distribution (at $U = 4 - \frac{1}{3m^2_{\pi^\pm}}(m^2_K - m^2_\pi - 2m^2_{\pi^0})$) is an interesting feature due to the $\pi\pi$ rescattering that will be discussed extensively in the appendix A .

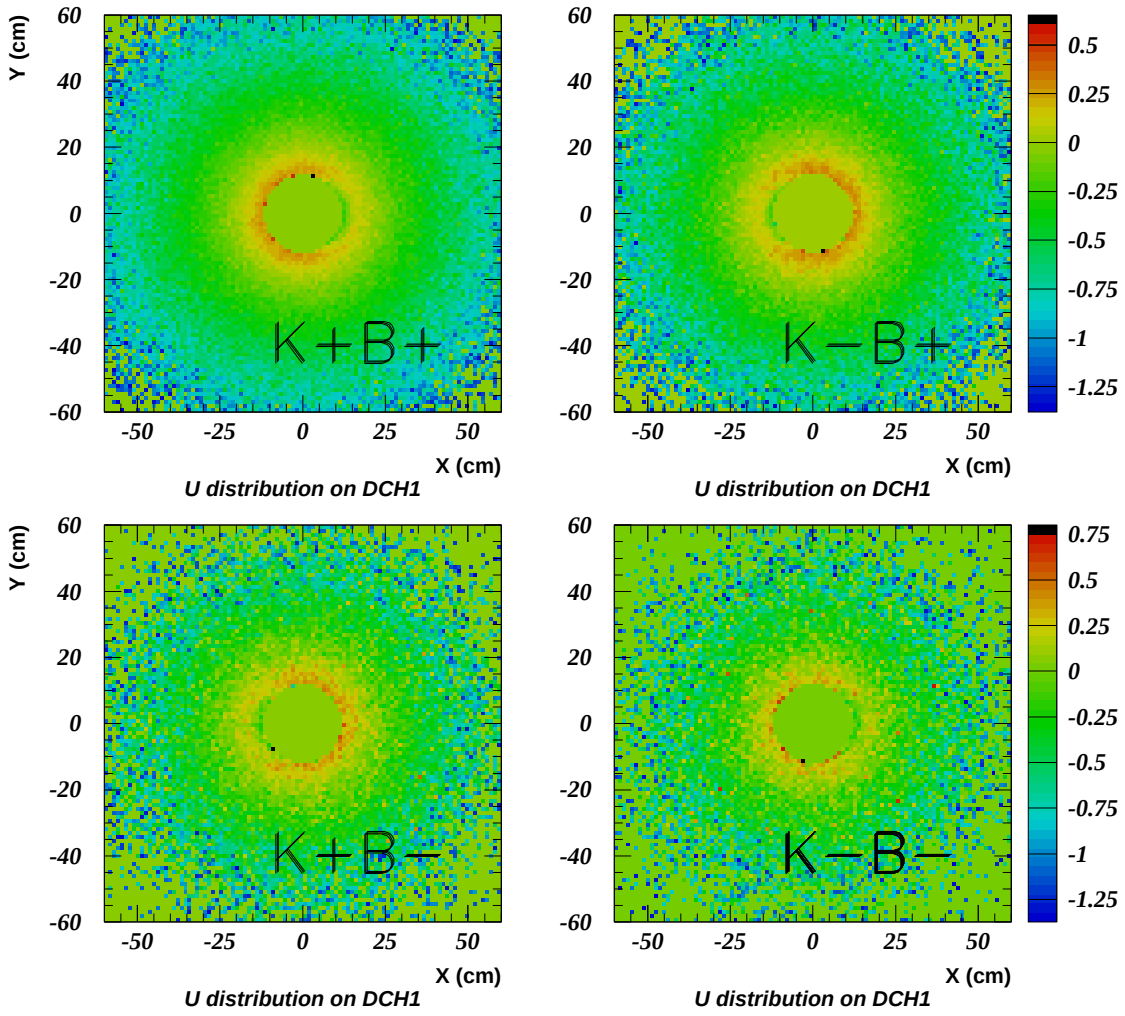

Figure 3.19: Distribution of the average value of the U variable (color scale) as a function of the impact point coordinate X and Y of the charged pion on the DCH1, for different kaon charge and magnetic field orientation. The acceptance (as evident near the center) depends on the sign of these quantities. As we will discuss later, the acceptance for charged pions deflected in the same direction (for instance the K+B+ and the K-B-) is similar.

Chapter 4

Corrections in the $K^{\pm} \to \pi^{\pm}\pi^0\pi^0$ mode

During data reprocessing or analysis procedures, corrections are applied in order to take into account some known effects. Thanks to the good resolution of DCH and LKr, physical properties of the decays can be employed to fine tune the detectors. The possibility to perform some of these corrections as a function of time during the data taking, by using directly some decay channels, is very useful to control the asymmetrical characteristics of the detectors. In this section we will discuss the main corrections for the LKr and the magnetic spectrometer and their importance for the asymmetry measurement.

4.1 LKr energy corrections

Several kind of corrections are applied to the LKr energy estimation at different levels, during the data taking and the reprocessing. For historical reasons, or for opportunity, these corrections are applied:

- During the reconstruction
- When reading Compact (in particular making Super Compact)
- When reading Super Compact

Most of these corrections are studied using some kind of physical process as a reference or with dedicated runs or particular procedures. We will try to summarize the most important effects that can play a role in the energy measurement and the procedure for the determination of the corrections. Many of these effects have been investigated already during the ε'/ε era but the correction factor values have been re-checked and, eventually, re-computed in the 2003 (and 2004) data taking.

4.1.1 Correction during the reconstruction

In the cluster reconstruction several effects are taken into account. Most of these corrections have been studied with special electron runs or analyzing the neutral

K_{e3} decay. The detailed description of these corrections can be found in [100] [101] [102] [103] [104]. Here we want just to mention the most relevant ones:

- Pedestal variation: the first samples of the event are used to compute the pedestal and to check the stability;
- Correction to the cluster energy:
  - Energy variation with the X,Y position in the cell: due to several effects linked to the charge collection;
  - Space charge correction: this effect has been reduced increasing the HV and is actually a very small correction;
  - Energy lost in the beam hole and in the outer radius;
  - Energy intercalibration: The better precision is obtained by using the K_{e3} decays instead of the direct measurement of the circuits transconductance;
  - Energy sharing between adjacent cluster: special algorithm is applied for cluster closer than 11 cm;
  - Low energy losses: to compensate the energy measurement for the presence of passive material in front of the active part of the calorimeter and the low energy bias due to the zero suppression in the Data Concentrator.
- Correction to the cluster position:
  - X,Y position correction: due to the zig-zag shape of the ribbons and imperfections in the cells geometry;

All the corrections contribute to improve the LKr resolution and uniformity. For instance in plot 4.1 the effect of the intercalibration in the E/p for electrons is shown while in plot 4.2 and 4.3 the E/p as a function of the electron impact point position in the cell is presented before and after the corrections. In plot 4.4 the correction for the cluster energy sharing improves the dependence of the π^0 mass on the distance between the γs. Several plots showing the quality of the LKr corrections can be found in the reference given above.

4.1.2 Energy scale factor

The accurate definition of the absolute energy scale is important for the correct reconstruction of the neutral pions. While the study with the K_{e3} provides a method to control and define the intercalibration among the LKr cells, different methods were used to measure the *overall scale factor*. During the ε'/ε era this value was computed by fitting the position of a veto counter (called AKS) located $\sim$ 6 m downstream of the K_S target, reconstructing the decay vertex of the $K_S \to \pi^0\pi^0$. Another method was used in order to cross-check the previous result and to apply a most fine correction: the, so called, *eta runs*. The idea is to produce η particles

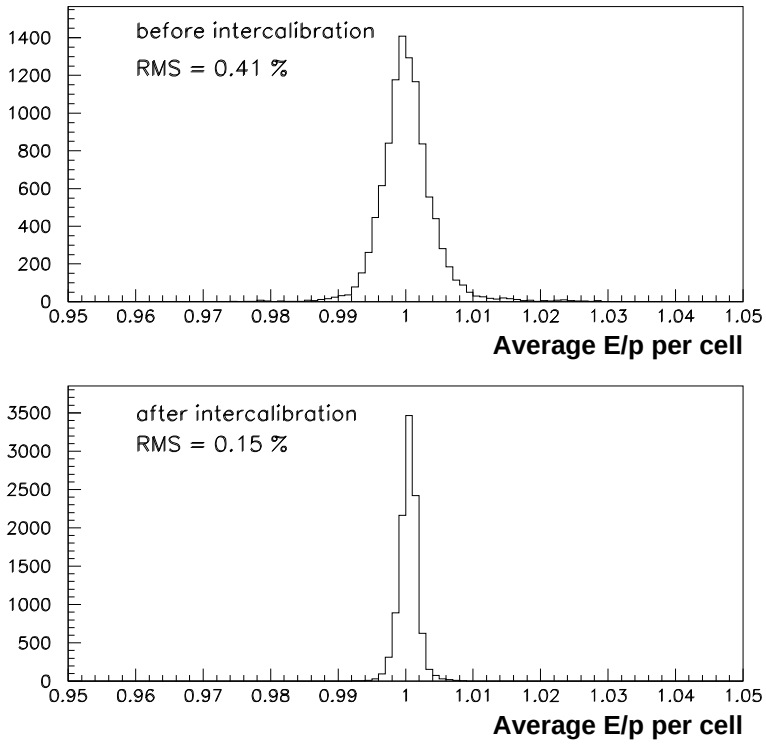

Figure 4.1: Effect of the intercalibration based on the K_{e3} constants on the measured electron E/p.

in two thin polythene targets, located in known position[1], replacing the $K^{\pm}$ beam (or the K_L beam) with a π^- beam. The *eta* decays, with a lifetime of $5.1 \cdot 10^{-19}$ s, in $3\pi^0$ or in 2γ; the energy scale is adjusted matching the reconstructed target position with the real one. In this way, corrections at level of 10^{-4} are obtained with respect to the AKS fitting method. In the 2003 run only the eta technique was employed. A quite good stability of the energy scale factor was found with respect to the previous years and a small eta factor adjustment was applied. For historical reasons this correction is applied in two steps: both in Raw and in Compact. In spite of the importance of the energy scale for the reconstruction of the neutral events, no effects are expected in the asymmetry because, as we will see, only differences between K^+ and K^- collection can play some role.

4.1.3 Non linearity correction

The LKr non-linearity has been studied by using a pure sample of neutral K_{e3} decay in a wide energy region between $\sim 5GeV$ and $\sim 100GeV$. After corrections for other effects (chambers misalignment, resolution bias and non uniformity) the non linearity has been measured and corrected to remain within $\pm 0.1\%$ over the whole energy range by studying the E/p for isolated electrons (fig. 4.5). For high

[1]In a reference system in which the 0 is in the KS target position (for historical reason this is the standard reference system also in the 2003 data taking, where the KS target has been dismounted) the nominal eta target positions were 653 cm and 2115 cm

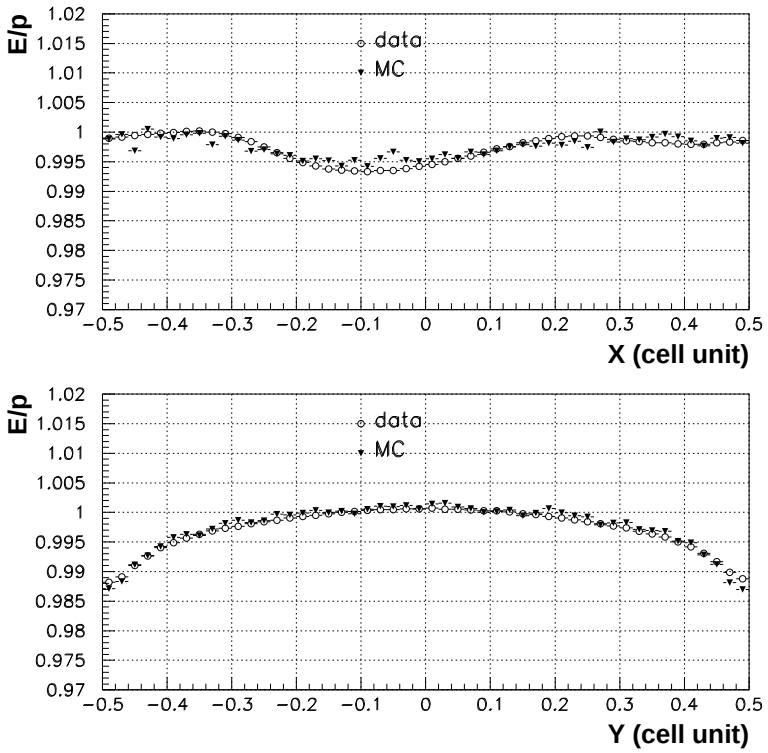

Figure 4.2: The E/p variation with respect to the impact position inside the cell is correctly predicted by a detailed MonteCarlo.

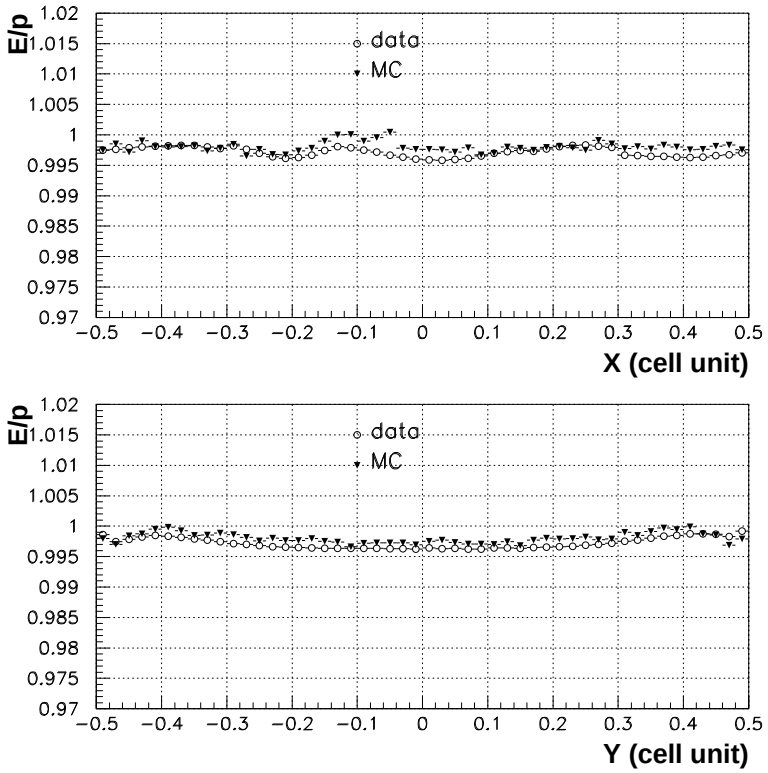

Figure 4.3: After the corrections the residual dependency is quite small, both in X and Y directions.

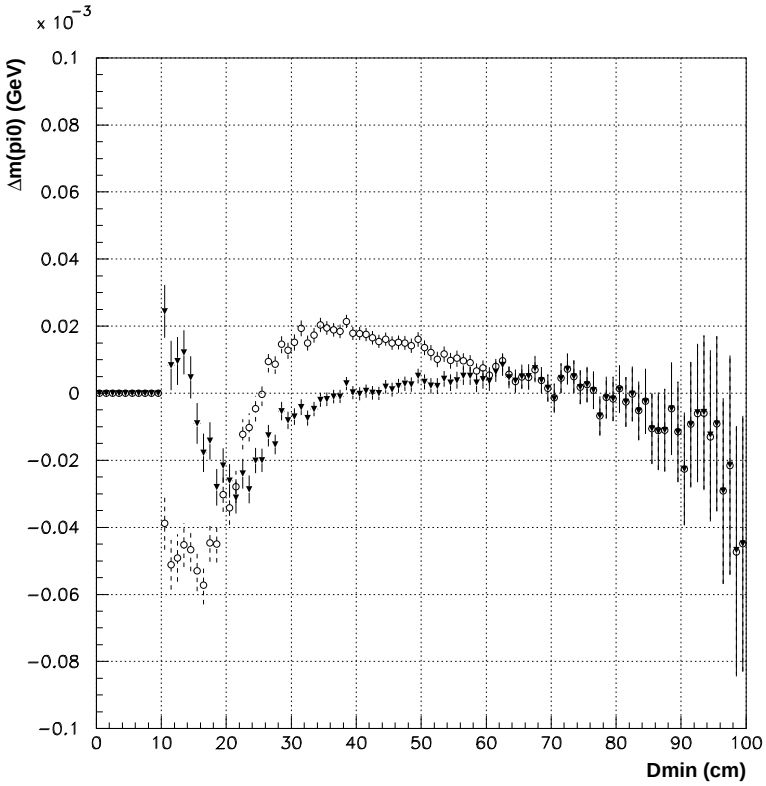

Figure 4.4: The recostructed π^0 mass dependence on the gamma clusters distance improve after the cluster corrections (black points).

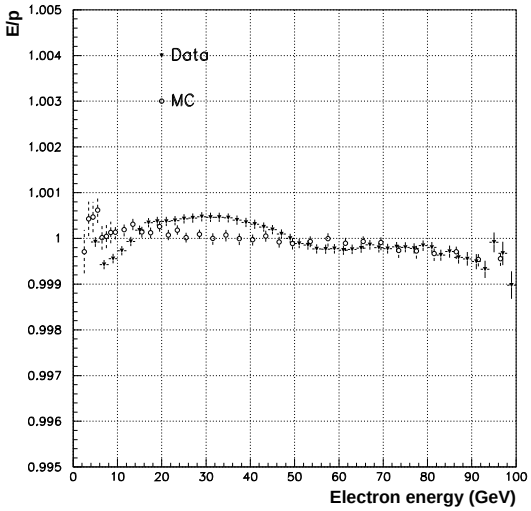

Figure 4.5: In a wide range of energy the LKr non linearity is below 0.1% as obtained from studies with neutral K_{e3}. No correction is needed in this energy range.

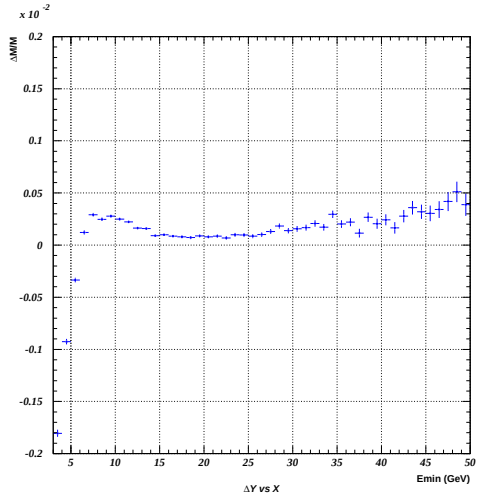

Figure 4.6: The study of the π^0 mass as a function of the low energy photon in $K^0 \to 3\pi^0$ decays allows to implement an "ad-hoc" correction for the energy non-linearity of the LKr for energies below 11 GeV.

cluster energy the MC reproduces the LKr behaviour quite well: this is due to the cell geometrical variation ($\sim 1\%$) between front and back of the calorimeter that is correctly simulated. Above 10 Gev the correction for non linearity is not necessary: parameterizing this correction as:

$$\Delta E = \alpha + \beta E^2 \tag{4.1}$$

the actual value of the α and β parameters are indeed zero. Studies based on the $2\pi^0$, $3\pi^0$ events (with neutral kaons) and η runs indicate a conservative range for those parameters as $\alpha = \pm 10 MeV$ and $\beta = \pm 2 \cdot 10^{-5} GeV^{-1}$.

By studying the π^0 mass in $K \to 3\pi^0$ decay a strong non linearity has been found below 6 GeV (fig. 4.6) and an "ad-hoc" correction has been derived for this range of energy. The source of this non linearity at low energy is not completely understood, but is probably due to the non Gaussian tails in the resolution generated by the hadronic shower production in the LKr. The correction is parametrized by a third degree polynomial obtained by directly fitting the experimental data and applied to all the clusters with energy below 11 GeV. This correction is applied into the $\pi^+\pi^0\pi^0$ reconstruction because more than 50% of the photons are in the range 5 to 11 GeV.

4.2 Projectivity correction

The accurate reconstruction of the angle between photons and between photons and charged pion is needed to select $K^{\pm} \to \pi^{\pm}\pi^0\pi^0$ decays and to define the values of the kinematical variables which characterize them. For this purpose the precise knowledge of the transverse and longitudinal positions absolute scale of the detector elements is needed. The ribbon structure of the LKr was built in such a way that the axis of each ionization cell is pointing to a point P (the projectivity point) along the beam axis at 109.98 m in front of the LKr. A reference plane is defined at the longitudinal position corresponding to the beginning of the active LKr and the pitch of the cells was measured (in the cold conditions) at this plane. For photons originating from close to the projectivity point P, the transverse coordinates of the reconstructed center of their shower development is then (see fig. 4.7.) independent of the longitudinal position at which the energy of the shower is deposited. For photons originating at some distance (in the position D) from P a small correction (usually $< 0.1cm$) to the center of the transverse coordinates of the energy deposition at the reference plane is applied which depends on the distance of the decay vertex from the LKr and on the average depth, $< d_{SW} >$, of the longitudinal energy deposition of the shower inside the LKr. This average depth depends logarithmically on the energy of the showers and can be estimated from computer simulation but it has been directly measured with K_{e3} using the comparison of the extrapolated transverse coordinates of the charged electrons. In particular, from fig. 4.7, the real X_{tr} gamma coordinate can be deduced form the X_P position (measured by the LKr) with the relation

$$X_P \simeq X_{TR} + d_{SW}\theta \tag{4.2}$$

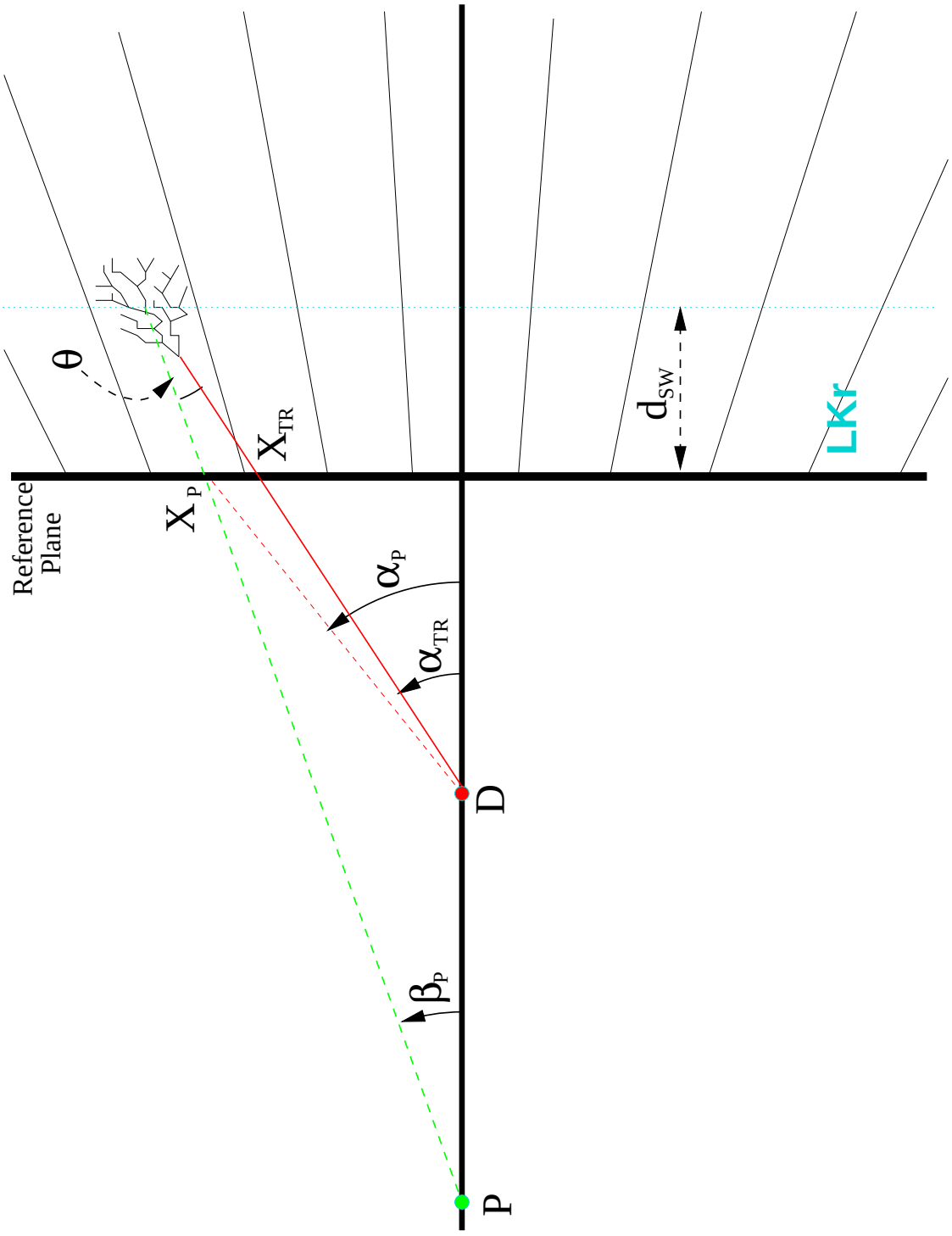

Figure 4.7: A small correction to the transverse position measured by the calorimeter at the reference plane position (X_P) is needed for decays coming far from the projectivity point (from the D position), taking into account the projectivity structure of the ribbons and the fact that the shower core is at depth d_{SW} into the LKr.

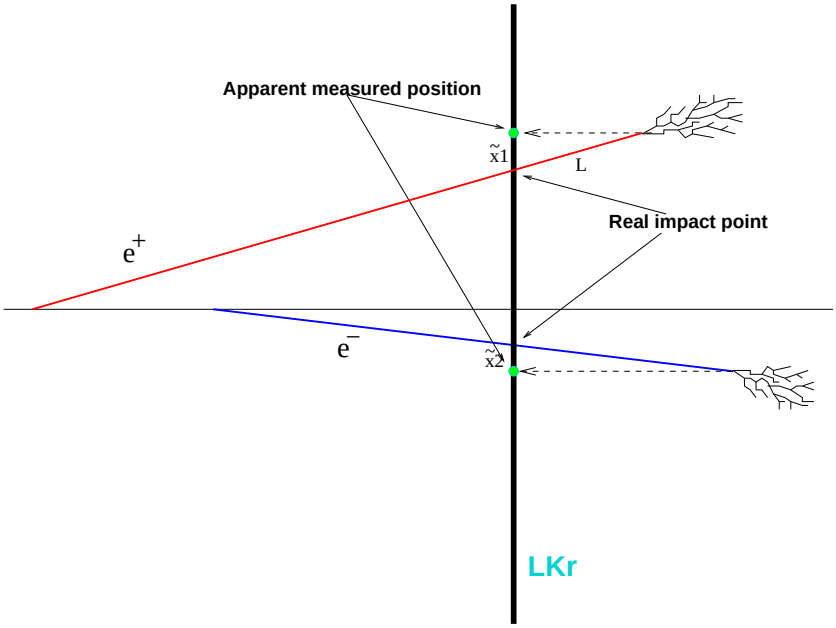

Figure 4.8: The difference ($\tilde{X}$) between the extrapolated (from the DCH4) and the measured point has different sign for electrons of opposite sign (because of the spectrometer magnet they arrive on the LKr with opposite angles). By minimizing the quantity ($< \tilde{X_1} > + < \tilde{X_2} >)/2$ (in energy bins) it is possible to compute the shower depth L (see text).

in which the small angle approximation is used ($sin\theta \simeq tg\theta \simeq \theta$). In the other hand the angle θ is given by:

$$\theta = \beta_P - \alpha_{TR} \simeq -\frac{X_P}{P} + \frac{X_{TR}}{D}$$

then the eq. (4.2) becomes:

$$X_{TR} = X_P \cdot \left(\frac{1 + \frac{d_{SW}}{P}}{1 + \frac{d_{SW}}{D}} \right) \simeq X_P \cdot (1 + \frac{d_{SW}}{P} - \frac{d_{SW}}{D})$$

That gives the true transverse at the LKr reference plane position.

4.3 LKr to DCH alignment

The relative position between LKr and DCH is fixed, at the beginning of the run, and no online procedure was set to yield a continuous calibration. The comparison between the extrapolated position of the electrons measured by the spectrometer and the correspondent cluster position on the LKr, could be useful to measure the LKr to DCH residual misalignment. The selection of the frequent (BR: 4.87%) K_{e3} decay[2] could provide a quite pure electron sample useful for this purpose. The K_{e3} decay is selected through the following procedure:

[2]In this case we are talking about the charged K_{e3} decay i.e. $K^{\pm} \to e^{\pm}\pi^0\nu$

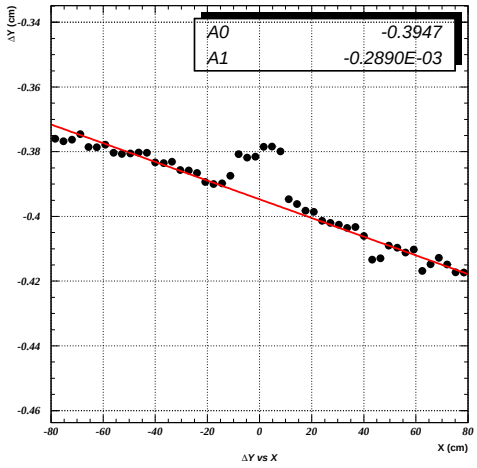

Figure 4.9: Fit of the Y offset. Both in X and Y, the central part is excluded from the fit because biased by the beam pipe.

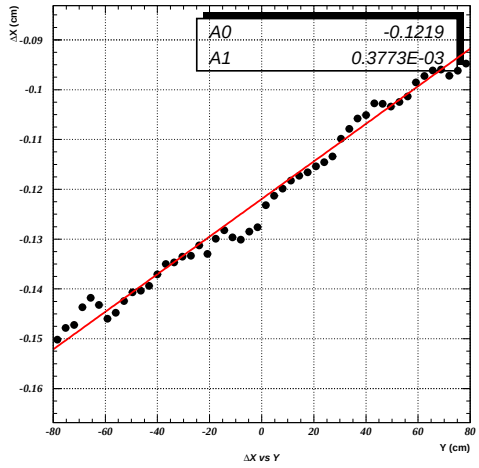

Figure 4.10: Fit of the X offset. Small fluctuations for the LKr alignment are still possible during the run. The values given in the text are the average.

- A list of "good tracks" and "good clusters" is compiled according to general quality cuts (momentum in the spectrometer, acceptance of DCH and LKr, energy, etc.);
- The electron track is selected asking for $E/p > 0.9$;
- Only events with at least one "good" electron track and two "good" gamma clusters are accepted;
- The *neutral vertex* is obtained by imposing the nominal π^0 mass on the photons pair; the *charged vertex* is obtained as the intersection of the charged pion track with the nominal beam line direction;
- The track and the clusters are selected minimizing the difference between the longitudinal neutral and charged vertex position;
- The difference between the two vertex definition must be less than 4 m;
- A cut in the missing mass square (the mass of the neutrino), $-0.13 < M^2_{missing} < 0.26 GeV^2$, is done to increase the purity of the selected events.

In this way a sample of electrons is selected. The small ($< 1\%$) contribution of the background (mainly $\pi^+\pi^0$) is not important for this kind of measurement. Due to the projective structure of the LKr calorimeter, the depth of the shower has to be calculated in order to find the real impact point. The shower depth can be deduced looking for the average value of the differences, in the X direction, between the extrapolated point (from DCH4) and the measured point for opposite electron charge. Indeed for tracks of opposite deflection (fig. 4.8) we can imagine to move the LKr surface until the shower depth L. In this point the quantity $(< \tilde{X}_1 > + <$

$\tilde{X}_2 >)/2$ (where the averaged, on different angles but in energy bin, is used) is zero if there is no LKr-DCH shift otherwise is minimum. The shower depth obtained is (the 0 is at the LKr surface, and the distances are in cm):

$$z_{shower} = 16.5 + 4.3 \cdot log(E)$$

where the logarithmic energy gives, as expected, the relation between the energy and the shower maximum position. To compute the shift between LKr and DCH we can fit the distribution ΔX vs Y and ΔY vs X, with the functions:

$$\begin{aligned} \Delta X &= \delta X + \Theta Y \\ \Delta Y &= \delta Y - \Theta X \end{aligned} \tag{4.3}$$

where δX and δY are the shift values and Θ is a possible rotation angle. In the plot in fig. 4.9 and fig. 4.10 it is possible to see the result of this fit, yielding $\delta X \sim -0.12$ cm, $\delta Y \sim -0.39$ cm, $\Theta \sim 3 \cdot 10^{-4}$ rad for the LKr shift[3].

A global rigid shift of the LKr cannot introduce any bias on the U measurement as defined in par. 3.4 , because the angles between the photons remain the same. Nevertheless the LKr shift could introduce a systematic bias on the Kaon mass reconstructed in the $K^{\pm} \to \pi^{\pm}\pi^0\pi^0$ channel, because the different angle between the charged pion and the photons.

4.4 Internal DCH alignment: α and β correction

A precise knowledge of the chambers relative position in the spectrometer is fundamental in order to avoid momentum mismeasurement. For this purpose special *muon runs* were taken with the spectrometer magnet off. In this kind of runs an approximatively parallel and wide muon beam illuminates rather uniformly all chambers. The X and Y of the muons in each chamber, are used to correct a posteriori the wires position in the reconstruction program. Obviously the muon runs aren't synchronous with the normal data taking because the muon beam production is alternative to the kaon beam in the apparatus. Anyway, thanks to the good resolution of the spectrometer, the K decays themselves can be used in order to correct the misalignment. The most useful decay to study this effect is the $K^{\pm} \to \pi^{\pm}\pi^{+}\pi^{-}$. Let us suppose that a small misalignment is present along the X direction in the DCH4. Once the direction of the spectrometer magnetic field and the direction of the DCH4 shift is fixed, in the K^+ decay the measured angles of two even charged pions (the pions with charge plus) are, for instance, overestimate while the angle of the odd pion is underestimate. Due to this the measured momentum of the charged tracks is lower or higher (respectively) than the real one. The invariant mass of the kaon is computed from the pions' four-momenta and, in this example, we could observe that:

$$M_{meas.}(K^+) < M_{PDG}(K^{\pm})$$

On the contrary for the K^-, with the same argument, we have:

$$M_{meas.}(K^-) > M_{PDG}(K^{\pm})$$

[3]It is not so important to define if the LKr or the DCH are shifted with respect to an absolute reference frame. Only the relative, small, shift plays some role.

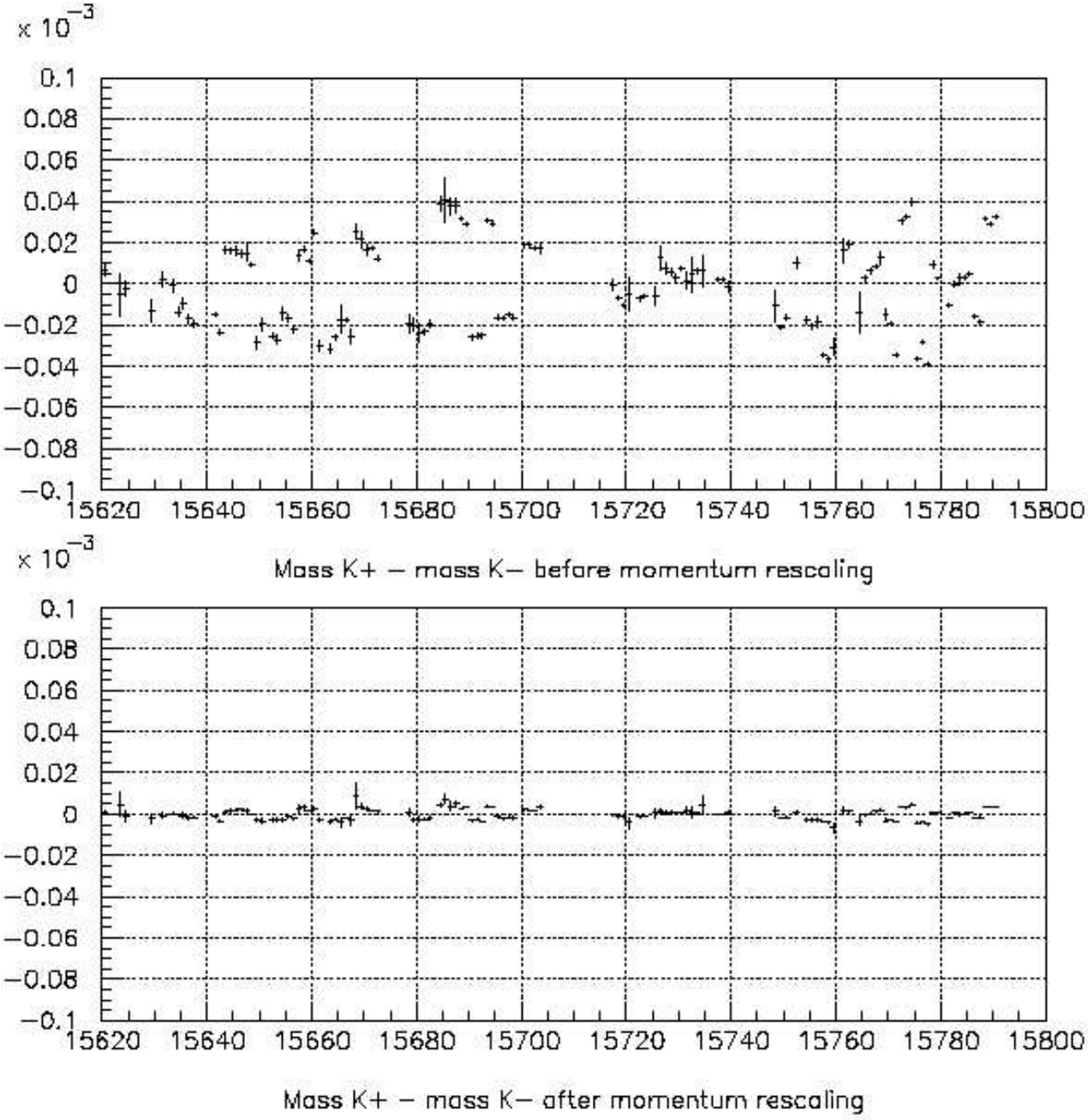

Figure 4.11: Difference between positive and negative charged kaon masses as a function of the run number, as computed in the $K^{\pm} \to \pi^{\pm}\pi^{+}\pi^{-}$ decay. In the Y axis the difference between the PDG and the reconstructed mass, in GeV, is shown. After the momentum rescaling (in two step) the difference between the two masses (maximum 50 KeV) is strongly reduced (in the second plot).

Moreover we would have an inversion in this relations changing the spectrometer magnetic field sign:

$$M_{meas.}(K^+) < M_{meas.}(K^-) \text{ for B-}$$
$$M_{meas.}(K^+) > M_{meas.}(K^-) \text{ for B+}$$

This is exactly the behaviour observed on the data studying the kaon mass as a function of the Run number (as we will see in the next chapter the spectrometer magnetic field is periodically changed), as is shown in the upper plot in fig. 4.11 [97] where each point is the difference between K^+ and K^- masses computed through the decay $K^{\pm} \to \pi^{\pm}\pi^+\pi^-$, rather than correcting directly the transverse position of the chambers. An empirical correction can be implemented to the measured pion momentum in order to require that the Kaon mass is the same in K^+ and in K^- decay:

$$P_{corr} = P_{meas.} \cdot (1 + \eta\alpha P_{meas})$$

where $\eta = \pm 1$ according to the pion's charge and :

$$\alpha = -sign(B) \cdot \frac{< M(K^+) > - < M(K^-) >}{1.7476}$$

where B is the spectrometer magnetic field and $< M(K) >$ are the mean values of the measured kaon masses in the run. The correction is applied iteratively recomputing a second time the α values after a first interaction. The fact that the average values of the K^+ and K^- masses are not centered on the nominal kaon mass and that this value depends on the the spectrometer magnetic field ($< M > (B^+) \geq < M > (B^-)$) is due to the energy scale of the spectrometer and the fact that the magnetic field is not exactly equal in the two polarities $|B^+| \neq |B^-|$ [98]. The problem is fixed defining the β parameter as:

$$\beta = -\frac{< M(K) > - M(K)_{PDG}}{0.2 \cdot M(K)_{PDG}}$$

and rescaling the pion momentum according to the $(1 + \beta)$ factor. After the application of the α and β correction the difference between K^+ and K^- mass is below 10 KeV and very close to the nominal kaon mass. In the second part of fig. 4.11 the effect of the correction is shown.

The α and β correction is an indirect method to check the spectrometer characteristics and the accuracy of the magnetic field inversion. Other kind of indirect checks are also employed by using K_{e3} and $K^+ \to \pi^+\pi^0_{Dalitz}$ decays. In order to check the spectrometer alignment, a special run is taken in which a low intensity kaon beam was directly sent through the spectrometer in several points (along the horizontal, vertical and 45° directions) as in the fig. 4.12. Thanks to the relative monochromaticity of the kaon beams, the spectrometer answer was checked for each kaon's charge and magnetic field orientation, finding similar result as in the alignment rescaling procedure described above [98] [99]. The spectrometer field inversion is checked by using Hall probes (6 probes around the beam pipe ahead, behind and inside the dipole magnet and one temperature compensated probe to study temperature effects (fig. 4.13). Using this probes the spectrometer field variation can be traced at level of 0.2 Gauss in the center of the magnet and 0.5 Gauss at 1 meter from the center.

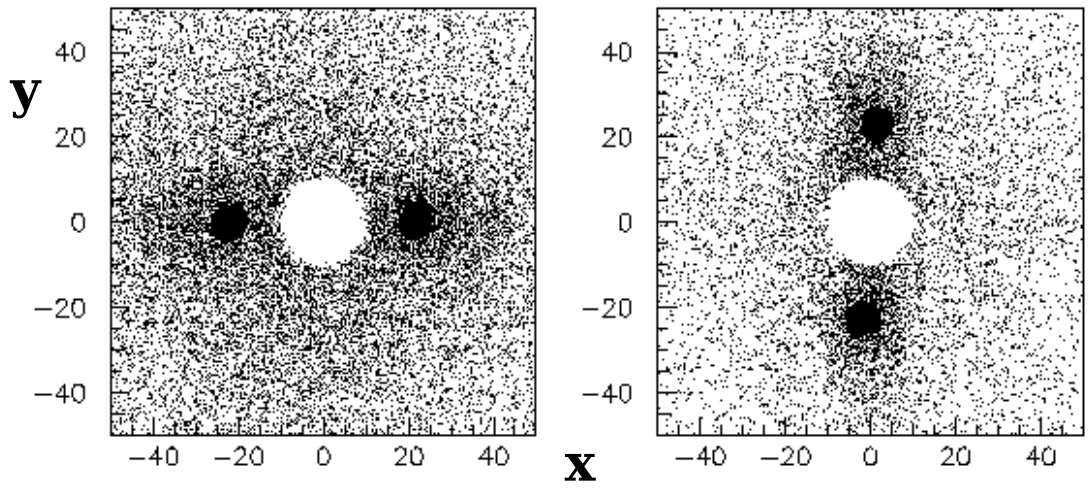

Figure 4.12: The impact points of the intensity reduced kaon beam on the spectrometer. The measured momentum is compared with different kaon charge and magnetic field orientation in order to study the spectrometer alignment (in particular in the region near the beam pipe where *short wires* (terminating at the center of the ring) are used).

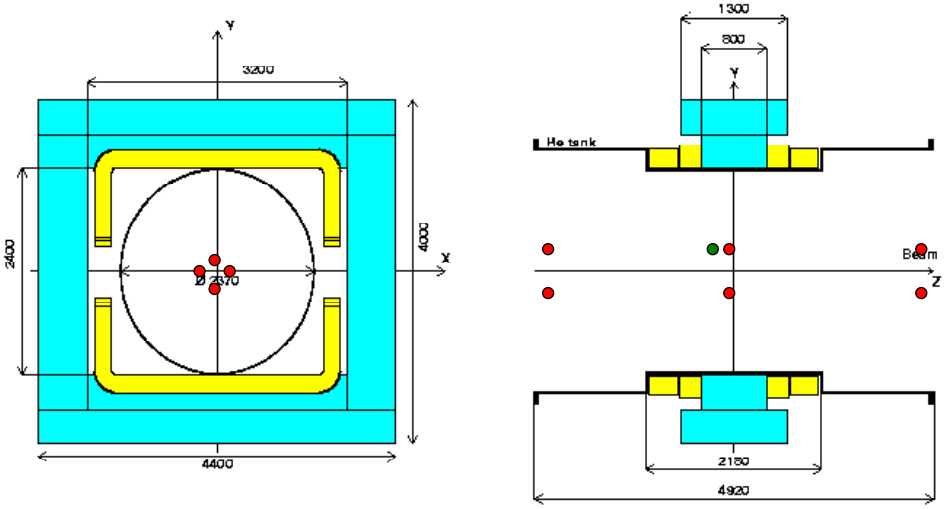

Figure 4.13: The red dot represents the position off the Hall probes to measure the magnetic field inside and near to the MNP33 magnet. The transverse and longitudinal view are shown

4.5 Blue Field effect

As discussed in par. 2.2.2, in the decay region is present a stray magnetic field, called *Blue field* after the colour of the tube in which the decay region is contained. The main component of this field is due to the earth magnetic field. Obviously it is not possible to invert this field: this fact, as we will see, is very dangerous for the asymmetry measurement because the possibility of inverting the magnetic fields present in the apparatus is important to equalize the detector acceptance. Actually the effect of the Blue Field alone cannot introduce directly biases in the asymmetry measurement: our measurement is sensitive to the coupling of two detector asymmetries. If the Blue Field effect only was present, the opposite effect on the charged pion momentum measurement would be canceled in the comparison between K^+ and K^-. On the other hand, a different chambers acceptance coupled with the calorimeter misalignment can introduce a systematic bias in the measurement. If we use the definition U1 (as defined in par. 3.4) the U variable is reconstructed by using only the LKr informations. Thanks to this, the effect of the blue field cannot directly influence the asymmetry measurement, but some effects could be present because of the cut on the invariant kaon mass, for the calculation of which the presence of the reconstructed charged pion is required. In the plot 4.14 (red points) it is possible to see the effect of the blue field if the reconstructed kaon mass is plotted as a function of the angle ϕ in a transverse plane (in the DCH1 position), defined as the angle between the horizontal axis and the vector joining the center of the beam to the impact point of the charged pion track (the positive direction is anti-clockwise and the zero on the right at Y=0). The mass ratio between the positive and negative kaons is not constant (red points in fig. 4.15) and this could appear as a bias in the acceptance and in the density of the Dalitz plot. In the plot 4.16 the distribution of the kaon mass for both charges on the DCH1 is shown. To correct for this effect all the charged tracks are, separately, traced through the blue field and their direction is modified according to the measured field (fig. 2.9). In this way the *slope at vertex* (before the Blue Field influence) can be deduced for each track. After this procedure the corrected mass (color scale in GeV) distribution on the DCH1 is more symmetric and flat (plot 4.17), the modulation with the ϕ angle and the dangerous bias on the kaon mass ratio disappears (small blue triangles in plot 4.14 and 4.15).

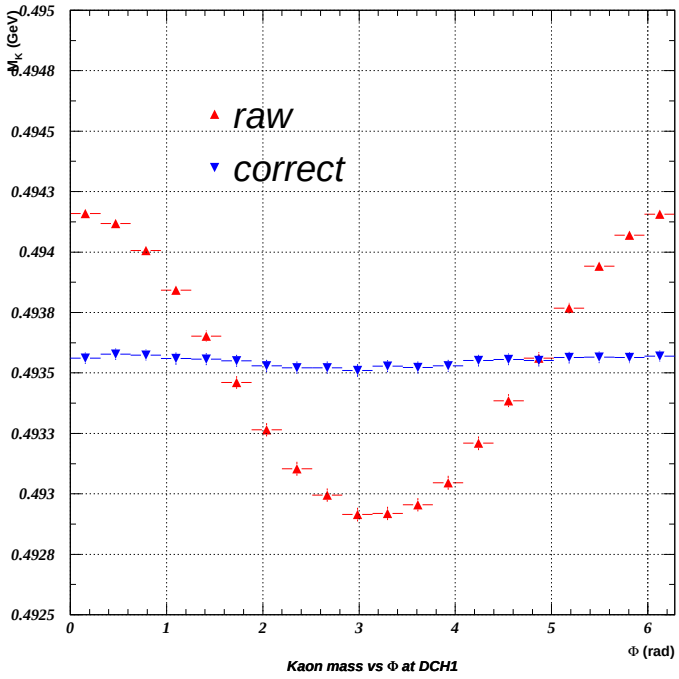

Figure 4.14: Dependence of the kaon mass on the position of the charged pion hit on DCH1. The red triangles show the kaon mass modulation before the Blue Field and misalignment correction, for the blue triangles all the corrections are applied.

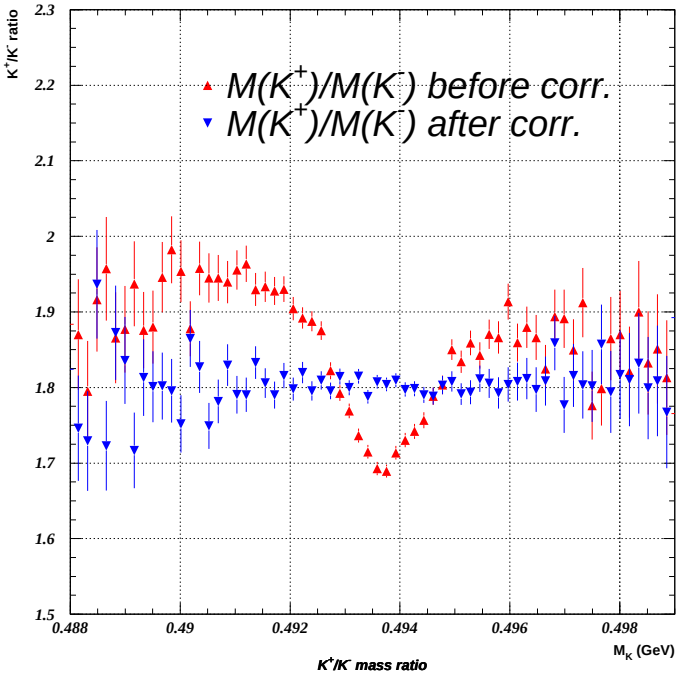

Figure 4.15: The ratio between the kaon mass for positive and negative charge before (red) and after (blue) the correction shows a different behaviour.

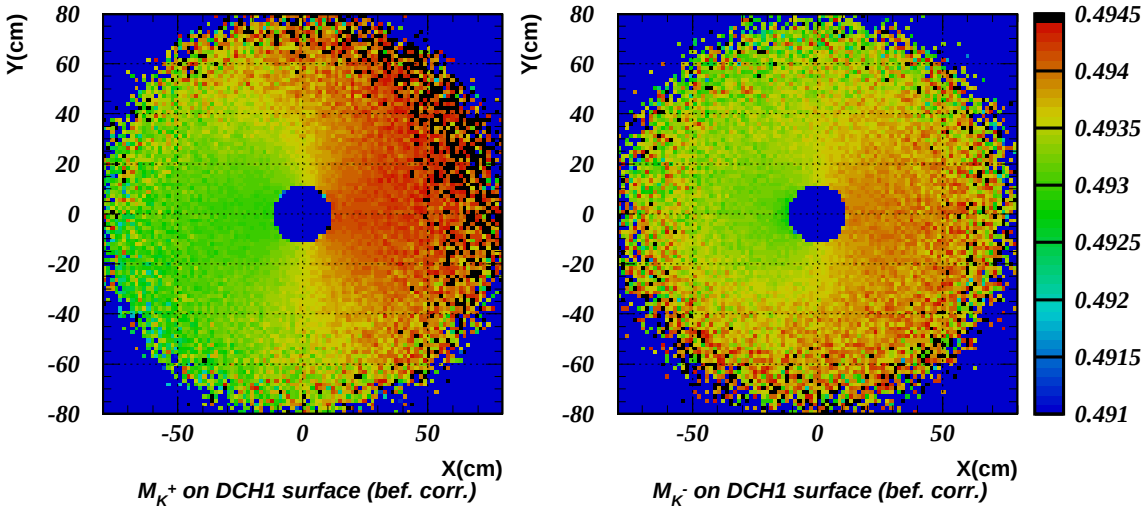

Figure 4.16: Before the blue field and misalignment correction the kaon mass distribution (color scale) shows a particular pattern on the DCH1 face projection, different between positive and negative kaons.

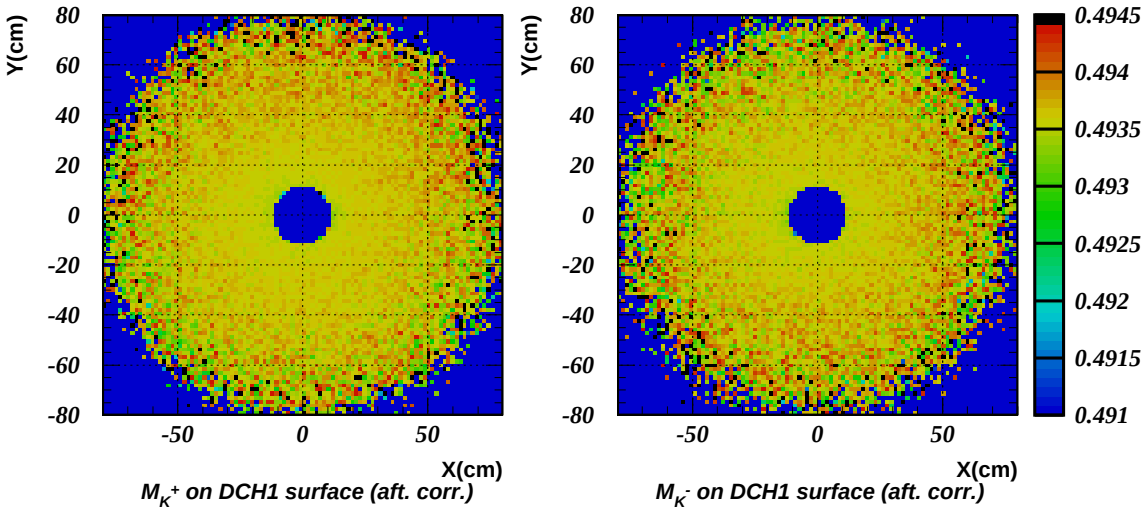

Figure 4.17: After the corrections the kaon mass distribution (color scale) is more flat on the whole DCH1 surface.

Chapter 5

Strategy of the Analysis

Any difference between K^+ and K^- decays would be a signal of direct CP violation. The most obvious observable sensitive to CP violation is the asymmetry in the partial decay width between charged conjugate final state for both $K^\pm \to \pi^\pm\pi^0\pi^0$ and $K^\pm \to \pi^\pm\pi^+\pi^-$ decays. The standard model predicts very small values for this asymmetry, in part as consequence of the integration over the whole phase space and experimentally it would be necessary to control very accurately the relative K^+ and K^- flux to detect the asymmetry in this way. Instead of the partial decay widths it is better to compare the shape of the Dalitz plot distribution, defining a suitable observable that is sensitive to the CP violation effect. In this chapter the strategy of the analysis will be described while the results obtained will be shown in the chapter 6.

5.1 Definition of the measurement

As discussed in the par. 3.4, the Dalitz Plot is defined using Lorentz invariants according to the definition given in eq. (1.53). In presence of CP violation the CM energy distribution of π^+ in $K^+ \to \pi^+\pi^0\pi^0$ and of π^- in $K^- \to \pi^-\pi^0\pi^0$ are expected to differ from each other. The CM energy of the charged pion is directly linked to the invariant mass of the $\pi^0\pi^0$ pair and hence to the U variable that can be written as:

$$U = \frac{M_{00}^2 - s_0}{m_\pi^2} \tag{5.1}$$

where M_{00}^2 is the $\pi^0\pi^0$ invariant mass and s_0 is a constant number, given by:

$$s_0 = \frac{m_K^2 + m_\pi^2 + 2m_{\pi^0}^2}{3}$$

where m_K, m_π and m_{π^0} are the kaon, charged pion and neutral pion masses, respectively. The U definition above is independent from the charged pions and can be reconstructed by using the LKr information only. This is an important issue of the measurement, because, in first approximation, the detector asymmetries between K^+ and K^- can contribute to the U distribution only through different detector acceptance. For instance any eventual mismeasurement between π^+ and π^- in the spectrometer (par. 4.4) can affect the U distribution only indirectly through the cut

in the invariant $\pi^{\pm}\pi^0\pi^0$ mass.
The definition in the eq. (5.1) is not unique (as already mentioned in the par. 3.3.5): in fact the $s_3 = (P_K - P_3)^2 = (P_1 + P_2)^2$ invariant can be obtained both from the two π^0's and, alternatively, from the Kaon four momentum and the charged pion. In the later case the U distribution is totally determined by the KABES and the Spectrometer. The considerations above on the possibility to measure the interesting variable in a charged independent way are not valid any longer, but for control purposes it is important to quote the same quantity in a totally independent way. And in fact this second possibility will be exploited only as a cross check. The U definition by using the LKr only will be called **U1**, **U2** if KABES and the Spectrometer are used instead of the LKr[1]. Often we will refer with **U** to the **U1** definition.

Assuming equal detector acceptance and detection efficiency for K^+ and K^-, the difference Δg in the slope of the U dependence of the Dalitz plot density distribution, can be defined naively by considering the ratio R between the normalized U distribution:

$$R(U) = \frac{N^+(U)}{N^-(U)} \tag{5.2}$$

By using the standard expansion of the matrix element we have that:

$$R(U) = \frac{1 + g^+U + hU^2 + kV^2 + ...}{1 + g^-U + hU^2 + kV^2 + ...}$$

which, assuming $h, k << g$:

$$R(U) \sim 1 + \frac{\Delta g U}{1 + gU} \tag{5.3}$$

with $\Delta g = g^+ - g^-$ and $g = (g^+ + g^-)/2$. We notice that any differences between number of K^+ and K^- decays does not affect R, and hence Δg, given that $N^+(U)$ and $N^-(U)$ are normalized over the (common) U range. It is possible, as a better approximation, to take into account the value of h ($h = 0.051$ [4]) and use:

$$R(U) \sim 1 + \frac{\Delta g U}{1 + gU + hU^2} \tag{5.4}$$

In the plot 5.1 the function R(U) as defined before, is shown for different values of Δg and for $g = 0.638$ [4]. In the plot 5.2 the different behaviour of a linear function (obtained assuming $g = h = 0$) and of an approximated ratio (obtained assuming $h = 0$) with respect to the standard ratio (defined by eq. (5.4)) is shown for the same Δg value. These functions are very different in the left part of the Dalitz plot, where the acceptance is maximal (fig. 5.3). For this reason the result is sensitive to different approximation of fitting function as we will discuss later.

The expected statistical error on Δg in fitting R(U), is given by:

$$\delta(\Delta g) = A \cdot \sqrt{\frac{1}{N^+} + \frac{1}{N^-}}$$

[1] U2 is equally obtained, with worst resolution but easily, assuming the nominal beam direction and nominal momentum.

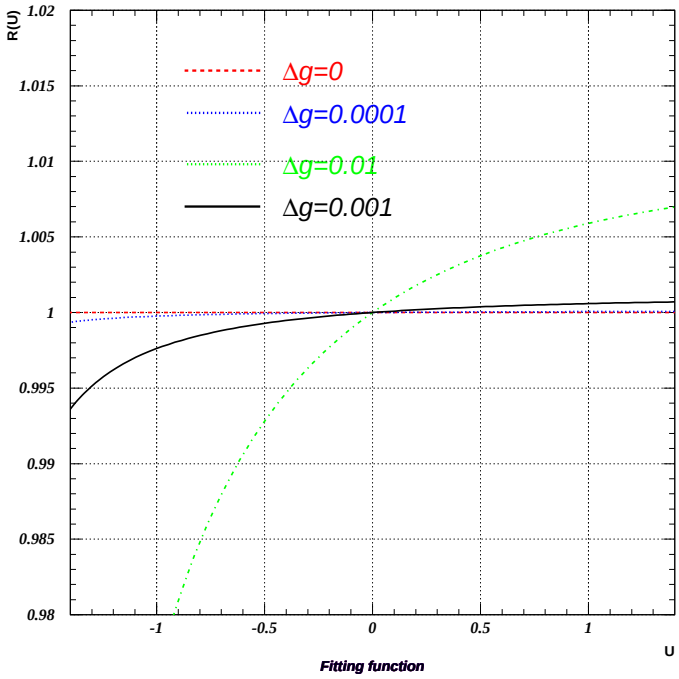

Figure 5.1: The left part of the Dalitz plot is the most sensitive region to different Δg values.

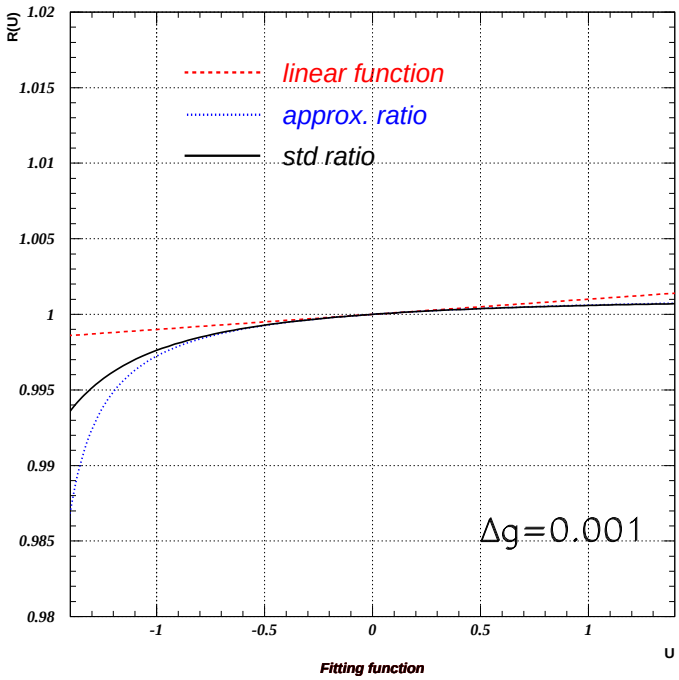

Figure 5.2: Behaviour of different function used to fit the K^+ and K^- U distribution ratio. The discrepancy visible at negative value of U is important because of the relevant acceptance in this Dalitz plot region.

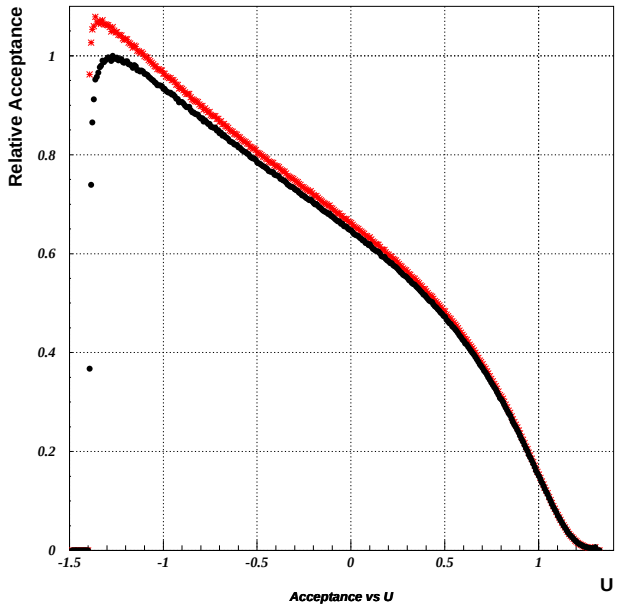

Figure 5.3: Acceptance as a function of U . The acceptance has a the maximum in the left part of the Dalitz plot, where the fitting function is more sensitive to the slope value. The red curve (with small stars) shows as the acceptance improves if the selection was based on the minimization of a χ^2-like ($\chi^2 = (\Delta Z/a)^2 + (\Delta M_K/b)^2$ where a=120 cm and b=0.0022 GeV are the resolution averaged values, for the neutral vertexes difference ΔZ and $\Delta M_K = M_K - M_{PDG}$) instead of the neutral vertexes longitudinal position difference.

where N^+ and N^- are the number of kaon decays collected in the two charges and A is called *error factor* and it can be evaluated with a toy MC. In the following table 5.1 the error factors for the introduced functions are shown: Fitting R(U) to the

fit function	A (error factor)
linear function	~ 1.8
approximated ratio (h=0)	~ 0.7
standard ratio (5.3)	~ 0.9

Table 5.1: Error factor for different fitting functions.

experimental U distribution ratio allows to extract the Δg value relevant to direct CP violation **only** under some important prescription. Indeed the expression (5.2) is rigorously valid only in the case in which the detection efficiency and the geometrical acceptance for K^+ and K^- decays is the same. The eq. (5.2) can be rewritten by including possible detector asymmetries as:

$$R = \frac{N^+(U) \cdot \eta^+ \epsilon^+}{N^-(U) \cdot \eta^- \epsilon^-} \tag{5.5}$$

where η represents the detector acceptance (geometrical acceptance, different beam

geometry, ...) and ϵ the collection efficiency (trigger efficiency, charged detection asymmetry,...). In order to take under control any detector asymmetries, η, we could use, in principle, a MonteCarlo simulation to correct the U spectra. Since we want to keep the systematics error at level of 10^{-4}, the MonteCarlo cannot be trusted to simulate the detector asymmetries at this level of precision. A more reliable technique has to be introduced. The main source of possible detector asymmetries comes from the presence of magnetic fields both in the spectrometer and in the beam transport line. In eq. (5.5), the nominator and the denominator refer to the normalized $N^+(U)$ and $N^-(U)$ U distribution for K^+ and K^- that can be collected in various experimental conditions. For a fixed orientation, up ($\uparrow$) or down ($\downarrow$), of the spectrometer magnetic field (the letter **B** in the following) charged pions of opposite sign are of course deflected towards opposite sides of the detector and the relative acceptance could be quite different. However as it is schematically shown in fig. 5.4, if the B field is reversed then it is possible to collect the charged pion of opposite sign in the same side of the detector. This is very important because following this strategy of data taking we can construct K^+ and K^- ratios, as in the eq. (5.5), in which the deflection of the pions is towards the same side of the detector. In particular it is possible to define two kinds of ratios:

$$R_s = \frac{B(\uparrow)K^+}{B(\downarrow)K^-} \tag{5.6}$$

$$R_j = \frac{B(\downarrow)K^+}{B(\uparrow)K^-} \tag{5.7}$$

$$\tag{5.8}$$

where the under-script represents the Jura and Saleve side of the detector. The same procedure can be applied to the achromat magnetic fields[2] $A(\uparrow \text{ or } \downarrow)$. Four single ratios[3] are defined exploiting the field combinations:

$$R_{su} = \frac{A(\uparrow)B(\uparrow)K^+}{A(\uparrow)B(\downarrow)K^-} \tag{5.9}$$

$$R_{ju} = \frac{A(\uparrow)B(\downarrow)K^+}{A(\uparrow)B(\uparrow)K^-} \tag{5.10}$$

$$R_{sd} = \frac{A(\downarrow)B(\uparrow)K^+}{A(\downarrow)B(\downarrow)K^-} \tag{5.11}$$

$$R_{jd} = \frac{A(\downarrow)B(\downarrow)K^+}{A(\downarrow)B(\uparrow)K^-} \tag{5.12}$$

$$\tag{5.13}$$

where the subscript letters U and V, stands for the Up and Down "polarity" in the Achromat. In the ratios in the previous equations the parameters η, defined in eq. (5.5), cancels out because they depends on the acceptance asymmetry and

[2]In the achromat system there are several magnetic fields in order to split and recombine the charged kaon beams. The sign of the achromat is defined as the path (Up or Down) followed by the K^+.

[3]The reason for the name "single" will be clear in the next section.

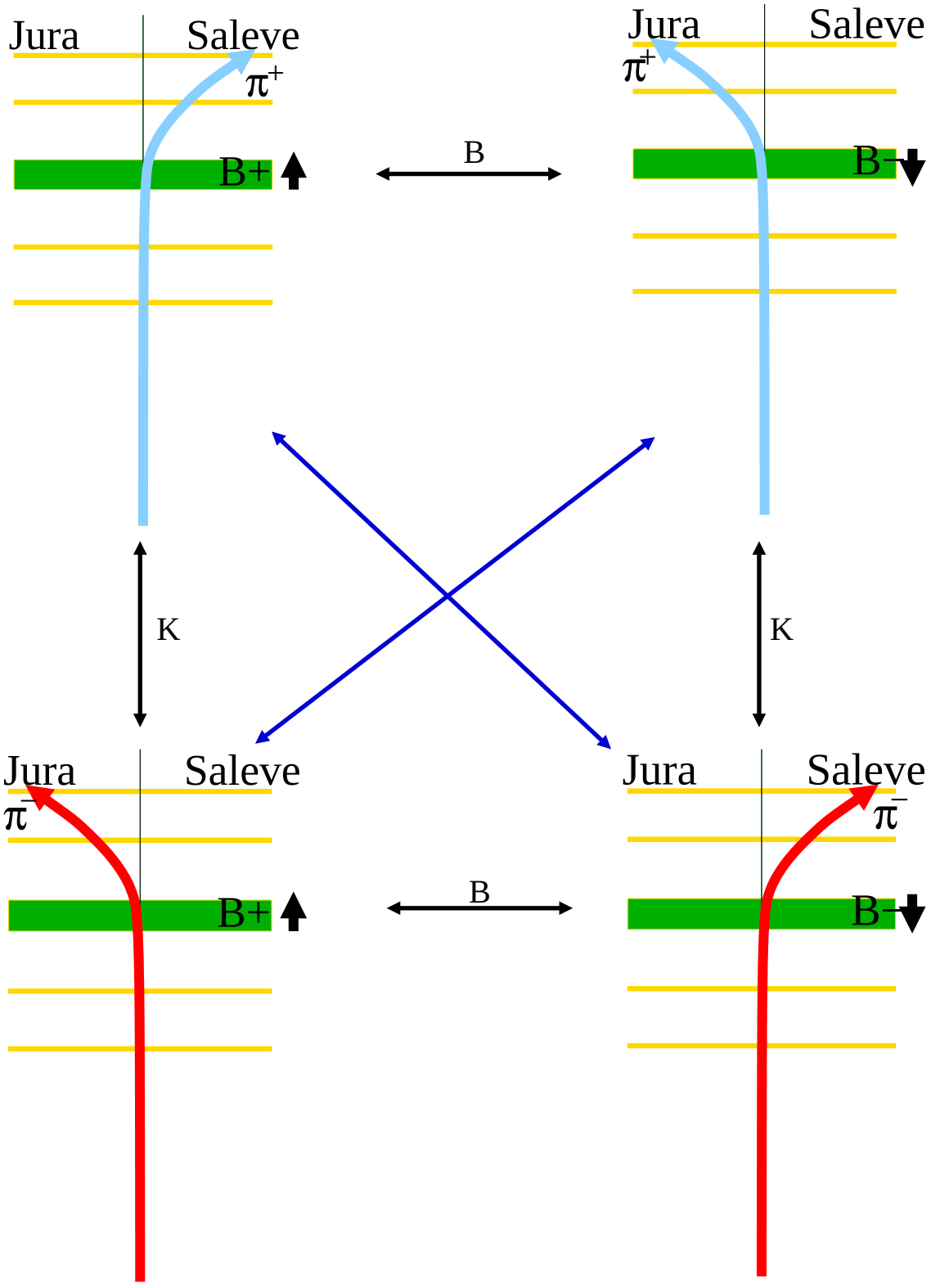

Figure 5.4: By reversing the B field direction and the Kaon charge the same geometrical distribution is obtained. In first approximation the positive charged events collected with a positive B field have the same acceptance with respect to the negative charged events collected with negative magnetic field. According to the position of the mountains with respect to the beam line direction, the left and right side of the detector are called Jura or Saleve. This convection is internally adopted to avoid ambiguities due to the left and right definition.

each ratios is defined in the same side (Jura and Saleve) of the detector separately. Due to the relatively long time needed to reverse the magnets polarity, during the 2003 run, the spectrometer magnet orientation has been changed each day and the achromat polarity each weak. This scheme of data taking defines a subdivision of the whole run in:

- *DaySample* **DS**: represents the smallest data unit in which both the B (spectrometer) and the A (achromat) magnetic fields are stable. Usually a day sample is indeed $\sim$ 24 hours long, according to the daily basis of the B field inversion.

- *SuperSample* **SS**: is a collection of subsequents DS in which all the A and B field combinations[4] are present. The SuperSample duration is undetermined, but at least one achromat inversion has to be included.

In the whole 2003 Run 3 SS and 44 DS has been defined after the bad burst and bad period rejection, as we will discuss later. Although the left-right acceptance asymmetries cancel in the eq. (5.13) ratios, it is important to notice that in each of these ratios the numerator and the denominator are collected at different time according to the change of the magnetic fields. For this reason the ratios are sensitive to *time instabilities of the detector*. Any time variation of the acceptance and/or of the collection efficiency, both local (regarding a small part of the detector) and global (regarding the whole detector), of the detector can introduce a bias in the ratios, if this effect depends on the U variable. In fact, due to the fact that we are looking for any difference between the *shape* of the U distribution between K^+ and K^-, any effect that is U independent cannot generate "fake" slope in the ratio. In the definition of the single ratios, we exploit the fact that the time variation effect is intrinsically reduced at the smallest period that we have, the inversion of the spectrometer magnetic field, instead of the perfect equalization of the beam line up-down asymmetries. In fact other kind of ratios could be in principle defined as:

$$R^* = \frac{A(\uparrow)B(\uparrow)K^+}{A(\downarrow)B(\downarrow)K^-}$$

In this case the geometrical time independent acceptance effect in the numerator and in the denominator cancels perfectly in principle, but the two kaon charges are collect very far (one week) each other. According to the discussion above, we prefer the single ratios definition given in the equation (5.13), in which the problems induced by the left-right asymmetry and the time instability are considered most relevant with respect to the up-down asymmetry in the beam transport line.

5.2 The Double ratio and the quadruple ratio

As mentioned above, the periodical inversion of the spectrometer magnetic fields allows the cancellation of the left-right detector asymmetries, but the fact that the

[4]Obviously we have 4 combinations of magnetic fields $A\uparrow B\uparrow$, $A\uparrow B\downarrow$, $A\downarrow B\uparrow$, $A\downarrow B\downarrow$ which all the ratios in eq. (5.13) can be defined.

opposite sign kaons are collected in subsequent days can introduce a time bias, if the detector acceptance or efficiency change between the two periods in which the B field is reversed. In order to decrease the contribution of the time variation it is possible to construct the *double ratios*:

$$R_u = R_{us} * R_{uj} = \frac{A(\uparrow)B(\uparrow)K^+}{A(\uparrow)B(\downarrow)K^-}\frac{A(\uparrow)B(\downarrow)K^+}{A(\uparrow)B(\uparrow)K^-} \tag{5.14}$$
$$R_d = R_{ds} * R_{dj} = \frac{A(\downarrow)B(\uparrow)K^+}{A(\downarrow)B(\downarrow)K^-}\frac{A(\downarrow)B(\downarrow)K^+}{A(\downarrow)B(\uparrow)K^-}$$

In this case any global time variation of the detector (in the sense that this variation does not depend on the left-right acceptance) cancels because in each double ratios the numerator in the first ratio is collected at the same time with the denominator of the second ratio and vice-versa in the second ratio. In this case the fitting function (5.3) must be modified as follow:

$$R \sim \left(1 + \frac{\Delta g u}{1 + gu + hu^2}\right)^2 \sim 1 + \frac{2\Delta g u}{1 + gu + hu^2} \tag{5.15}$$

On the other hand it is possible to construct the double ratios in the same way as before but involving the achromat instead of the side of the detector. The relations:

$$R_j = R_{uj} * R_{dj} = \frac{A(\uparrow)B(\downarrow)K^+}{A(\uparrow)B(\uparrow)K^-}\frac{A(\downarrow)B(\downarrow)K^+}{A(\downarrow)B(\uparrow)K^-} \tag{5.16}$$
$$R_s = R_{us} * R_{ds} = \frac{A(\uparrow)B(\uparrow)K^+}{A(\uparrow)B(\downarrow)K^-}\frac{A(\downarrow)B(\uparrow)K^+}{A(\downarrow)B(\downarrow)K^-}$$

allow to study the contribution of the different path in which the kaons travel through the achromat. Finally the best control of the systematic biases is obtained in the *quadruple ratio*:

$$R_4(u) = R_{us}R_{uj}R_{ds}R_{dj} = \frac{A(\uparrow)B(\uparrow)K^+}{A(\uparrow)B(\downarrow)K^-}\frac{A(\uparrow)B(\downarrow)K^+}{A(\uparrow)B(\uparrow)K^-}\frac{A(\downarrow)B(\uparrow)K^+}{A(\downarrow)B(\downarrow)K^-}\frac{A(\downarrow)B(\downarrow)K^+}{A(\downarrow)B(\uparrow)K^-} \tag{5.17}$$

for which the fitting function must be modified again with respect to the eq. (5.15):

$$R \sim \left(1 + \frac{\Delta g u}{1 + gu + hu^2}\right)^4 \sim 1 + \frac{4\Delta g u}{1 + gu + hu^2} \tag{5.18}$$

In the following usually we will refer to Δg as the value extracted from the eq. (5.18), if not differently indicated.

In the quadruple ratio case, a threefold cancellation is exploited:

- beam line differences cancellation: is obtained with the comparison of K^+ and K^- traveling along the same path in the achromat.
- detector asymmetries cancellation: is obtained by comparing decays collected in the same side, Jura or Saleve, of the detector.

- global time-dependent effect: is obtained from the fact that the K^+ and the K^- are collected simultaneously.

The only important residual effect that does not cancel out in the quadruple ratio (5.17), is the time variation of the detector with a characteristic time scale smaller than the B field spectrometer alternation period ($\sim$ 1 day) coupled with some acceptance asymmetry. Several kind of effects will be studied in the next chapters as possible sources of systematic biases. We want to stress here that, thanks to the intrinsic robustness of the quadruple ratio, any effect to be a real systematic problem has to present the following characteristics:

- time dependence: according to the discussion above
- U dependence: otherwise the effect cannot bias the comparison of the shape of the U distributions.
- charge dependence: in the sense that this effect has to distinguish between K^+ and K^-.

Not trivial sources of systematics come from the coupling between two effects (for instance the effect of the earth magnetic field, we will see, is relevant when is coupled with the acceptance variations).

5.3 Detector asymmetry

In previous section the procedure to extract the physical value of the possible asymmetry between the projection of the Dalitz Plot along the U coordinate in the two kaon charges has been presented. It Is possible to construct other quantities which are independent on any asymmetry coming from CP violation, but that are sensitive to detector asymmetries, in order to check any induced effect. To formalize this we can rewrite the matrix element parameterizing the acceptance[5] contributions as:

$$f(U) = (1 + gU) \cdot F(U) \cdot G(U) \tag{5.19}$$

where for simplicity, the matrix element expansion has been stopped at the linear term. The function F(U) is the *field dependent factor*; it represents the detector asymmetry introduced by the spectrometer magnetic field (in particular when it is coupled with the Blue Field). For this reason there are two different functions $F^{\uparrow}(U)$ and $F^{\downarrow}(U)$ according to the B field. In the same way the function G(U) is the *geometry dependent factor*, introduced to represent the detector asymmetry between the left and the right side. According to the definitions above there are two G functions: $G_S(U)$ for $B(\uparrow)K^+$ and $B \downarrow K^-$, $G_J(U)$ for $B \downarrow K^+$ and $B(\uparrow)K^-$.

[5]We are neglecting the achromat component because we want make the point on the central detector asymmetry.

Exploiting the eq. (5.19), six kinds of ratios can be constructed:

$$R_S = \frac{B(\uparrow)K^+}{B(\downarrow)K^-} = \left(1 + \frac{\Delta g}{1 + gU + hU^2}\right)\frac{F^\uparrow(U)}{F^\downarrow(U)} \tag{5.20}$$
$$R_J = \frac{B(\downarrow)K^+}{B(\uparrow)K^-} = \left(1 + \frac{\Delta g}{1 + gU + hU^2}\right)\frac{F^\downarrow(U)}{F^\uparrow(U)}$$

$$R_+ = \frac{B(\uparrow)K^+}{B(\downarrow)K^+} = \frac{F^\uparrow(U)G_S(U)}{F^\downarrow(U)G_J(U)} \tag{5.21}$$
$$R_- = \frac{B(\uparrow)K^-}{B(\downarrow)K^-} = \frac{F^\uparrow(U)G_J(U)}{F^\downarrow(U)G_S(U)}$$

$$R_\uparrow = \frac{B(\uparrow)K^+}{B(\uparrow)K^-} = \left(1 + \frac{\Delta g}{1 + gU + hU^2}\right)\frac{G_S(U)}{G_J(U)} \tag{5.22}$$
$$R_\downarrow = \frac{B(\downarrow)K^-}{B(\downarrow)K^+} = \left(1 - \frac{\Delta g}{1 + gU + hU^2}\right)\frac{G_S(U)}{G_J(U)}$$

The quantities defined in eq. (5.20) are the same (apart from the achromat polarity) as defined in the eq. (5.13). For this we refer to the term in parenthesis as the *physical term* that contains the CP violation observable Δg. The meaning of the additional factors (ratios of field dependent factors) is that the single ratios, R_S and R_J, are biased if magnetic fields influence on different way the K^+ and the K^- U distributions. In the eq. (5.20) the factor G(U) cancels out because the single ratios are constructed to involve the same side of the detector. In the R_+ and R_-, defined by eq. (5.21) the physical terms cancel out because the ratio is done between same kaon sign. The result is a combination of field and geometry dependent factors. The numerator and the denominator in the latter eq. (5.22) are collected at the same time, with the same field; for this reason the factor F(U) goes away.

By using these 6 ratios it is possible to define 3 independent *double ratios* in the following way:

$$R_{SJ} = R_S \cdot R_J = \frac{B(\uparrow)K^+}{B(\downarrow)K^-} \cdot \frac{B(\downarrow)K^+}{B(\uparrow)K^-} = (1 + \frac{2\Delta g}{1 + gU + hU^2}) \tag{5.23}$$

$$R_{+-} = R_+ \cdot R_- = \left(\frac{F^\uparrow(U)}{F^\downarrow(U)}\right)^2 \tag{5.24}$$

$$R_{\uparrow\downarrow} = R_\uparrow \cdot R_\downarrow = \left(\frac{G_S(U)}{G_J(U)}\right)^2 \tag{5.25}$$

The eq. (5.23) corresponds to the eq. (5.15) and it allows to extract the Δg without any bias due to the left-right asymmetry of the detector and the inversion of the magnetic field. The other two double ratios, eq. 5.24 and 5.25, are sensitive to the detector asymmetry only and we will use these "fake" asymmetry to check the detector asymmetry.

5.4 LKr and DCH corrections in the asymmetry measurement

As discussed in chapter 4 several kind of corrections are applied at different stages during data reconstruction and in the analysis. Most of these corrections have not direct influence in the asymmetry measurement because they are intrinsically charge independent. Anyway the coupling of some of these effects with the acceptance asymmetries could introduce systematics biases. The most sensitive observable to study the contribution of the possible effects is the shape of the distribution in reconstructed kaon mass. Thanks to the fact that the U variable is intrinsically charged independent being constructed only with the gammas informations, any bias on the charged part of the decay becomes relevant only through the kaon mass cut and, then, the selection acceptance. For instance the presence of the Blue field (see par. 4.5) introduces a small splitting between the K^+ and K^- masses, that could not be corrected with the inversion of the spectrometer field. For the same reason also the spectrometer internal misalignment, compensated with the α and β correction (see par. 4.4), introduce a charged dependent splitting between K^+ and K^- masses. This last effect is negligible in most of the 2003 data, due to the small value of the correction. Anyway it is relevant in about half of the SS-1 but for uniformity reason the correction is applied to the whole Run[6]. The calorimeter corrections play a marginal role in the asymmetry measurement. In fact in this case, in spite of the fact that the U distribution is constructed using the LKr informations, the neutrality of the gammas assures that any effects can contribute only from the acceptance definition. The LKr misalignment[7] (see par. 4.3) in particular cannot change the angle between the π^0 and then the value of the U variable. The change of the angle between the charged pion and the neutrals could introduce only effect on the kaon mass. The effect of the LKr shift partially compensates the Blue field effect for some field and kaon charge configuration but not for the other configuration. This is an example of coupling of two effects that could give a sizable contribution (through the acceptance) to the systematic error if they are not corrected. The LKr imperfect projectivity has to be suitably compensated (see par. 4.2) because, depending on the vertex position and the angle of the photons on the LKr, it affects the reconstructed U value. The coupling of this with any acceptance asymmetry between K^+ and K^-, could generate a systematic contribution to the measurement. In the fig. 5.5 it is possible to see the effect of these corrections on the Δg value, changing the cut on the reconstructed kaon mass, with and without the corrections discussed above. The corrections allow to reduce the contribution to the systematics error due to the acceptance of the analysis cuts, as will be describe below.

[6]In the analysis of the charged mode, $K^{\pm} \to \pi^{\pm}\pi^+\pi^-$, the α and β correction is most important, both for the cut on the kaon mass and the fact that the U distribution is constructed using the spectrometer only.

[7]There is no way to say if the misalignment is due to a real LKr or spectrometer shift. With LKr misalignment we mean a relative misalignment between the two detectors assuming, arbitrarily, the spectrometer in nominal position.

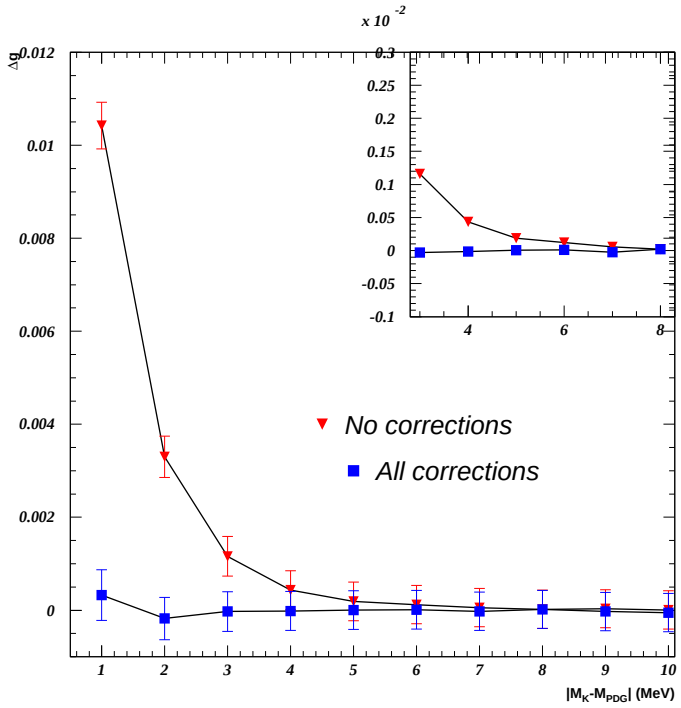

Figure 5.5: Dependence of the Δg value on the cut on the reconstructed kaon mass with respect to the nominal kaon mass: $|M_K - M_{K,PDG}| < N \cdot (MeV)$, where N is the cut value on the X axis. In the included plot a magnification of the central region is shown. The value chosen for the final determination of Δg is N=6

5.5 MonteCarlo

Thanks to the simultaneous collection of K^+ and K^- decays and the cancellation of the detector acceptance differences, our measurement does not need MonteCarlo simulation. Nevertheless a very detailed GEANT-based [105] MonteCarlo has been developed in order to check the sensitivity of the result to various systematic effects. This MonteCarlo, called **CMC** (Charged Monte Carlo), includes:

- Complete description of the detector geometry and data reconstruction.
- Detailed simulation of the kaon beam optics and transport, through the achromat and beam line.
- Simulation of the "blue field" in the decay region.
- Simulation of the beam movement according to the measurement of the beam position obtained directly from the real data.
- The spectrometer simulation includes the change of each single wire efficiency during the run and the change in the misalignment; the measured position of the dead cells in the LKr is also included.

- Interaction of the particles with the matter, pion decay in flight and other physical effects are included in the simulation.
- The CMC output can be changed according to the various data formats (see 3.1) in order to use the same analysis tools that in the real data analysis.

The electromagnetic shower simulation in the LKr is based on shower libraries in order to increase the speed of the MonteCarlo production. For this reason CMC does not reproduce the tails of the E/p for electron or the energy deposition of the pions. For the same reason the MonteCarlo is not suitable to describe the overlap between the photon and the pion cluster.

Thanks to the fact that CMC includes the whole time dependent description of the beam behaviour and the DCH efficiency, the agreement between data and MonteCarlo is very satisfactory as, for instance, it is possible to see in the plot 5.6, in which the comparison is made, between CMC and the real data, for the X coordinate of the beam position (averaged in a run) at level of DCH1 as a function of the run number. As we will see in the next chapters, the CMC simulation is used in order to check the result and to study the systematics but not to apply correction to the distributions. Another very fast C++ based MonteCarlo has been employed in order to study possible biases, with a very large statistics. This MonteCarlo, called **Flyo** [106], includes the detector geometry with a parametrization of the resolution in the various sub-detector, the interaction of the particles with the matter, the earth magnetic field and other effects with a sufficient precision to give reliable results.

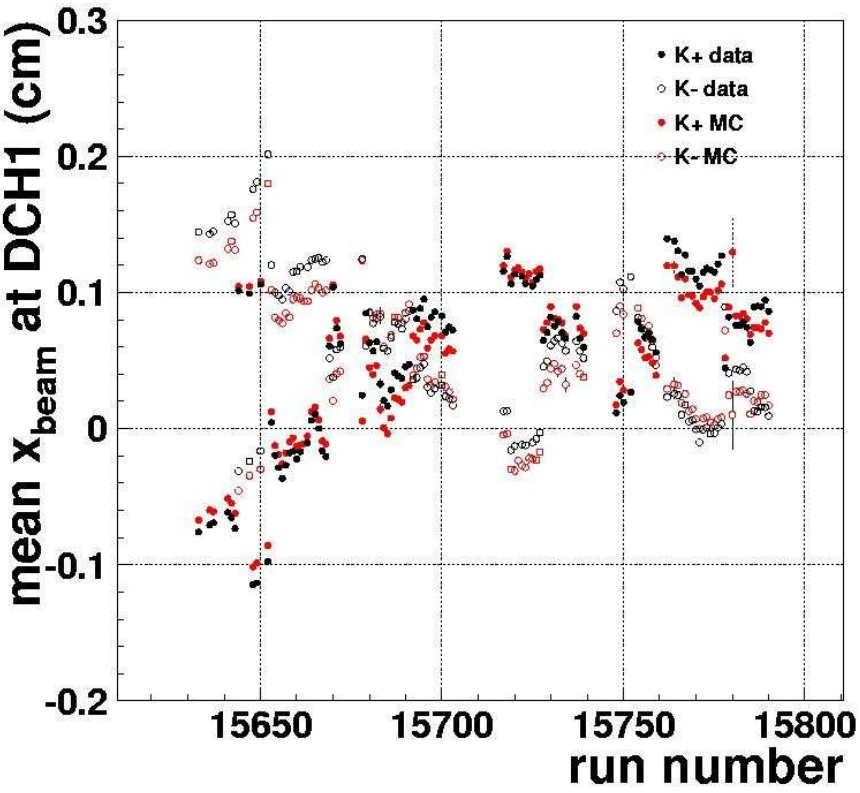

Figure 5.6: The CMC MonteCarlo is able to reproduce beam movements during the run below 1 mm level. The agreement between data and MonteCarlo is very satisfactory.

Chapter 6

The $\triangle g$ measurement in 2003 data

After the bad burst rejection, $\sim$ 120000 good bursts are used for the asymmetry measurement. The quality of the data is checked as a function of several kinematical variables during the run. The periods with unstable trigger conditions are excluded from the final analysis, special care is adopted in order to symmetrize the geometrical distribution of the charged L1 trigger component during the last SuperSample. The final result based on $\sim 47 \cdot 10^6$ $K^{\pm} \to \pi^{\pm}\pi^0\pi^0$ decays collected in the 2003 data taking is:

$$A_g = (1.8 \pm 2.2_{stat}) \cdot 10^{-4}$$

6.1 Bad Bursts in 2003

All the read out systems are checked stand alone in order to define the quality of the data taking. A burst is rejected if the Drift chambers (DCH) or the LKr read out does not work properly or in case any other part of the trigger system fails (the Hodoscope (HODC), the neutral trigger (NUT), the trigger chain status register (PMB) or the Mass box (MBX)). In addition the **PHYS** bad burst is defined if in the burst there are less than 1000 events in the standard 3 charged π loose selection (HyperCompact selection) due to very small beam intensity (for accelerator or beam line transport problems) and/or a general trigger malfunctioning[1]. The runs that are flagged as "test" or problematic for some know failure of some part of the detector or completely empty, are excluded through the PHYS bad burst flag. In fig. 6.1 the statistics reduction due to the bad burst selection is shown. More than 11K bad burst are excluded out of 130K burst collected. The reasons in the various SuperSamples are different: in the SS1 the MBX and DCH bad burst rejection is more relevant while in the SS2 most of the burst are excluded due to the NUT failure. The amount of bad burst in each category is summarized in fig. 6.2.

6.2 Quality of the data

In order to check the quality of the data several kinematical quantities are computed during the run. The reconstruction of the kaon mass is a good indication of the

[1]Usually there are $\sim$ 11000 good $K^{\pm} \to \pi^{\pm}\pi^+\pi^-$ per burst.

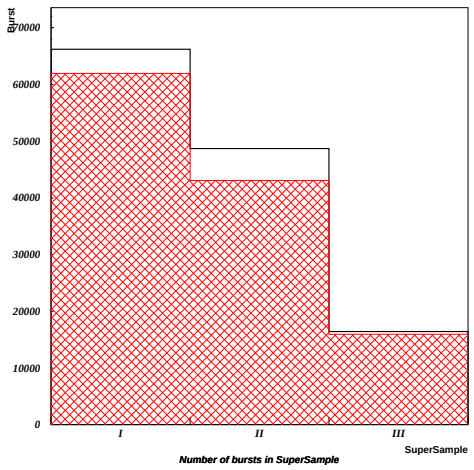

Figure 6.1: Reduction (in red) of the burst statistics in the SuperSample (total reduction $\sim 10\%$)

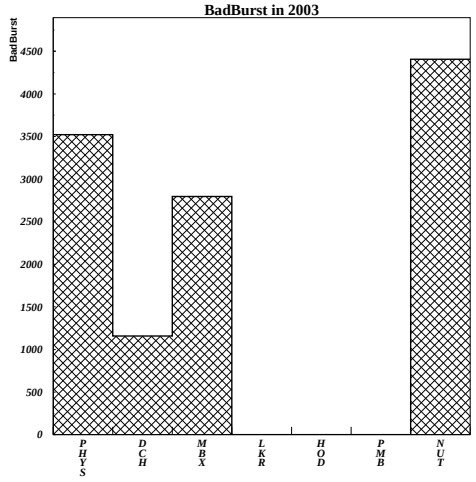

Figure 6.2: Conditions to flag a burst as bad burst. Most of MBX and DCH bad burst are located in SS1 while the NUT bad bursts are concentrated in SS2.

relative detectors miscalibration (fig. 6.3). After all the corrections presented in the chap. 4 the averaged kaon mass value is (493.65 ± 1.00) MeV, ~ 25 KeV away from the PDG central value[2]. The COG (Center of gravity) is a good beam stability indicator (fig. 6.4 and 6.5). More than the precise alignment along the beam line direction, differences between the K^+ and K^-, COG position could be a signal of variation of acceptance.

In the same way a good indicator of the beams behaviour is the ratio K^+/K^- (fig. 6.6) . The final result is insensitive to the relative ratio between the two charged kaon, but a big fluctuation with respect to the standard value will be a signal of problems in the beam transportation line.

The plot 6.7 shows the statistics collected as a function of the run number after bad burst rejection. The study of the trigger efficiency during the run is a important tool to discover problem in the data acquisition. The topic of the trigger efficiency will be covered in detail later; in the next sections two problems in the trigger chain will be discussed for which special care in the definition of the sample useful for the asymmetry measurement is needed.

6.2.1 NTPEAK problem

During a part of the data taking, in SS2, the neutral component of the trigger (NTPEAK), which exploits only informations from the LKr calorimeter, was less efficient and its behaviour was labelled "problematic" in the run book. In the standard period the L1code0, that is essentially Q1*NTPEAK, is the main strobe of the L2 1TRK-P algorithm and only a small part of events fires the Q2 signal (L1code2). Due to a technical problem (from run 15652 to run 15753) the NTPEAK

[2]The discrepancy is due to γ conversions and is totally irrelevant for the asymmetry measurement purpose.

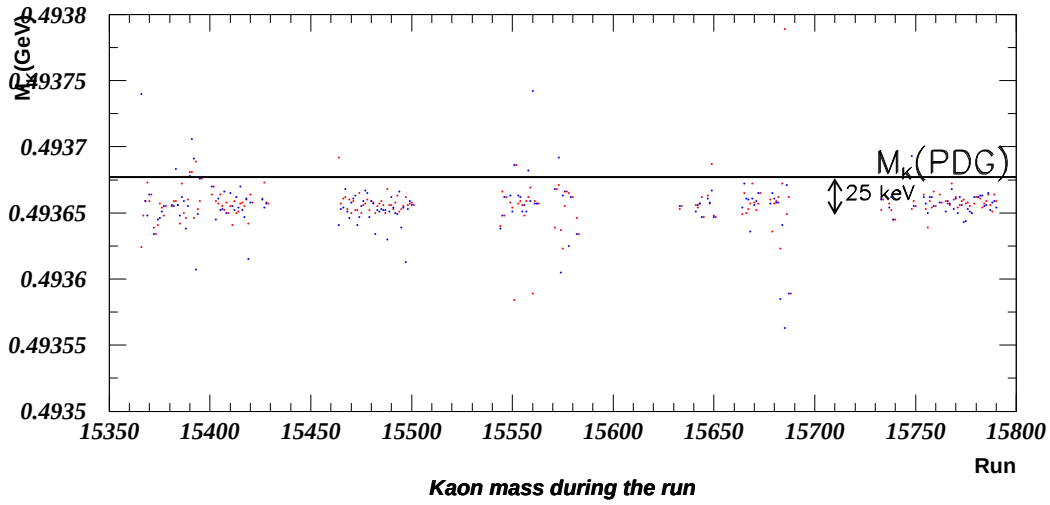

Figure 6.3: Reconstructed kaon mass in the "neutral" mode. After all the corrections the negative (blue) and positive (red) kaon masses are the same.

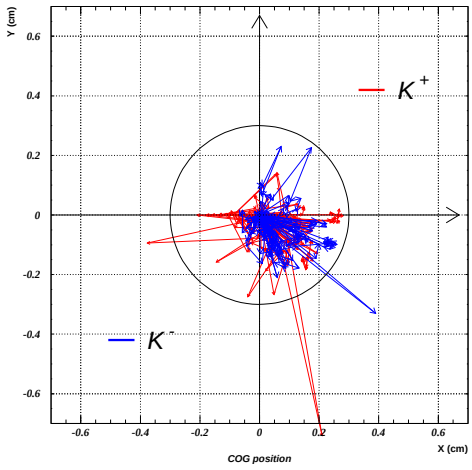

Figure 6.4: Position of the center of gravity (COG) in the transverse plane at LKr level. Each point is obtained as average in a single Run. During the whole data taking the COG (both in K^+ and K^- decays) is quite stable around the center of the detector.

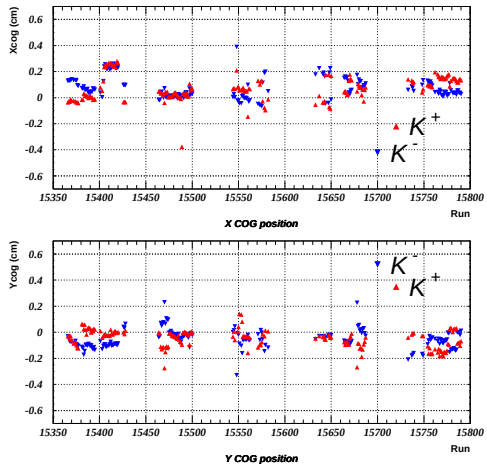

Figure 6.5: Both in X and Y direction the COG displacement is below $\sim 2mm$ during the whole 2003 Run. Effect of the achromat inversion and beams steering are visible in both projections.

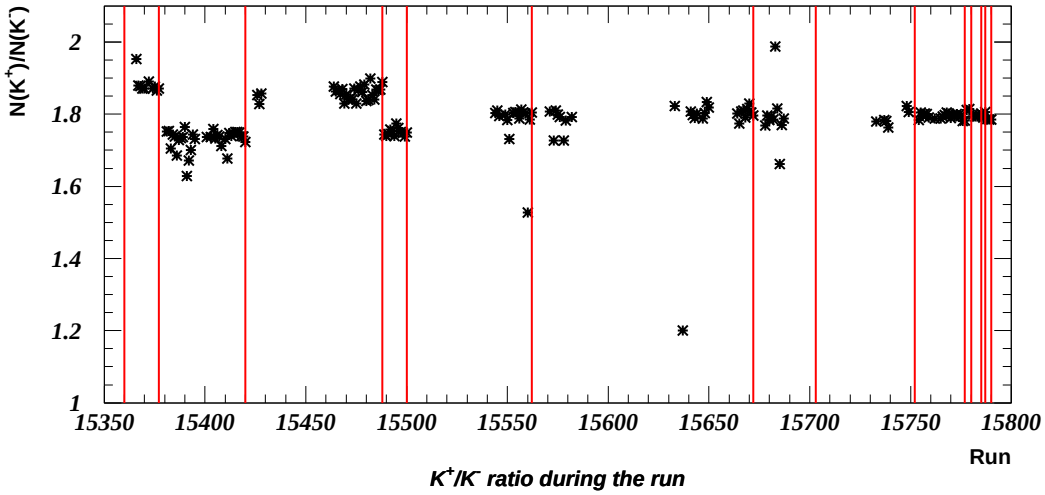

Figure 6.6: N(K^+)/N(K^-) ratio. The difference is due to the production process. In the first part of the run the effect of the achromat inversion (red lines) is quite evident, while after a better beams focusing the ratio becomes insensitive to the path follows in the achromat.

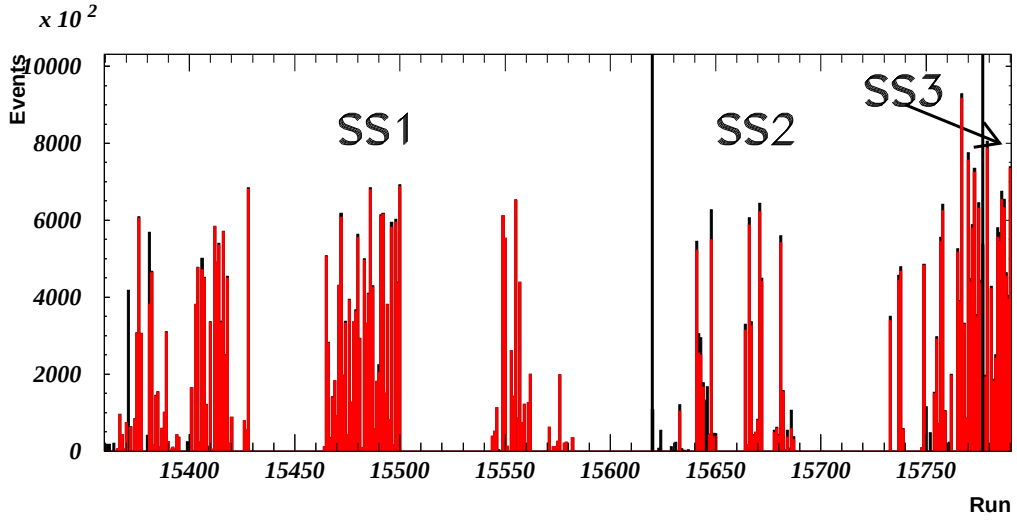

Figure 6.7: Statistics collected during the run. In red the events collected after bad burst selection (total reduction $\sim 5\%$).

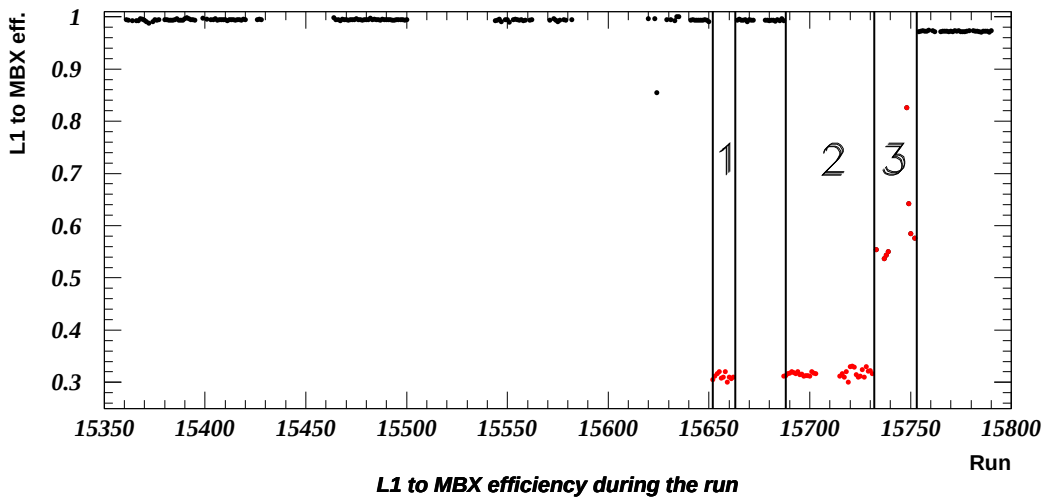

Figure 6.8: NTPEAK trigger problem. Before the problem the L1 to MBX (L1code0) inefficiency was $\sim 0.7\%$. In the two periods [15652-15663] and [15688-15732] the inefficiency increases to $\sim 70\%$ (the NTPEAK has been switched off from the L1, the plot shows the Q2*!AKL efficency) while in the period [15733-15753] was $\sim 40\%$ because the Y projection has been included in the L1code0. After the problem fix the inefficiency was stable but higher than in the begin ($\sim 3\%$).

has been switched off from the L1 to avoid the saturation of the readout during the periods indicated with 1 and 2 in fig. 6.8 (during the period 3 the efficiency has been partially recovered using only the NTPEAK Y view). In those periods the main strobe to the 1TRK-P comes from the code 2. For that reason most of the events collected ($\sim 98\%$) have two hits in the hodoscope. There are two reason for which an event with one single charged track expected could have two charged hits in the hodoscope: an accidental particle[3] or a photon conversion. A detailed CMC simulation [107] shows that most of this kind of events comes from photon conversions on the DCH flanges, beam pipe, AKL and Kevlar windows. The kinematics of this events is different with respect to the standard ones distorting the recostructed quantities as the Kaon mass ($\sim 30 KeV$ higher that in the events without conversions) and the U distribution. The detector acceptance is different and could, in principle, introduce a bias in the asymmetry measurement. Anyway due to the fact that the conversion affects in the same way the positive and negative kaon, the bias on the asymmetry is quite small ($\sim 0.6 \cdot 10^{-4}$ of difference including or excluding the Q2 events). To work with a cleaner sample and to avoid to put an additional (small) systematic error we prefer to exclude the whole bad NTPEAK period (the periods 1 and 2). This gives an increase of the total statistical error of $\sim 6\%$ after a re-arrangement of the SuperSample definition to balance the field

[3]Usually the parallel muon aren't recostructed from the spectrometer due to the condition described in par. 3.3.1 (fig. 3.2).

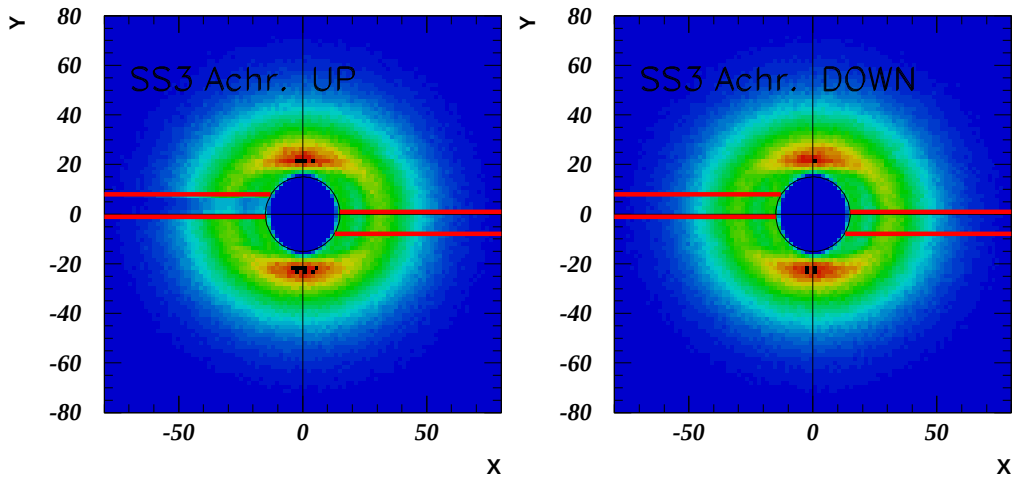

Figure 6.9: During the first part of the SS3 (achromat UP) (in the left) the charged hodoscope was less efficient in an horizontal slab. The counter involved in this problem has been excluded offline in the whole SuperSample together with the counter symmetric with respect to the center of the detector (red lines in the figures).

inversion periods.

6.2.2 CHOD problem

In the first part of the SS3 (during the UP polarities of the achromat) one horizontal counter in the charged hodoscope was less efficient due to a problem with the HV supply (fig. 6.9). The effect is an increasing in the L1 trigger inefficiency[4]. In addition, being this inefficiency highly localized in a particular zone of the detector acceptance and unstable in time, it could be a source of an effect that is not cancelled in the left-right compensation in the quadruple ratio. In order to equalize the L1 trigger acceptance different kinds of cuts have been studied looking to the influence on the Δg measurement in Data and MonteCarlo. In the fig. 6.10 three possible options to implement the balanced cut are shown. The Δg in the SS3 is not sensitive to the cut chosen as it is shown in the table 6.1, where the asymmetry is computed with the various cut applied in the Achromat UP period (where the problem is present) or in both the achromat periods (the whole SS3). It is possible to see that the cancellation of the left-right $(A_J - A_S)$ asymmetry is obtained, both in data and in MonteCarlo, only if the cut is applied in both the achromat polarities. The statistical reduction, in SS3, due to the "crossed" cut is $\sim 7.7\%$ while with the "double" cut is $\sim 15.3\%$, for this reason the former is preferred to the latter. The "crossed" cut is preferred to the "single" cut, because is, in principle, more symmetric with respect to magnetic field inversion.

[4]The trigger inefficiency measurement and systematics will be discussed in the chapter 8.

Cut	A_{JS} (data)	$A_J - A_S$ (data)	A_{JS} (MC)	$A_J - A_S$ (MC)
no cut	-0.8 ± 8.0	-6.6 ± 8.0	-3.4	-0.3
Single ($A \uparrow$)	-1.9 ± 8.1	-14.5 ± 8.1	-2.3	-9.5
Single ($A \uparrow\downarrow$)	0.2 ± 8.2	-3.7 ± 8.2	-3.0	-0.2
Double ($A \uparrow$)	-0.2 ± 8.2	-25.0 ± 8.2	-2.9	-19.0
Double ($A \uparrow\downarrow$)	-1.8 ± 8.4	-3.9 ± 8.4	-3.4	-1.0
Crossed ($A \uparrow$)	-0.1 ± 8.1	-15.0 ± 8.1	-2.8	-10.1
Crossed ($A \uparrow\downarrow$)	-1.8 ± 8.2	-3.9 ± 8.2	-3.2	-0.3

Table 6.1: Various cuts effect on asymmetry in SS3. The error in the MC is the same that in the real data. All the numbers are given in unit of 10^{-4}.

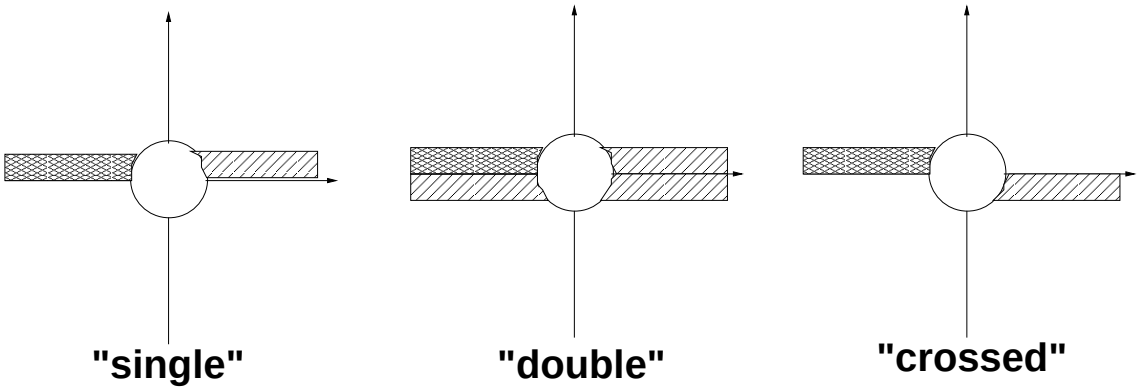

Figure 6.10: Three possible cut solutions (*single*, *double*, *crossed*) to exclude the inefficient part of the charged hodoscope. The crossed cut is chosen to minimize the systematic contribution of the cut giving also a small contribution in the statistical reduction.

6.3 The results

In the whole 2003 data taking (from June,22 2003 to September,7 2003) more than $47 \cdot 10^6$ kaon decays in the "neutral" mode has been collected. This, together with the similar amount collected during the 2004 data taking, represents by far the largest sample of fully reconstructed $K^{\pm} \to \pi^{\pm}\pi^0\pi^0$ ever collected. In the table 6.2 the detailed statistics is presented with the number of events observed in the various categories of achromat, magnetic field and kaon charge. The final ratio between positive and negative kaon charge (~ 1.8) is just the reflection of the difference in the kaon production at the target level, while in the other categories some care has been adopted in order to equalize (as better as possible) the statistics. The plot 6.11 shows the fit in the three SuperSamples with the quadruple ratio technique while in the table 6.3 the obtained results on Δg are presented. The results on the double ratio component as defined in the previous chapter are also shown. The final result:

$$\Delta g(2003) = (2.3 \pm 2.8) \cdot 10^{-4}$$

is obtained with *weighted average* between three independent measurement performed in three SuperSamples. By using the relation (1.78) and the present value of

the linear slope [4] ($g = 0.638 \pm 0.020$) the asymmetry parameter is [108]:

$$A_g = (1.8 \pm 2.2_{stat}) \cdot 10^{-4}$$

where only the statistical error is shown. In the next chapters the systematic error will be discussed.

Category	SS1	SS2	SS3	2003 data sample
$\mathbf{A}(\uparrow)\mathbf{B}(\uparrow)K^+$	4762877	3546522	826393	9135792
$\mathbf{A}(\uparrow)\mathbf{B}(\uparrow)K^-$	2571080	1973212	459581	5003873
$\mathbf{A}(\uparrow)\mathbf{B}(\downarrow)K^+$	3791738	2634354	1015361	7441453
$\mathbf{A}(\uparrow)\mathbf{B}(\downarrow)K^-$	2070495	1471747	568689	4110931
$\mathbf{A}(\downarrow)\mathbf{B}(\uparrow)K^+$	3719563	2315624	631165	6666352
$\mathbf{A}(\downarrow)\mathbf{B}(\uparrow)K^-$	2124639	1285831	348000	3758470
$\mathbf{A}(\downarrow)\mathbf{B}(\downarrow)K^+$	4176158	1691672	1249374	7117204
$\mathbf{A}(\downarrow)\mathbf{B}(\downarrow)K^-$	2395389	941154	694800	4031343
$\mathbf{A}(\uparrow)$	13196190	9625835	2870024	25692049
$\mathbf{A}(\downarrow)$	12415749	6234281	2923339	21573369
$\mathbf{B}(\uparrow)$	13178159	9121189	2265139	24564487
$\mathbf{B}(\downarrow)$	12433780	6738927	3528224	22700931
K^+	16450336	10188172	3722293	**30360801**
K^-	9161603	5671944	2071070	**16904617**
Total	25611939	15860116	5793363	**47265418**

Table 6.2: The whole statistics collected in the 2003 data taking subdivided in three SuperSamples. The last row shows the integrated events in the various categories.

	SS1	SS2	SS3
Δg_s	10.7 ± 5.3	2.2 ± 7.1	-5.0 ± 11.1
Δg_j	-2.5 ± 5.3	-1.8 ± 6.9	-0.5 ± 11.8
Δg_d	-2.4 ± 5.4	-0.8 ± 7.7	-0.3 ± 11.8
Δg_u	11.3 ± 5.2	1.1 ± 6.2	-5.1 ± 11.2
Δg	4.3 ± 3.8	0.3 ± 4.9	-1.8 ± 8.2
$\Delta g(2003)$		2.3 ± 2.8	

Table 6.3: Asymmetry results. All the numbers are expressed in unit of 10^{-4}. Only the statistical error is shown.

6.4 Detector asymmetry

In the par. 5.3 it has been discussed how several quantities can be defined in order to quantify and study the possible asymmetries of beam line or detectors. In particular the ratios defined by eq. (5.24) and (5.25), in which any possible physical asymmetries cancel, are directly sensitive to the field inversion factor and to the left

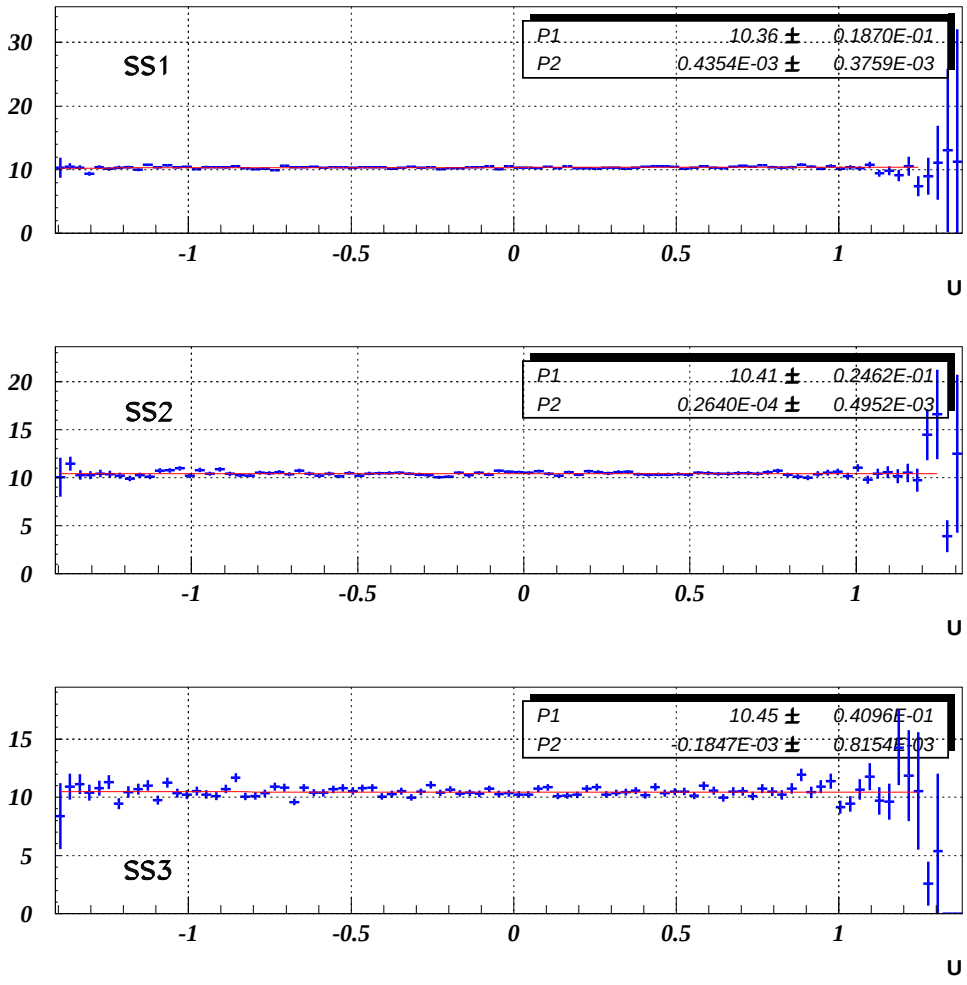

Figure 6.11: Final quadruple ratio in each SuperSample.

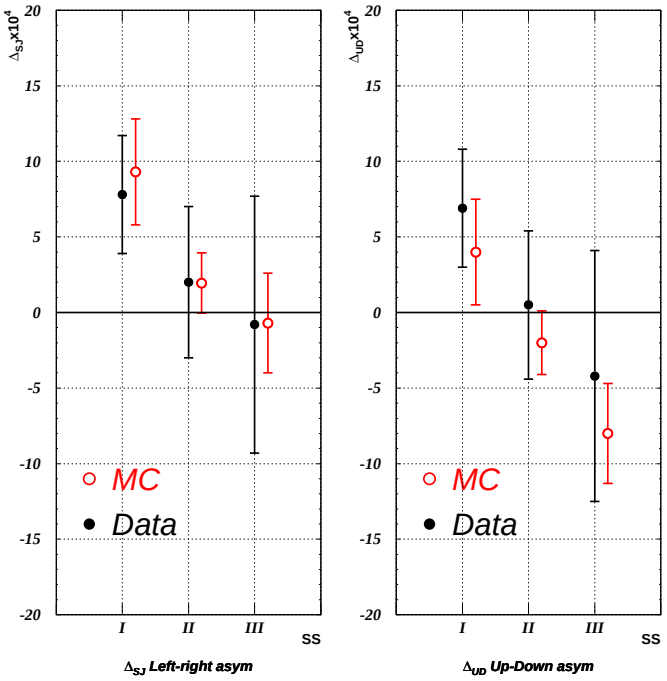

Figure 6.12: The agreement between the detector asymmetries in data and in MonteCarlo is a good indication that no unpredictable effects are present in the measurement.

and right asymmetry factor. In the table 6.4 the results are obtained for the two different achromat polarities with a linear fit. Most of the asymmetries are within

	SS1	SS2	SS3
A_{+-} (Achr. $\uparrow$)	7.8 ± 10.2	1.2 ± 11.9	-28.4 ± 21.8
A_{+-} (Achr. $\downarrow$)	12.5 ± 10.4	11.9 ± 14.8	26.9 ± 22.6
$A_{\uparrow\downarrow}$(Achr. $\uparrow$)	2.8 ± 10.2	14.0 ± 11.9	53.7 ± 21.8
$A_{\uparrow\downarrow}$(Achr. $\downarrow$)	22.9 ± 10.4	23.8 ± 14.8	22.0 ± 22.6

Table 6.4: Detector asymmetries. All the numbers are in unit of 10^{-4}.

2σ from 0. Another way to study the contribution of the detector asymmetries is to use the CMC MonteCarlo, in which the critical time dependent effects, as drift chambers wires inefficiency or beam geometry, are well simulated. The asymmetries (Δg) extracted from the double ratios component of the quadruple ratio, eq. (5.14) and (5.16), define the two quantities:

$$\Delta g_{JS} = \frac{\Delta g_J - \Delta g_S}{2} \tag{6.1}$$

$$\Delta g_{UD} = \frac{\Delta g_U - \Delta g_D}{2} \tag{6.2}$$

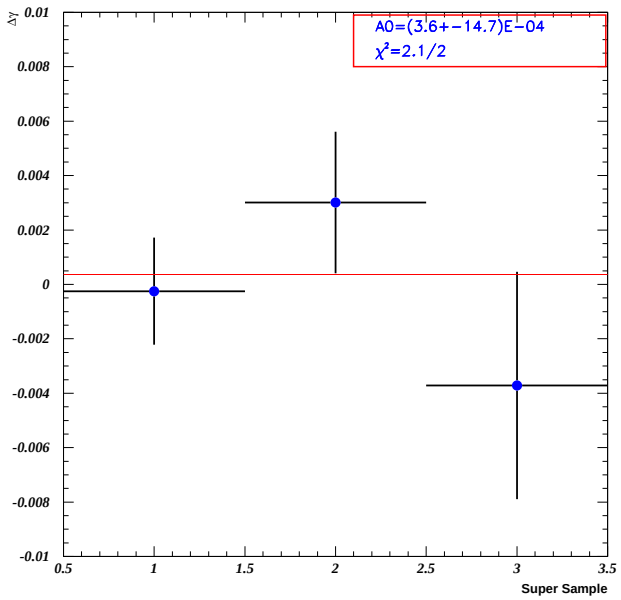

Figure 6.13: $\Delta\gamma$ asymmetry. The fact that $\Delta\gamma$ is compatible with 0 is a cross check of the Δg measurement.

We prefer to use these quantities, instead of the "fake" asymmetries used on the data as in the table above, because in spite of the fact that the meaning of these is not so clear as in the eq. (5.24) and (5.25), they are directly related to the cancellations that we have in the quadruple ratio. In plot 6.12 the good agreement between data and MonteCarlo means that the detector asymmetries are under control.

6.5 Slope V asymmetry

The asymmetry measurement in the Dalitz Plot V projection (defined in eq. (1.53), can be also written as $V = \frac{2m_K}{m_\pi^2}|E_1^* - E_2^*|$ where E_1^* and E_2^* are the CM energy of the two neutral pions.) is a cross check of the procedure. Indeed, as we know, due to the Bose symmetry, the V linear coefficient of the matrix element expansion is zero; no asymmetry can be detected along this direction. To verify that, we use the same procedure with respect to the Δg calculation, assuming the following matrix element expansion:

$$|M^{\pm}(U,V)|^2 \sim 1 + gU + \gamma|V| + hU^2 + kV^2 + ...$$

where the next parameter, γ, represents the linear slope along the V direction. The quadruple ratio is defined as in eq. (5.17) but by using the V projections instead of the U projections:

$$R_4(V) = R_{us}(|V|)R_{uj}(|V|)R_{ds}(|V|)R_{dj}(|V|)$$

The fact that γ is small (in principle is 0) allows to use the linear function $1+\Delta\gamma V$, to extract the asymmetry in the linear component of the V projection. In fig. 6.13 the result for each SuperSample is shown. The final result, $\Delta\gamma = (3.6 \pm 14.7) \cdot 10^{-4}$, is compatible with no asymmetry in the V projection, as expected.

6.6 The U2 asymmetry measurement

In par. 5.1 we have seen that the U variable could be measured in two independent ways: with the LKr (U1 definition) and with the spectrometer (U2 definition). The first method is, in principle, more *straightforward* because only the neutral π^0's are involved directly into the measurement and the charged pion only contributes through the signal acceptance. Another reason to prefer the first definition is the resolution of the U variable. In plot 6.14, obtained with the CMC MonteCarlo, the difference between the resolutions is shown. In the U1 case the resolution is better in the left part of the Dalitz plot, where we have big acceptance and big fit lever arm, in the U2 case the best resolution is in the right side, which is strongly affected by low values for the acceptance (fig. 5.3). This could be also seen in the comparison between the two U distributions in fig. 6.15, where the smearing effect of the bad resolution is present in the opposite side of the physical range. By using the same procedure described above, it is possible to extract the asymmetry parameter Δg in a different way. The fitting limits for the U2 ratios have to be restricted in the $[-1:1]$ range, because the different contribution of detector effects at the border of the Dalitz plot. In the table 6.5 the results obtained are shown. As is also evident from the plot 6.16 the results are in good agreement within the statistical error. The systematic difference is due to the presence of different systematic contributions.

	U1	U2
SS1	7.5 ± 5.9	10.3 ± 5.9
SS2	-0.5 ± 7.7	6.9 ± 7.7
SS3	1.3 ± 12.6	6.1 ± 12.6
Tot	4.2 ± 4.4	8.7 ± 4.4

Table 6.5: Δg results for U1 and U2 assuming -1. and 1. as fitting limits, to avoid fitting problems in the U2 ratios. The results by using the two different U definitions are fully compatibles.

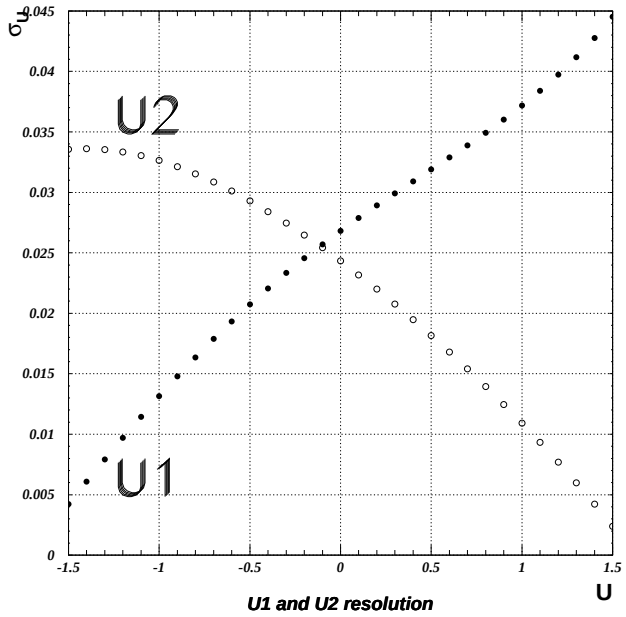

Figure 6.14: Comparison of U1 and U2 resolution. The best U1 resolution is in the left part while the best U2 resolution is in the right part of the Dalitz plot.

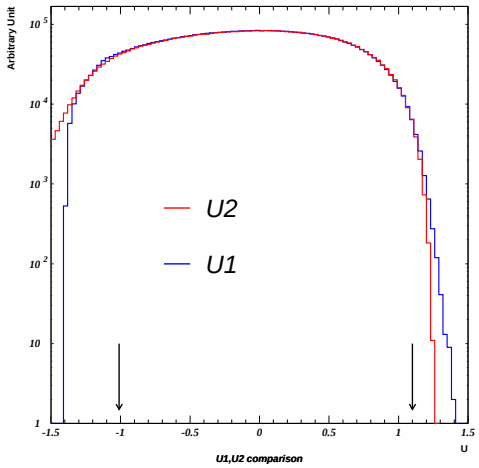

Figure 6.15: Comparison between U1 and U2 distributions.

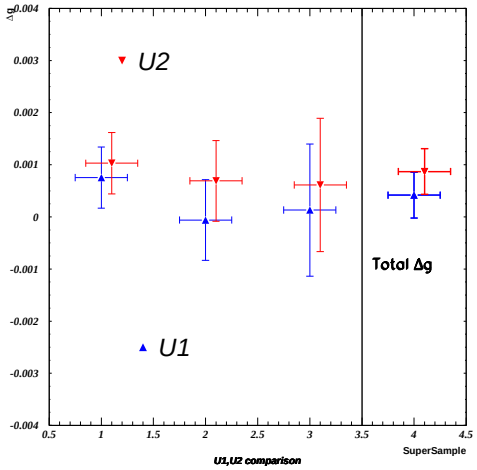

Figure 6.16: Comparison between the Δg obtained with the two U definitions in the various SuperSamples and total asymmetry.

Chapter 7

Systematic effects study

The control of the systematic error below the level of the statistical one, it is a crucial point in the experimental technique. Thanks to the simultaneous collection of two kaon charges and acceptance equalization obtained inverting the main magnetic fields, no effect is expected to introduce systematic uncertainties at first order. Contributions from the coupling of several effects are analyzed studying the final result dependence on different cuts definition and switching on and off the relevant corrections. In some case a MC simulation is employed in order to understand selection, resolution or fitting effects. The main systematic bias could come from the effects related to the hadronic shower development in the LKr (in particular the cut on the distance between charged pion impact position and the nearest gamma cluster) and from the coupling between the charged pion decay in flight and the small differences in the K^+ and K^- acceptance. The total systematic error, excluding the contribution of the trigger that will be discussed in the next chapter, is $1.0 \cdot 10^{-4}$ including the systematics uncertainty due to the error on the g slope value (external uncertainty).

7.1 General discussion

The experimental technique and the strategy of the measurement should give, in principle, a measurement free from systematics. In particular the quadruple ratio guarantees the potential instrumental asymmetries cancellation in the condition that they are stable in time or if the changes of the apparatus characteristics have a period larger than the inversion of the relevant magnetic fields. In addition only U dependent effects can give a systematic slope: the accidental activity in the LKr is an example of an improbable direct source of systematics due to this consideration. The different interaction of the charged pions with the detectors material it is, eventually, a second order effect (through the acceptance) because the "neutral" definition of the U variable (U1 definition): the charged pion is used only to tag the event and to compute the Kaon mass for the event selection.

Particular care has been devoted to check every possible systematic contributions to the asymmetry measurement. In fact coupling of different effects can introduce systematic biases. An example is the already mentioned Blue Field coupled with a small uncorrected difference between K^+ and K^- acceptance affecting the asymme-

try through the cut in the kaon invariant mass (fig. 5.5). The study of the uncertainties introduced by the coupling among small sources, is not a trivial task. For this reason it is a prudent choice to quote the final systematics error using estimates which are rather upper limit to the real systematics.

7.2 Acceptance and spectrometer systematics

In this section the acceptance related systematics will be discussed. In this category we include also the systematics due to the beam geometry and to all the effects related to the charged part of the decay, because they can influence the result only coupling with the acceptance definition.

7.2.1 Detector acceptance

The dependence of the measured asymmetry on the acceptance definition has been studied directly on the data by changing the definition of the cuts. Concerning geometrical effect the external edge of the detectors is of little relevance due to comparatively low density of tracks, while on the other hand the events with a charged pion with small kinetic energy in the CM are close to the right hand of the Dalitz Plot and tend to occupy the central part of the spectrometer. The events in this part of the Dalitz Plot have a small lever arm and hence little statistical weight in the result of the fit for the slope. In the plot 7.1, the slope asymmetry Δg is plotted changing the lower limits of the radial cut at the DCH1. The uncorrelated part of the error in the blue point is shown with respect to the nominal cut (in red). No systematic uncertainty is assigned to this cut as well as to the LKr internal radial cut (fig. 7.2) or at DCH4. The shape of the external LKr cut has been changed without, as expected, any significant variation of the asymmetry value.

7.2.2 Beam geometry

The beam geometry systematics has been studied changing the cut on the center of gravity (COG) computed at the LKr level. The charged pion track is extrapolated from the DCH1 and the DCH2 ignoring the magnetic deflection until the LKr position; the measured spectrometer momentum and the extrapolated position are used to compute the COG. From the plot 7.3 a systematics of $0.3 \cdot 10^{-4}$ is assigned.

7.2.3 Blue tube correction systematics

The systematics due to the Blue field correction to the charged pion track is evaluated by varying artificially the measured magnetic field map used in the event reconstruction (fig. 2.9). For variation of $\pm 10\%$ from the map values, an upper limit to this systematic of $\sim 0.1 \cdot 10^{-5}$ is assigned by the measurement of the Δg variation. The same result is obtained with the MonteCarlo.

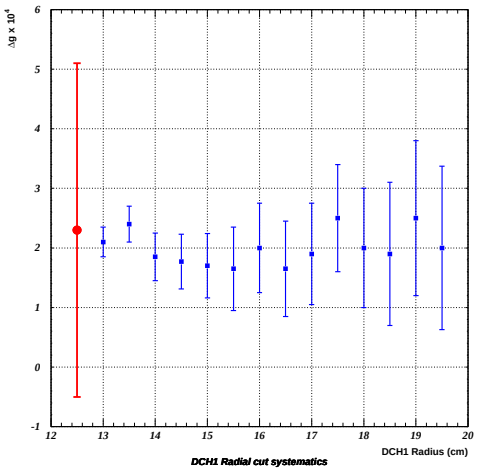

Figure 7.1: Study of the systematics due to the DCH1 radial cut. The Δg value is recomputed changing the cut on the radial position of the charged track at DCH1. The uncorrelated part of the error for each point is shown with respect to the nominal cut at 12.5 cm (in which the whole statistical error is assigned)

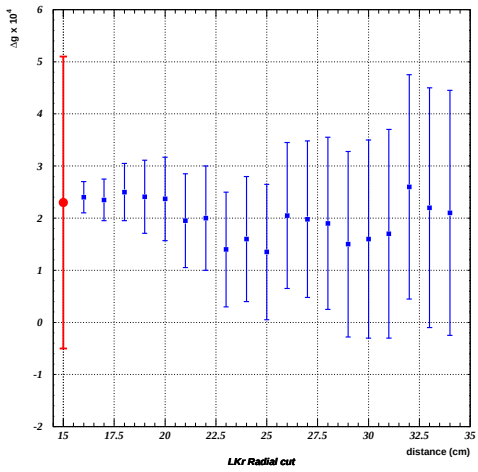

Figure 7.2: Δg dependence on the radial cut at LKr. The uncorrelated errors are referred to the nominal cut at 15 cm.

7.2.4 Spectrometer alignment and momentum scale

The spectrometer alignment and momentum scale systematics has been found negligible (below $0.1 \cdot 10^{-4}$) by studying the variation of the result removing the α and β correction. Indeed our definition of the U variable is insensitive to the charged pion momentum measurement, the only effect could appear through the cut on the recostructed kaon mass, as several times discussed. Part of the systematic discrepancy shown in the comparison between the asymmetry computed with the U1 and the U2 definition (plot 6.16) is due to this effect.

7.2.5 Mass tails cut

Discussing the importance of the corrections in chapter 5, we have already shown in fig. 5.5 the Δg dependence on the cut in the recostructed mass. In fig. 7.4 the asymmetry is recomputed as a function of the cut value on $|M_K - M_{PDG}|$, after all corrections. The nominal value of this cut is 6 MeV and all the uncorrelated errors shown are referred to this point. The scan is performed in step of 250 KeV. No systematics is assigned to the cut on the Kaon mass. This is not a trivial result because in the Kaon mass computation several effects[1] take part due to the presence of the charged pion.

[1]These effects are responsible of the asymmetric tails in fig. 3.12

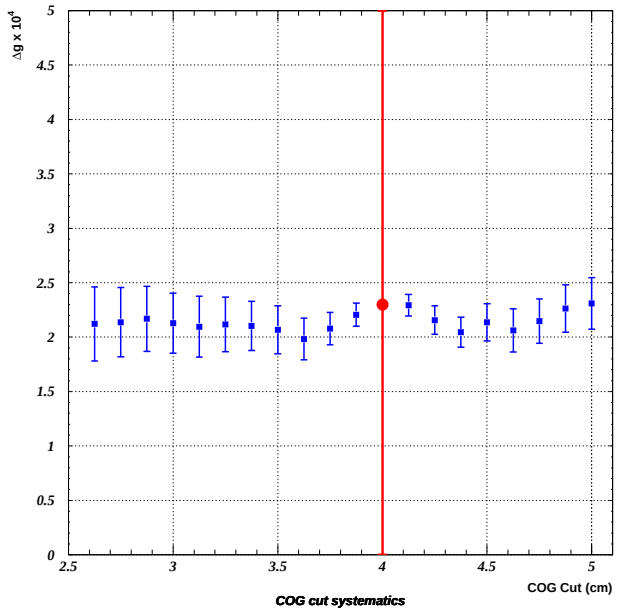

Figure 7.3: The beam geometry uncertainties are evaluated by studying the Δg value as a function of different cuts on the beam center of gravity.

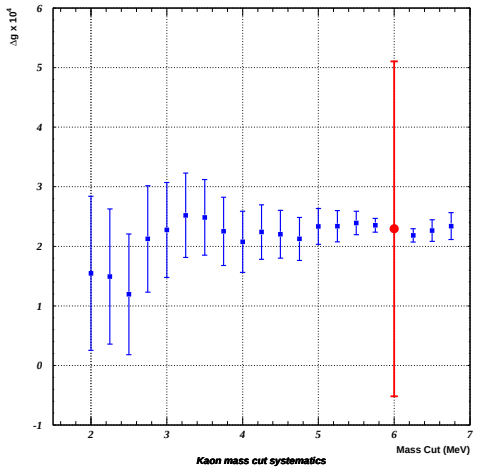

Figure 7.4: After all corrections no systematics is assigned changing the cut on $||M_K - M_{PDG}| < N(MeV)$ with respect to the standard $N = 6$.

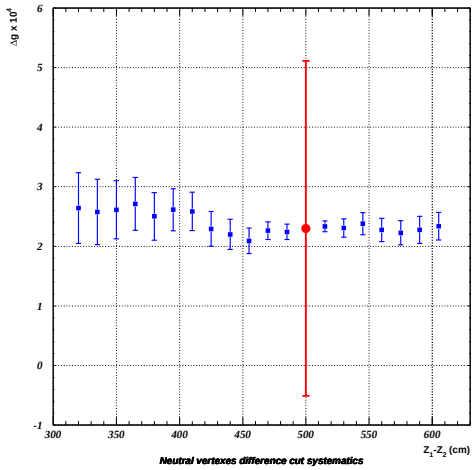

Figure 7.5: No systematics is observed changing the cut on the neutral vertexes distance with respect to the nominal cut (500 m). The uncorrelated part of the error is shown in the blue dots.

7.2.6 HOD inefficient slab

The systematics due to the cut introduced during the SS3 SuperSample (par. 6.2.2) to cope with the geometrical dependence of the Q1 inefficiency has been evaluated both in data and in MonteCarlo recomputing the Δg before and after the cut. In the experimental Δg this difference is at level of $\sim 0.8 \cdot 10^{-4}$ while in MonteCarlo is $0.1 \cdot 10^{-4}$. This small discrepancy between the two evaluations, is due to the Q1 inefficiency in the case in which no slab cut is applied in the SS3 (the L1 trigger is not simulated in the MonteCarlo). In any case due to relatively small statistics in SS3, no systematics is assigned in the final Δg result.

7.2.7 Pion decay

The $\pi \to \mu\nu$ decay is studied to exclude the possibility that the coupling with slightly different acceptance between K^+ and K^- decays, could be the source of fake asymmetry. The knowledge of any possible instrumental asymmetry is an important requirement of the Δg measurement. In general this is obtained through the study of the subdetectors behaviour exploiting the high resolution in the reconstructed quantities. In the case of the Muon Veto the resolution both in position and energy, is definitely worst. For this reason it was preferred to exclude the MUV from the analysis. A large sample of MonteCarlo has been used to compute the Δg allowing or not the pion decay: the difference does not exceed $0.5 \cdot 10^{-4}$. In fig. 7.6 the change in the asymmetry is shown as a function of the maximum Z position allowed for the pion decay (with respect to the 0 fixed in the last point). The dependence on the acceptance is the source of this systematics.

7.3 LKr related systematics

The LKr is the only detector used to construct directly the U variable. No relevant systematics is expected because of the intrinsic charge independence of the photon detection. However a different interaction of the π^- with respect to the π^+ in the Liquid Kr can perturb in different way the gammas clusters reconstruction, giving a charge dependent systematics. Resolution effects in the U measurement can generate dilution of an eventual slope (the events migration among the bins cannot generate a slope by itself).

7.3.1 Track to cluster distance cut and cluster to cluster distance

The different π^+ and π^- interaction in the LKr could be an intrinsic source of systematics giving asymmetric contribution to K^+ and K^- reconstruction. Indeed the wide hadronic shower from the π in the LKr can distort in different way the gammas clusters in K^+ and K^- decays. This can influence in different way the π^0 kinematics and the U distribution or it can introduce different acceptance in the events selection. In both cases a systematic uncertainty in the asymmetry measurement arises.

In order to avoid contamination to the energy measurement in the pure electromagnetic clusters the distance between the hadronic cluster and the nearest gamma's cluster is required to be greater than 15 cm, at level of event selection. To study the residual systematics due to this cut, the asymmetry has been analyzed as a function of this distance. From the plot 7.8 an upper limit of $0.5 \cdot 10^{-5}$ is assigned. The same systematics has been studied in a different way. The gamma cluster energy is corrected from the *extra energy* coming from the hadronic cluster. This extra energy was studied in the $K^0 \to e^{\pm}\pi^{\mp}\nu$ events during the neutral kaons program (in 2002) measuring the contamination in the electron E/P from the hadronic shower [109]. The correction factor ω to the gamma's energy,$E_{true} = \omega E_{cluster}$ is given by:

$$\omega = a_1 - (a_2 \cdot e^{-a_3 d} + a_4 \cdot e^{-a_5 d}) \qquad \text{for d} > 18 \text{ cm} \tag{7.1}$$

$$\omega = a_6 + a_7 \cdot d \qquad \text{for d} < 18 \text{ cm} \tag{7.2}$$

where d is the gamma cluster to pion impact point distance and the coefficients $a_1 = 1.999$, $a_2 = 0.333$, $a_3 = 0.12 \;\; cm^{-1}$, $a_4 = 1.0$, $a_5 = 8.04 \cdot 10^{-6} \;\; cm^{-1}$, $a_6 = 0.952$ and $a_7 = 8 \cdot 10^{-4} \;\; cm^{-1}$ are empirically deduced (correction A). This correction over-corrects somewhat the cluster energy for pion to cluster distance smaller than 30 cm (fig. 7.7). A further improvement to this correction is obtained introducing the dependency on the pion momentum (correction B) Thanks to these corrections the expected energy value is close to the measured one, for a large range of pion to cluster distance. The difference in the Δg value obtained with this correction

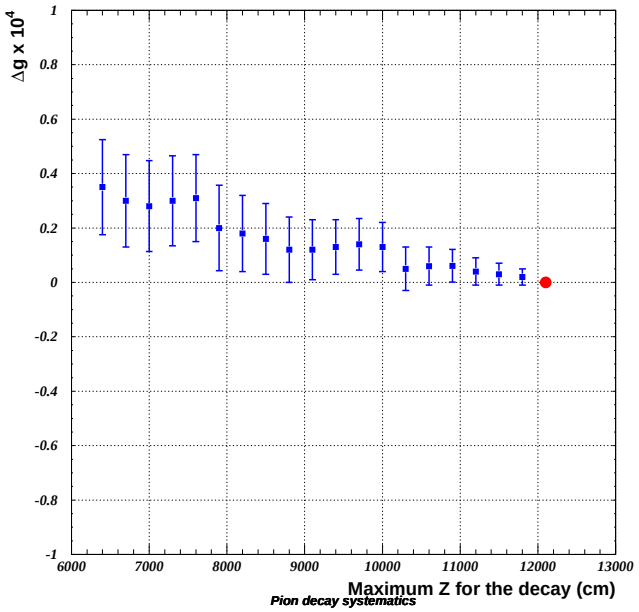

Figure 7.6: By changing in the MC the maximum longitudinal vertex allowed for the pion decay, it is possible to say that the source of this systematics is in the different acceptance between K^+ and K^- in which the $\pi^{\pm}$ in the final state decays in $\mu\nu$.

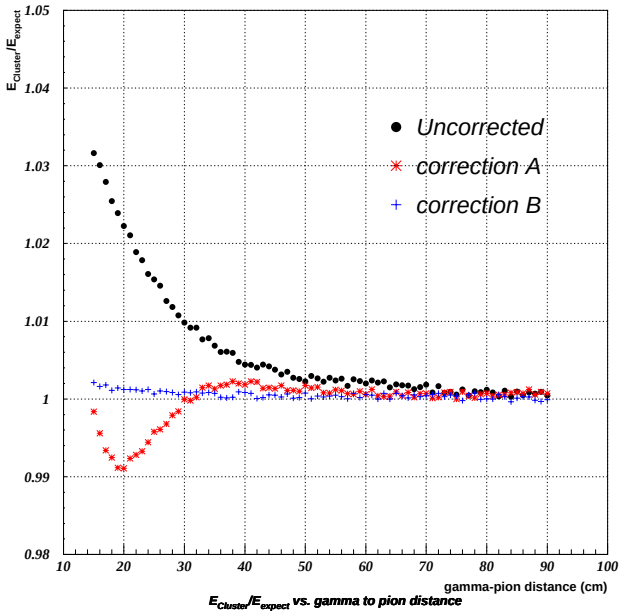

Figure 7.7: The ratio between the measured and the expected energy in the π^0s hypothesis depends on the hadronic cluster distance.

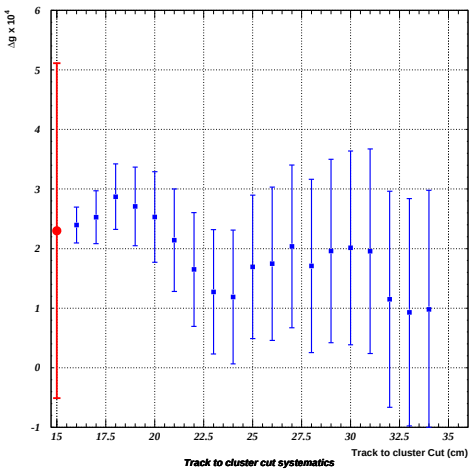

Figure 7.8: A systematic behaviour is observed studying Δg as a function of the track impact point on the LKr to nearest cluster distance

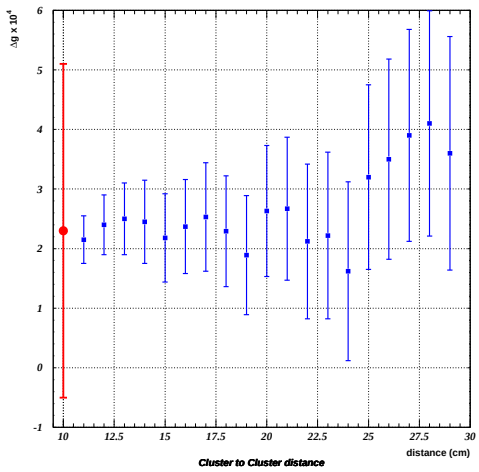

Figure 7.9: No effect is observed changing the minimum allowed distance among gamma clusters.

is assigned as systematics. The value obtained of $0.5 \cdot 10^{-5}$ is fully compatible with the previous estimation.

In order to avoid distortions in the gamma energy measurement, a cluster isolation is imposed asking for the minimum distance of 10 cm between each gamma cluster. To study the systematics due to this condition the minimum distance allowed has

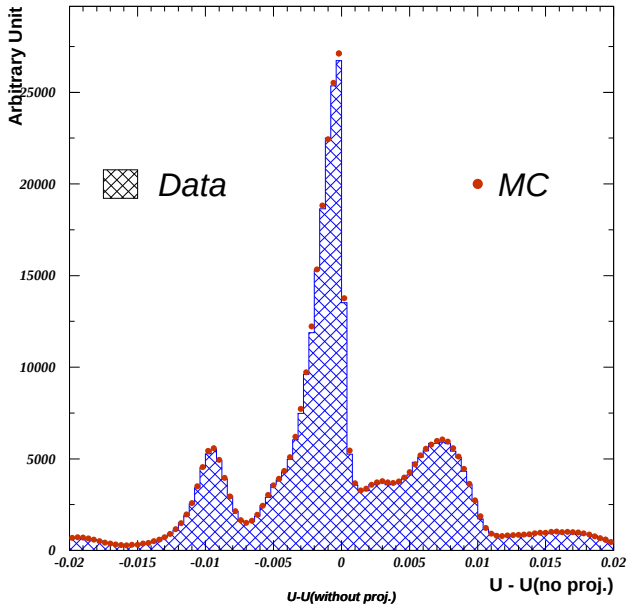

Figure 7.10: Difference between U variable with and without the projectivity correction. It is no easy to understand the shape of this distribution because it is modulated by the acceptance of 4 photons, but it is perfectly in agreement with MonteCarlo. In any case 90% of the U variation is below 0.015 (half of the bin width employed in the standard fit).

been changed in step of 1 cm starting from 10 cm. The Δg has been recomputed for each value of the cut: no systematics needs to be assigned for this cut as can be recognized from fig. 7.9 in which the uncorrelated part of the error with respect to the point at 10 cm, is shown.

7.3.2 Projectivity correction systematics

The projectivity correction is applied to the gammas: the U distribution (in the U1 definition) can be influenced in principle from this correction. The fact that some effect can modify the U distribution is not sufficient to give a systematics on the Δg measurement. The necessary condition is that such effect distinguish between K^+ and K^- decay. In addition the projectivity correction effect is very small (plot 7.10) well below the U resolution and the bin width used for the fitting. However the projectivity influences the selection acceptance; the coupling with others subtle effects could produce a systematic effect. To study the systematics due to this correction the projectivity point has been moved in $\pm 8m$ and the correction recomputed. No effect is detected on the asymmetry.

7.3.3 Wrong gamma pairing

The presence of systematics due to the gamma pairing has been evaluated from a large sample of simulated events. The percentage of wrong pairing is at level of

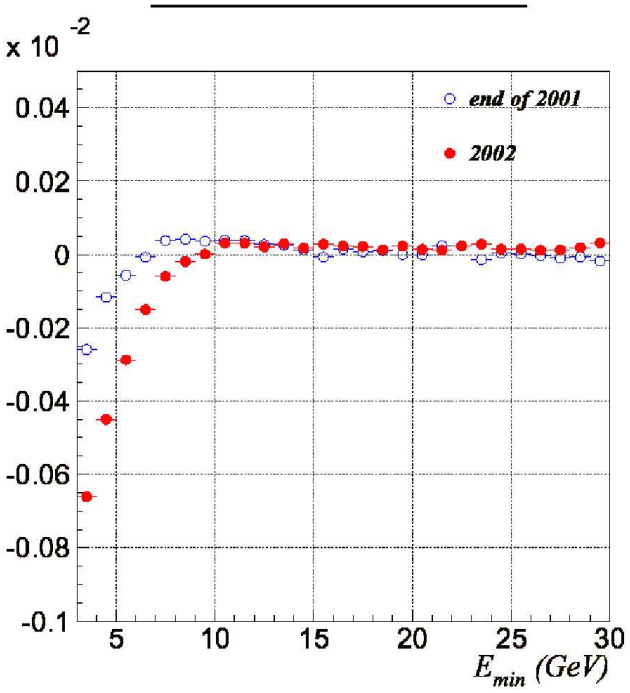

Figure 7.11: LKr linearity with two different threshold values. The non linearity below 10 changes between 2001 to 2002. In the Y scale the difference between the reconstructed π^0 and the π^0_{PDG} masses, in GeV, is shown.

$\sim 0.2\%$. Due to the selection method these events aren't equally distributed in the Dalitz Plot. In fact the events coming from the left part of the U distribution are more frequently affected by the mispairing because the π^0 in this phase space region are almost at relative rest in the di-pion CM frame. In the MonteCarlo the asymmetry has been evaluated including and excluding the events in which there is a wrong pairing, obtaining a difference of $< 0.1 \cdot 10^{-4}$.

7.3.4 Neutral vertex difference cut

The selection A, used as standard selection, is based on the minimization of the differences between the reconstructed longitudinal position of the two π^0s vertexes. A cut of $|\Delta Z| < 5m$ is applied in order to decrease the background contribution. No systematics at level of 10^{-5} is assigned by changing then maximum ΔZ allowed in the range $3.20 \div 6.05$ m in step of 15 cm (fig. 7.5).

7.3.5 LKr non-linearity

In the par. 4.1.3 the LKr non linearity has been discussed. In a wide energy range the LKr linearity is in $\pm 0.1\%$, while below $\sim 11 GeV$ a sizable non linearity has been detected studying the difference between the nominal π^0 mass and the reconstructed invariant mass of photon pairs originating from known vertex as a function of the low energy photon. In this energy range a special correction has to be applied at

the SC level (see par. 4.1.3). The correction is relevant because more than $\sim 50\%$ of the photons, in $\pi^{\pm}\pi^0\pi^0$ decays, have energy below $11GeV$. The non linearity is due to the data-concentrator ADC threshold; this is evident in the plot 7.11, in which the non-linearity is shown in 2001 and in 2002 data, when the DC threshold was changed from 36 to 72 ADC counts [110]. The non linearity correction, obtained by fitting the distribution in the plot above, is applied to all the gammas below 11 GeV before the event reconstruction. The systematics assigned to this effect is $0.1 \cdot 10^{-4}$ and it is obtained from the difference between the asymmetry calculated with and without this correction.

7.4 Accidentals

The accidentals contribution to the Δg measurement has been evaluated by changing the number of allowed extra clusters or extra tracks. In the standard analysis no requirement is imposed on the total cluster and track numbers. An extra track is defined as an additional track in time ($\pm 5ns$) with the event[2]. The extra track, as defined for this study, cannot be a ghost track (the systematics due to the ghost tracks, defined in par. 3.3.1, is studied a part). The extra clusters are defined as all the additional clusters in $\pm 5ns$ with respect to the event, farther than 15 cm from any tracks impact point and farther than 10 cm with respect to all the other clusters. In plot. 7.12 and 7.13, obtained changing the number of allowed extra tracks and clusters, respectively, a $0.2 \cdot 10^{-4}$ systematics is assigned to the accidental activity in the spectrometer while no systematics contribution is observed by the accidentals in the LKr. A different method is also used to confirm that there is no contribution from the accidentals clusters, using the simulation. The extra clusters energy spectra and position on the LKr are measured directly on the data, for K^+ and K^-. This distribution are used to random generate an extra cluster to overlay the standard MonteCarlo at level of the events reconstruction. The asymmetry is recomputed with overlayed MonteCarlo in which the accidentals are added both proportionally to the rate measured in the real data and with 1 accidental for every event. An effect of only $0.9 \cdot 10^{-4}$ is detected in the latter case, in which a rate ~ 25 times higher than in the real data taking is present. In the case in which the accidentals are in the real quantity the asymmetry is not significantly affected. The possibility that the accidental activity can influence the reconstruction at clusters or tracks level, is not included in this study. In principle the energy deposition of accidental particles out of time (in particular early) with respect to the interesting event, can influence the LKr cluster reconstruction (and partially the spectrometer track reconstruction). However this effect is very small because the out of time accidental activity can be evaluated (releasing the time cuts) at level of $< 10^{-4}$ with respect to the "in time" events; in addition only charge asymmetric and U dependent effects can influence the asymmetry. For all these reasons the contribution from the out of time accidentals is considered negligible.

[2]Being the time event defined as the time average of the LKr clusters.

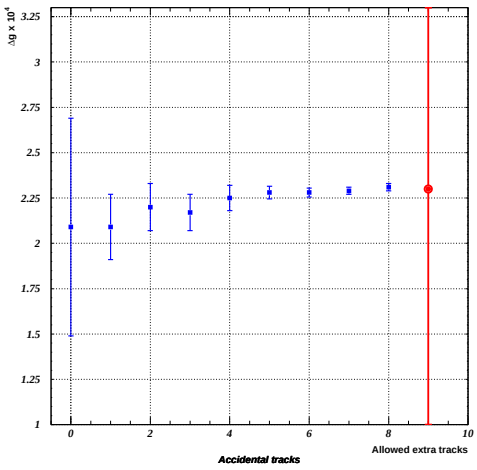

Figure 7.12: The effect due to the pile up in the spectrometer is studied changing the allowed extra tracks with respect to the no cut in this number (point 9).

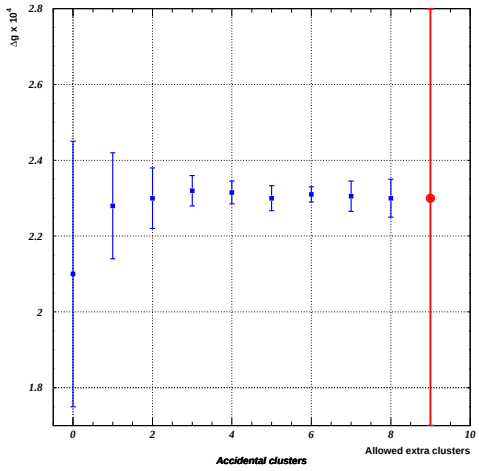

Figure 7.13: The asymmetry does not depends on the number of extra clusters. As usually the red point is the no limit while the blue points indicate the Δg value recomputed for each number of extra clusters.

7.5 U calculation

The standard bin width used in the fit to obtain the final result is 0.03 (100 bins in the range -1.5,1.5). The effect of the bin size on the asymmetry has been evaluated changing the bin width. In particular a special binning in which the width of each bin is proportional to the U resolution has been used. The resolution in U1 goes from 0.006 in the left part of the Dalitz plot to 0.04 in the right part (fig. 6.14). The standard 0.03 width is safely wide in the left part, but in the right part the resolution is larger than the standard width and significant migration effect among the bins can arise. In fig. 7.14 is shown the U distribution in which the bin width is chosen to be at least 3σ with respect to the U1 resolution in that point: in that case the bin width varies between 0.02 and 0.12 . A total of 56 bins are defined in the standard range (-1.5:1.5) instead of 100 bins. The fitting procedure is exactly the same that in the standard way (quadruple ratio, standard ratio as fitting function) and the results obtained are summarized n the following table:

	U1(std)	U1(var.bins)
SS1	4.3 ± 3.8	3.9 ± 3.8
SS2	0.3 ± 4.9	0.2 ± 7.0
SS3	-1.8 ± 8.2	-1.7 ± 8.2
Tot	2.3 ± 2.8	2.0 ± 2.8

The total systematics is $0.3 \cdot 10^{-4}$. Other studies increasing or decreasing the bins size indicate a possible upper limit at $0.4 \cdot 10^{-4}$ that is conservatively chosen

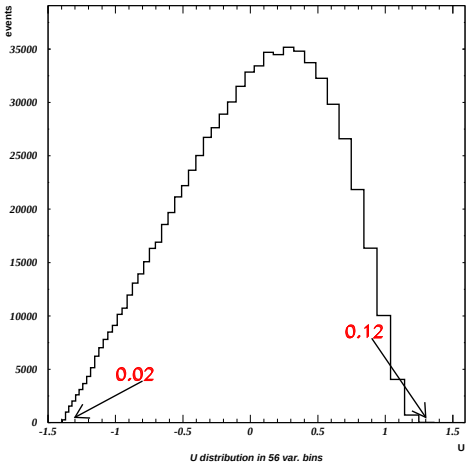

Figure 7.14: U distribution in which the bin width is proportional to the local U resolution.

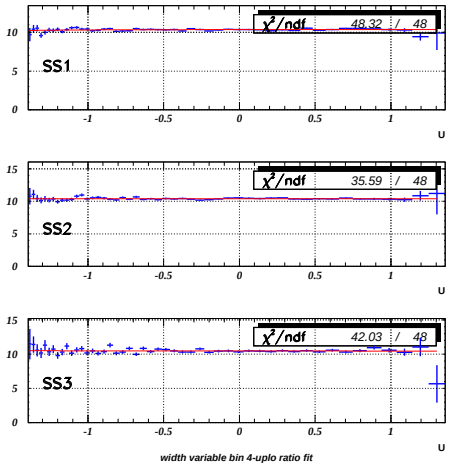

Figure 7.15: The Δg value it is obtained from the ratio of U distributions with bin width variable to study the systematics due to the binning.

for the final systematics table.

7.6 External uncertainty

To extract the value of Δg the standard ratio is used. The uncertainty on the g value is taken into account as external uncertainty (the uncertainty on the h value is neglected because of the relatively small quadratic component value). The present[3] PDG value is $g^0 = (0.638 \pm 0.020)$. The easiest approach to the evaluation of this systematics is to consider the maximum and minimum fluctuation ($\pm 1\sigma$) of the g value within the error and then recompute the Δg value. A systematics of $0.3 \cdot 10^{-4}$ is assigned with this method. Due to the fact that the g value modify the fitting function shape this systematics could be an artifact of the statistical error variation. To study this uncertainty a toy MonteCarlo has been employed [111]. Five hundred samples of $5 \cdot 10^7$ events have been produced with $N(K^+)/N(K^-) = 1$ including a small differences in the Dalitz plot distribution of $\Delta g = 3 \cdot 10^{-4}$ near to the measured central value. Acceptance and resolution are included by using smooth functions obtained by fitting the distributions obtained with CMC MonteCarlo. For each of the 500 samples, three values of Δg are extracted using g^0, $g^0 + 1\sigma$, $g^0 - 1\sigma$. The differences between the $\Delta g(g = g^0) - \Delta g(g = g^0 + 1\sigma)$ and $\Delta g(g = g^0) - \Delta g(g = g^0 - 1\sigma)$ are plotted separately and fitted with a Gaussian (fig. 7.17). The average value of Δg shift due to the g variation is slightly smaller than $0.3 \cdot 10^{-4}$ in both cases. A systematics of $0.3 \cdot 10^{-4}$ is finally assigned as upper limit to the external uncertainty due to the uncertainty of the g value.

By using the value measured in [130] $g = 0.645 \pm 0.010$ fully compatible with the PDG value $g = (0.638 \pm 0.020)$ this external error becomes negligible. This value

[3]Before the NA48/2 linear slope measurement and redefinition.

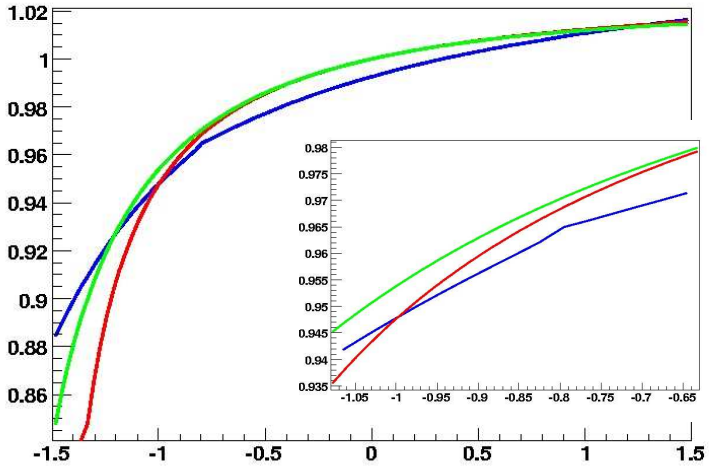

Figure 7.16: In green the standard ratio, in red the approximated ratio and in blue the ratio obtained with the cusp function, for $\Delta g = 3 \cdot 10^{-4}$ and g=0.638 [4]

of g was obtained by considering a different matrix element expansion, to keep in to account the presence of the cusp structure already shown in the fig. 3.17. In this sense the meaning of g is slightly different with respect to the standard Taylor expansion eq. (1.61). The function describing the cusp structure would be more correct to use to extract Δg. We chose to use the standard ratio (5.4) instead of the cusp function (fig. 7.16) to be coherent with the literature and the previous experiments. Anyway the use of the alternative ratio constructed with the cusp function $f_{cusp}(U)$:

$$R_{cusp}(U) \sim 1 + \frac{\Delta g U}{f_{cusp}(U)}$$

gives a Δg value greater of $0.2 \cdot 10^{-4}$ with respect to the standard ratio fit[4]. However no systematics is assigned because in terms of each parametrization chosen each result is correct (while the meaning of the Δg is slightly different in each definition).

7.7 Other systematics

Several other sources of systematics have been checked.

The ghost track rejection (described in par. 3.3.6) reject 1.5% of good events and the asymmetry measured removing the ghost tracks rejection procedure does not change at level of 10^{-5}. The dependence of the asymmetry on the transverse vertex position is checked by changing the procedure to calculate it. Usually the transverse vertex position is calculated propagating back from the DCH1 the charged pion track through the Blue field as far as the longitudinal plane identified by the neutral vertex position. A fast method to find the transverse vertex position

[4]While the approximated ratio fit gives a result $0.8 \cdot 10^{-4}$ smaller

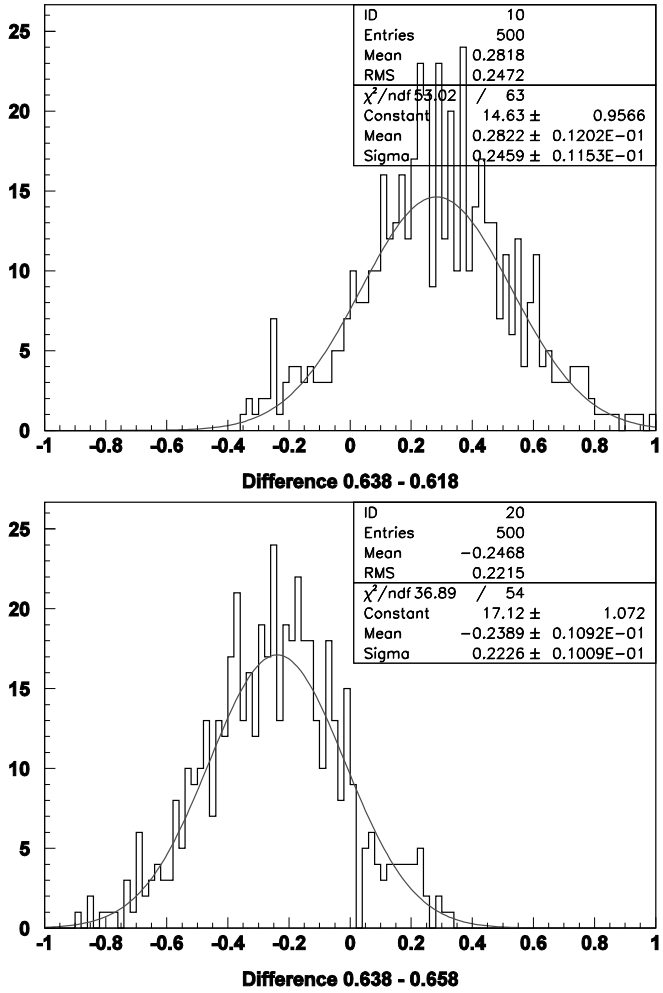

Figure 7.17: Distributions of the differences between the Δg measured in the nominal g^0 value and $g^0 - 1 \cdot \sigma$ and $g^0 + 1 \cdot \sigma$, in 500 MonteCarlo different samples.

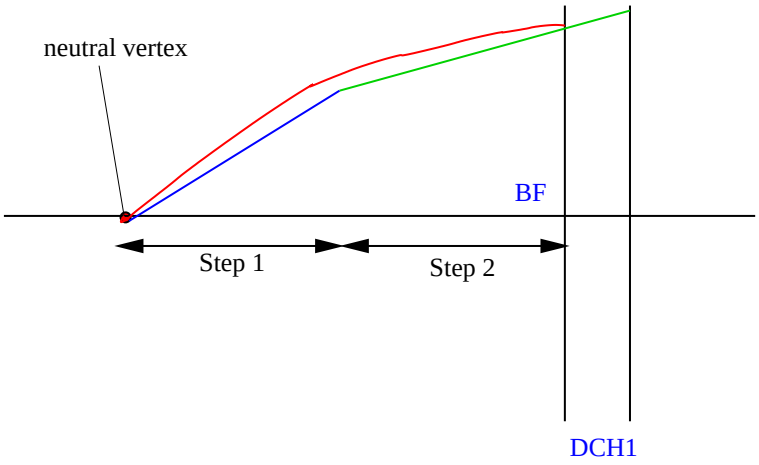

Figure 7.18: The transverse vertex position could be obtained extrapolating in 2 steps instead of the slower back tracking in the blue field.

has been defined using the MonteCarlo: instead of the full back propagation step by step is equivalent to subdivide the distance between the decay vertex in two parts; in the first part the Blue field corrected slopes at the vertex are used and in the second part the slopes measured at DCH1 (fig. 7.18). The Δg result is in practice insensitive to any change in the extrapolation: for instance by ignoring the Blue Field or assuming the transverse coordinate in the (0,0) position the Δg result does not change.
All the other checks in other minor effects give negligible contribution to the systematics error.

7.8 Comments on systematics error

The systematics are summarized in table 7.1. Most of them are conservative estimations of small effects. Several checks have been done without any significant systematics ($< 0.1 \cdot 10^{-4}$); we have cited the most significant studies performed. The MonteCarlo has been used only to check the results and to understand the detector behaviour, but most of the systematics have been studied without MonteCarlo. This has been possible due to the specific features of the experimental technique (the quadruple ratio), the quality of the data and the use of the LKr informations only[5].

[5]However in the charged mode asymmetry analysis the systematics uncertainty is at the same level as in the neutral [113]

Systematics	$\delta(\Delta g)$ (in units of 10^{-4})
Beam geometry and charged track acceptance	0.3
Blue Field correction	0.1
$\pi \to \mu$ decay	0.5
LKr related effects:	
Track to cluster distance	0.5
LKr non-linearity	0.1
U binning	0.4
Accidentals	0.2
External uncertainty	0.3
Total systematics	$0.9_{syst.} \pm 0.3_{ext.}$

Table 7.1: Summary of systematics uncertainties to the measured Δg.

Chapter 8

Trigger efficiency and systematics

The $\pi^{\pm}\pi^0\pi^0$ trigger is subdivided in two levels. The first one requires at least one charged particle hit in the charged hodoscope and four shower peaks in the LKr calorimeter. The L2, by using the information coming from a preliminary reconstruction in the spectrometer, requires the missing mass with respect to the charged track (interpreted as a charged pion) to be far from the π^0 mass, in order to reduce the acquisition of the most frequent $K \to \pi^{\pm}\pi^0$. The efficiency of the two trigger levels has to be measured in order to understand whether it could have an influence on Δg. The asymmetry measurement does not depend on the numbers of events in the K^+ or K^- decays (the linear slope depends only on the shape of the U Dalitz variable distribution), and, in principle, trigger corrections have to be applied only in case of U dependence. This dependence can be evaluated but with precision limited by the statistics of the control samples. As consequence a systematic uncertainty is expected due to the limited number of events collected in the control trigger.

In this chapter the measurement of the trigger efficiency, the sources of the trigger systematic errors and the techniques used to reduce them are described.

8.1 The trigger chain

We have already discussed the NA48/2 trigger system in par. 2.3 and the online trigger selection used to collect $K^{\pm} \to \pi^{\pm}\pi^0\pi^0$ decays in par. 3.2. The system is essentially composed by two parts: the L1, which is a dedicated hardware system and the L2, based on software fast reconstruction of magnetic spectrometer information. The L1 itself is composed by two parts: the *charged* part, coming from the hodoscope and a *neutral* part from the LKr calorimeter. In particular, for what concern the $K^{\pm} \to \pi^{\pm}\pi^0\pi^0$, the L1 is defined by the coincidence of the Q1 (CHOD) condition and the NTPEAK (LKr) condition as described in par. 3.2.1. Here we are ignoring the Q2 component of the L1 that, in standard condition, has a small contribution to the total trigger collection with a relatively small purity[1]. If the L1 requests are fulfilled, the L2 trigger (also known as MassBox (MBX)) receives the signal to apply

[1] In par. 6.2.1 we have discussed a period in which, for technical problems, the Q2 component becomes predominant.

the 1TRK-P ("one track P") algorithm to the current event (par. 3.2.2). The two codes that can strobe the 1TRK-P algorithm are:

- L1code0: $(Q1 + Q2) * [NTPEAK + (Q1/10 * LKR(minbias)) + (Q1*!Q2 * 1\mu*!AKL/D4) * (KMU3\_PRE)]$
- L1code2: $(Q1 + Q2) * [Q2*!AKL + Q1/100 + KLrandom]$

However in standard condition 99.9% of $K^{\pm} \to \pi^{\pm}\pi^0\pi^0$ have the L1code0 bit set and more than 90% of these passes through the Q1*NTPEAK, while the rest is triggered by the Q1/10*LKR(minbias) component. The M_{FAKE} is computed assuming the charged pion mass for the charged track by using the formula (3.1). If M_{FAKE} is smaller than 475 MeV/c^2 then the event is selected.

Summarizing the trigger chain is essentially (neglecting the Q2 component and other small contributions):

$$L1(Q1 * NTPEAK) * L1(MBXnotBusy) * L2(\text{MBX 1TRK-P})$$

During the 2003 data taking the MBX dead time was negligible and the contribution to the total trigger efficiency can be neglected.

The timing of the trigger is given by the $(Q1 + Q2)$ in the L1. This time sets the timestamp of the trigger as reference for the neutral component of the L1 and for the MBX fast reconstruction. In order to reduce the inefficiency due to the time alignment between the Q1 (giving the time reference) and the NTPEAK, the coincidence is triplicated (in the sense that also the time slice preceding the (Q_1+Q_2) timestamp and the following are accepted for the NTPEAK signal) at level of the trigger supervisor. Thanks to that the inefficiency coming from the wrong L1 time alignment has been measured as negligible.

The relevant sources of trigger inefficiency are:

- Q1 inefficiency
- NTPEAK inefficiency
- MBX inefficiency (including effect to the timing)

The L2 trigger words are described in table 8.1 with typical rates during a standard burst. A general description can be found in [114]. For the $K^{\pm} \to \pi^{\pm}\pi^0\pi^0$ decays apart from the main MB-1TRK-P trigger, the N-MBIAS, NT-NOPEAK, and NT-PEAK are used as control triggers.

8.2 L1 signals

The two components of the L1 trigger are studied separately. To measure the efficiency of a given trigger a control trigger is needed. The control trigger has to be uncorrelated relative to the trigger under study, i.e. a different detector should at the origin of the trigger for the control events with respect to the detector responsible of the trigger for which the efficiency has to be measured. For instance calorimetric control trigger can be used to measure the Q1 inefficiency while a non calorimetric

Trigger Word			
name	Trigger	D	N
MB-2VTX	2 vertex	1	22K
MB-1VTX	1 vertex	1	13K
MB-WDOG	MB(NOT IN TIME)	1	0.2K
C-PRE	$Q2 \cdot \overline{AKL} + Q1/100$	100	3.3K
MB-1TRK-P	anti-$\pi^+\pi^0$ cut	1	14.5K
MB-1TRK-3	anti-K_{l2} cut	20	0.8K
MB-1TRK-2	K_{e2} cut	20	0.7K
MB-ZFAKE	Massbox debugging	200	0.4K
NT-NOPEAK	NUT($COG < 30cm \cdot Z < 9500cm \cdot E_{LKR} > 15GeV$)	80	1K
N-MBIAS	T0N	200	0.6K
NT-PEAK	NUT($NX > 2$ OR $NY > 2$)	50	1.3K
KMU3-PRE	$Q1 \cdot \overline{Q2} \cdot 1\mu \cdot \overline{AKL} \cdot NUT(E_{LKR} > 15GeV)$	50	0.5K
LKR-CAL-NZS	Not zero suppression	1	off
LKR-CAL-ZS	Zero suppression	1	off
PULSE	HAC/PMB pulser	1	off
2BODY-PRE	KE2-PRE/80+KMU2-PRE/100+Q1/100	50	0.3K
RND	random	10	50
KE2-PRE	$Q1 \cdot \overline{Q2} \cdot \overline{1\mu} \cdot \overline{AKL} \cdot NUT(E_{LKR} > 15GeV) \cdot E_{HAC} < 10GeV$		
KMU2-PRE	$Q1 \cdot \overline{Q2} \cdot 1\mu \cdot \overline{AKL} \cdot NUT(E_{LKR} < 10GeV)$		
KMU3-PRE	$Q1 \cdot \overline{Q2} \cdot 1\mu \cdot \overline{AKL} \cdot NUT(E_{LKR} > 15GeV)$		

Table 8.1: List of the L2 trigger words. Typical trigger rates are shown in the last column afterwards the application of the downscaling factors in the column D.

trigger has to be used to measure the NTPEAK inefficiency. The trigger correction for the secondary components of the L1 will be neglected: in particular the Q2 component (in the L1code2 strobe) is negligible in the standard data collection and the LKr(minbias) part of the L1code0 (it fires if the LKr total energy is greater than 10 GeV) is highly efficient but collected with poor statistics because of the downscaling.

8.2.1 Q1 efficiency

To measure the Q1 efficiency the NTPEAK and the T0n (selected using the trigger word) are chosen as control trigger. The NTPEAK fires if more than 2 peaks are present in at least one view of the Neutral trigger while the T0n gives positive answer if some energy is present in the fiber hodoscope inside the LKr. In both cases this two control triggers are uncorrelated with the charged hodoscope. However both these triggers have characteristics that limit the statistics: the NTPEAK fires only if other particles (preferably gammas) are presents together with the charged particle that is responsible of the Q1, the T0N intrinsic efficiency strongly depends on the energy deposition in the neutral hodoscope fibers (par. 2.2.7). In addition a downscaling (D=50 for NTPEAK and D=200 for T0n) is applied in order to reduce

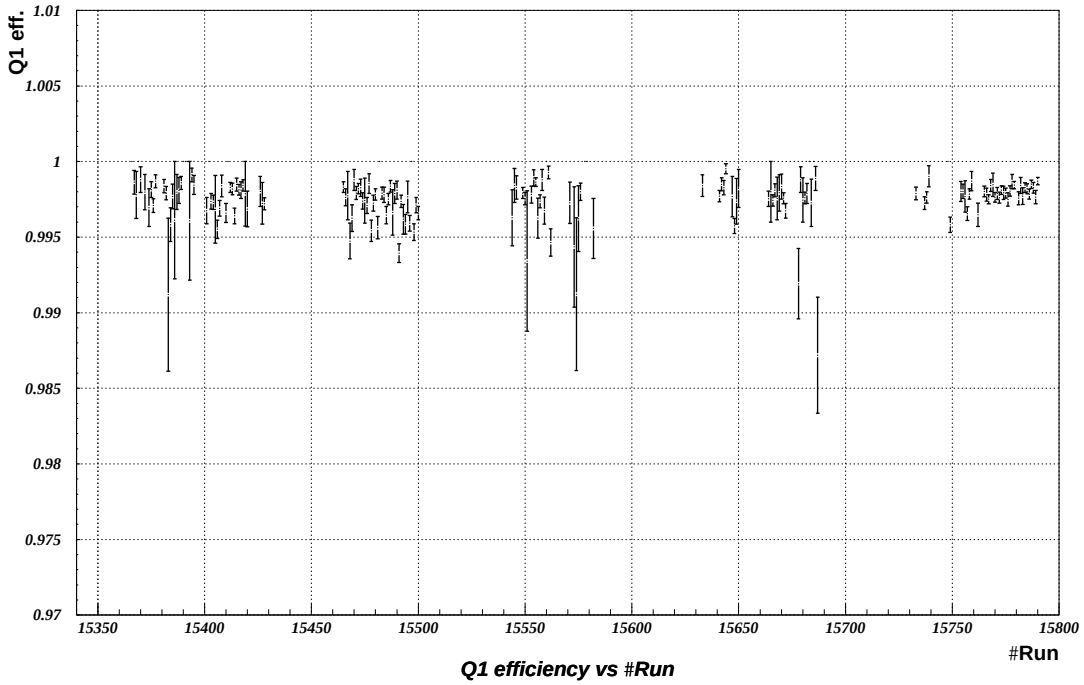

Figure 8.1: The Q1 efficiency during the data taking is usually greater than 99.5%.

the bandwidth occupancy. A total of $1. \cdot 10^6$ NTPEAK and $3.4 \cdot 10^5$ T0n events are collected[2]. If the Q1 condition is fulfilled a bit in a digital register, called Pattern Unit (PU), is set to 1. The Q1 efficiency is measured selecting goods $K^{\pm} \to \pi^{\pm}\pi^0\pi^0$ and then asking if in correspondence of an affirmative NTPEAK or T0n trigger, the PU bit corresponding to the Q1 signal is set to 1. In this procedure the intrinsic PU efficiency is supposed to be 100%. In plot 8.1 the Q1 efficiency is shown as a function of the run number[3]. The average efficiency measured is $(99.76 \pm 0.08)\%$. In table 8.2 is shown in detail the Q1 efficiency in each SuperSample and for each charge. Let us notice that the agreement of the Q1 efficiency between the two charges can be directly established at level of $\sim 10^{-3}$ only, due to the limited statistics in the control samples.

The main source of Q1 inefficiency is "geometrical". Indeed small cracks exist in the position corresponding to the end of the horizontal (in the horizontal plane) and vertical (in the vertical plane) scintillator bars. In fig. 8.2, in which the inefficiency is plotted as a function of the charged pion impact point on the hodoscope, it is possible to see the "cross" generated by this effect.

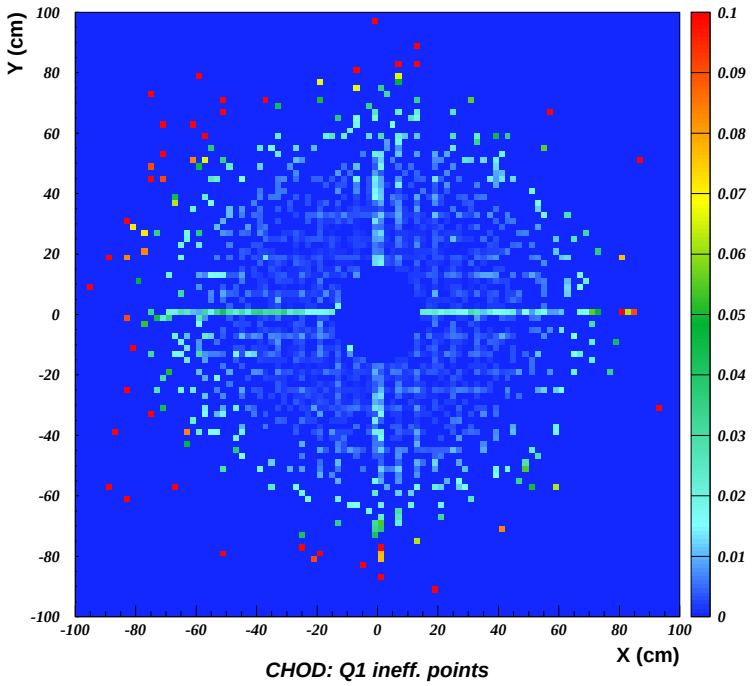

Figure 8.2: Q1 inefficiency (color scale) as a function of the charged pion impact point on the charged hodoscope. The "cracks" generated by the small gaps between the scintillator bars in adjacent quadrant are quite evident (see par. 2.2.5 for charged hodoscope description.).

	SS1	SS2	SS3	SS123
charge +	$(99.76 \pm 0.11)\%$	$(99.77 \pm 0.08)\%$	$(99.83 \pm 0.04)\%$	$(99.77 \pm 0.09)\%$
charge -	$(99.74 \pm 0.13)\%$	$(99.77 \pm 0.10)\%$	$(99.80 \pm 0.07)\%$	$(99.75 \pm 0.12)\%$
charges +/-	$(99.75 \pm 0.09)\%$	$(99.77 \pm 0.07)\%$	$(99.82 \pm 0.04)\%$	$(99.76 \pm 0.08)\%$

Table 8.2: Q1 trigger efficiency per SuperSample and Kaon charge.

8.2.2 NTPEAK efficiency

In principle the T0n can be used to measure the NTPEAK efficiency; but the small statistics ($\sim 3.4 \cdot 10^5$ events) and the correlated energy dependence (the peaks efficiency depends on the cluster energy, as well as the t0n efficiency depends on the energy deposition in the neutral hodoscope) suggests another choice as reference sample. A good choice is:

$$1\text{TRK-P} \cdot Q1/10 \cdot LKR(minbias)$$

indeed $(Q1/10) \cdot LKR(minbias)$ is the secondary component of the L1code0 strobe to the MBX (see par. 8.1). In this case we have $\sim 5.1 \cdot 10^6$ events in the control

[2]The OR between the two condition is slightly smaller than the sum
[3]This plot is obtained after the hodoscope symmetrization described in par. 6.2.2.

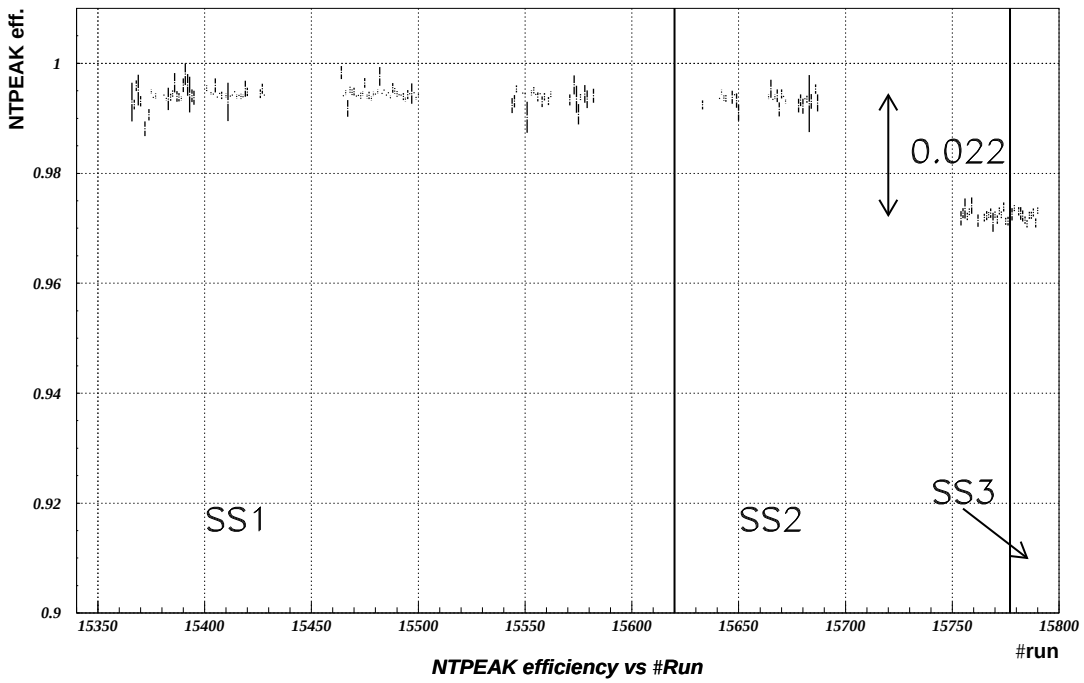

Figure 8.3: NTPEAK efficiency during the data taking. A "jump" of $\sim 2.2\%$ is observed between the begin and the end of the Run.

sample. The $Q1/10$ and $LKR(minbias)$ are read from the PU while the 1TRK-P is obtained from the L2 trigger word. In the plot 8.3 the NTPEAK efficiency as a function of the run number is shown after the exclusion of the problematic runs (in period 1 and 2) as explained in par. 6.2.1. As already pointed out the NTPEAK inefficiency increased after the problematic period at level of $\sim 3\%$ instead of $\sim 0.5\%$ of the first part of the data taking for reasons not well undertstood. This is clear in table 8.3 where the efficiency in each SuperSample is presented[4]. The inefficiency in SS3 (after the NTPEAK problem) do not have a different geometrical distribution on the LKr (plot 8.4) with respect to SS1. In this case also, due to the limited statistics in the control sample, it is not possible to say below the level of $\sim 10^{-3}$ if the NTPEAK trigger efficiency is the same in K^+ and K^- decays.

	SS1	SS2	SS3	SS123
charge +	$(99.42 \pm 0.11)\%$	$(94.38 \pm 0.15)\%$	$(97.23 \pm 0.10)\%$	$(97.66 \pm 0.12)\%$
charge -	$(99.43 \pm 0.13)\%$	$(94.32 \pm 0.22)\%$	$(97.25 \pm 0.13)\%$	$(97.68 \pm 0.16)\%$
charges +/-	$(99.42 \pm 0.09)\%$	$(94.40 \pm 0.13)\%$	$(97.24 \pm 0.08)\%$	$(97.67 \pm 0.10)\%$

Table 8.3: Details of the NTPEAK efficiency per SuperSample and Kaon charge.

[4]The low efficiency in SS2 is due to the period 3 in the plot 6.8, not excluded from the data sample.

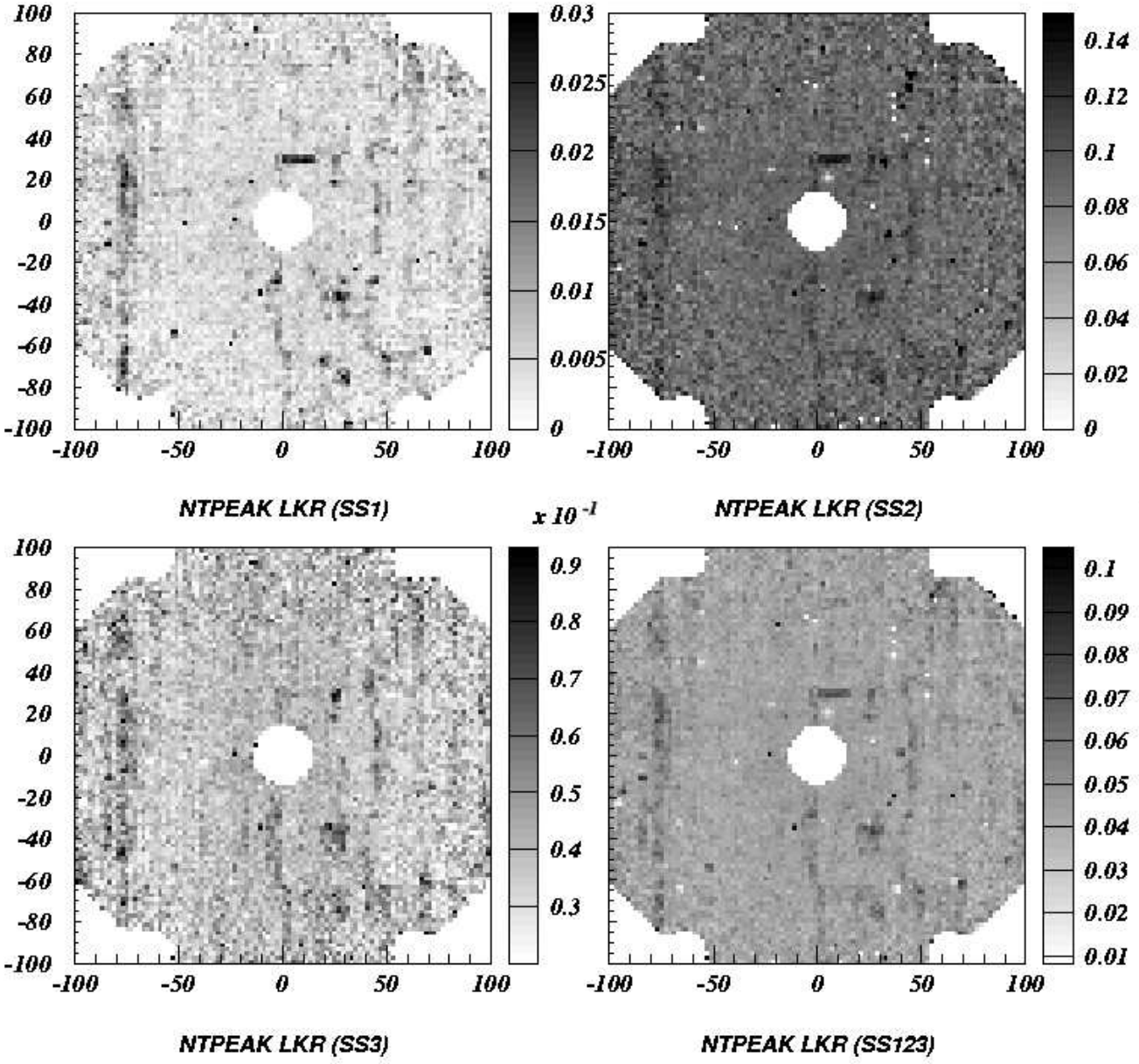

Figure 8.4: NTPEAK inefficiency (grey scale) distribution projected on the LKr. Not particular pattern are visible after the NTPEAK problem. The various plots have different normalization because of the different NTPEAK efficiency in the SuperSample.

8.3 L2 trigger (MBX)

The application of the L2 algorithm is decided according to the type of strobe signal received. We are not interested here in all the several possibilities present in the MBX logic. We have already presented how the MBX works in par. 2.3.1 and the algorithm used to select $K^{\pm} \to \pi^{\pm}\pi^0\pi^0$ decays in par. 3.2.2; anyhow in fig. 8.5 the MBX algorithm is schematically shown. We do not want to go too much into details and further informations can be found in [115]. To summarize the main points in the procedure are:

- the charged particle *coordinates* are constructed in the **AB cards** correlating the drift time measured in each pair of planes (A-B) composing a DCH view (X,Y,U,V) using Look Up Tables.
- For each chamber the $XYUV$ algorithm constructs the **spacepoints** if the hits in each view are compatibles.
- The spacepoints are combined in the Event Worker to construct **tracks**.
- Others physical object, like vertex, CDA, track momentum and missing mass, are constructed starting from the tracks informations.

For $K^{\pm} \to \pi^{\pm}\pi^0\pi^0$ only one charged track is used for the MBX online reconstruction. To allow the vertex position and CDA reconstruction, "fake" spacepoints are added in the algorithm to define a "fake" charged track corresponding to the beam axis. If the calculated vertex and the CDA satisfy the cuts (the vertex has to be in the physical decay region and the $CDA < 5cm$) the ZFAKE bit is set (and recorded in the PU) and the computation can be continued. For each spacepoint (1 real + 1 fake) pair in the DCH4 the M_{FAKE}, defined by eq. (3.1), is computed. If at least one combination with $M_{FAKE} < 475MeV/c^2$ is found, the MFAKE bit is set and the L2 1TRK-P is defined.

8.3.1 MBX efficiency

The best control trigger for the MBX-1TRK-P efficiency measurement is the NT-PEAK. In principle also the T0n and the NT-NOPEAK can be employed but the NTPEAK is preferred due to higher statistics. However the NT-NOPEAK will be used in the systematics computation in the period in which the NTPEAK problem was present, to avoid too large systematics error (par. 8.5). In plot 8.6 the L2 efficiency as a function of the run number is shown. the averaged efficiency value are presented in table 8.4, but is quite evident the high variability of the L2 trigger performance; the main reason for that is due to the DCH wires efficiency as shown in plot 8.7 and 8.8. In these plots the inefficiency on DCH1 and DCH4 with respect to the charged pion impact point position is shown. In the plots in which the inefficiency during the DS12 is shown, the presence of a problem in a horizontal band in DCH4 (reflecting also in DCH1 because only the fully reconstructed tracks are recorded) is quite evident. This was due to a problem in the DCH4 HV. The others reasons for MBX inefficiency are discussed in the next section.

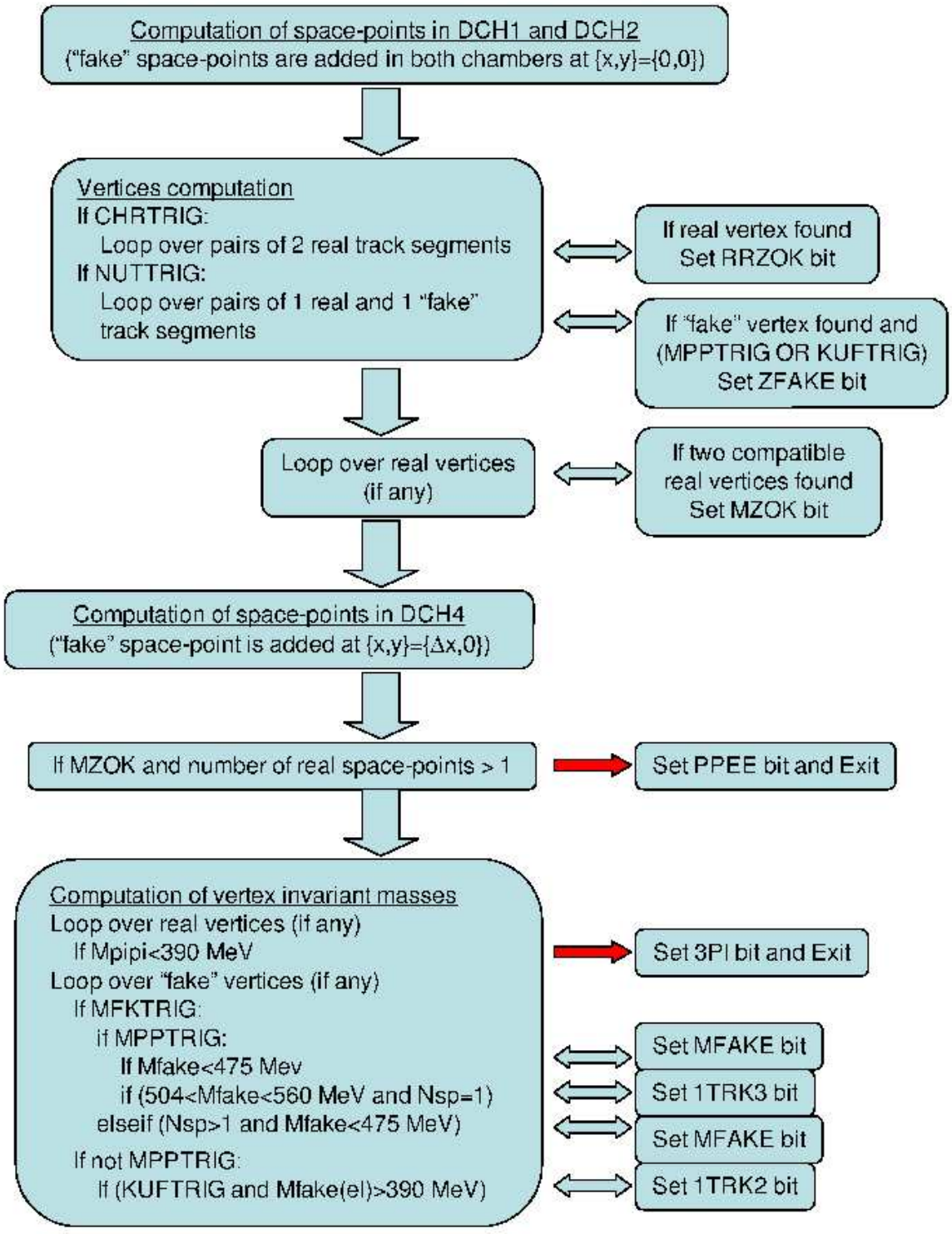

Figure 8.5: MBX algorithm schematics. The MFAKE bit is set according to the condition on the reconstructed M_{FAKE} defined in eq. (3.1).

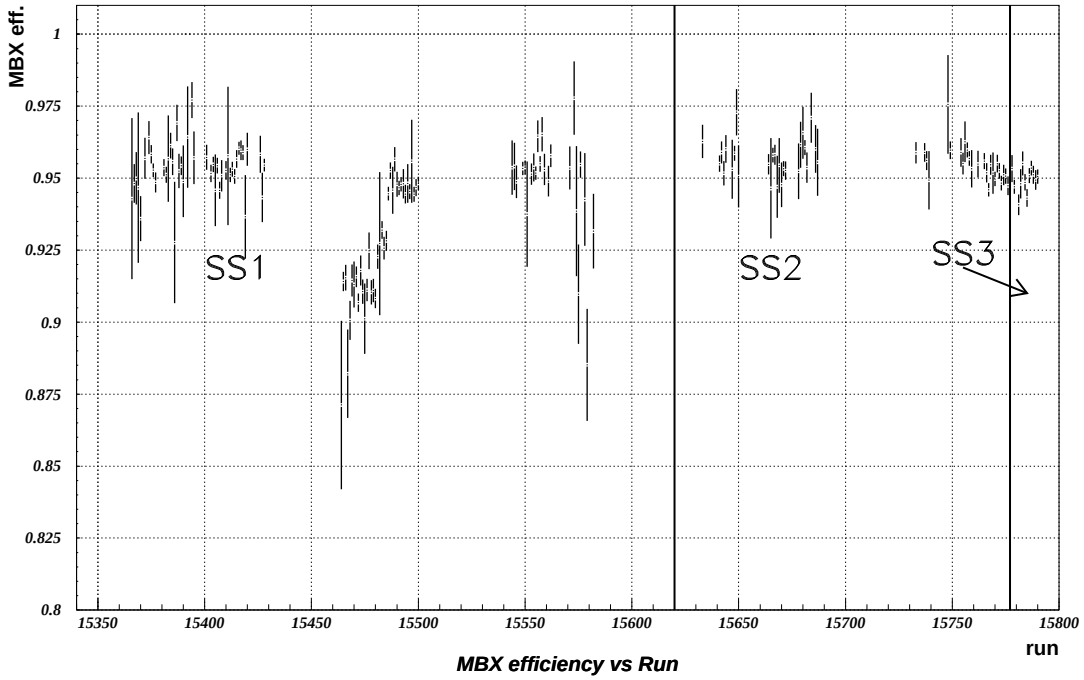

Figure 8.6: MBX efficiency during the Run. In the middle of SS1 the MBX in efficiency increased due to high wires inefficiency in DCH4.

	SS1	SS2	SS3	SS123
charge +	$(94.38 \pm 0.69)\%$	$(95.43 \pm 0.74)\%$	$(94.73 \pm 0.30)\%$	$(94.73 \pm 0.68)\%$
charge -	$(94.51 \pm 0.92)\%$	$(95.68 \pm 0.71)\%$	$(94.66 \pm 0.40)\%$	$(94.89 \pm 0.82)\%$
charges +/-	$(94.42 \pm 0.56)\%$	$(95.51 \pm 0.56)\%$	$(94.70 \pm 0.24)\%$	$(94.78 \pm 0.54)\%$

Table 8.4: MBX inefficiency per SuperSample and Kaon charge.

8.3.2 Sources of MBX inefficiency

Two classes of inefficiency can be identified in the MBX pathology:

- geometrical inefficiency;
- timing related inefficiency.

As mentioned above most of the MBX inefficiency is due to local wires inefficiency. This source is classified as geometrical in the sense that depends on some geometrical properties of the apparatus. In this case some space point can not be reconstructed by the MBX algorithm because some hit on some view is lost. We can include in the geometrical sources of inefficiency also the Overflow case. A bit in the PU is set if the hits in a DCH single plane are more than 16 . Usually this happens in case of photons conversion in the beam pipe in the spectrometer region. Events like this can produce a huge multiplicity of hits in the chambers.

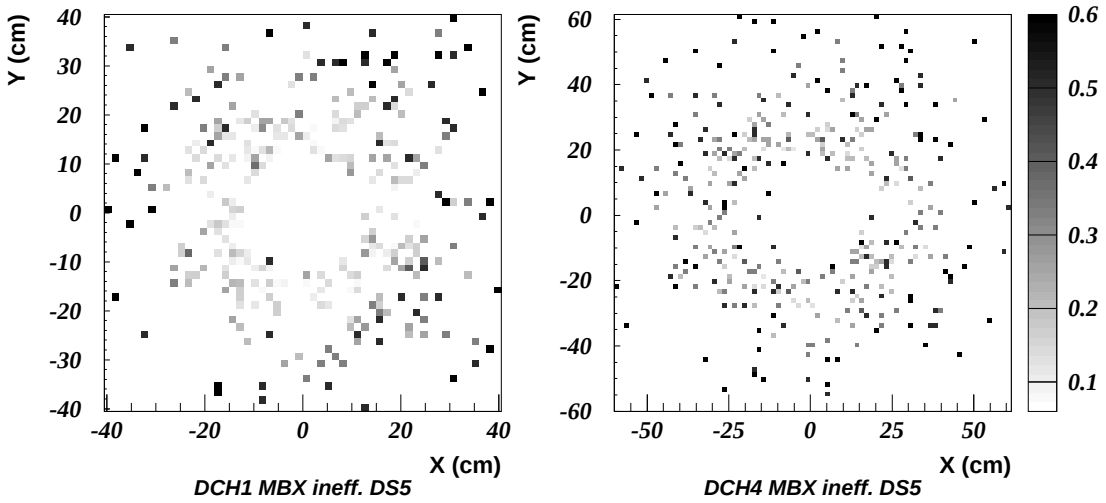

Figure 8.7: MBX trigger inefficiency (gray scale) as a function of the hit position in DCH1 and DCH4 during a standard day sample (DS 5).

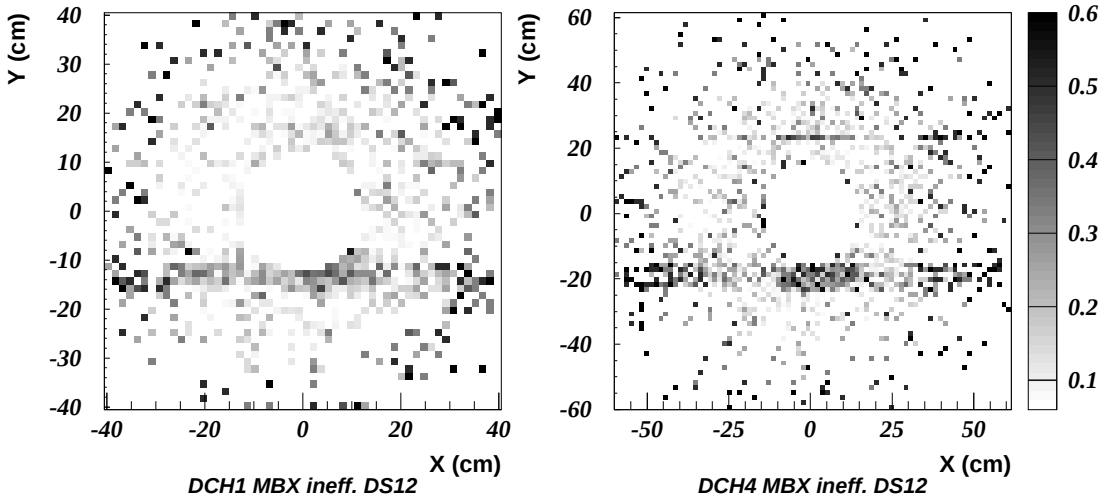

Figure 8.8: In the DS12 a problem in DCH4 produces a local inefficiency in L2 trigger (MBX).

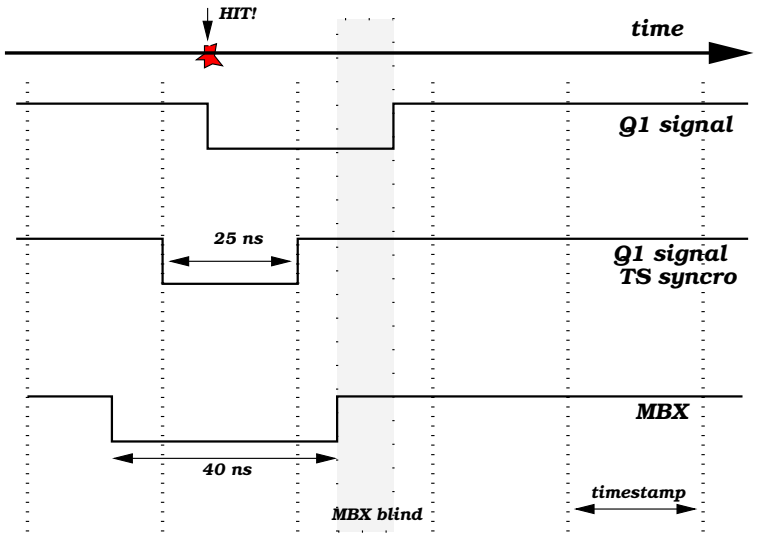

Figure 8.9: The event time reference is given by the hodoscope signal.

By using a "fake" track and the online reconstructed track the longitudinal vertex position and CDA is computed. If the vertex position is outside of the decay region the ZFAKE bit in the PU is not set. The online resolution on the vertex position and CDA is worst than the one which can be obtained offline: some event reconstructed in the physical boundary using the offline data may not be selected by the MBX, due to this effect. Also the online reconstructed missing mass has different resolution with respect to the offline. The MFAKE bit, from which the final trigger word 1TRK-P is deduced by Trigger Supervisor, is not set if the the M_{FAKE} condition, defined by the formula (3.1), is missed.

In the second category, the timing related inefficiency, we include:

- MBX dead time;
- OUT-OF-TIME answer;
- synchronization with the Q1 reference time.

The first two sources are negligible for what concern the total inefficiency. The last one is more important and includes several contributions. To better understand the problem we refer to the fig. 8.9. The trigger time is given by the Q1 signal at L1. When a charged pion hits the CHOD the Q1 signal is generated and the Timestamp (25 ns wide) in which the event happened is identified. Mainly due to the discriminators dead time the Q1 is blind for a certain time ($\sim 30ns$) after the event. By using the Q1 time as reference a 40 ns windows is opened by the MBX to compute the quantities useful to the online algorithms. If an accidental particle (fig. 8.10) arrives before with respect to the charged pion coming from the real Kaon decay, the trigger TS and the reference time is set in correspondence of the first particle. If the charged pion arrives in the Q1 dead time region, or in the same TS defined by the accidental particle, no further MBX analysis is possible. The time reference is used by the AB cards (par. 8.3) to compute the coordinates

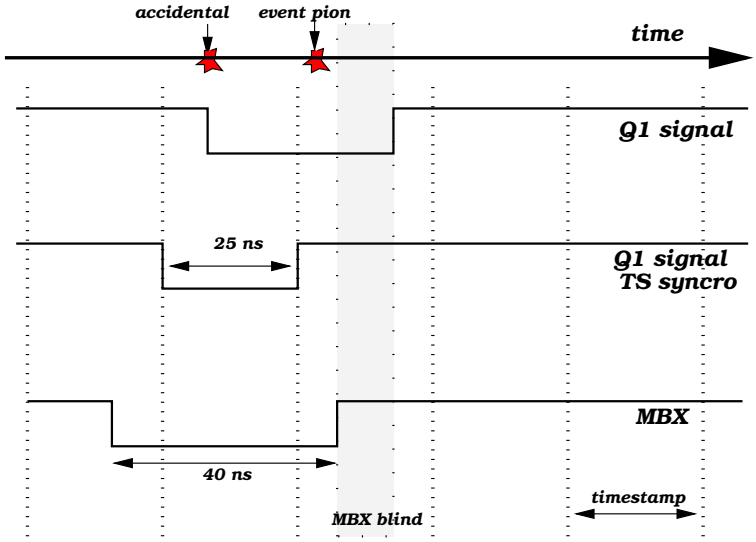

Figure 8.10: If an accidental particle arrives early with respect to the charged pion, the Q1 reference time starts early with respect to the event.

(using the drift time): if this time is "wrong" for the charged pion, the coordinates are not built in a correct way and this results in MBX inefficiency.

In the par. 8.5.1 a more quantitative description of this inefficiency sources will be given.

8.4 L1 correction and systematics

In order to understand if the trigger efficiency plays some role in the asymmetry measurement a trigger correction has to be applied to the U distribution to take into account the eventual dependence of the kinematical observable on the trigger properties. The trigger correction is, in general, applied in the following way:

- Compute the trigger efficiency as a function of U for each DS for each kaon charge (44x2).
- Correct the U distribution in each DS for each kaon charge according to the trigger efficiency and propagating properly the error.
- Sum, for each SuperSample, the DS with the same fields (achromat and B field) orientation for each charge, in order to obtain the 8 quantities useful to define the quadruple ratio.
- Fit in the standard way the trigger-corrected quadruple ratios in each SuperSample.
- Extract the $\Delta g^{trigger}$ with weighted average among the results in each SuperSamples.

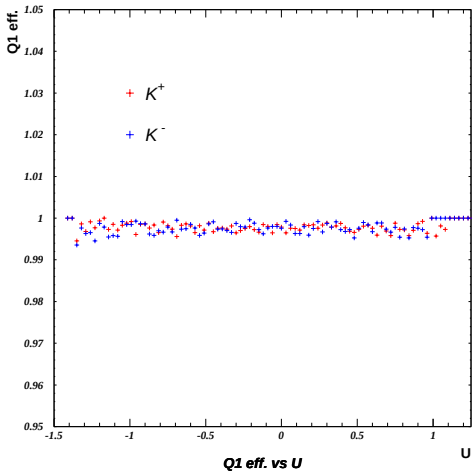

Figure 8.11: Qualitative example of Q1 efficiency as a function of the U distribution during one DS (the errors are not shown).

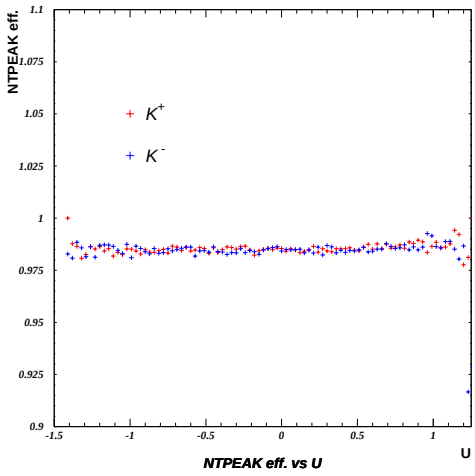

Figure 8.12: Qualitative example of NTPEAK efficiency as a function of the U distribution during one DS (the errors are not shown).

- the comparison with the standard Δg gives the correction and the systematics error.

The L1 trigger can be factorized in two parts, Q1 and NTPEAK, because they are completely uncorrelated. Concerning the Q1 correction in plot 8.11 the trigger efficiency as a function of the U variable is shown as example. In plot 8.13 the Q1 inefficiency as a function of the DS is shown. The application of the procedure

	Raw (Δg)	Q1 corr. (Δg^{Q1})	Δ
SS1	4.3 ± 3.8	4.9 ± 4.0	0.6 ± 1.2
SS2	0.3 ± 4.9	-1.4 ± 5.2	-1.7 ± 1.7
SS3	-1.8 ± 8.2	-3.8 ± 8.4	-2.0 ± 1.8
SS123	2.3 ± 2.8	1.0 ± 3.0	-1.3 ± 1.0

Table 8.5: The Q1 trigger correction and systematics are obtained from the difference between the corrected and the uncorrected Δg. All numbers are in units of 10^{-4}.

described above leads to the results presented in table 8.5 . The final correction and error is $(-1.3 \pm 1.0) \cdot 10^{-4}$. The value of the correction is fully compatible with statistical fluctuations and it is not applied to the asymmetry result. The uncorrelated part of the difference between the error with and without trigger correction, $\delta(\Delta g) = 1.0 \cdot 10^{-4}$, is considered, for the moment, as systematics error for the Q1.

Similar procedure is applied to NTPEAK (in plot 8.14 the inefficiency as a function of the DS is shown while in plot 8.12 the U dependence on the NTPEAK trigger efficiency is shown.). The correction is applied in DS basis and the asymmetry is recomputed. The results are summarized in table 8.6. The final correction is $(-0.8 \pm 1.3) \cdot 10^{-4}$. Like in the Q1 trigger case the correction is not applied to

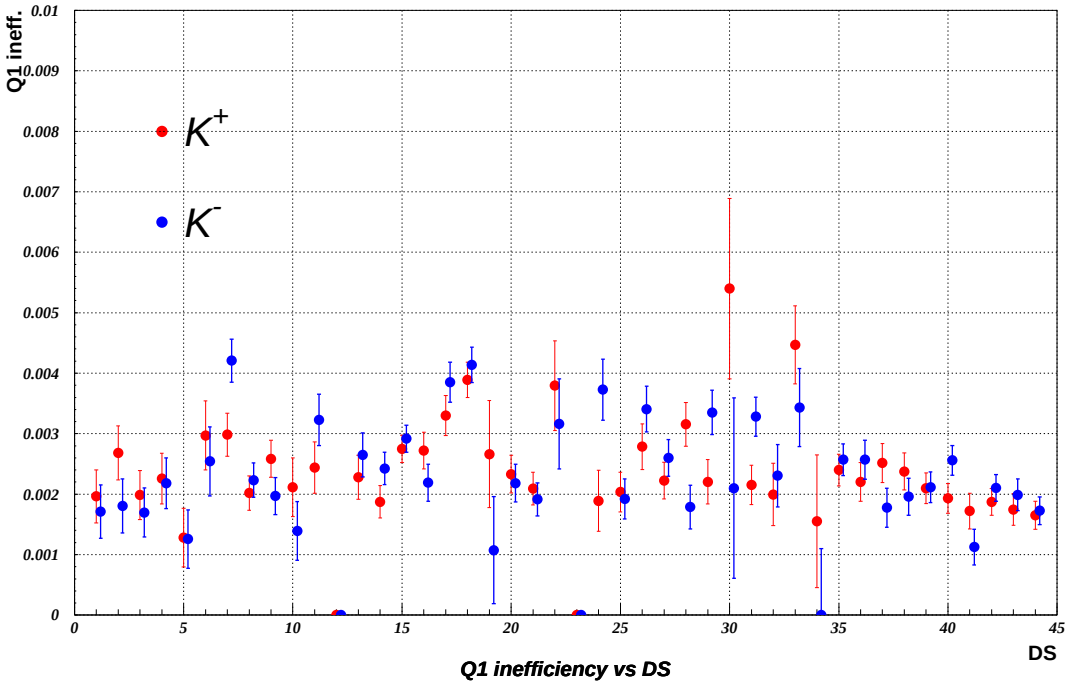

Figure 8.13: Q1 inefficiency as a function of the Day Sample for K^+ and K^-.

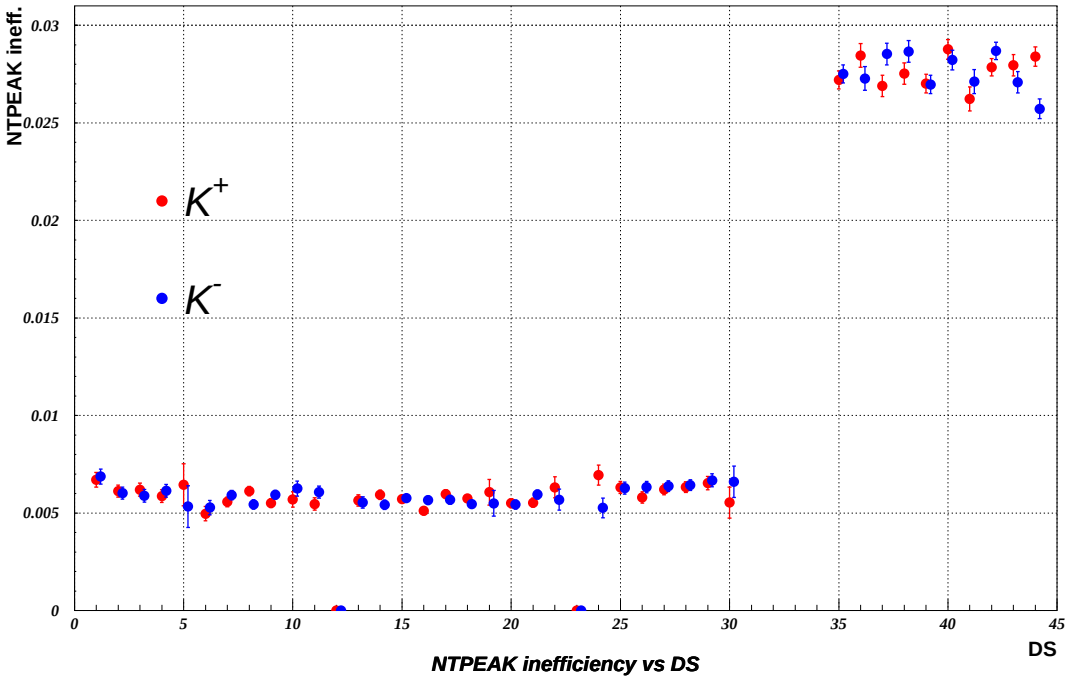

Figure 8.14: NTPEAK inefficiency as a function of the day sample for K^+ and K^-. The points between DS30 and DS35 are out of the Y scale.

the asymmetry result but the error is considered as systematics uncertainty linked to the neutral part of the L1 trigger.

	Raw (Δg)	NTPEAK corr.(Δg^{NTPK})	Δ
SS1	4.3 ± 3.8	3.6 ± 2.7	-0.7 ± 2.7
SS2	0.3 ± 4.9	5.4 ± 8.1	5.1 ± 6.4
SS3	-1.8 ± 8.2	-14.1 ± 9.3	-12.3 ± 1.8
SS123	2.3 ± 2.8	1.5 ± 2.5	-0.8 ± 1.3

Table 8.6: NTPEAK trigger correction and systematics. All numbers are in units of 10^{-4}.

Both systematics uncertainties depend on the statistics collected in the control sample. There is no evidence of real systematic problem due to a bias of the L1 trigger components, but we can not demonstrate, at the moment, this fact below the level of accuracy given by the statistical accuracy.

8.4.1 Q1: 1 track events technique

The charged tracks used to measure the Q1 trigger efficiency are the best choice for our purpose in the sense that they have exactly the same geometrical and kinematical distribution with respect to the charged pion that we use in the construction of the U distribution to calculate Δg. This is quite natural because the Q1 events are a subset of the whole $K^{\pm} \to \pi^{\pm}\pi^0\pi^0$ statistics. In spite of that, as explained above, the total amount of events used to compute the Q1 efficiency is relatively small, and as consequence the systematics can not be determined below the level of 10^{-4}. We will describe now a technique to increase the statistics in the control sample using all the events with a charged track in the spectrometer.

A generic good track can be simply selected looking for:

- minimum radius at DCH1 > 12.5 cm
- minimum radius at DCH4 > 13.5 cm
- track momentum > 5 GeV
- track quality > 0.6
- longitudinal vertex position between -1800 and 8000 (assuming the beam axis in (0,0))
- CDA< 5 cm (assuming the beam axis in (0,0))

The number of events in the control sample (NTPEAK or T0n) increases by a factor ~ 76 with respect to the number of $K^{\pm} \to \pi^{\pm}\pi^0\pi^0$. The problem is that the geometrical and kinematical distribution for this kind of events (coming mainly from $K^{\pm} \to \pi^{\pm}\pi^0$ and $K^{\pm} \to \mu\nu$ decays) is different with respect to the neutral three pions decay distribution. To correct the U distribution properly the Q1 efficiency calculated with all the 1 charged track events have to be "reweighted" according to

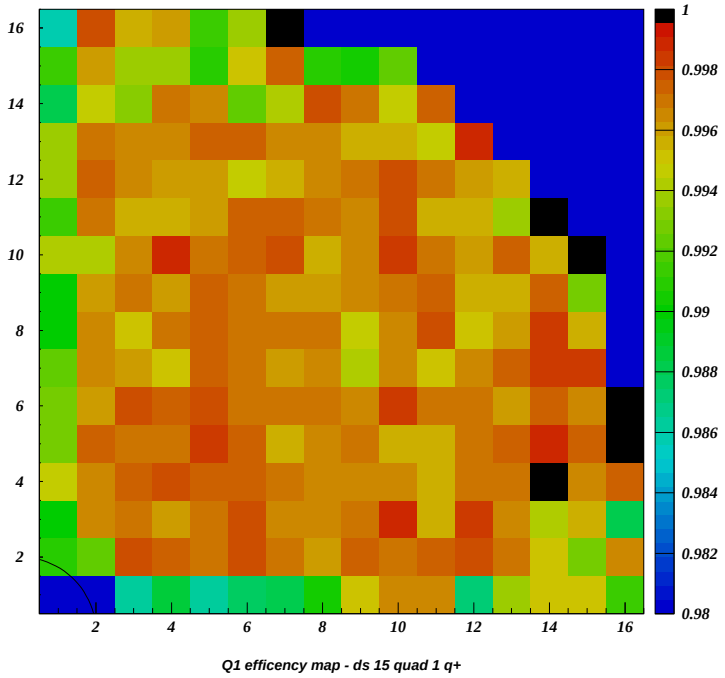

Figure 8.15: Q1 efficiency (color scale) map constructed with 1 tracks events for positive tracks in DS15, for the second quadrant. The lost of efficiency in the first row and first column is due to the "cracks" between the quadrant.

the kinematic of the $K^{\pm} \to \pi^{\pm}\pi^0\pi^0$. The charged hodoscope is subdivided in cells. The cells are constructed by considering the geometrical size of the hodoscope plastic scintillator, in horizontal and vertical plane: each cell is the smallest possible, for each cell only one counter both in horizontal and vertical plane is involved. Due the different size of the plastic scintillator bars in the inner and outer part of the CHOD the cells dimension (and the shape) changes. In this way 908 different cells are defined. In fig. 8.16 is sketch, for example, the grid defining the cells on the second quadrant. Assuming the hodoscope efficiency reasonably constant in each cell, the efficiency map can be constructed using the large sample of the 1 track events. These maps can be defined for each DS and for each charged track sign (plus or minus). In the plot 8.15 one example of this kind of efficiency map for the first quadrant, positive charged track and DS 15 is shown. By considering impact point position of the charged pion coming from a $K^{\pm} \to \pi^{\pm}\pi^0\pi^0$, several U distribution can be plotted according to the cell hit in the CHOD. For instance in plot 8.17 and 8.18 are shown examples of U distribution for events in which the charged pion was in the cells in green in fig. 8.16. For each DS and for each kaon sign these "partial" U distributions can be corrected according to the Q1 maps defined above, constructed using all the 1 track events. The "integral" U distribution is obtained summing the 908 partial U distributions. In this way the efficiency with smaller error calculated with higher statistics of the 1 track events, is correctly applied to the signal events. The Δg can be extracted using these corrected U distribution with the standard procedure.

In the table 8.7 the results with new technique are shown. The correction and the systematics thanks to this new method is demonstrated to be negligible (below 10^{-5} level).

	Raw (Δg)	Q1 new corr. (Δg^{Q1})	Δ
SS1	4.3 ± 3.8	4.3 ± 3.8	$0. \pm 0.1$
SS2	0.3 ± 4.9	0.4 ± 4.9	0.1 ± 0.1
SS3	-1.8 ± 8.2	-2.0 ± 8.2	0.2 ± 0.1
SS123	2.3 ± 2.8	2.3 ± 2.8	0.0 ± 0.0

Table 8.7: By measuring the Q1 efficiency with all tracks the Q1 systematics becomes negligible at level of 10^{-5}.

8.4.2 L1 systematics

In spite of the fact that the NTPEAK condition (which is the second element for the L1 decision) is entirely given by the neutral part of the $K^{\pm} \to \pi^{\pm}\pi^0\pi^0$ decay a systematic uncertainty of $1.3 \cdot 10^{-4}$ has to be assigned. This is due to the limited statistics collected in the control samples used to measure the NTPEAK trigger efficiency, but it is not at all proved that a real systematic effect exists. The Q1 trigger the problem is considered using the most large sample of 1 charged track events. In the Q1 case no systematic uncertainty has been assigned because no relevant difference has been measured with and without the Q1 trigger correction using the large total sample of 1 charged track events. In the case of NTPEAK however no process with 4 photons most frequent of $K^{\pm} \to \pi^{\pm}\pi^0\pi^0$ exists and a technique similar to that described for the Q1 cannot be applied.

The whole L1 trigger systematic uncertainty is $1.3 \cdot 10^{-4}$, but it should be kept in mind that the source of this error is statistical.

8.5 L2 MBX correction and systematics

The L2 trigger correction is applied with a similar procedure with respect to the procedure described for the L1 (par. 8.4). The MBX efficiency is very unstable, depending mostly on the wires efficiency. For instance in plot 8.19 the fluctuations in the middle of SS1 are quite evident. In particular the efficiency in DS 12 was so much worst that it has been decided to exclude this DS from the final sample used for the asymmetry analysis. Excluding this DS, also in the case of the L2 trigger, no correction is applied because the correction is fully compatible with 0 within the error, as shown in table 8.8. The systematic uncertainty is $3.9 \cdot 10^{-4}$ and, also in this case, is due to the limited statistics in control sample. In the next section we will see as this error can be reduced.

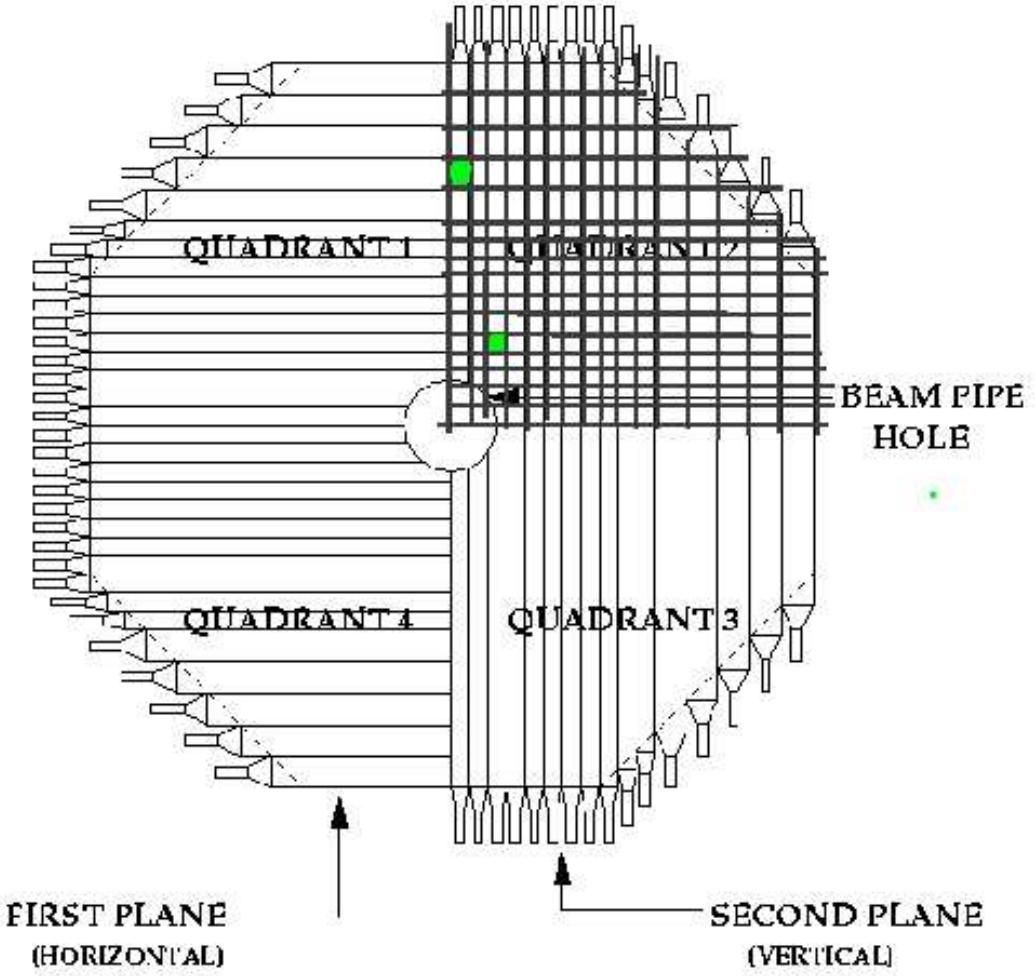

Figure 8.16: Cells definition on CHOD second quadrant. The U distribution in the green cells is shown in fig. 8.17 and 8.18.

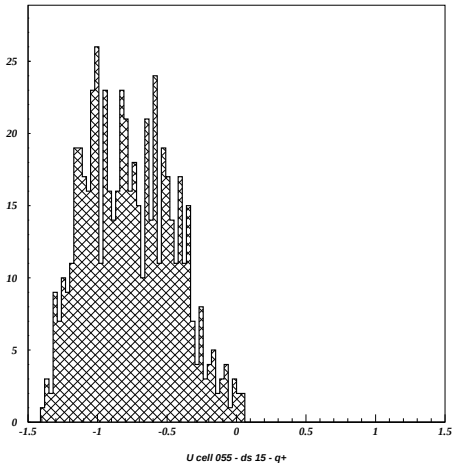

Figure 8.17: U distribution for events in which the charged pion hits the green cell (the farther from the center) in fig. 8.16.

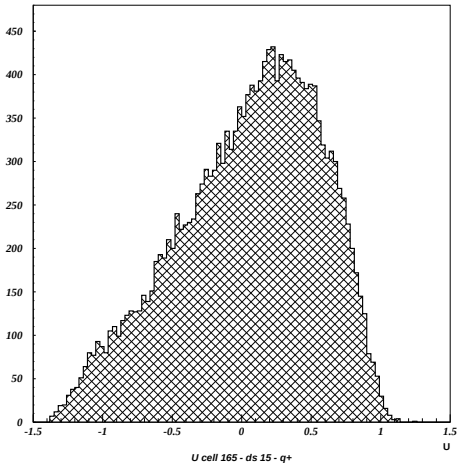

Figure 8.18: U distribution for events in which the charged pion hits the green cell (the closer to the center) in fig. 8.16.

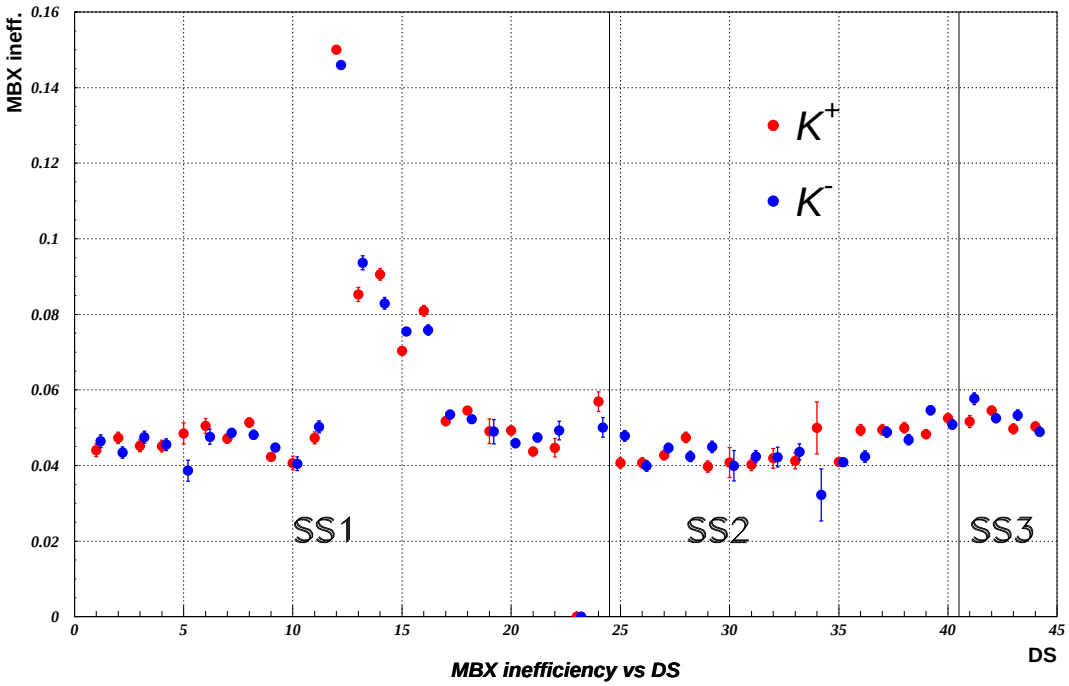

Figure 8.19: The MBX inefficiency as a function of DS for K^+ and K^- is shown. The "jump" in SS1 is discussed in par. 8.3.1 . The DS12 is excluded from the final data sample due to the high MBX inefficiency.

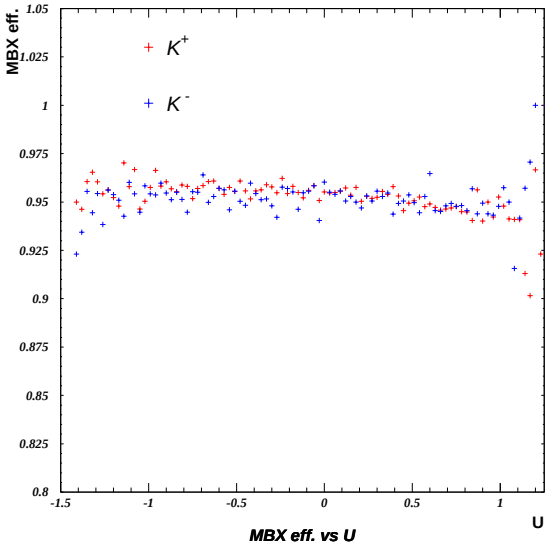

Figure 8.20: MBX efficiency as a function of U during one DS (the errors are not shown).

	Raw (Δg)	MBX. (Δg^{MBX})	Δ
SS1	4.3 ± 3.8	8.2 ± 6.3	3.9 ± 5.0
SS2	0.3 ± 4.9	2.4 ± 8.0	2.1 ± 6.3
SS3	-1.8 ± 8.2	-17.2 ± 13.9	-15.4 ± 11.2
SS123	2.3 ± 2.8	4.2 ± 4.8	1.9 ± 3.9

Table 8.8: The MBX corrections and systematics. All the numbers are in units of 10^{-4}.

8.5.1 MBX simulation and MBX MonteCarlo

In order to reduce the systematics due to the MBX, the sources of the inefficiency have to be understood and eventually simulated properly. In par. 8.3.2 we have described the sources of MBX inefficiency. This can be quantitatively studied by using a MBX simulation [116] [117]. The offline simulation of the online MBX algorithm is composed by a first part that read the informations from the raw data, then a subroutine called "cartab" builds the coordinates (as the AB cards) and translate the offline format in a format compatible with the following routines. This routines are the same with respect to the online MBX routines (vertex reconstruction, M_{FAKE} calculation, etc.). All the properties and inefficiency time related can be only partially simulated because is not easy to simulate the online MBX working condition (accidentals rate, readout rates, MBX time budget and load, MBX dead-time, etc). In this sense the MBX simulation is essentially a simulation of the inefficiency of the geometrical part of the MBX procedure. About 8000 raw data bursts have been studied selecting the MBX inefficiency events and looking for the inefficiency sources with the help of the simulation. The big part ($\sim 67\%$) of this inefficiency is due to the wires inefficiency as shown in plots 8.21 (DCH1), 8.22 (DCH2) and 8.23 (DCH4).

Looking to the events with the ZFAKE bit set to 0 and removing the $CDA < 5cm$ condition in the offline reconstruction it is possible to see the that most of them are rejected by the CDA condition (fig. 8.24). About on half of the events with $CDA < 5cm$ ($\sim 27\%$ of the total ZFAKE=0 events) can be explained because the vertex is reconstructed outside of the allowed fiducial region. The other part can be explained with the presence of an accidental particle that arrives early with respect to the charged pion, as discussed in par. 8.3.2. In the plot 8.25 the number of hits for DCH1 and DCH2 is plotted for events with $CDA < 5cm$. Usually a single track has, in average, 8 hits (one for each plane) in each chamber. The peak at the 16 hits position indicates the presence of a second track. This second track is not present in the reconstructed event because of the condition, at reconstruction program level, to exclude tracks not originating from the physical decay volume (par. 3.3.1). Most of these quasi parallel tracks are muons. The muons hit the CHOD giving a Q1 signal. The wrong time reference introduced by the muons early with respect to the charged pion, gives problems in the AB card coordinates reconstruction. In the so called "banana plot" (a plot with in the x-axis the A plane drift time and in the Y-axis the B plane drift time) the good events (the efficient events for which the hit coordinates are constructed in a correct way) are located in an limited area (with a banana shape) as in plot 8.26. The similar plot constructed for inefficient

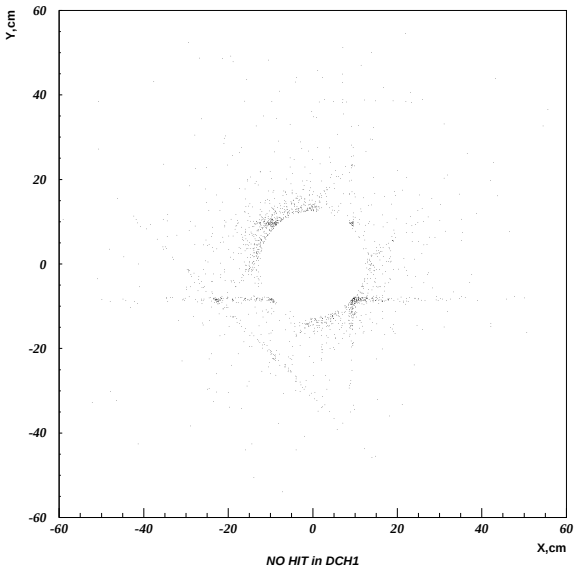

Figure 8.21: Looking for the charged pion impact point position at DCH1 in the offline reconstruction for events in which no hit in DCH1 are identified by the MBX simulation, the inefficient wires can be distinguished.

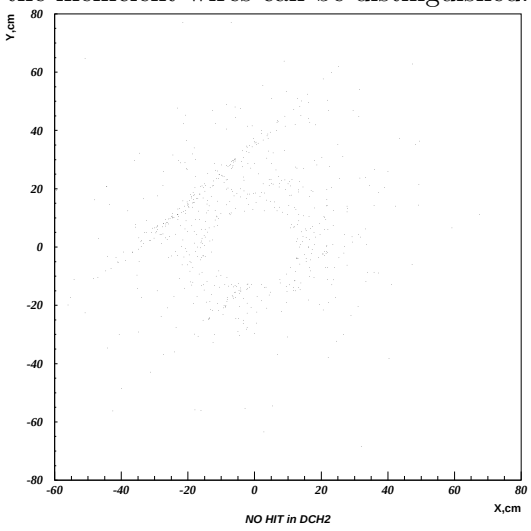

Figure 8.22: The picture on DCH2 is less clear due to the limited statistics.

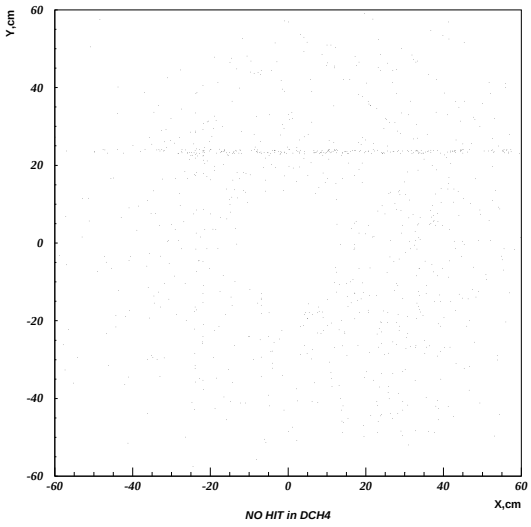

Figure 8.23: In DCH4 at least one inefficient wire, in the events considered, can be identified.

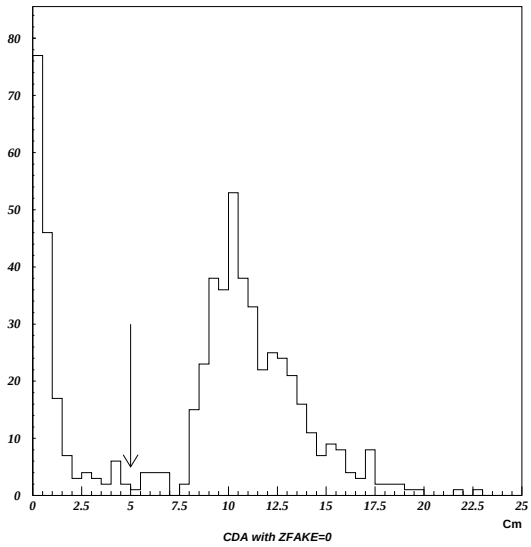

Figure 8.24: CDA distribution for events with ZFAKE=0.

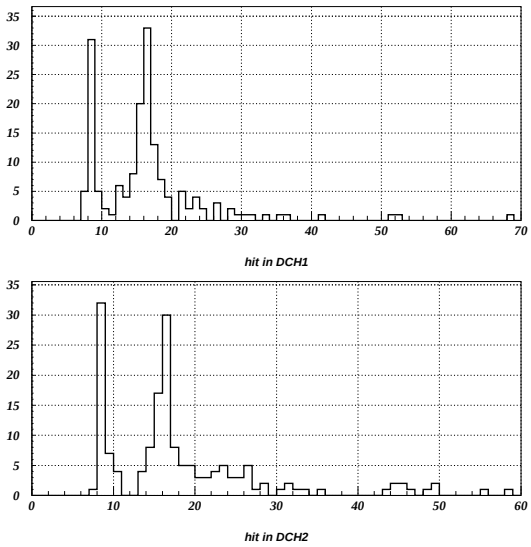

Figure 8.25: Number of MBX reconstructed hits in DCH1 and DCH2 for events with $CDA < 5cm$ and ZFAKE=0. The peak on 8 hits is given by one track while the peak on 16 hits indicates the presence of a second track.

event in which a parallel muon is presented shows a non regular shape (plot 8.27), indicating that the AB card coordinates construction fails. The different resolution in the M_{FAKE} reconstruction explains part of the remaining events.

The MBX simulation says that most of the inefficient events can be justify with geometrical inefficiency, the other part is due to the Q1 timing effect. In principle the geometrical part can be simulated with the CMC MonteCarlo in which the MBX algorithm has been included. To check the Data-MonteCarlo agreement cuts are applied on the real data in order to isolate the pure geometrical part. These cuts are essentially:

- OVFLW=0 the overflow condition (due to conversions, MBX dead time, excessive MBX load, etc.) cannot be properly simulated.
- Q1 Timestamp $\neq 5$. The TS=5 is the trigger word time stamp.
- $N_{acc} = 0$ exclude the accidental tracks to avoid timing problem (the parallel muons aren't excluded by this condition but, partially, by the condition above).

A statistics similar to the Data has been produced with the CMC MonteCarlo in which the wires efficiency is included. In the MonteCarlo case the MBX simulation is called for each event, for this reason the control sample to measure the MBX inefficiency is the whole data sample. In plot 8.28 the good agreement between MonteCarlo and the geometrical part of the data is shown. This allows to use the MonteCarlo to evaluate the systematics due to the MBX. For the SS123 the difference in Δg measured for all events and for the only MBX triggered events, is $(0.11 \pm 0.21) \cdot 10^{-4}$. This number is considered as the systematics due to the

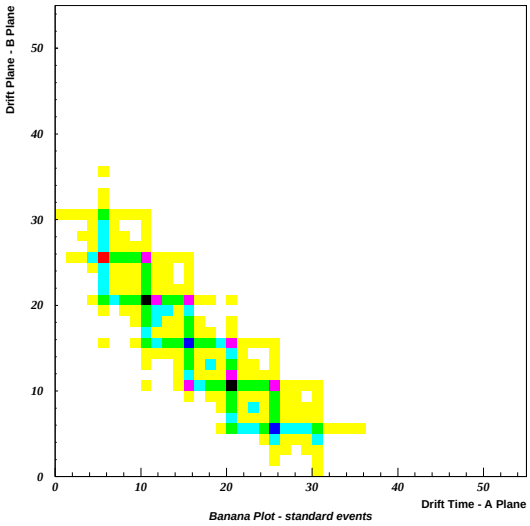

Figure 8.26: The "banana" plot is obtained comparing the plane A and plane B drift time for each view in a DCH.

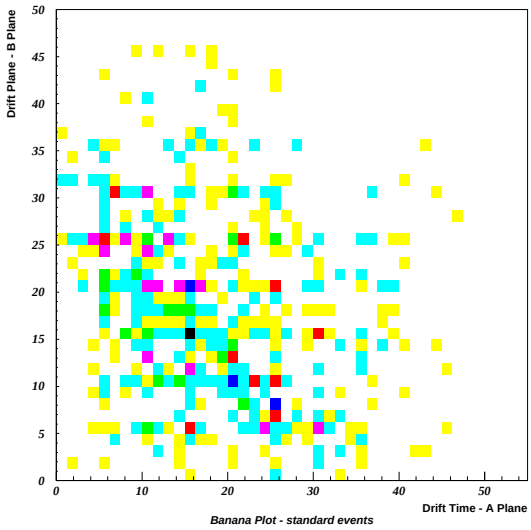

Figure 8.27: In case of events triggered by accidentals the "banana" shape is not present.

geometrical part of the MBX inefficiency. The systematics due to the timing related part has to be included. This is done studying the difference in Δg applying the cuts described above to isolate the geometrical part of the MBX. The total MBX systematics obtained with this procedure is $0.4 \cdot 10^{-4}$.

8.6 Trigger systematics

To summarize:
The L1 and L2 trigger systematics has been evaluated. The L1 systematics connected to the charged trigger part (Q1) is negligible. The Q1 systematics has been studied by using all the events with one charged track to measure the Q1 efficiency for small cells on the CHOD and re-weighting the $K^{\pm} \to \pi^{\pm}\pi^0\pi^0$ Dalitz plot distribution in each cell. The L1 trigger neutral part (NTPEAK) systematics, can not be studied in a similar way. The systematics has been evaluated from the difference between the Δg extracted from U distributions corrected and uncorrected with the NTPEAK trigger efficiency. The L2 trigger systematics has been evaluated simulating the geometrical part of the inefficiency, after a detailed study with the online MBX code on the offline raw data to define the sources of inefficiency. The time related component of the inefficiency has been evaluated on the real data. In the table 8.9 the systematics due to the whole trigger chain are summarized.

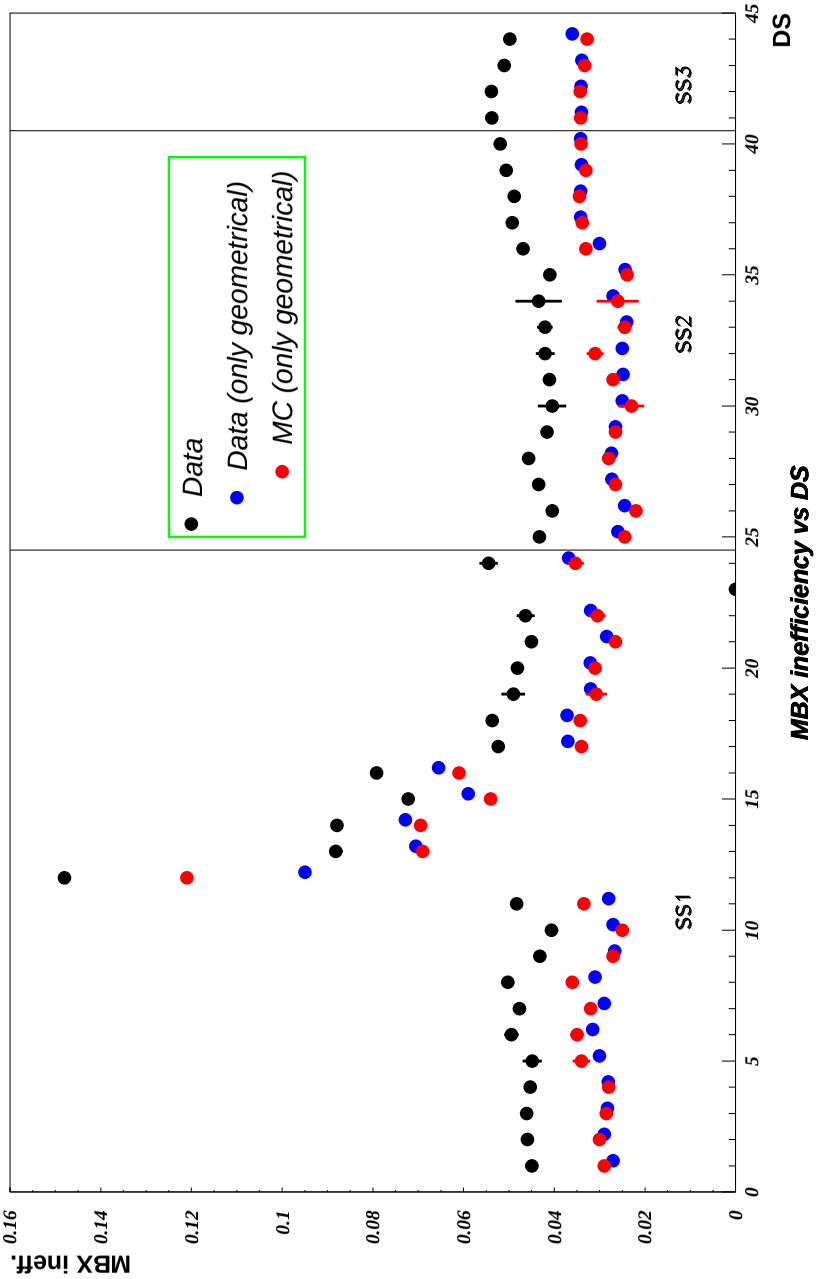

Figure 8.28: Isolating the MBX inefficiency geometrical part in the real data, the MC agreement is very satisfactory.

L1:	Q1	$< 10^{-5}$
L1:	NTPEAK	$1.3 \cdot 10^{-4}$
L2:	MBX	$0.4 \cdot 10^{-4}$
Trigger syst.		$1.4 \cdot 10^{-4}$

Table 8.9: Summary of the systematics due to the trigger components.

Chapter 9

The 2003 Final result

The results shown in the last three chapters are summarized and commented. Some check on the result stability as a function of several observable are presented in the second part of the chapter.

9.1 Summary of systematics effect

Several systematics effects have been investigate. The main systematics comes from the limited statistics in the control sample to measure the NTPEAK efficiency. Our capacity to measure the error on the trigger correction is used as upper limit on the systematics. This is a conservative approach because is not easy to imagine charge dependent effects that can bias the neutral part of the L1 trigger. However our attitude for all the systematics has been:

- Be conservative: the systematics comes from coupling of several effects (no systematics are possible from first order effect thanks to the quadruple ratio technique and the simultaneous collection of K^+ and K^-);
- Few as possible *a priori* assumption: to avoid undervaluation of complex effects;
- Limited use of MonteCarlo simulation: we can not trust our MonteCarlo at level of better than 10^{-4};
- Ignore possible correlation of systematics effect.

In the table 9.1 the systematics uncertainties are listed.

9.2 The 2003 final result

The final result based on more than $47 \cdot 10^6$ K decays ($\sim 30 \cdot 10^6$ K^+ and $\sim 17 \cdot 10^6$ K^-) collected during ~ 45 days of data taking in 2003 by the NA48/2 experiment at CERN is

$$\begin{aligned} \Delta g &= (2.3 \pm 2.8_{stat.} \pm 1.3_{trig.} \pm 1.0_{syst.} \pm 0.3_{ext.}) \cdot 10^{-4} = \\ &= (2.3 \pm 3.3) \cdot 10^{-4} \end{aligned} \tag{9.1}$$

LKr related effects	0.7
Beam geometry and charged track acceptance	0.3
$\pi \to \mu$ decay	0.5
Accidentals	0.2
Trigger L1	1.3
Trigger L2	0.4
Total systematic uncertainty	1.6
External uncertainty	0.3

Table 9.1: Summary of systematic uncertainties. All numbers are in units of 10^{-4}.

The asymmetry parameter A_g^0 is deduced from the measured value of Δg using the relation $A_g^0 = \Delta g/2g$. The result is:

$$\begin{aligned} A_g^0 &= (1.8 \pm 2.2_{stat.} \pm 1.0_{trig.} \pm 0.8_{syst.} \pm 0.2_{ext.}) \cdot 10^{-4} = \\ &= (1.8 \pm 2.6) \cdot 10^{-4} \end{aligned} \tag{9.2}$$

The precision of the measurement is limited by the statistics; the systematics error is at level of the statistical one.

9.3 Stability Checks

To be confident that our measurement is well under control, several checks have been done: we have already presented some of them speaking about the detector asymmetries and the fake asymmetries agreement with MonteCarlo.

The asymmetry has been studied in *bins* of several observables. We show here the most significant checks.

In plot 9.3 Δg is studied in bins of Kaon beam momentum. Each bin is 1.2 GeV/c wide in the range 54 to 66 GeV/c. The good χ^2 shows that not relevant bias is introduced by the eventual small difference between the two kaon paths through the achromat.

The study of the asymmetry in bins of the longitudinal decay vertex position (fig. 9.5) shows a good agreement in the whole useful range (the plot is shown in the range 0 to 7000 cm, with 10 bins 700 cm wide, because of the small statistics outside these boundaries). Indeed thanks to the quadruple ratio technique not evident difference in the K^+ and K^- acceptances is expected.

A further check on the acceptance detector asymmetry is shown in plot 9.7 in which the ratio d_{LKr}/mom_K, where d_{LKr} is the distance between the decay vertex and the LKr calorimeter and mom_K the kaon momentum, is shown using 20 bins. This ratio is a good indication of the detector radial asymmetry: indeed the radial acceptance is strongly determined by the longitudinal vertex position for a given kaon momentum. The maximum and minimum values for this observable, shown in plot 9.6, are fixed by the range allows for mom_K and d_{LKr}. The independence of the result with respect to the reconstructed Kaon mass (plot 9.9), 10 bins in the range 489.7 MeV/c^2 to 499.7 MeV/c^2, and the $|V|$ variable (plot 9.11), 10 bins in

the range 0. to 2.4, is an indication of the stability of the result with respect to the charged pion measurement and the decay kinematics.

Some of the detector characteristics are checked in the following three plots. In plot 9.13 the Δg is studied in 10 bins (in the range -6 to 6 ns) of the time difference between spectrometer and LKr. In plot 9.15 the spectrometer acceptance is checked studying the Δg dependence on the charged pion radial position at DCH1 level. The result in 19 bins in the range 13 cm to 48 cm shows a good stability. The χ^2 of plot 9.17, 10 bins in the range 17 cm to 80 cm, is quite good, indicating that there is no dependence on the radial position at the charged hodoscope, important for trigger purpose.

Finally the agreement between data and MonteCarlo is shown in plot 9.18, where the Δg values are extracted using double ratios in pairs of subsequent day sample.

Several other checks show a substantial independence of the measured Δg on every relevant detector or physical quantities.

9.4 Comments on the result

The result is obtained as average of three independent analysis that agree at level of few 10^{-5}. The small difference is due to the different order of cuts or other small differences and is fully compatible within the fluctuation due to the slightly different statistics. For this reason not adjunctive systematics is added and the final result is taken as arithmetics average. The possibility to control the systematics at level of 10^{-4} is due to the simultaneous collection of K^+ and K^- decays with very similar acceptance. The inversion of magnetic fields both in beam transport and in detector part allows to strongly reduce the influence of the detector intrinsic asymmetries. To exploit this possibility, a quadruple ratio is constructed using various field combinations instead of the simple ratio K^+/K^-. To decrease the contribution of the detector characteristics changes during the data taking the magnetic fields are frequently reversed (daily for the spectrometer magnet and on a weakly basis the field of the beam magnets). The subdetectors (DCH and LKr) high resolution on kinematical quantities allows to study the detector stability and characteristics following the small changes during the data taking.

The result shown in this work, and published on [108], is one order of magnitude more precise with respect to previous experimental results (fig. 9.1). The result is fully compatible with zero and with the SM prediction at the precision level of $\sim 3 \cdot 10^{-4}$.

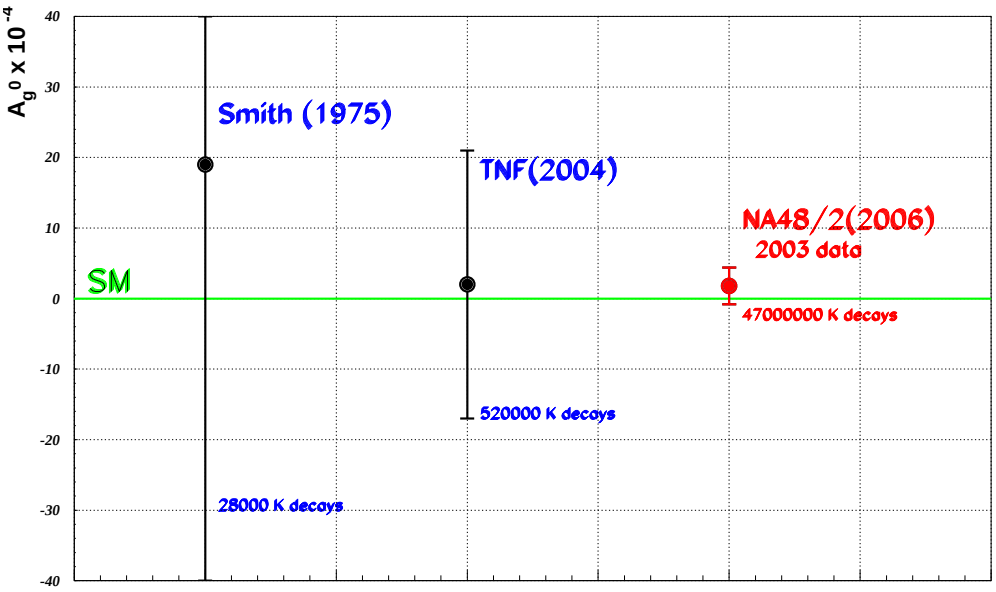

Figure 9.1: Comparison between the result presented in this thesis and previous A_g^0 measurements.

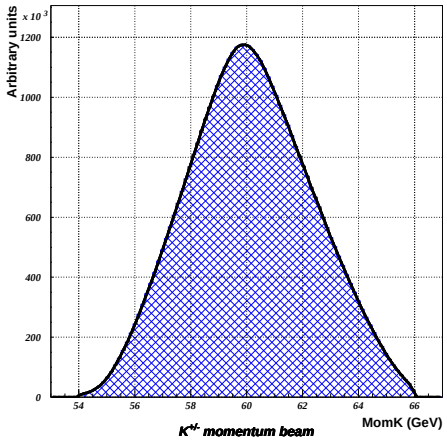

Figure 9.2: $K^{\pm}$ momentum beam distribution.

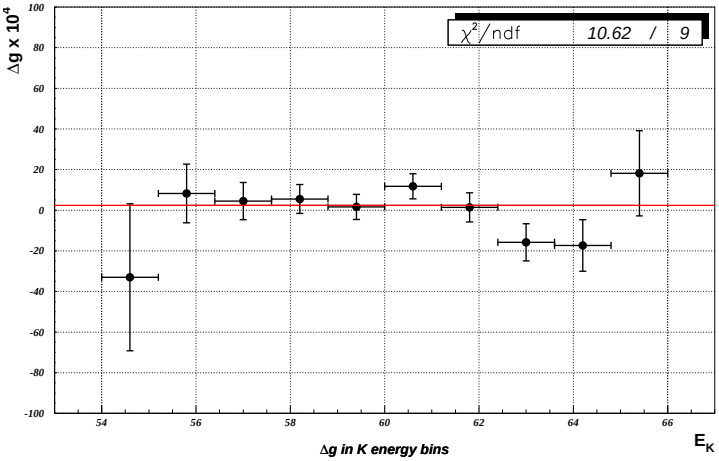

Figure 9.3: Δg in 10 bins of kaon momentum.

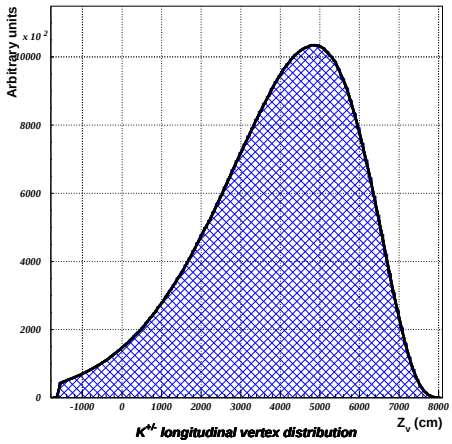

Figure 9.4: $K^{\pm}$ longitudinal vertex position.

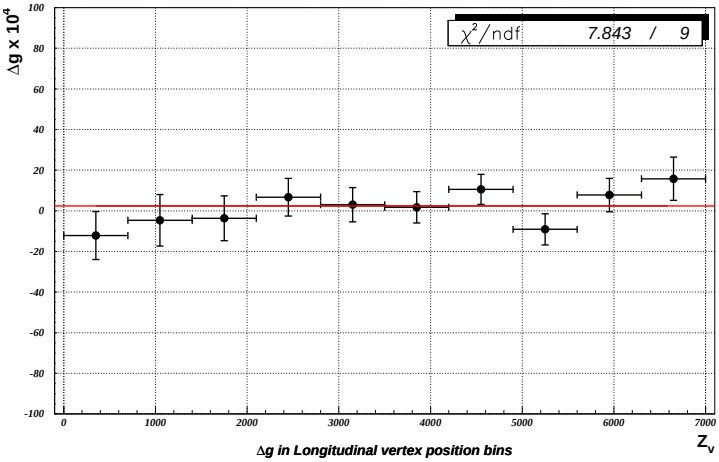

Figure 9.5: Δg in 10 bins of longitudinal vertex position.

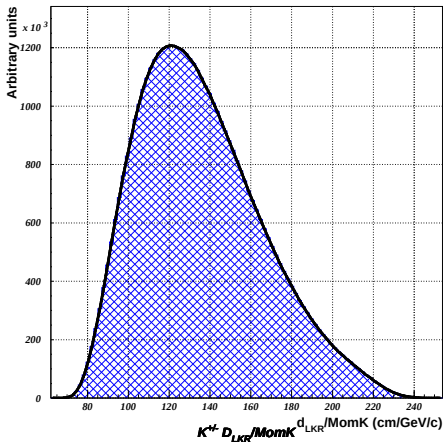

Figure 9.6: $K^{\pm}$ d_{LKr}/mom_K distribution.

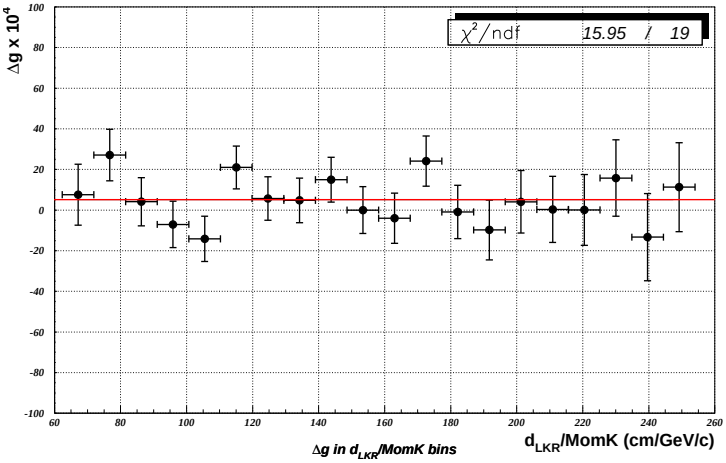

Figure 9.7: Δg in 20 bins of d_{LKr}/mom_K.

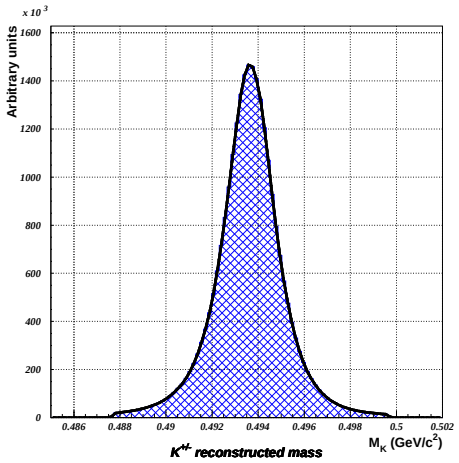

Figure 9.8: $K^{\pm}$ reconstructed kaon mass distribution.

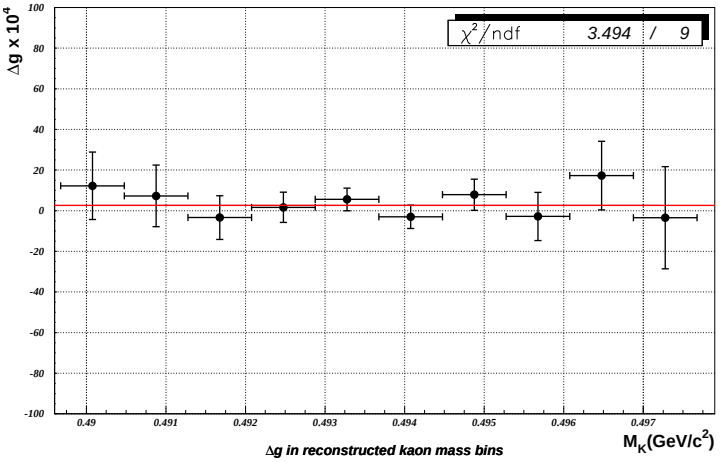

Figure 9.9: Δg in 10 bins of reconstructed kaon mass.

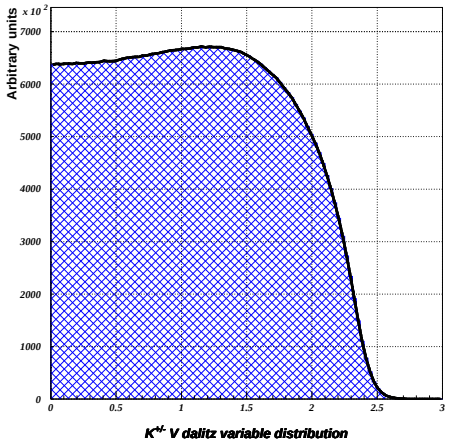

Figure 9.10: $K^{\pm}$ $|V|$ Dalitz variable distribution.

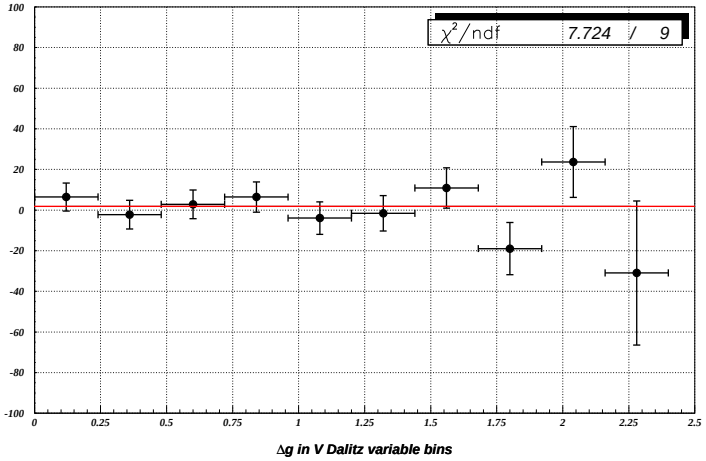

Figure 9.11: Δg in 10 bins of $|V|$ variable.

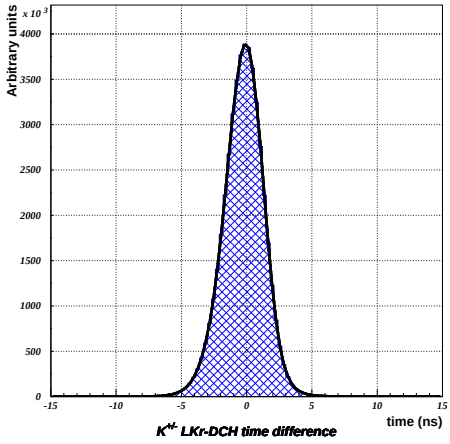

Figure 9.12: $K^{\pm}$ LKr-DCH time difference distribution

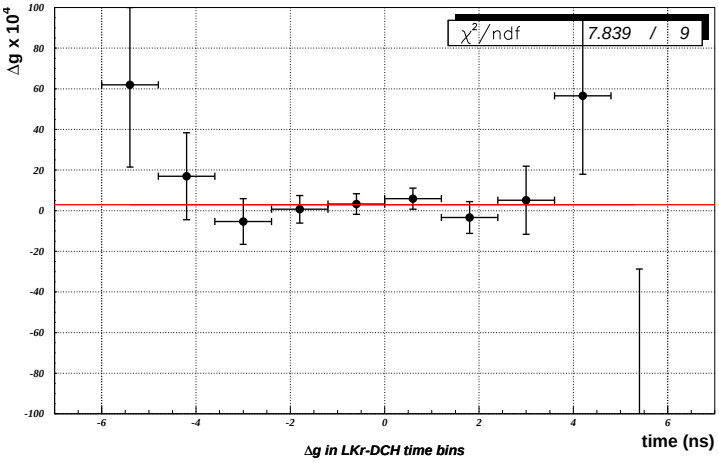

Figure 9.13: Δg in 10 bins of time difference between LKr and DCH.

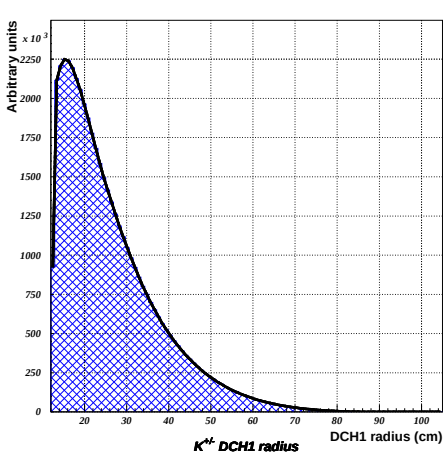

Figure 9.14: $K^{\pm}$ radial impact point position distribution at DCH1.

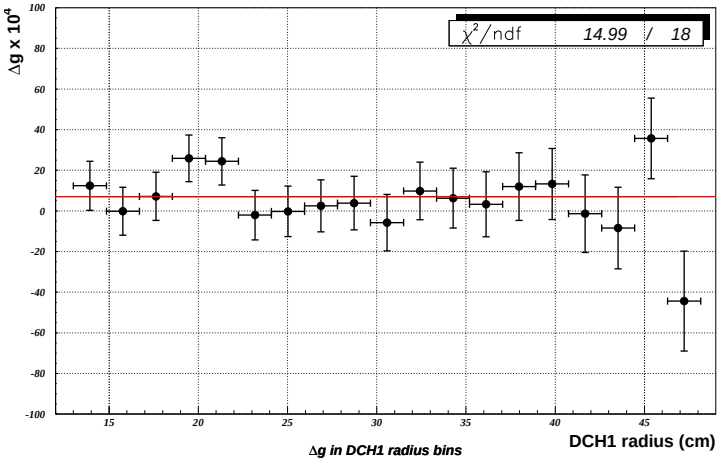

Figure 9.15: Δg in 19 bins of DCH1 radius.

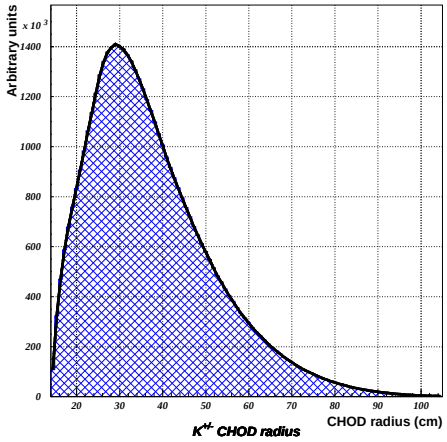

Figure 9.16: $K^{\pm}$ radial impact point position distribution at CHOD.

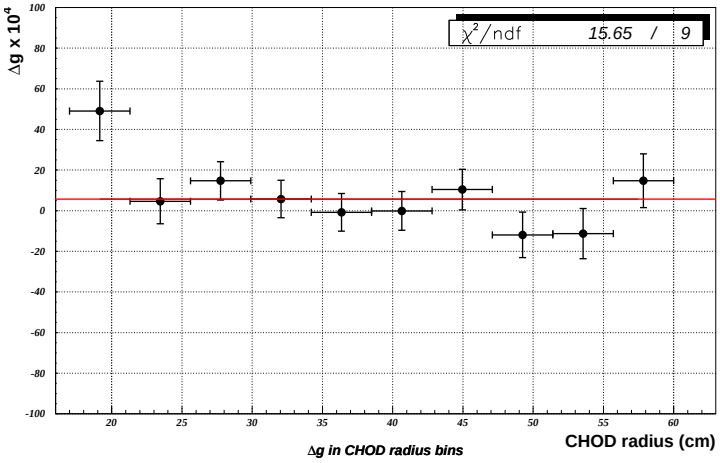

Figure 9.17: Δg in 10 bins of CHOD radius.

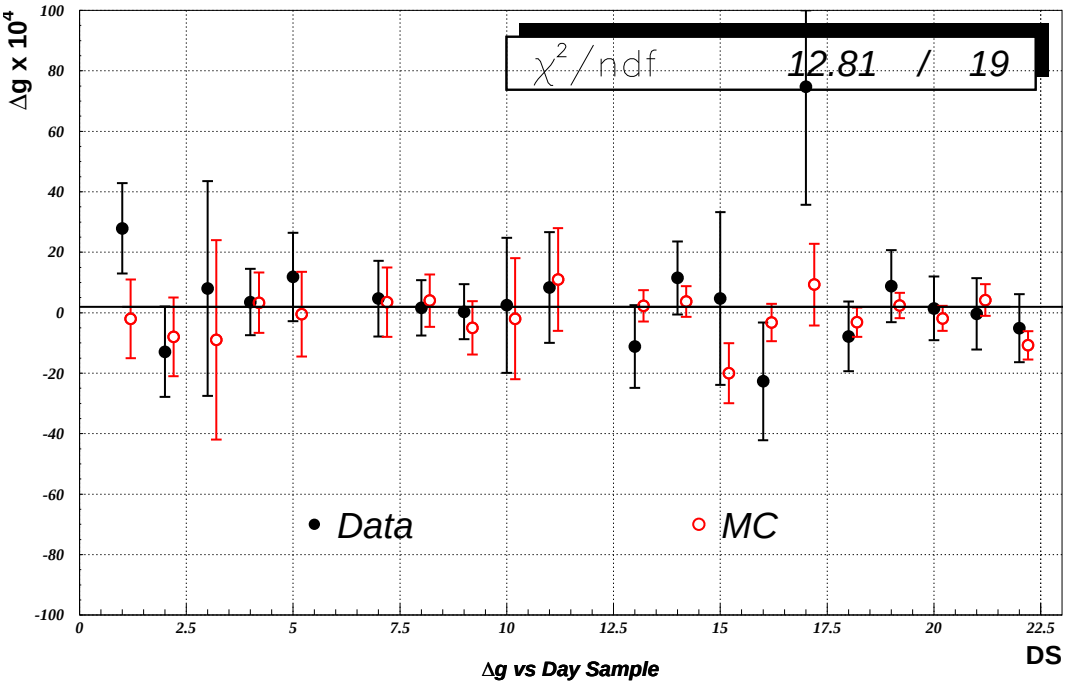

Figure 9.18: Δg (extracted with double ratio in DS pair) during the run. The MonteCarlo agreement is shown.

Conclusions

This thesis was devoted to the measurement of the CP violating parameter A_g in the charged kaon decay in three pions. In particular the work was focused on the so called "neutral" mode $K^{\pm} \to \pi^{\pm}\pi^0\pi^0$. This parameter is related to the difference in the shape between K^+ and K^- Dalitz plot distribution, and it is more sensitive to CP violation with respect to the partial decay rates comparison.

The NA48/2 experiment has collected the largest ever sample of K^+ and K^- decays. The two kaon beams of opposite charge were simultaneous and collinears in the decay region. The particular care adopted to equalize every charged asymmetric detector effects both during the data taking and the analysis has allowed to limit the systematic uncertainty at the level of few 10^{-4} , compatible to the statistical error. The sensitivity obtained reduces substantially the previously existing gap between the experimental results and the SM extensions that predict an enhancement of the A_g^0. The SM prediction of $\sim 10^{-5}$ is fully compatible with our result of:

$$A_g^0 = (1.8 \pm 2.6) \cdot 10^{-4} \ .$$

Further steps to prove the SM prediction require both a very intense kaon beam and a new detector design to control the systematics at level of few 10^{-5}. The simultaneous collection of K^+ and K^- decays would be employed in order to reduce eventual effects related to the time stability of the detector. Techniques to equalize the acceptance during the data taking have to be applied to avoid detector biases. Nowadays not other experiments have been proposed to measure the asymmetry parameter, both in "neutral" and in "charged" mode, with a better precision of the $2.6 \cdot 10^{-4}$ reached by NA48/2.

Appendix A

Dalitz plot structure and linear slope asymmetry: cusp effect

Thanks to the large statistics collected and the high accuracy and resolution in the measurement of the $\pi^0\pi^0$ invariant mass in $K^\pm \to \pi^\pm\pi^0\pi^0$ a cusp like effect has been put in evidence in the U distribution . In correspondence with $m_{\pi^0\pi^0} = m_{\pi^+\pi^-}$ a clear discontinuity appears in the derivative of the U distribution. It can be explained as due to virtual $\pi^+\pi^- \to \pi^0\pi^0$ charge exchange scattering. Studying this effect the $(a_0 - a_2)$ pion scattering length can be deduced.

A.1 Structure in Dalitz plot

In plot A.1 the reconstructed U distribution is shown with a fine binning and at $U \sim -1.12$ a sudden change in derivative of the events distribution function is evident. Previous experiments were not able to see this structure because of the smaller statistics and the much worse resolution on the recostructed U Dalitz variable[1]. For instance in fig. A.2 the U and $|V|$ distribution obtained by the ISTRA+ experiment [118] is shown with ~ 252000 $K^- \to \pi^-\pi^0\pi^0$ events. No evidence of singularity has been observed in the position in which we observe the particular structure and the χ^2 of the fit was 502/558 (2D Dalitz Plot fit). In the same way in 1998 the HYPERON-2 experiment[119] and an experiment in 1975 at PS [120], based respectively on 33000 $K^- \to \pi^-\pi^0\pi^0$ and 115000 $K^\pm \to \pi^\pm\pi^0\pi^0$ events, did not see any anomaly in the U distribution (fig. A.3 and A.4). In the following we will use the $M^2_{\pi^0\pi^0}$ (or M^2_{00}) instead of the U distribution. This two observables are totally equivalent being linked by the eq. (3.2).

A.2 Interpretation of the structure

The observed anomaly position at precisely *two times the nominal charged pion mass* $m_{\pi^\pm}$. suggests, essentially, two possible phenomenological interpretations:

[1]Sometimes the U variable, used in this dissertation, is called with the letter Y (and the variable V corresponds to the letter X), specially in past experiments and theoretical works.

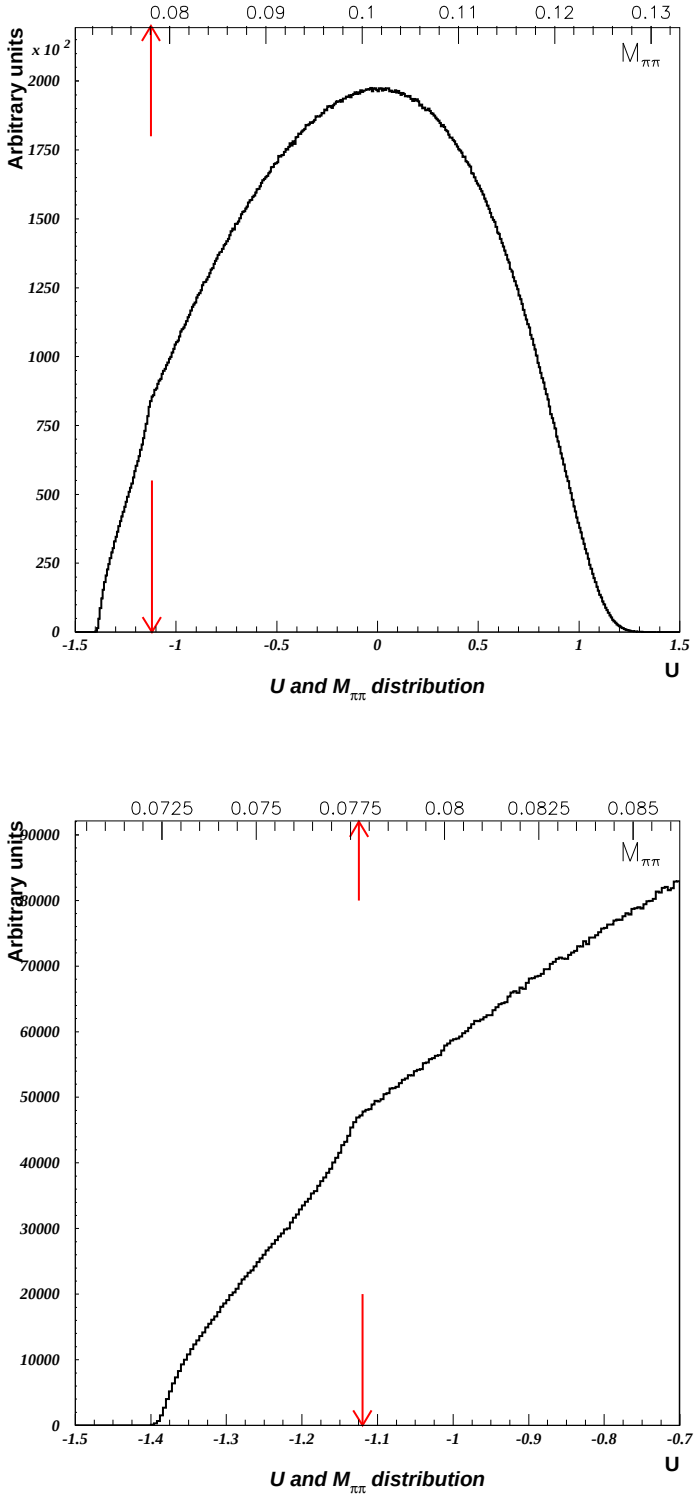

Figure A.1: U distribution plotted with 420 bins in the range -1.522 to 1.712. In the upper part of the plot the corresponding scale for the $M^2_{\pi^0\pi^0}$ distribution is shown. The threshold of $\pi^+\pi^-$ production is in the position $4m_{\pi^+} = 0.7792$ or $U = -1.124$: with this binning the singularity lies in the 51^{st} bin. In lower plot the interesting region is zoomed.

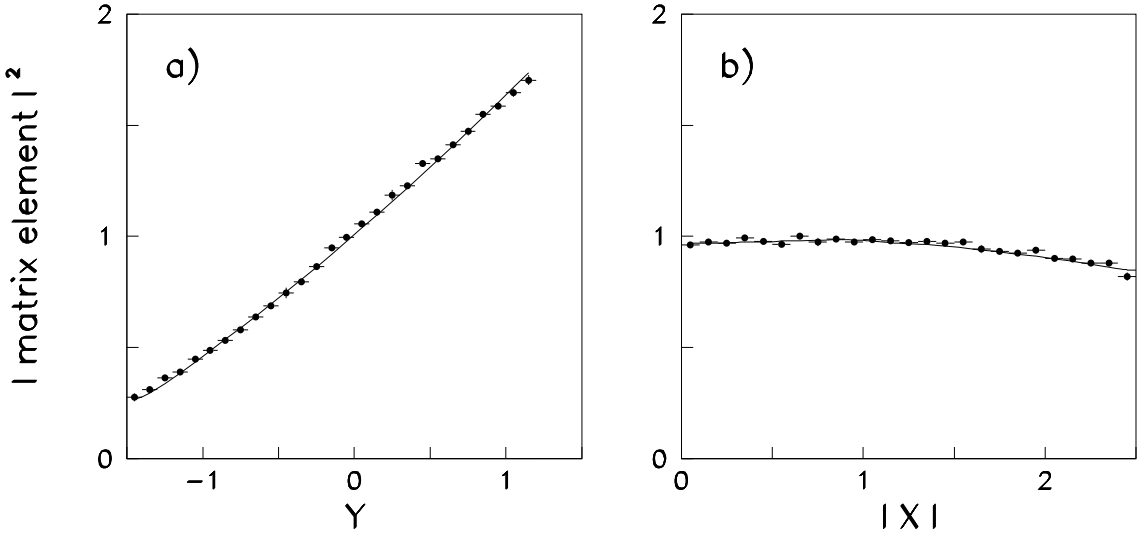

Figure A.2: ISTRA+ experiment result for the U (Y) and V(X) fit (in each plot the U and V are integrated in the Dalitz plot along the other variable). The result of the fit with the usual parametrization is $g = 0.627 \pm 0.011$, $h = 0.046 \pm 0.013$ and $k = 0.001 \pm 0.004$ ($\chi^2 = 502/558$), with no structure around $U \sim -1.12$.

- The creation of bounded electromagnetic states of charged pions pair in short lived *pionic* atoms (also known as *pionium*), that decays hadronically in $\pi^0\pi^0$ with a lifetime of [121] $\sim 3. \cdot 10^{-15}$ s:

$$\pi^+\pi^- \rightarrow \text{ pionium } \rightarrow \pi^0\pi^0$$

- The reaction, driven by strong interaction, of virtual charge exchange *rescattering*:

$$\pi^+\pi^- \rightarrow \pi^0\pi^0$$

In both cases the $\pi^+\pi^-$ pions originate from the $K^\pm \rightarrow \pi^\pm\pi^+\pi^-$ decay. As will be explained in the next sections by for the main contribution comes from the second effect: the strong rescattering. In particular the different phase relative to the direct transition $K^\pm \rightarrow \pi^\pm\pi^0\pi^0$ of the rescattering process contribution before and after the threshold, is the source of the "cusp" structure observed.

A.2.1 The Cabibbo approach

In a first paper on this subject [122], N.Cabibbo explained the main features of this cusp effect and its connection to the $\pi\pi$ scattering lengths. The argument is summarized below. The amplitude contribution $\mathcal{M}_0$ from the dominant three body decay, represented by the diagram in fig. A.5, is reasonably described by a simple expansion:

$$\mathcal{M}_0(s_1, s_2, s_3) = A^0_{av} \cdot (1 + \frac{g^0(s_3 - s_0)}{2m_{\pi^+}} + ...) \qquad \text{(A.1)}$$

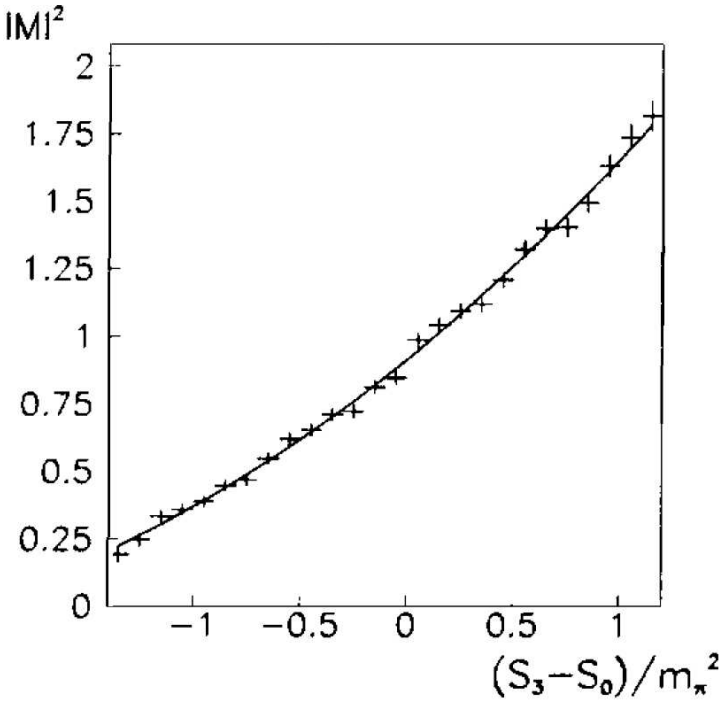

Figure A.3: U distribution for 33000 $K^- \to \pi^-\pi^0\pi^0$ decays [119] . The fit results are $g = 0.736 \pm 0.014$, $h = 0128 \pm 0.015$ and $k = 0.0197 \pm 0.0045$. The χ^2 per degree of freedom is 1.5.

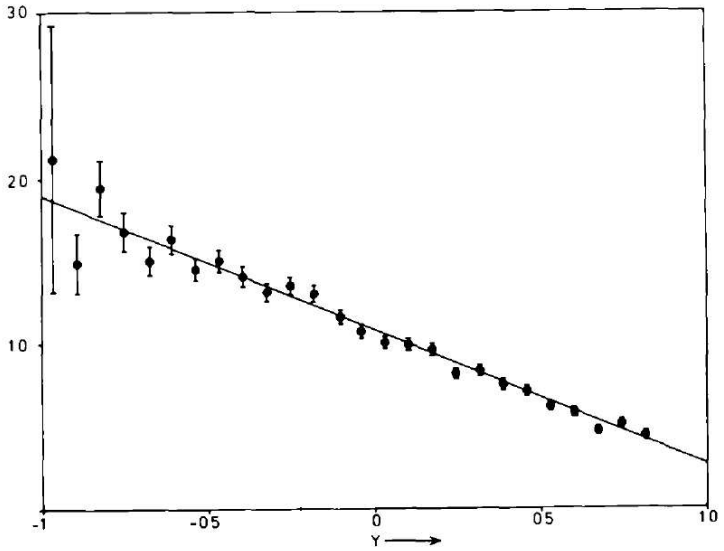

Figure A.4: U distribution for ~ 115000 $K^\pm \to \pi^\pm\pi^0\pi^0$ [120] events . The values obtained are $g = 0.510 \pm 0.060$ and $h = 0.009 \pm 0.040$. The χ^2 is 24.5/23. The slope in the figure is negative because the different normalization (see [120] for further details).

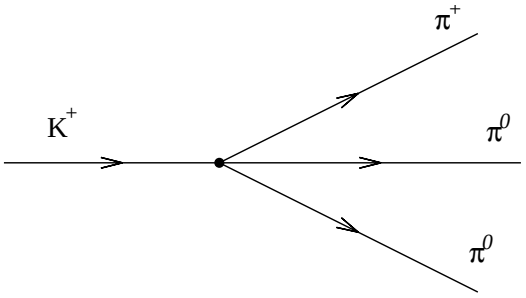

Figure A.5: Direct $\pi^0\pi^0$ production.

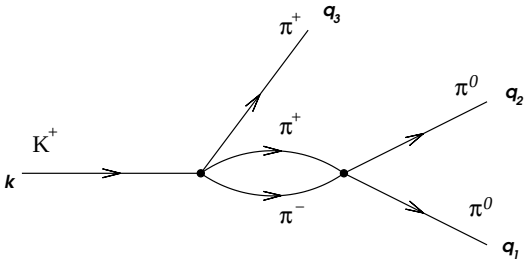

Figure A.6: $\pi\pi$ rescattering diagram.

The charge exchange process, described by the diagram in fig. A.6, has to be taken into account in order to study the contribution in the Dalitz plot near the threshold of $2m_{\pi^+}$. Therefore the total amplitude can be written as:

$$\mathcal{M}(K^+ \to \pi^+\pi^0\pi^0) = \mathcal{M}_0 + \mathcal{M}_1$$

where the $\mathcal{M}_0$ is defined by eq. (A.1) and $\mathcal{M}_1$ is the contribution coming from the charge exchange process in $K^+ \to \pi^+\pi^+\pi^-$ decay, with the condition

$$\mathcal{M}_1 = 0 \qquad \text{for} \qquad s_3 = s_{\pi\pi} = (q_1 + q_2)^2 = M^2_{\pi^0\pi^0} = 4m^2_{\pi^+}$$

The $\mathcal{M}_1$ can be evaluated with a simple approach based on a simplified Lagrangian assuming unitarity and analyticity only [122]. The result, near the threshold, is:

$$\mathcal{M}_1 = -\frac{2(a_0 - a_2)m_{\pi^+}}{3}\mathcal{M}_{+,thr}(J + K) \tag{A.2}$$

where $\mathcal{M}_{+,thr}$ is the $K^+ \to \pi^+\pi^+\pi^-$ amplitude in the threshold position, written as:

$$\mathcal{M}_{+,thr} = A^+_{av}\left(1 + \frac{g^+ \cdot (m^2_K - 9m^2_{\pi^+})}{12m^2_{\pi^+}}\right) \tag{A.3}$$

In eq. (A.2) the quantity $(a_0 - a_2)$ is the difference between the pion scattering lengths for I=0 and I=2. The graph contribution has been split in two parts, J and K. The K part can be reabsorbed in the $\mathcal{M}_0$ redefinition because it can be simply redefined as a polynomial expansion in terms of $(s_{\pi\pi} - 4m^2_{\pi^+})$ while the J contribution has a particular behaviour depending on the threshold. Indeed it is:

$$J = J_{below} = \pi v_- \tag{A.4}$$

$$J = J_{above} = -i\pi v_+ \tag{A.5}$$

The subscript below and above refers to the position with respect to the $2m_{\pi^+}$ threshold; in fact v_- and v_+ are defined as:

$$v_- = \sqrt{\frac{4m^2_{\pi^+} - s_{\pi\pi}}{s_{\pi\pi}}} \qquad \text{for} \qquad s_{\pi\pi} < 4m^2_{\pi^+} \tag{A.6}$$

$$v_+ = \sqrt{\frac{s_{\pi\pi} - 4m^2_{\pi^+}}{s_{\pi\pi}}} \qquad \text{for} \qquad s_{\pi\pi} > 4m^2_{\pi^+} \tag{A.7}$$

With these prescriptions the $\mathcal{M}_1$ component of the total amplitude has different behaviour below and above the threshold:

$$\mathcal{M}_1 = -2\frac{(a_0 - a_2)m_{\pi^+}}{3}\mathcal{M}_{+,thr}\sqrt{\frac{4m_{\pi^+}^2 - s_{\pi\pi}}{s_{\pi\pi}}} \text{ for } s_{\pi\pi} < 4m_{\pi^+}^2 \tag{A.8}$$

$$\mathcal{M}_1 = 2i\frac{(a_0 - a_2)m_{\pi^+}}{3}\mathcal{M}_{+,thr}\sqrt{\frac{s_{\pi\pi} - 4m_{\pi^+}^2}{s_{\pi\pi}}} \text{ for } s_{\pi\pi} > 4m_{\pi^+}^2 \tag{A.9}$$

The last equations show as the amplitude $\mathcal{M}_1$ changes from real to imaginary at the $\pi^+\pi^-$ threshold production. The total amplitude can be written as:

$$\mathcal{M}^2 = \begin{cases} (\mathcal{M}_0)^2 + (\mathcal{M}_1)^2 + 2\cdot\mathcal{M}_0\mathcal{M}_1 & s_{\pi\pi} < 4m_{\pi^+}^2 \\ (\mathcal{M}_0)^2 + |\mathcal{M}_1^2| & s_{\pi\pi} > 4m_{\pi^+}^2 \end{cases} \tag{A.10}$$

Below threshold the terms $\mathcal{M}_0\mathcal{M}_1$, with a sign minus given by the sign in eq. (A.8), gives a destructive interference while above threshold no interference terms appear. In fig. A.7 the differential decay rate with respect to the $M_{\pi^0\pi^0}$ invariant mass given by the equation:

$$\frac{d\Gamma}{dM_{\pi^0\pi^0}} = \left[(M_{\pi^0\pi^0}^2 - 4m_{\pi^0}^2)\cdot\left(1 - \frac{(M_{\pi^0\pi^0} + m_{\pi^+})^2}{m_K^2}\right)\cdot\left(1 - \frac{(M_{\pi^0\pi^0} - m_{\pi^+})^2}{m_K^2}\right)\right]^{1/2}\cdot|\mathcal{M}|^2$$

where $\mathcal{M}$ is defined by eq. (A.10), it is shown assuming, in fig. A.7, $(a_0 - a_2)m_{\pi^+} = 0.265$ [4] and no rescattering $a_0 - a_2 = 0$. This formulation is valid in the limit of exact isospin symmetry. A parameter e can be defined to take into account the isospin breaking effect:

$$e = \frac{m_+^2 - m_0^2}{m_0^2} \sim 0.065$$

in this way the quantity formulas above can be redefined using:

$$a_x = (1 + \frac{e}{3})\frac{(a_0 - a_2)}{3} \tag{A.11}$$

instead of $(a_0 - a_2)/3$. Another contribution at this order comes from the $\pi^0\pi^0 \to \pi^0\pi^0$ rescattering that can be included in the formulation above using another amplitude term $\mathcal{M}_2$. The value of this new term is:

$$\mathcal{M}_2 = -\frac{(a_0 + 2a_2)m_{\pi^0}}{3}\mathcal{M}_{0,thr}\left(-i\sqrt{\frac{s_{\pi\pi} - 4m_{\pi^0}^2}{s_\pi\pi}}\right)$$

where $\mathcal{M}_{0,thr}$ is the unperturbed $\mathcal{M}_0$ calculated at threshold. The contribution of this term is smaller than the $\mathcal{M}_1$ term and it does not change behaviour crossing the threshold.

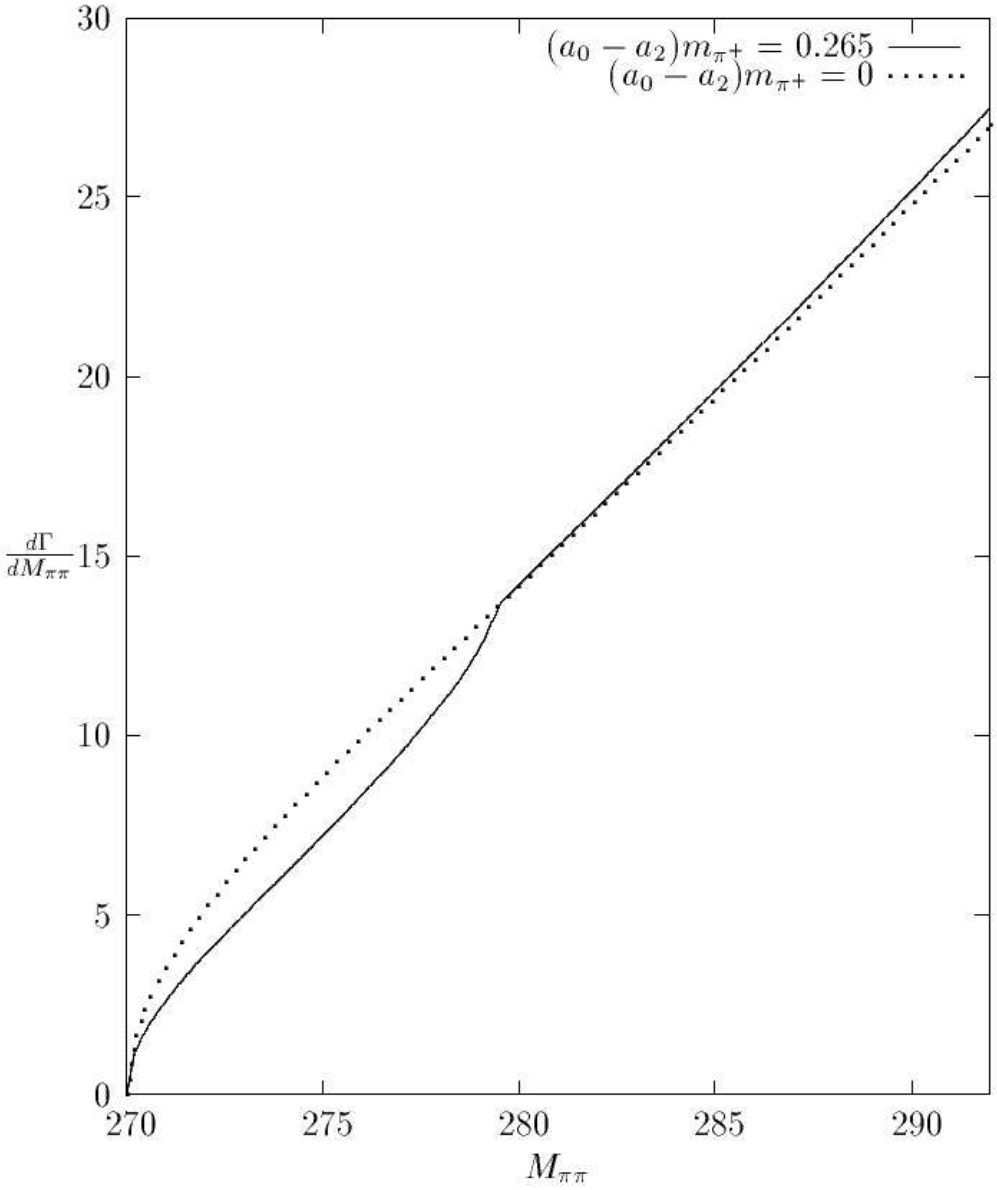

Figure A.7: $\pi^0\pi^0$ invariant mass distribution (in arbitrary units) assuming no rescattering (dots) and $(a_0 - a_2)m_{\pi^+} = 0.265$ (solid line). The departure from the no rescattering condition is quite evident below the $\pi^+\pi^-$ threshold.

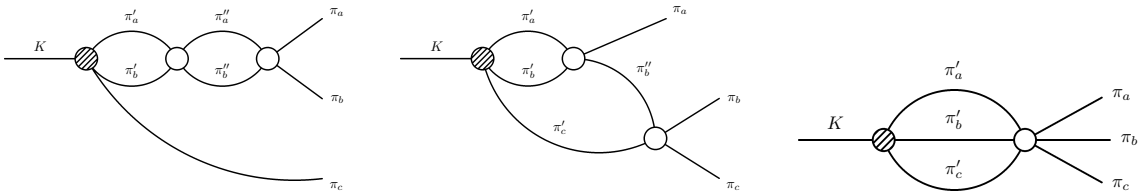

Figure A.8: Some example of two loops contributions. The last irreducible $3\pi \to 3\pi$ needs ChPt to be treated, but its contribution to the whole amplitude turns out negligible.

A.2.2 The Cabibbo-Isidori model

Both the leading perturbative amplitude $\mathcal{M}_1$ and the small neutral pions rescattering $\mathcal{M}_2$ described in the previous section are "1 loop" corrections to the tree level amplitude $\mathcal{M}_0$. Other high order contributions have to be included in the theory. In a following paper [123], by N. Cabibbo and G. Isidori, this is done in a systematic way using the unitarity and the analyticity of the S matrix only, to expand the amplitudes in terms of $\pi\pi$ scattering lengths. In this sense the higher order diagrams with 2 loops can be treated as expansions in terms of the square of pion scattering lengths (a_0 and a_2). The general result obtained stopping the expansion at a^2 order (fig. A.8), is that the full amplitude can be expressed as:

$$|\mathcal{M}|^2 = (ReA_{00+})^2 + \Delta_A + v_\pm(s_{\pi\pi})\Delta_{cusp} + O(a_i^3)$$

where the velocities $v_\pm$ are defined in eq. (A.6) and

$$\Delta_A = (ImA_{00+})^2 + v_\pm^2(s_{\pi\pi})(ImB_{00+})^2$$

$$\Delta_{cusp} = \begin{cases} -2ReA_00{+}ImB_{00+} & s_{\pi\pi} < 4m_{\pi^+}^2 \\ 2ReA_{00+}ReB_{00+} + 2ImA_{00+}ImB_{00+} & s_{\pi\pi} < 4m_{\pi^+}^2 \end{cases} \tag{A.12}$$

we refer to [123] for the explicit expression of the various terms. Here we want just to qualitatively comment the functional form. The component A_{00+} in the limit of no-rescattering becomes the $\mathcal{M}_0$ leading component. Assuming the possibility of strong rescattering the $\mathcal{M}_0$ has to be modified including linears and quadratics scattering length terms[2] . The B_{00+} terms are responsible of the cusp structure. In particular the ImB_{00+} is directly proportional to a_x. The negative square-root behaviour below threshold already described at first order one loop level with linear a_x term, comes from the first equation in (A.12). The presence of an ImB_{00+} term also in the second equation in (A.12) turns out, that with this more complete theory, a second square-root behaviour, relatively smaller than the leading one, could be observed in the region above the $\pi^+\pi^-$ threshold. This means that the full description of the $\pi^+\pi^0\pi^0$ amplitude introduces, in general, a modification of the unperturbed $\mathcal{M}_0$ (fig. A.9), due to the effects given by the high order rescattering, in the whole $M_{\pi^0\pi^0}$ spectrum. Using this approach the expected theoretical error on the extraction of a_x is at level of 5%. A further reduction of the theoretical uncertainty can be reached with the study of the higher order terms $O(a^3)$ and calculating radiative corrections.

[2]In particular the terms $a_{+0} = a_2/2$ coming from $\pi^+\pi^0 \to \pi^+\pi^0$, $a_{00} = (a_0 + 2a_2)/3$ from $\pi^0\pi^0 \to \pi^0\pi^0$ and a_x defined in eq. (A.11) for the $\pi^+\pi^- \to \pi^0\pi^0$.

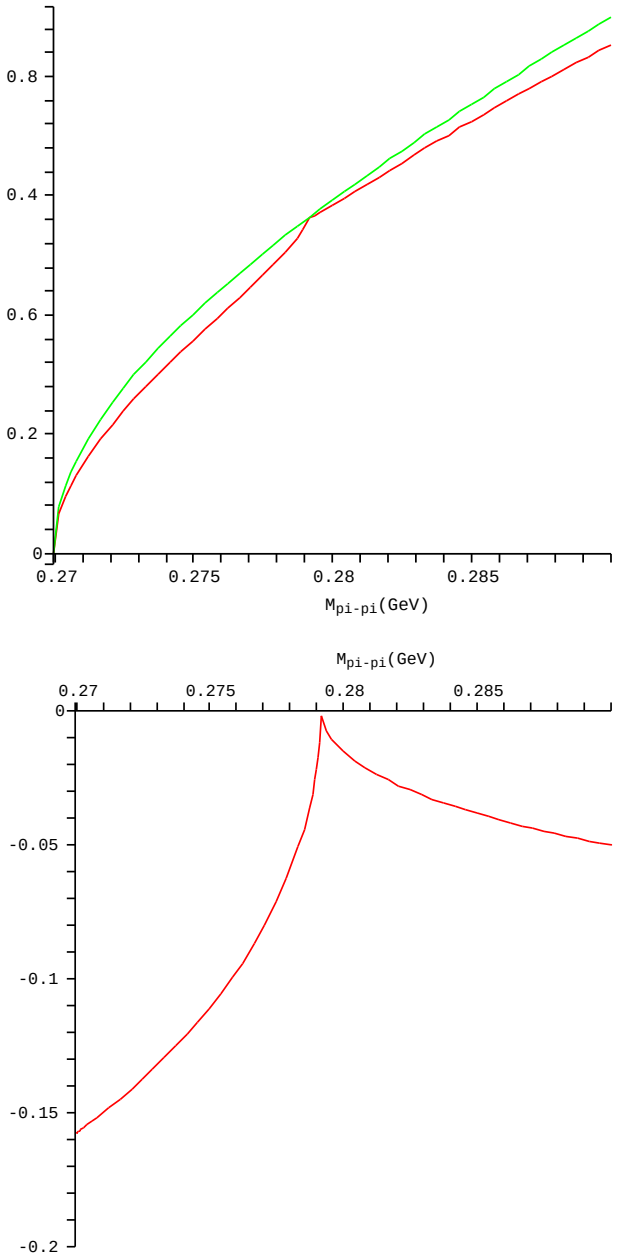

Figure A.9: In the upper plot the differential decay distribution in arbitrary units with respect to the $\pi^0\pi^0$ mass is shown. The departure from the simple polynomial expansion is now evident also above the threshold (see for comparison fig. A.7 based on one loop Cabibbo approach). This can be easily observed in the lower plot in which the ratio between the two curves is presented.

The same error has been obtained by Gamiz et al. [124] [125] studying the the full final state interaction phases in the framework of the Next to Leading Order (NLO), $O(p^6)$ in ChPt.

A.2.3 The CGKR approach

In the Cabibbo-Isidori approach is explicitly missed the possibility to include automatically electromagnetic effects. The expansion is, indeed, expressed in terms of scattering lengths powers, generated by the strong rescattering in final state. The systematics approach resulting is very flexible to include higher order effects, but it is not easy to automatically take into account for the radiative corrections, coulomb scattering or other electromagnetic effects. Colangelo et al. in [126] attempt to solve the problem using an approach based on a non relativistic effective Lagrangian. The result, including tree, one loop and two loops diagram can be expressed as a double expansion of kinetic energy (ϵ^2) and of the threshold parameter a. The Lagrangian allows to include higher order contribution proportional to the velocity (the Cabibbo-Isidori theory is valid for terms linear in pions relative velocity) and electromagnetic effects. The amplitudes for the one loop graph (until the order $a\epsilon^3$) agree with the Cabibbo-Isidori amplitudes, but some departure is presented away from the threshold region (in particular for high values of $s_{\pi\pi}$) (fig. A.10) if the two loops are considered. The final goal of this approach is to reach an error at level of 1%.

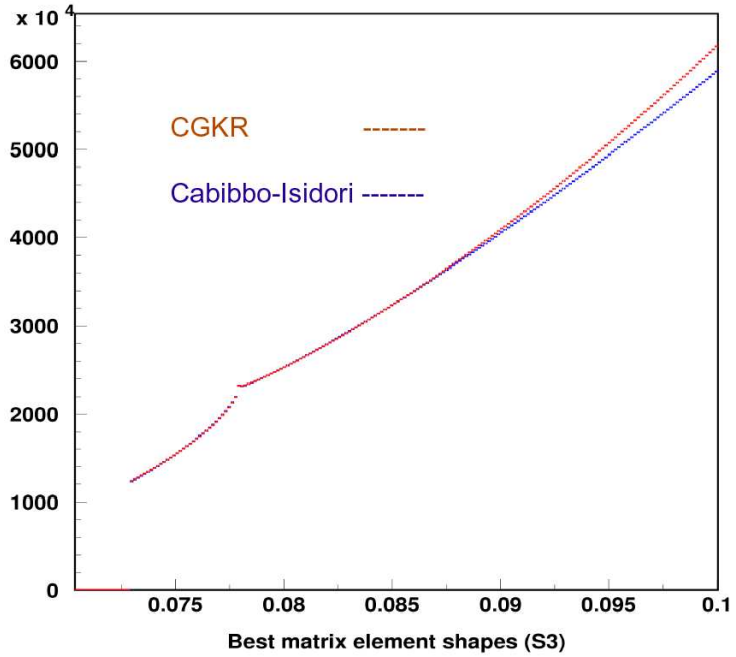

Figure A.10: Comparison between the prediction given by the Cabibbo-Isidori theory and the CGKR theory. The difference, coming from $a^2\epsilon^2$ terms in the two loops amplitudes, appears mainly far from the threshold region [127].

A.2.4 The electromagnetic bound state: the Pionium

The experimental search for the pionic atoms in the Kaon decay was the original reason that triggered the NA48/2 accurate study of the $K \to 3\pi$ Dalitz Plot. The pionic atoms, electromagnetic bound states of two opposite charged pions, was for the first time theorized in 1961 by Uretsky and Palfrey [128]. Starting from 1972 experiments have produced and studied pionic atoms through pion production in pion proton inelastic interactions. It was already realized in [128] that the pionium could also be formed in particle decays, in particular in the charged and neutral kaon, in the η and $\eta^{'}$ and in $\Psi(2S)$ and $\Upsilon(2S)$ decays. According to [129], the table A.1 shows the BR for pionic atom production (the pionium is indicate with $A_{2\pi}$).

In particular the relative pionic atoms production width in the K^+ decay with

$Br(K^+ \to \pi^+ A_{2\pi})$	$\sim 5.5 \cdot 10^{-7}$
$Br(K^0 \to \pi^0 A_{2\pi})$	$\sim 1.1 \cdot 10^{-7}$
$Br(\eta \to \pi^0 A_{2\pi})$	$\sim 2 \cdot 10^{-8}$
$Br(\eta^{'} \to \eta A_{2\pi})$	$\sim 6.2 \cdot 10^{-7}$
$Br(\Psi(2S) \to \Psi(1S) A_{2\pi})$	$\sim 1.4 \cdot 10^{-8}$
$Br(\Upsilon(2S) \to \Upsilon(1S) A_{2\pi})$	$\sim 5.2 \cdot 10^{-8}$

Table A.1: BR for pionic atoms production in mesons decay.

respect to the $\pi^+\pi^0\pi^0$ and $\pi^+\pi^+\pi^-$ channels[3] is:

$$\frac{\Gamma(K^+ \to \pi^+ A_{2\pi})}{\Gamma(K^+ \to \pi^+\pi^0\pi^0)} \sim 2.6 \cdot 10^{-5}$$

$$\frac{\Gamma(K^+ \to \pi^+ A_{2\pi})}{\Gamma(K^+ \to \pi^+\pi^+\pi^-)} \sim 0.8 \cdot 10^{-5} \tag{A.13}$$

The pionium decays, with a lifetime, in the order of $\sim 3. \cdot 10^{-15}$ s, mainly through the process $A_{2\pi} \to \pi^0\pi^0$. The pionium lifetime can be related to the scattering lengths as will be explain in par. A.4.

A.3 Experimental results

In plot A.1 the experimental $M^2_{\pi^0\pi^0}$ distribution is shown in 420, 0.0015 GeV^2/c^4 wide, bins. The results shown here are based on $2.3 \cdot 10^7$ events in SS2 and SS3 (2003). They are published in [130]. Thanks to the recipes given by the theoretical work described in the previous section[4] it is possible to extract the scattering lengths values. The detector acceptance and the resolution are obtained with MonteCarlo simulation (fig. A.11). Two analysis has been performed using a Toy MonteCarlo, in which the main detector effects (particles interaction, trigger efficiency, etc.) are

[3]The number given here is calculated using the latest PDG results [4], while the result in the table A.1 are the original Silagadze [129] results.

[4]The fit using the CGKR approach is in progress.

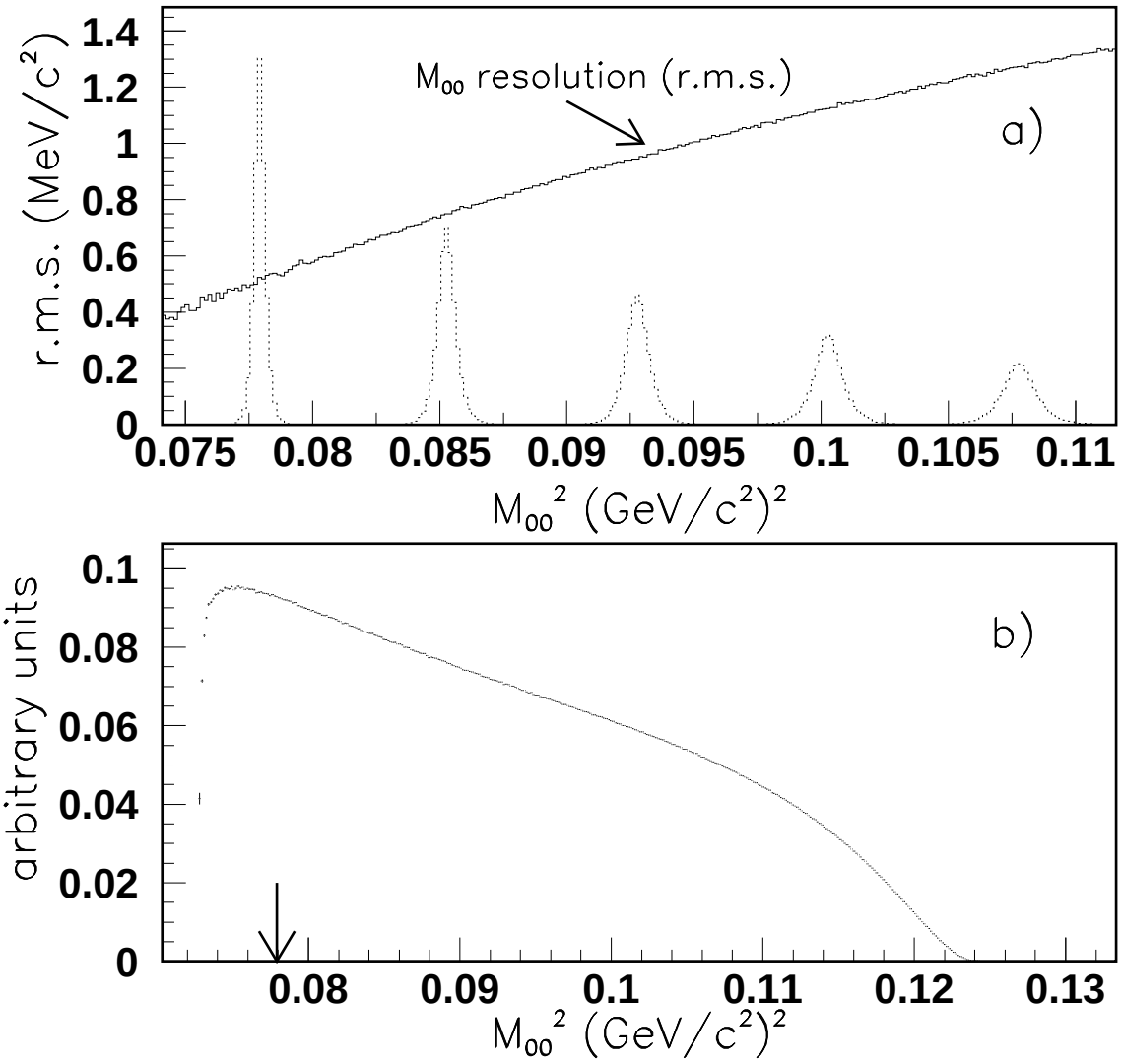

Figure A.11: a) $M_{\pi^0\pi^0}$ resolution. The gaussians in the plot's background show as the $M^2_{\pi^0\pi^0}$ looks like after the reconstruction for five generated values. No evident not gaussian tails are observed; b) Detector acceptance as a function of $M^2_{\pi^0\pi^0}$; both resolution and acceptance have not singular behaviour in correspondence of the cusp observed on real data (indicated by the arrow in the acceptance plot).

taken into account, and with the complete CMC MonteCarlo in which all the secondary particles are traced through the detector and the beam movement and the DCH wires efficiency change during the run according to the real conditions. The two approaches agree perfectly.

Several checks has been done in order to exclude that the observed cusp was due to some instrumental effects and, at the same time, to validate the MonteCarlo from which the fitting procedure depends. The acceptance and the resolution do not have any singular behaviour in the cusp position. In the same ways the L2 trigger cut, studied with a large K_{e3} sample, is not responsible of the cusp structure. In plot A.12 the ratio between the photon energy for events in small intervals just above and below the threshold is plotted. The agreement between data (dots) and MonteCarlo (solid line), in which the Cusp is not included, says that the shape of the photon energy is correctly described by the MonteCarlo in different $M_{\pi^0\pi^0}$ regions and therefore that the Cusp can not be generated by instrumental effect, at least in the considered observables. Several others variables has been taken into account to understand if some not simulated effect can modify the shape of the $M_{\pi^0\pi^0}$ distribution. For instance the gamma distributions on the calorimeter are considered studying the variable in plot A.13, with the same technique described above.

The effect due to the wrong pairing is not responsible of the singularity, according to simulation. The Cusp does not depend on the Kaon charge or on magnetic fields orientation in the achromat or in the spectrometer. In conclusion the Cusp observed in the $M_{\pi^0\pi^0}$ distribution is not an instrumental effect , but is a real physical effect.

A.3.1 Experimental 1D fits

The matrix element depends on the two Dalitz Plot variables U and V, the $\pi^0\pi^0$ invariant mass (s_3) and the $\pi^+\pi^0$ invariant masses (s_1 and s_2). We will described here the results obtained with a 1D fit along the $M_{\pi^0\pi^0}$ direction integrating on the other coordinate (the average $< s_1 >=< s_2 >= (3s_0 - s_3)/2$ is used in the matrix element performing the fit). To take into account the acceptance and the resolution a 420x420 *transfer matrix* T_{ik} is obtained with MonteCarlo simulation. This matrix quantifies the probability that an event generated with a $M_{\pi^0\pi^0}$ in the i-th bin is detected in reality in the k-th bin. Five parameters are used to fit the distribution obtained after the transfer matrix correction:

- g,h: the unperturbed polynomial expansion $\mathcal{M}_0$ linear and quadratic terms.
- $(a_0 - a_2)m_{\pi^+}$: the term generated by the $\pi^+\pi^- \to \pi^0\pi^0$ appearing through the $\mathcal{M}_1$ component.
- $a_2 m_{\pi^+}$: the term appearing in the $\mathcal{M}_2$ component, from the neutral pions rescattering $\pi^0\pi^0 \to \pi^0\pi^0$.
- N: the normalization.

The first attempt is to try to fit, in the range 0.070 to 0.097 $(GeV/c^2)^2$, the experimental distribution with the standard polynomial expansion given by $\mathcal{M}_0$. In

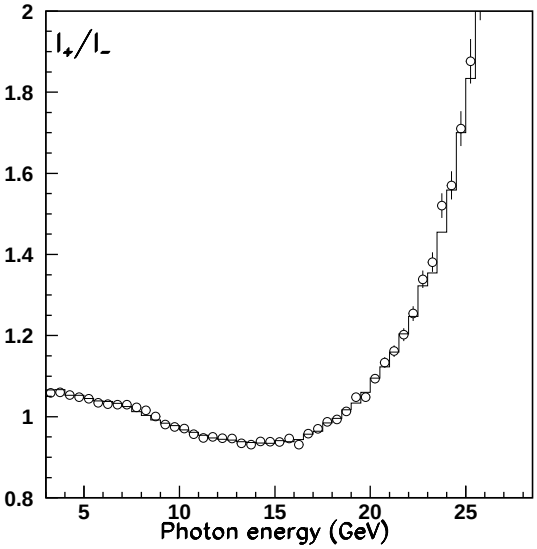

Figure A.12: Ratio between gamma energy distributions in an interval above ($M_{\pi^0\pi^0} > 4m_{\pi^2}$) and below ($M_{\pi^0\pi^0} < 4m_{\pi^2}$) the threshold for data (dots) and MonteCarlo (solid line).

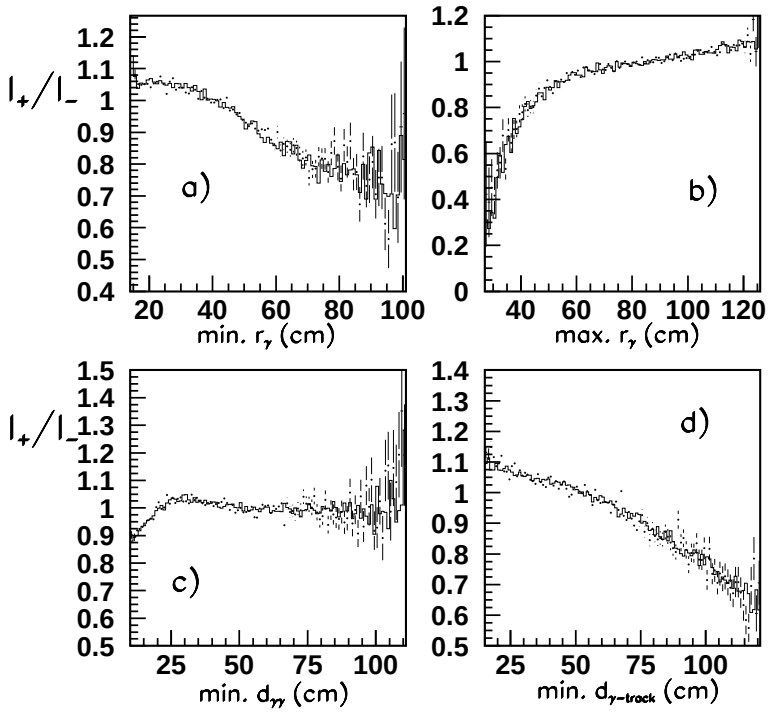

Figure A.13: The same that in the upper plot but for the following distribution: a) minimum gamma distance from the LKr center ; b) maximum gamma distance from the LKr center ; c) minimum distance between photons at LKr; d) minimum distance between the track extrapolated impact point position and the nearest gamma at LKr.

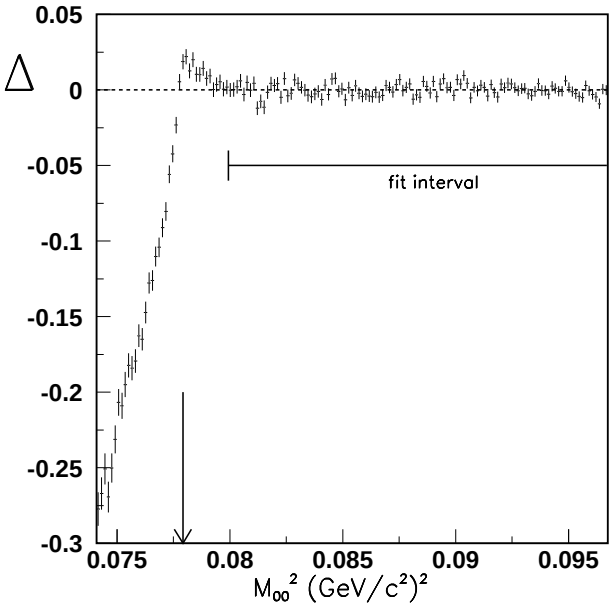

Figure A.14: $\Delta = (data - fit)/data$ is shown as a function of $M_{\pi^0\pi^0}$. The cusp threshold is indicated by an arrow. The fit χ^2 is reasonable only if the fit is restricted to the indicated fit interval.

plot A.14 the quantity $\Delta = (data - fit)/fit$ is shown. The fit disagrees totally with the data specially for value below the $\pi^+\pi^-$ threshold. The obtained χ^2 is 15000/139. The χ^2 , and the quality of the fit, improves if we consider the fit in the region for $M^2_{\pi^0\pi^0} > 80MeV^2/c^4$ (the measured χ^2 in this region is 133/139). This is a clear indication that the standard expansion is not suitable to fit the data in the whole range. The second step is to use the one loop theory described in par. A.2.1 in which the amplitudes $\mathcal{M}_1$ and $\mathcal{M}_2$ are considered. The behaviour below threshold observed in the previous fit disappears as can be recognized in fig. A.15 (plot (a)), and the χ^2 becomes 420/148. The further improvement ($\chi^2 = 155/146$) is shows in plot (b) in fig. A.15 in which the fitting model includes the two loops contribution as described in par. A.2.2.

A point still missed is the contribution due to the pionium. It is not so easy to include into the fit the electromagnetic pionic bound state because the pionium appears, in this plot, as a delta function, eventually smeared by resolution, placed in the position of the singularity given by two square root dependences (above and below the threshold according to fig. A.9). An excess of events is observed in the (Data-Fit) plot A.16, but this is only a $\sim 2\sigma$ effect with respect to the "background" level. The measured pionium decay rate, with respect to the $K^\pm \to \pi^\pm\pi^+\pi^-$ rate, is (only the statistical error is shown):

$$\frac{\Gamma(K^+ \to \pi^+ A_{2\pi})}{\Gamma(K^+ \to \pi^+\pi^+\pi^-)} \sim (1.6 \pm 0.7) \cdot 10^{-5}$$

that is in reasonably agreement with the prediction given in eq. (A.13). The results in the pionium will improve as soon as the whole statistics will be analyzed. Including this contribution the χ^2 of the fit improves ($\chi^2 = 149/145$) (fig. A.15 plot (c))

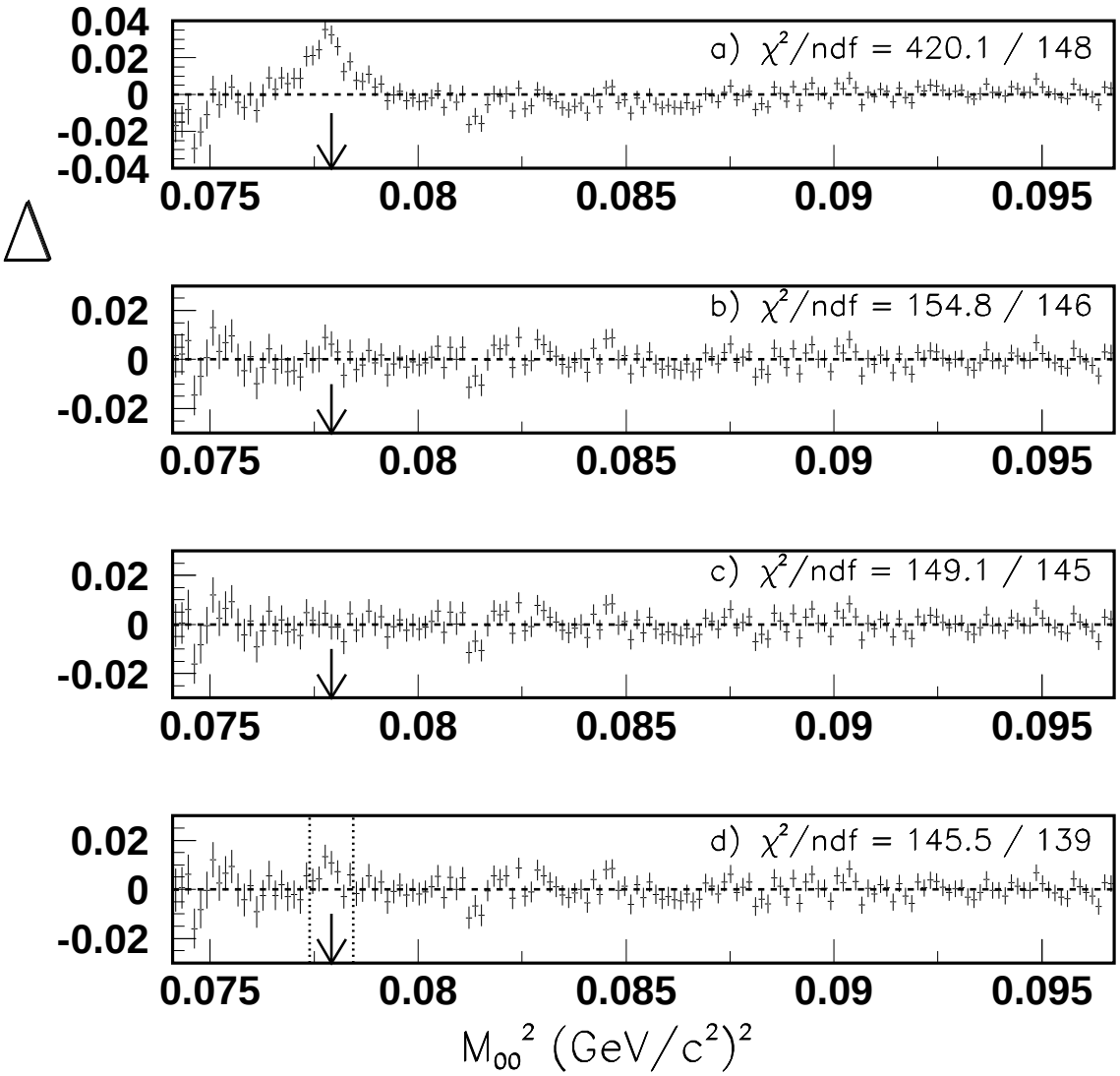

Figure A.15: The application of the rescattering hypothesis improves the quality of the fit (always in the range 0.070 to 0.097 $(GeV/c^2)^2$: (a) one loop rescattering [122]; (b) two loops rescattering [123]; (c) pionic atoms included; (d) fit performed excluding 7 bins around the 51^{th} (threshold position).

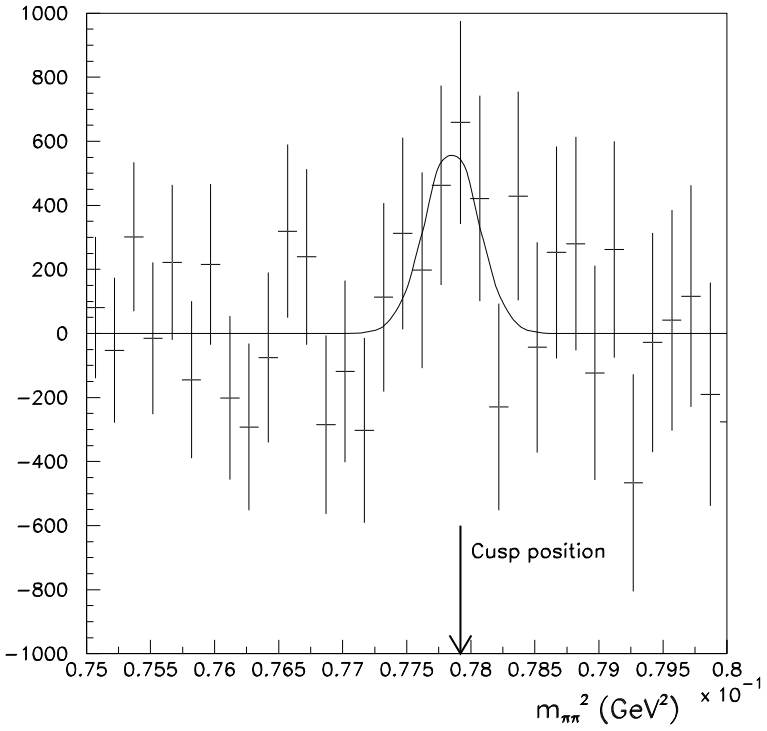

Figure A.16: An excess of events is observed near the threshold position $4m^2_{\pi^+} = 0.077919$ and it is interpreted as a signal due to the pionium formation.

but, since the radiative corrections and other effects critical for the pionic atoms generated at the threshold position are still missed, we prefer to exclude 7 bins around the $\pi^+\pi^-$ threshold position. The fit result is shown in the last plot in fig. A.15 in which a χ^2 of 149/145 is obtained. In the table A.2 the results[5] obtained for the 4 relevant fitting parameters are shown with their statistical error:

$(a_0 - a_2)m_{\pi^+}$	(0.268 ± 0.010)
$a_2 m_{\pi^+}$	(-0.041 ± 0.022)
g_0	(0.645 ± 0.004)
$h^{'}$	(-0.047 ± 0.012)

Table A.2: Results from the fit excluding 7 bins around the threshold position.

A.3.2 Systematics

Several systematics uncertainties study was made on the results obtained. In [130] can be found some detail on that. Here we want just to show the systematics table A.3 The main systematics on $(a_0 - a_2)m_{\pi^+}$ come from the upper limit variation from 0.097 to 0.107 GeV^2/c^4 in the fitting interval and the distance between charged

[5]The isospin breaking effect is taken into account as described explain in eq. (A.11). The other rescattering diagrams are corrected with different factors, as explain in [130]

Parameter	acceptance	Trigger	Fit interval	K charge	π-γ dist.	LKr lin.	Total
$(a_0 - a_2)m_{\pi^+}$	0.001	0.001	0.0025	-	0.002	0.001	$\pm$0.004
$a_2 m_{\pi^+}$	0.012	0.005	0.006	-	-	-	$\pm$0.024
g_0	0.002	0.002	0.002	0.008	-	-	$\pm$0.009
$h^{'}$	0.009	0.003	0.006	-	-	-	$\pm$0.011

Table A.3: Systematics uncertainties summary.

pion and nearest gamma on the calorimeter. An additional external error has to be added to take into account the theoretical uncertainties in the model used to fit the experimental data. This error is obtained moving in the experimental range the value of the parameter R, defined as the ratio between the weak amplitudes of $K^{\pm} \to \pi^{\pm}\pi^{+}\pi^{-}$ and $K^{\pm} \to \pi^{\pm}\pi^{0}\pi^{0}$ and used in the models employed to fit the data. This error influence the $(a_0 - a_2)m_{\pi^+}$ parameter only, and is quoted as $\pm$0.003. An additional external 5% error has to be included to take into account the neglected high-order terms in the scattering lengths expansion as explain in par. A.2.2. This corresponds to an error of $\pm$0.013 on $(a_0 - a_2)m_{\pi^+}$.

A.3.3 Results

Taking into account the systematics error the results obtained are the following:

$$(a_0 - a_2)m_{\pi^+} = (0.268 \pm 0.010_{stat} \pm 0.004_{syst} \pm 0.013_{ext}$$

$$a_2 m_{\pi^+} = -0.041 \pm 0.022_{stat} \pm 0.014_{syst}$$

$$g_0 = 0.645 \pm 0.004_{stat} \pm 0.009_{syst}$$

$$h^{'} = -0.047 \pm 0.012_{stat} \pm 0.011_{syst}$$

From the same analysis performed with a 2D fit is evident the presence of a k parameter (the coefficient of the V^2 term in the standard polynomial expansion) at level of $\sim$ 1%. The present [4] value is $k = (0.004 \pm 0.007)$ fully compatible with 0. The effect on the $(a_0 - a_2)m_{\pi^+}$ and $a_2 m_{\pi^+}$ given by the presence of this additional term has been measured as negligible, but, clearly, the g_0 and $h^{'}$ central value changes.

A.4 Alternative ways to measure pion scattering lengths

A part of the technique presented here there are other ways to measure the pion scattering lengths. The angular distributions in the $K^{+} \to \pi^{+}\pi^{-}e^{+}\nu$ (K_{e4}) can be related to the $\pi\pi$ phase shift and the $\pi\pi$ scattering length[131]. NA48/2 has presented recently the K_{e4} measurement based on a partial sample of $\sim$ 370000 events [132]. The result obtained is:

$$a_0 m_{\pi^+} = 0.256 \pm 0.008_{stat} \pm 0.007_{syst} \pm 0.018_{theor} = 0.256 \pm 0.021$$

partially in disagreement with the best previous result coming from the E865 experiment [133]: $a_0 m_{\pi^+} = 0.216 \pm 0.013$. The problem of this approach is that to extract the scattering length value an extrapolation, using theoretical external input, has to be done from the region in which the angular distributions can be better measured. Other model independent approaches are, for this reason, very useful to cross check the results. The measurement of the pion lifetime, for instance, can be related to $|a_0 - a_2| m_{\pi^+}$ [128] [134]. The DIRAC experiment at CERN [135] recently has published the first pionium lifetime measurement and the result[136]:

$$|a_0 - a_2| m_{\pi^+} = 0.264^{+0.033}_{-0.020}$$

in agreement with our measurement. Finally $a_0 m_{\pi^+}$ has been measured also from the scattering $\pi^{\pm} p \to \pi^{\pm}\pi^{+} n$ process at threshold. The best result obtained with this technique is [137] $a_0 m_{\pi^+} = 0.204 \pm 0.016$.

From this very short review of the experimental techniques is quite evident that the $K^{\pm} \to \pi^{\pm}\pi^0\pi^0$ cusp is a competitive technique to measure the pion scattering length $(a_0 - a_2) m_{\pi^+}$. The expected experimental error analyzing the full data sample is at level of $\sim 1.5\%$ which is equal or better to the uncertainty in the theoretical prediction given with an error from $\sim 1.5\%$ to $\sim 5\%$ [138] [139]. This precision is quite unusual in the hadronic physics environments.

Appendix B

The Charged asymmetry measurement

During the 2003 data taking $1.67 \cdot 10^9$ $K^{\pm} \to \pi^{\pm}\pi^{+}\pi^{-}$ have been collected. The result obtained on the "charged" slope asymmetry will be briefly presented, showing the main differences with respect to the neutral asymmetry. Further details on the charged asymmetry can be found in [113] [140].

B.1 Data selection and analysis strategy

The $K^{\pm} \to \pi^{\pm}\pi^{+}\pi^{-}$ events online selection is based at L1 on the Q2 signal (condition compatible with at least two hits in the charged hodoscope) and at L2 on the fast three tracks reconstruction, plus small contributions from other conditions. The L1 trigger efficiency is very high and stable (the inefficiency is $\sim 0.9 \cdot 10^{-3}$) while the L2 inefficiency (MB-VTX2 and MB-VTX1) varies from $\sim 1.5\%$ in the first part

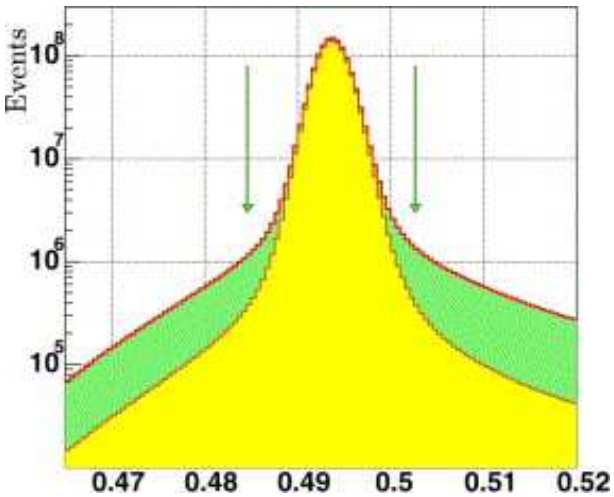

Figure B.1: Recostructed three charged tracks invariant mass. The background, indicated in the green area employing a MonteCarlo simulation, is due to the charged pion decay in flight.

of the data taking, to $\sim 0.6\%$ in the second part, according to the variation of the wires efficiency as already pointed out in chap. 8. The $K^{\pm} \to \pi^{\pm}\pi^{+}\pi^{-}$ events offline reconstruction is based uniquely on the Spectrometer information. An event is selected if at least three good in time tracks (the ghost and the worst quality tracks are excluded from the selection) come from the same vertex. The vertex is obtained fitting the tracks direction given by the DCH1 and DCH2 taking into account the earth magnetic field. For each reconstructed vertex a χ^2 is defined to give an estimation of the vertex extrapolation quality. A cut on reconstructed kaon transverse momentum is used to reduce the background coming from pion decay in flight and tracks interaction on inert material. The reconstructed three tracks invariant mass (fig. B.1), with a $\sigma \sim 1.7\ MeV/c^2$, is used to select the signal with a cut $|M_{3\pi} - M_K| < 9\ MeV/c^2$ around the nominal kaon mass [4]. The signal is affected by a small background coming mostly from the pion decay in flight and from the very small contribution of the $K \to 3\pi\gamma$ decay (mentioned just for completeness).

With this selection $1.67 \cdot 10^9$ events are selected in the 2003 data taking. The U variable is defined in the same way as in neutral case (eq. (1.53)) and can be written, for instance, in terms of the invariant mass of the two pions with the same electric charge, $|M_{12}|$, as:

$$U(M_{12}) = \frac{\left(M_{12}^2 - \frac{m_K^2}{3}\right)}{m_\pi^2} - 1$$

The V variable is defined as:

$$|V| = \frac{|M_{13}^2 - M_{23}^2|}{m_\pi^2}$$

where the pion number 3 has the opposite charge of the pions 1 and 2. In fig. B.4 the Dalitz Plot distribution and in fig. B.3 its U projection are presented . In this case (differently from the neutral case (fig. 3.15)), the experimental distribution shows three *depletion regions* due to the physical hard cut induced by the presence of the beam pipe in the spectrometer. For the odd pion the cut on the Dalitz Plot right hand, and for the even pions the cuts on the left hand. In addition the beam pipe introduces small acceptance differences that can appear as systematics differences. For this reason the K^+ and K^- acceptance are equalized with the "virtual pipe" cut: a radial DCH inner cut ($R > 11.5$ cm) is applied with respect to the actual K^+ and K^- beam position and not with respect to the nominal, common, direction (which is assumed collinear to the experiment longitudinal axis). The beams actual position is measured during the run, from the averaged transverse vertex coordinates.

The spectrometer internal alignment is fine tuned looking to the differences of the reconstructed K^+ and K^- masses during the run. The sensitivity of the mass shift between K^+ and K^- is $\sim 1\ KeV/c^2$ for $\sim 1\mu m$ of DCH4 shift in the direction (X) of the magnetic deflection. In plot B.4 the measured ΔM is shown during the run.

The invariant mass dependence on the azimuthal odd pion impact point position (fig. B.5) is corrected taking into account the "Blue Field" as explain in par. 4.5.

The strategy of the analysis is exactly the same as described for the neutral case. The Δg is extracted from quadruple ratio, obtained exploiting the U distribution

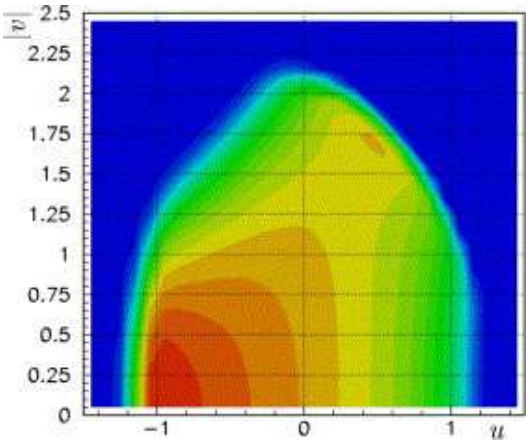

Figure B.2: $K^{\pm} \to \pi^{\pm}\pi^{+}\pi^{-}$ Dalitz Plot.

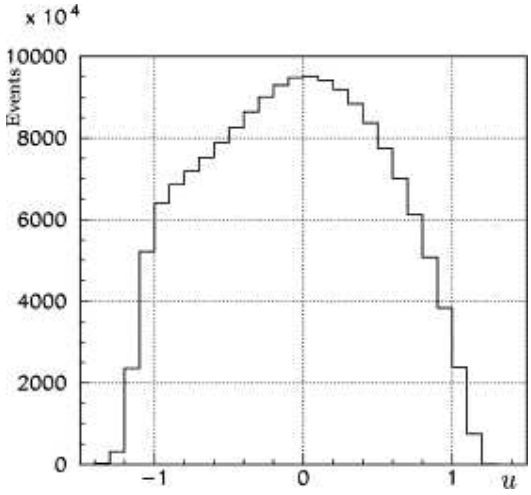

Figure B.3: U projection of the $K^{\pm} \to \pi^{\pm}\pi^{+}\pi^{-}$ Dalitz Plot.

constructed with different magnetic field combinations, in order to allow the cancellation of the detector asymmetries. The fitting function in this case is simplified with respect to the neutral case (eq. (5.4)), because some cancellation is allowed by the relative smallness of the charged linear slope value $g^{+} = -0.216$ [4]:

$$R(U) \sim 1 + \Delta g U \tag{B.1}$$

The SuperSample (SS) and the DaySample (DS) definition is slightly different (because of the different bad period rejection and the statistics balance in each SS) with respect to the neutral case. In table B.1 the statistics collected in each SS and the Δg extracted (with the statistical error only), after the L2 trigger correction, in each SS is shown.

SS	K^{+} (in 10^6)	K^{-} (in 10^6)	$\Delta g \times 10^{-4}$
SS0	448.0	249.7	-0.8 ± 1.8
SS1	270.8	150.7	-0.5 ± 1.8
SS2	265.5	147.8	-1.4 ± 2.0
SS3	86.1	48.0	1.0 ± 3.3)
SS0123	1070.4	596.2	-0.7 ± 1.0

Table B.1: Statistics and Δg in 2003 $K^{\pm} \to \pi^{\pm}\pi^{+}\pi^{-}$.

B.2 Systematics

Several sources of systematics are studied. Similar considerations as in the neutral mode can be done. The systematic uncertainty has to be considered as an upper limit. In table B.2 the systematics contributing to the final error are summarized. The acceptance and beam systematics is evaluated with the variation of the "virtual pipe" cut definition. The systematic uncertainty due to the spectrometer alignment

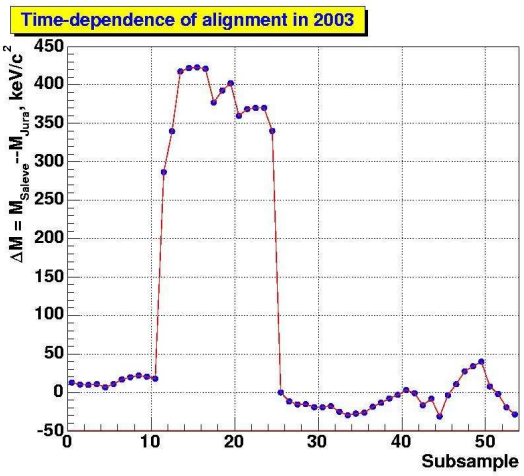

Figure B.4: Difference between the K^+ and K^- invariant mass during the run. The variation depends on the internal spectrometer alignment.

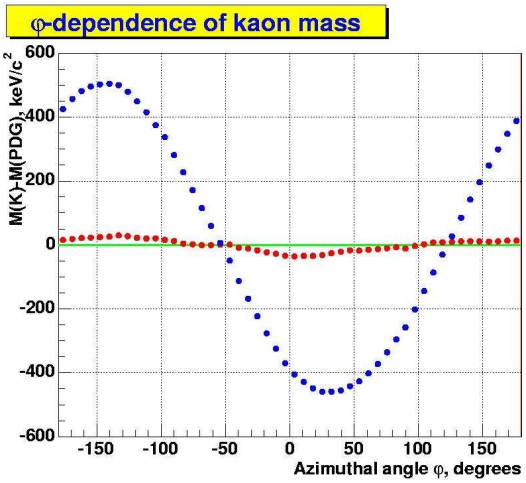

Figure B.5: Before the Blue Field correction a 500 KeV/c^2 oscillation amplitude can be detected looking to the average value of the charged kaon mass as a function of the odd pion impact point position on DCH1 (blue curve). The situation improves if the correction described in par. 4.5 is applied (red curve).

(as well as the momentum scale systematics) has been reduced with the correction based on the study of the reconstructed kaon mass differences between K^+ and K^- and with respect to the nominal PDG value. The $\pi \to \mu\nu$ decay in flight systematics

Spectrometer alignment	± 0.1
Beam geometry and acceptance	± 0.3
Momentum scale	± 0.1
$\pi \to \mu$ decay	± 0.4
Accidentals	± 0.2
Trigger L1	± 0.4
Trigger L2	± 0.5
Total systematics uncertainties	$\pm 0.6_{syst} \pm 0.6_{trig}$

Table B.2: Summary of systematic uncertainties. All numbers are in units of 10^{-4}.

has been quoted using the MonteCarlo in which the effect can be switched on and off. The systematic uncertainty due to the U calculation is obtained extracting the result using different U definition including a 4C kinematic fit. The U definition differs mainly for the U resolution. The different accidental contribution in the K^+ and K^- beam is evaluated looking to the change of the final result allowing or not extra activity in the spectrometer. The trigger systematics have been evaluated applying the trigger correction and considering the associated uncorrelated component of the error. Also here the systematics due to the trigger are limited by the statistics in the control samples used to evaluate the trigger efficiency.

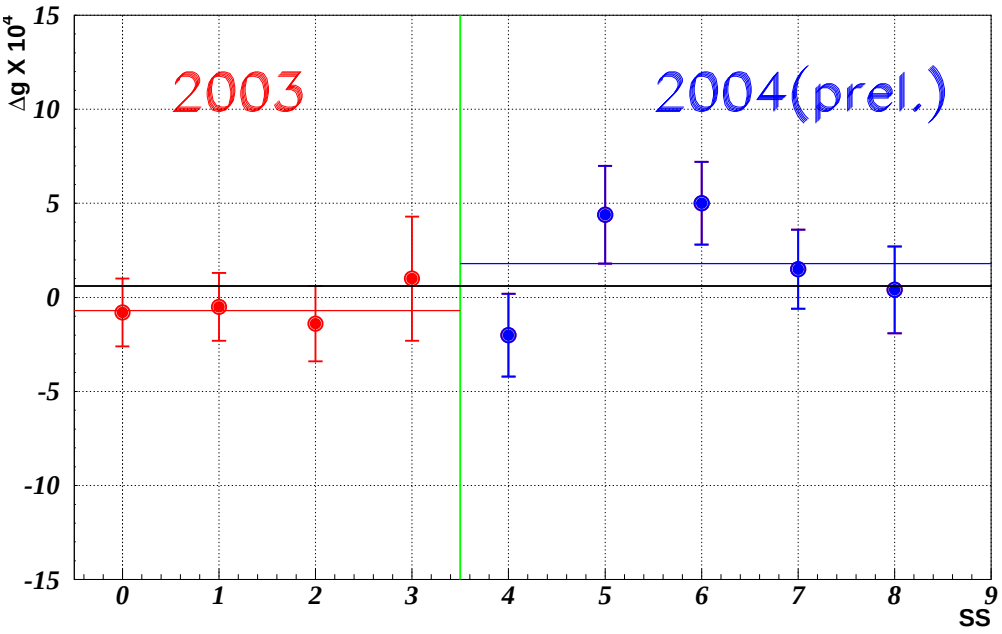

Figure B.6: The Δg obtained as a function of the SuperSample is presented. The red dots refer to the 2003 data taking (SS0123) while the blue dots to the preliminary result in the 2004 data taking (SS45678). The black line is the combined Δg preliminary result. The 2003 final result and 2004 preliminary result are $\sim 1.4\sigma$ away.

B.3 2003 result and 2003+2004 preliminary result

The difference of linear slopes between K^+ and K^- obtained on the 2003 data is:

$$\Delta g = (-0.7 \pm 0.9_{stat} \pm 0.6_{trig} \pm 0.6_{syst}) \times 10^{-4}$$

The charged asymmetry parameter is obtained using the formula $A_g^+ = \Delta g / 2g^+$:

$$A_g^+ = (1.7 \pm 2.1_{stat} \pm 1.4_{trig} \pm 1.4_{syst}) \times 10^{-4} = (1.7 \pm 2.9) \times 10^{-4}$$

The analysis on the whole statistics, 2003+2004 data taking, is on going. The *preliminary* result based on $3.11 \cdot 10^9$ events has been presented [141] as:

$$A_g^+ = (-1.3 \pm 1.5_{stat} \pm 0.9_{trig} \pm 1.4_{syst}) \cdot 10^{-4} = (-1.3 \cdot 2.3) \times 10^{-4}$$

after a revaluation of the main systematics (in plot B.6 the results in each SS are shown). In plot B.7 the present situation is summarized with respect to the previously existing results.

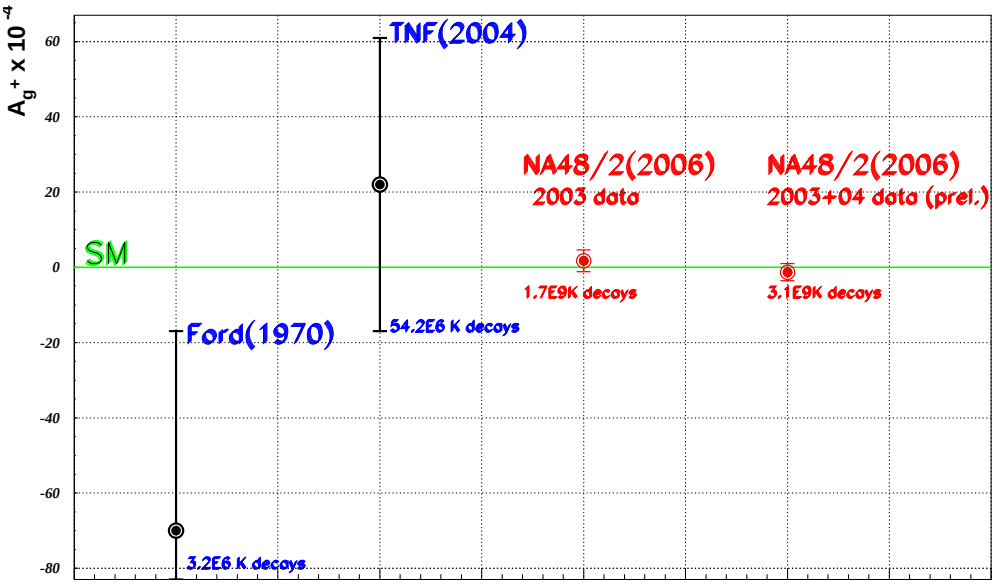

Figure B.7: Comparison between the experimental result on A_g^+ measurements. The 2003+04 NA48/2 result is still preliminary.

B.4 Differences with respect to the neutral analysis

The strategy of the analysis is practically the same in charged and neutral mode. Nevertheless some minor point is specific to the different analysis. Obviously the online selection and the offline reconstruction is totally different; the fact that the charged mode has more events with respect to the neutral mode requires the use of the HyperCompact format instead of the SuperCompact (par. 3.1). The contribution of the small spectrometer misalignment is, in the charged mode, enhanced with respect to the neutral mode due to the presence of three charged pions. In addition in the neutral mode the charged pion momentum mismeasurement contributes to the asymmetry *only* through the kaon mass reconstruction, because in the U definition only the neutral pions appear. In this case the charged pions momentum mismeasurement influence both the acceptance and the U measurement. The charged pions acceptance, mainly limited by the beam pipe in the spectrometer, is relevant in every part of the Dalitz Plot distribution while in the neutral case only the right hand part was affected. Particular care has to be applied to equalize this effect directly in the event selection (this cost $\sim$ 12% of the statistics) with the "virtual beam pipe" technique. In the neutral case the K^+/K^- ratio eq. (5.4) is more favourable because the presence of the pole in the left hand of the U distribution enhanced the statistical significance of the events in the part in which there is the better acceptance and resolution. In the charged mode the use of the linear

function (B.1) does not allow this advantage.

This is the reason way the final errors in the two modes are compatible in spite of the different statistics. Both the final results are in agreement with the standard model prediction and in both cases a factor ~ 10 in the experimental sensitivity with respect to the previous experiments is reached.

Appendix C

The 2004 neutral asymmetry: preliminary result

In 2004 NA48/2 has collected a statistics comparable with the 2003 data sample. Minor changes have been applied to the analysis technique and during the data taking. The final result based on 2003 and 2004 data taking has not been approved yet by the collaboration. We will present the differences between the 2003 and 2004, the statistics collected and the preliminary result obtained.

C.1 Differences between 2003 and 2004 data taking

The main change in the data taking strategy between the 2004 with respect to the 2003 is the most frequent magnetic fields reversing. Indeed in the quadruple ratio the only effect that can give , in principle, systematics contribution at the first order is the change of the detector characteristics with a typical time smaller than the correspondent field inversion. In 2004 data taking the B field is reversed with a period of ~ 3 hours while the achromat fields are reversed with a period of ~ 1 day. In this way 347, so called, Day samples (DS)[1] are defined in 2004.

The L1 inefficiency has been partially recovered adding the NT-NOPK signal in the L1 strobe to the MBX. This signal fires if the quantities calculated by the LUT in the neutral trigger, satisfy the following condition:

$$COG < 30cm \times Z < 95m \times ELKR > 15GeV$$

The trigger rate, from the L1code0, has increased of about a factor 2. To cope this higher quantity of data at L2 a *selective readout* has been implemented: the LKr and HAC are not read in 6/16 events triggered by the MBX-VTX2 and MB-VTX1 (the triggers employed for the three tracks events). This reduces the band width dedicated to the charged mode allowing the acquisition of a greater number of control triggers events for the neutral mode. In addition a new control trigger (NT-PK3) has been defined asking for more than 3 peaks in at least one NUT view. In table C.1 the 2004 downscalings are shown (see as reference the table 8.1 for the

[1]The name is the same than in 2003, but actually in 2004 a day sample is ~ 3 hours long.

corresponding quantities in 2003). Increasing the number of trigger in the control samples the inefficiency can be measured with better precision.

Control trigger	D
NT-PK3	1
NT-PRE	50
T0N	100
$Q1 * NT_M B$	100

Table C.1: Downscaling (D) for the 2004 1 tracks events control triggers. NT-PRE corresponds to NT-PK OR NT-NOPK.

C.2 Analysis

The analysis of the 2004 data is practically identical with respect to that in the 2003, with only the modifications due to the changes described in previous section. About $29{\cdot}10^6$ K^+ and $15.1{\cdot}10^6$ K^- has been selected, after removing bad bursts and a period with very big MBX inefficiency to DCH4 wires inefficiency. The systematics have been reevaluated on the whole statistics. The L1 trigger neutral signal systematics is reduced at level 0.8% thanks to the improvement of the L1 efficiency described above. Other systematic uncertainties are summarized in table C.2 and have to be regarded as preliminary. Thanks to the greater statistics with respect to the 2003, most of the systematics (being an upper limit due to the limited statistics in 2003) are reduced.

LKr related effects	0.5
$\pi \to \mu$ decay	0.2
Spectrometer and Momentum scale	0.1
Accidentals	0.2
Trigger L1	0.8
Trigger L2	0.6
Total systematic uncertainty	1.2
External uncertainty	0.3

Table C.2: Summary of systematic uncertainties in 2003+2004 data. All numbers are in units of 10^{-4}.

C.3 2003+2004 preliminary result

In table C.3 the preliminary result on the 2003+2004 is presented.

In plot C.1 the compatibility between the 2003 and 2004 results is shown.

2003	SS 1	4.3 ± 3.8
	SS 2	0.5 ± 5.0
	SS 3	-2.0 ± 8.2
2004	SS 4	5.6 ± 6.8
	SS 5	4.7 ± 5.1
	SS 6	3.5 ± 5.6
	SS 7	-1.4 ± 5.8
Total		2.7 ± 2.0

Table C.3: **Preliminary** asymmetry results in 2003+2004 data sample. All the numbers are expressed in unit of 10^{-4}. Only the statistical error is shown.

The combined preliminary result based on $\sim 91 \cdot 10^6$ $K^{\pm} \to \pi^{\pm}\pi^0\pi^0$ decays is:

$$\begin{aligned} \Delta g &= (2.7 \pm 2.0_{stat.} \pm 1.2_{syst.} \pm 0.3_{ext.}) \cdot 10^{-4} = \\ &= (2.7 \pm 2.4) \cdot 10^{-4} \end{aligned} \tag{C.1}$$

and in terms of A_g^0:

$$\begin{aligned} A_g^0 &= (2.1 \pm 1.6_{stat.} \pm 1.0_{syst.} \pm 0.2_{ext.}) \cdot 10^{-4} = \\ &= (2.1 \pm 1.9) \cdot 10^{-4} \end{aligned} \tag{C.2}$$

The final error being dominated by the statistical component. The preliminary 2003+2004 result and the 2003 result, both compatible with SM predictions, are summarized in fig. C.2

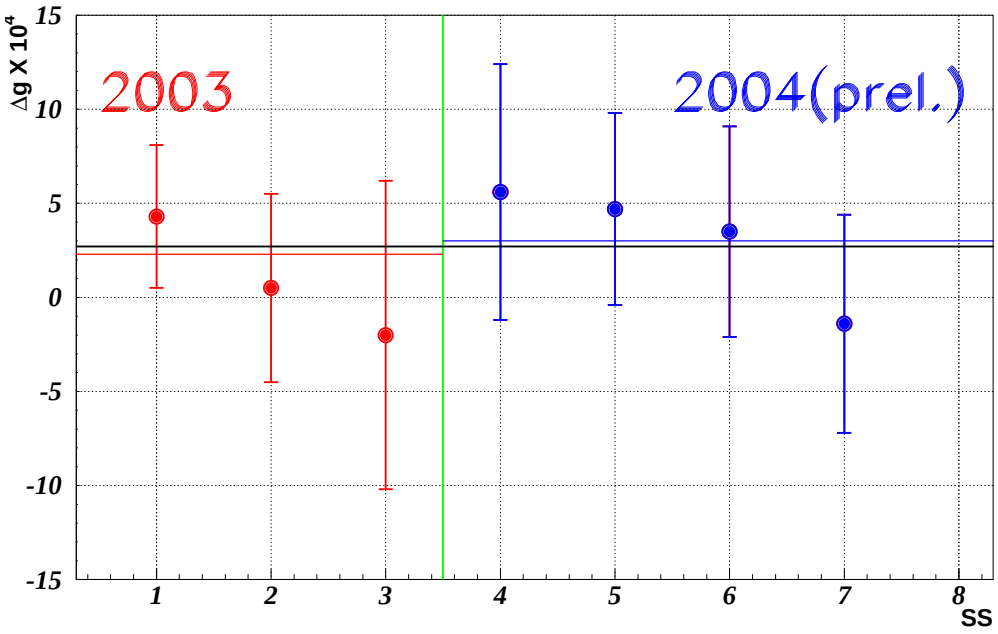

Figure C.1: The Δg obtained as a function of the SuperSample is presented. The red dots refer to the 2003 data taking (SS123) while the blue dots to the preliminary result in the 2004 data taking (SS4567). The black line is the combined Δg preliminary result. The 2003 final result and 2004 preliminary result are $\sim 0.25\sigma$ away.

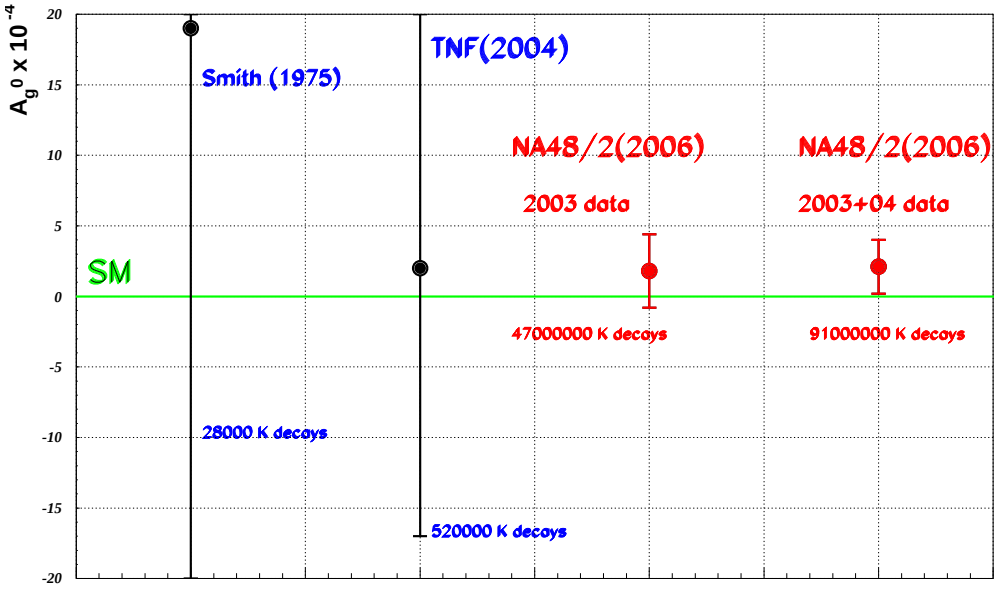

Figure C.2: Comparison between the NA48/2 2003 final result and the 2003+04 with respect to the previous experimental results. An improvement of a factor ~ 10 in sensitivity has been reached.

Bibliography

[1] E. Nother, Nachr. Kgl. Geo. Wiss. **235** (1918) 171.

[2] B. C. Regan, E. D. Commins, C. J. Schmidt and D. DeMille, Phys. Rev. Lett. **88** (2002) 071805.

[3] A. Angelopoulos *et al.* [CPLEAR Collaboration], Phys. Lett. B **444** (1998) 38.

[4] S. Eidelman *et al.* [Particle Data Group Collaboration], Phys. Lett. B **592** (2004) 1.

[5] W. M. Yao *et al.* [Particle Data Group], J. Phys. G **33** (2006) 1.

[6] C.S. Wu et al., Phys. Rev. **105** (1957) 1413.

[7] T.D. Lee & C.N. Yang, Phys. Rev. **104** (1956) 254.

[8] M. Goldhaber et al., Phys. Rev. **106** (1957) 826-828

[9] J.H. Christenson et al., Phys. Rev. Lett. **13** (1964) 138

[10] G. Luders, Dan. Mat. Fys. Medd. **28(5)** (1954) 1

[11] W. Pauli, *Niels Bohr and the developement of physics*, Pergamon Press, London, (1955) 202

[12] R. Carosi *et al.* [NA31 Collaboration], Phys. Lett. B **237** (1990) 303.

[13] M. H. Holzscheiter *et al.* [ATHENA Collaboration], Nucl. Phys. Proc. Suppl. **56** (1997) 336.

[14] M. H. Schacht, UMI-99-76053

[15] R. Bluhm, V. A. Kostelecky and N. Russell, arXiv:hep-ph/9810287.

[16] A. Apostolakis *et al.* [CPLEAR Collaboration], Phys. Lett. B **456** (1999) 297.

[17] R. Adler *et al.* [CPLEAR collaboration], Phys. Lett. B **364** (1995) 239 [arXiv:hep-ex/9511001].

[18] A. Angelopoulos *et al.* [CPLEAR Collaboration], Phys. Lett. B **444** (1998) 43.

[19] L. Prince-Ringuet and M. Lheritier, Compt. Rend. **219** (1944) 618.

[20] G.D. Rochester and C.C. Butler Nature **106** (1947) 885.

[21] A. Pais and O. Piccioni, Phys. Rev. **100** (1955) 1487.

[22] M. Adinolfi *et al.* [KLOE Collaboration], Nucl. Phys. A **663** (2000) 1103.

[23] M. Kobayashi and T. Maskawa, Prog. Theor. Phys. **49** (1973) 652.

[24] N. Cabibbo, Phys. Rev. Lett. **10** (1963) 531.

[25] L. Wolfenstein, Phys. Rev. Lett. **51** (1945) 164

[26] C. Jarlskog, Phys. Rev. Lett. **55** (1985) 1039.

[27] M. Bona *et al.* [UTfit Collaboration], arXiv:hep-ph/0605213.

[28] P. F. . Harrison and H. R. . Quinn [BABAR Collaboration], SLAC-R-0504

[29] K. Abe et al. (Belle), *Phys. Rev. Lett.* **93**, 021601 (2004)
B. Aubert et al. (Babar), *Phys. Rev. Lett.* **93**, 131801 (2004)

[30] M. S. Sozzi and I. Mannelli, Riv. Nuovo Cim. **26** (2003) 1 [arXiv:hep-ex/0312015].

[31] A. J. Buras and M. K. Harlander, Adv. Ser. Direct. High Energy Phys. **10** (1992) 58.

[32] U. Nierste, Nucl. Phys. Proc. Suppl. **86** (2000) 329 [arXiv:hep-ph/9910257].

[33] G. Buchalla, A. J. Buras and M. E. Lautenbacher, Rev. Mod. Phys. **68** (1996) 1125 [arXiv:hep-ph/9512380].

[34] S. Bosch, A. J. Buras, M. Gorbahn, S. Jager, M. Jamin, M. E. Lautenbacher and L. Silvestrini, Nucl. Phys. B **565** (2000) 3 [arXiv:hep-ph/9904408].

[35] S. Bertolini, J. O. Eeg and M. Fabbrichesi, Phys. Rev. D **63**, 056009 (2001) [arXiv:hep-ph/0002234].

[36] S. Bertolini, Frascati Phys. Ser. **28** (2002) 275 [arXiv:hep-ph/0206095].

[37] G. Barr et al. (NA31), *Phys. Lett. B* **317**, 233 (1993)

[38] J. R. Batley *et al.* [NA48 Collaboration], Phys. Lett. B **544** (2002) 97 [arXiv:hep-ex/0208009].

[39] A. Alavi-Harati *et al.* [KTeV Collaboration], Phys. Rev. D **67** (2003) 012005 [Erratum-ibid. D **70** (2004) 079904] [arXiv:hep-ex/0208007].

[40] R.H. Dalitz, Phil. Mag. **44**, (1953) 1068

[41] T. D. Lee and C. S. Wu, Ann. Rev. Nucl. Part. Sci. **16** (1966) 471.

[42] S. Weinberg, Phys.Rev.Lett.**87** (1960) 4.

[43] G. D'Ambrosio and G. Isidori, Int. J. Mod. Phys. A **13** (1998) 1 [arXiv:hep-ph/9611284].

[44] C. Zemach, Phys. Rev. **133** (1964) B1201.

[45] T. J. Devlin and J. O. Dickey, Rev. Mod. Phys. **51**, 237 (1979).

[46] L. F. Li and L. Wolfenstein, Phys. Rev. D **21**, 178 (1980).

[47] G. Isidori, L. Maiani and A. Pugliese, Nucl. Phys. B **381** (1992) 522.

[48] G. D'Ambrosio, G. Isidori, A. Pugliese and N. Paver, Phys. Rev. D **50** (1994) 5767 [Erratum-ibid. D **51** (1995) 3975] [arXiv:hep-ph/9403235].

[49] G. D'Ambrosio, G. Isidori and N. Paver, Phys. Lett. B **273** (1991) 497.

[50] J. Gasser and H. Leutwyler, Nucl. Phys. B **250** (1985) 465.

[51] F. J. Gilman and M. B. Wise, Phys. Rev. D **20** (1979) 2392.

[52] A. A. Belkov, A. V. Lanyov and G. Bohm, Czech. J. Phys. **55** (2004) B193 [arXiv:hep-ph/0311209].

[53] E. P. Shabalin, Phys. Atom. Nucl. **68** (2005) 88 [Yad. Fiz. **68** (2005) 89] [arXiv:hep-ph/0405229].

[54] H. Y. Cheng, Phys. Rev. D **43** (1991) 1579 [Addendum-ibid. D **44** (1991) 919].

[55] H. Y. Cheng, IP-ASTP-17-90

[56] E. Shabalin, Nucl. Phys. B **409** (1993) 87.

[57] A. A. Belkov, A. V. Lanyov, G. Bohm, A. Schaale and D. Ebert, Phys. Lett. B **300** (1993) 283 [arXiv:hep-ph/9305333].

[58] E. Shabalin, ITEP-8-98

[59] L. Maiani and N. Paver,

[60] E. Gamiz, J. Prades and I. Scimemi, JHEP **0310** (2003) 042 [arXiv:hep-ph/0309172].

[61] A. A. Belkov, A. V. Lanyov, G. Bohm and D. Ebert, Phys. Lett. B **232** (1989) 118.

[62] E. Shabalin, arXiv:hep-ph/0305320.

[63] G. Faldt and E. Shabalin, Phys. Lett. B **635** (2006) 295 [arXiv:hep-ph/0503241].

[64] G. D'Ambrosio, G. Ecker, G. Isidori and J. Portoles, JHEP **9808** (1998) 004 [arXiv:hep-ph/9808289].

[65] P. Fayet and S. Ferrara, Phys. Rept. **32** (1977) 249.

[66] A. Masiero and O. Vives, Nucl. Phys. Proc. Suppl. **99B** (2001) 228 [arXiv:hep-ph/0107276].

[67] A. Masiero and O. Vives, New J. Phys. **4** (2002) 4.

[68] W. Buchmuller and D. Wyler, Phys. Lett. B **121** (1983) 321.

[69] J. Polchinsky and M. Wise, Phys. Lett. B **125** (1983) 393.

[70] W. Fischler, S. Paban and S. Thomas, Phys. Lett. B **289** (1992) 373.

[71] A. Bartl, T. Gajdosik, W. Porod, P. Stockinger and H. Stremnitzer, Phys. Lett. D **60** (1999) 073003.

[72] A. Khalil and T. Kobayashi, Phys. Lett. B **460** (1999) 341.

[73] A. Pomarol and D. Tommasini, Nucl. Phys. B **466** (1996) 3.

[74] G. D'Ambrosio, G. Isidori and G. Martinelli, Phys. Lett. B **480** (2000) 164 [arXiv:hep-ph/9911522].

[75] G. Colangelo, G. Isidori and J. Portoles, Phys. Lett. B **470** (1999) 134 [arXiv:hep-ph/9908415].

[76] X. G. He, H. Murayama, S. Pakvasa and G. Valencia, Phys. Rev. D **61** (2000) 071701 [arXiv:hep-ph/9909562].

[77] Y. Grossman, Y. Nir and R. Rattazzi, Adv. Ser. Direct. High Energy Phys. **15** (1998) 755 [arXiv:hep-ph/9701231].

[78] Y. Nir, arXiv:hep-ph/9911321.

[79] J. Bijnens and J. Prades, JHEP **0006** (2000) 035 [arXiv:hep-ph/0005189].

[80] T. Hambye, S. Peris and E. de Rafael, JHEP **0305** (2003) 027 [arXiv:hep-ph/0305104].

[81] T. Hambye, G. O. Kohler, E. A. Paschos and P. H. Soldan, Nucl. Phys. B **564** (2000) 391 [arXiv:hep-ph/9906434].

[82] J. Prades, E. Gamiz and I. Scimemi, arXiv:hep-ph/0509346.

[83] K. M. Smith *et al.*, Nucl. Phys. B **60** (1973) 411. K. M. Smith *et al.*, Nucl. Phys. B **91** (1975) 45.

[84] G. A. Akopdzhanov *et al.*, Eur. Phys. J. C **40** (2005) 343 [arXiv:hep-ex/0406008].

[85] W. T. Ford, P. A. Piroue, R. S. Remmel, A. J. S. Smith and P. A. Souder, Phys. Rev. Lett. **25** (1970) 1370.

[86] W. S. Choong, Ph.D. thesis, Berkeley (2000) LBNL-47014

[87] D. J. Simon, CERN-PS-96-019-DI *Presented at the 5th European Particle Accelerator Conference -EPAC '96, Sitges, Spain, 10 - 14 Jun 1996*

[88] E. J. N. Wilson, *Prepared for CERN Accelerator School: Course on Advanced Accelerator Physics (CAS), Rhodes, Greece, 20 Sep - 1 Oct 1993*

[89] G. Brianti, *Prepared for 8th General Conference of the European Physical Society (EPS-8): Trends in Physics, Amsterdam, Netherlands, 4-8 Sep 1990*

[90] R. Batley *et al.*, CERN-SPSC-2000-003

[91] B. Peyaud, Nucl. Instrum. Meth. A **535** (2004) 247.

[92] Y. Giomataris, P. Rebourgeard, J. P. Robert and G. Charpak, Nucl. Instrum. Meth. A **376** (1996) 29.

[93] B. Hallgren *et al.* [NA48 Collaboration], Nucl. Instrum. Meth. A **419** (1998) 680.

[94] R. Arcidiacono, P. L. Barberis, F. Benotto, F. Bertolino, G. Govi and E. Menichetti, Nucl. Instrum. Meth. A **443** (2000) 20 [Nucl. Instrum. Meth. A **449** (2000) 651].

[95] G. Anelli *et al.*, CERN-SPS-2005-13

[96] L. Fiorini, PhD Thesis, SNS-Pisa, Winter 2005

[97] F. Marchetto, NA48 Collaboration meeting, 1.4.2004

[98] L. Di Lella, NA48 Collaboration meeting, 20.8.2003

[99] L. Di Lella, NA48 Collaboration meeting, 25.2.2004

[100] G. Unal, NA48-Note, 19 (2000)

[101] G. Unal, NA48-Note, 07 (2001)

[102] G. Unal, NA48-Note, 18 (2001)

[103] J. Ocariz, PhD Thesis, UniversitÃ© de Paris-sud, 1999

[104] A. Norton, NA48/2 Collaboration meeting, 25.02.2004

[105] R. Brun, R. Hagelberg, M. Hansroul and J. C. Lassalle, CERN-DD-78-2-REV (http://wwwasd.web.cern.ch/wwwasd/geant/)

[106] http://www.pi.infn.it/na48/flyo/flyoindex.html

[107] S. Balev, NA48 Collaboration meeting, 8.6.2005

[108] J. R. Batley *et al.* [NA48 Collaboration], Phys. Lett. B **638**, 22 (2006) [arXiv:hep-ex/0606007] cern-ph-ep-2006-006.

[109] E. Imbergamo, NA48-Note, 04 (2004)

[110] I. Mikulec, NA48/1 Collaboration Meeting, 3.4.2003

[111] S. Balev, NA48/2 Collaboration Meeting, 8.2.2006

[112] J. R. Batley *et al.* [NA48/2 Collaboration], Phys. Lett. B **633** (2006) 173 [arXiv:hep-ex/0511056].

[113] J. R. Batley *et al.* [NA48/2 Collaboration], Phys. Lett. B **634** (2006) 474 [arXiv:hep-ex/0602014].

[114] M. Sozzi *et al.* NA48-Note, 05 (2003)

[115] M. Sozzi, NA48/2 Collaboration Meeting, 16.9.2003

[116] G. Collazuol, PhD thesis, Universitá di Firenze, 2000.

[117] A. Formica, PhD thesis, Saclay DAPNIA, 2001.

[118] I. V. Ajinenko *et al.*, Phys. Lett. B **567** (2003) 159 [arXiv:hep-ex/0205027].

[119] V. Y. Batusov *et al.*, Nucl. Phys. B **516** (1998) 3.

[120] K. M. Smith *et al.*, Nucl. Phys. B **91** (1975) 45.

[121] H. Jallouli and H. Sazdjian, Phys. Rev. D **58** (1998) 014011 [Erratum-ibid. D **58** (1998) 099901] [arXiv:hep-ph/9706450].

[122] N. Cabibbo, Phys. Rev. Lett. **93** (2004) 121801 [arXiv:hep-ph/0405001].

[123] N. Cabibbo and G. Isidori, JHEP **0503** (2005) 021 [arXiv:hep-ph/0502130].

[124] E. Gamiz, J. Prades and I. Scimemi, arXiv:hep-ph/0602023.

[125] E. Gamiz, J. Prades and I. Scimemi, JHEP **0310** (2003) 042 [arXiv:hep-ph/0309172].

[126] G. Colangelo, J. Gasser, B. Kubis and A. Rusetsky, Phys. Lett. B **638** (2006) 187 [arXiv:hep-ph/0604084].

[127] G. Collazuol, talk given in "Workshop on exotic atoms", Trento , Italy , 19-23 Jun 2006.

[128] T. R. Palfrey and J. L. Uretsky, Phys. Rev. **121** (1961) 1798.

[129] Z. K. Silagadze, JETP Lett. **60** (1994) 689 [arXiv:hep-ph/9411382].

[130] J. R. Batley *et al.* [NA48/2 Collaboration], Phys. Lett. B **633** (2006) 173 [arXiv:hep-ex/0511056].

[131] N. Cabibbo and A. Maksymowicz, Phys. Rev. **137**, (1965) B438

[132] B. Bloch-Devaux, talk given in "QCD 2006", Montpellier , France , 3-7 Jul 2006

[133] S. Pislak *et al.*, Phys. Rev. D **67** (2003) 072004 [arXiv:hep-ex/0301040].

[134] A. Gashi, G. C. Oades, G. Rasche and W. S. Woolcock, Nucl. Phys. A **699** (2002) 732 [arXiv:hep-ph/0108116].

[135] B. Adeva *et al.*, CERN-SPSLC-95-1

[136] B. Adeva *et al.* [DIRAC Collaboration], Phys. Lett. B **619** (2005) 50 [arXiv:hep-ex/0504044].

[137] M. Kermani *et al.* [CHAOS Collaboration], Phys. Rev. C **58** (1998) 3431.

[138] G. Colangelo, J. Gasser and H. Leutwyler, Nucl. Phys. B **603** (2001) 125 [arXiv:hep-ph/0103088].

[139] J. R. Pelaez and F. J. Yndurain, Phys. Rev. D **71** (2005) 074016 [arXiv:hep-ph/0411334].

[140] E. Goudzovski, CERN Particule Physics Seminar, 1th Mar 2005

[141] E. Goudzovski, Rencontres de Physique de la Vallee d'Aoste 2006, La Thuile, Aosta , 6-11 Mar 2006